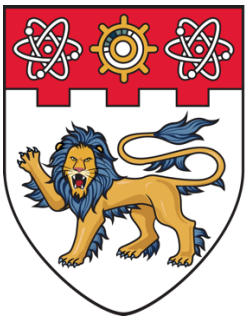

NANYANG TECHNOLOGICAL UNIVERSITY
SINGAPORE

MATERIAL PROPERTIES AND EXPLOSIVE SPALLING OF ULTRA-HIGH PERFORMANCE CONCRETE IN FIRE

LI YE

School of Civil and Environmental Engineering

2018

MATERIAL PROPERTIES AND EXPLOSIVE SPALLING OF ULTRA-HIGH PERFORMANCE CONCRETE IN FIRE

LI YE

School of Civil and Environmental Engineering

A thesis submitted to the Nanyang Technological University

in partial fulfilment of the requirements for the degree of

Doctor of Philosophy

January 2018

Acknowledgement

First of all, the author would like to express his sincere gratitude to his supervisor Professor Tan Kang Hai and Assistant Professor Yang En-hua, for their invaluable guidance, advice, and encouragement throughout the four years of his PhD program. Considerable thanks are also extended to Dr. Zhang Yao and Dr. Nguyen Minh Phuong for their assistance and valuable recommendations.

Special thanks should also extend to the technical staff from Protective Engineering and Construction Technology Laboratory, in particular, Mr. Chelladurai Subasanran, Mr. Tui Cheng Hoon, and Mr. Jee Kim Tian for their assistance in the experimental work.

The author would also like to thank all of the fellow graduate students in his group, i.e., Dr. Namyo Salim Lim, Dr. Weng Jian, Dr. Kang Shao Bo, Dr. Lee Siong Wee, Dr. Pham Anh Tuan, Mr. Cheng Kang, Ms. Fu Qiuni, Mr. Fan Shengxin, Mr. Ng Yan Hao, and Ms. Nguyen Thi Nguyet Hang for their support and friendship. Mr. Liu Jincheng and Mr. Zhang Dong are two members who deserve special mention for their time and effort on the experimental work.

Appreciation are also attended to Professor Pierre PIMIENTA, Dr. Nicolas PINOTEAU, Dr. Jihad MIAH, Dr. MEGE Romain, and Mr. Pierre-Jean DEGIOVANNI at CSTB (France) for their work and help during the spalling tests.

Finally, the author would like to express his utmost gratitude to his parents and his wife Xu Mengdi, who have given encouragement, understanding and support to the author.

Abstract

Ultra-High Performance Concretes (UHPC) has high strength (greater than 150 MPa), high durability, and enhanced fracture energies due to its densely packed microstructure and very low permeability. However, these good features make UHPC more vulnerable to explosive spalling in fire condition. Explosive spalling is generally characterized by a forcible removal of pieces or layers of concrete from the heated surface of a structural element. It compromises the load-carrying capacity of structures because it involves loss of integrity of structures, loss of concrete cross section, and exposure of steel reinforcements to fire. Several mechanisms responsible for explosive spalling have been proposed by a number of researchers. However, the exact mechanism for spalling of UHPC is not yet widely understood or accepted.

This work was aimed at investigating the behavior of UHPC at elevated temperature, especially explosive spalling of UHPC. The main factors involved are polypropylene fiber, polyethylene fiber, steel fiber, and aggregate size. Firstly, an experimental study was carried out to identify control UHPC matrix by Taguchi method. Secondly, residual mechanical properties of UHPC with PP fibers, steel fibers, and larger aggregates after exposure to elevated temperature (from 300 ℃ to 900 ℃) and after water quenching were investigated. Subsequently, the effects of polyethylene (PE)-steel fiber hybridization, water-to-binder ratio, and aggregate size on flexural performance of UHPC were investigated. The microstructure and phase change were investigated by means of field emission scanning electron microscope (FESEM) and X-ray diffraction (XRD).

Thereafter, the focus was switched to transport properties of UHPC. The influence of aggregate size and inclusion of PP and steel fibers on the intrinsic permeability of UHPC at hot state was first investigated. Then, the effects of fiber fraction, geometry, and induced microcracks on the intrinsic residual permeability of UHPC were investigated in detail. A model was proposed to predict residual permeability of UHPC based on image processing and quantification of microcracks.

In the last part, residual permeability was correlated to spalling extent of UHPC. Synergistic effects of combined polypropylene-steel fibers and combined polypropylene fiber-larger

aggregate on explosive spalling prevention of ultra-high performance concrete (UHPC) were investigated. Microstructural analysis highlighted the connectivity of empty PP fiber tunnels through multiple microcracks. This is one of the main differences between UHPC and normal strength concrete.

Table of Contents

Acknowledgement I

Abstract II

Table of Contents IV

List of Tables IX

List of Figures XI

Chapter 1 Introduction 1

1.1 Research background and motivation—fire risk of ultra-high performance concrete (UHPC) 1

1.2 Research objectives and tasks 5

1.3 Research scope and methodology 6

1.4 Novelties 9

1.5 Research roadmap and thesis outline 10

Chapter 2 Literature Review 13

2.1 Overview 13

2.2 Development of ultra-high performance concrete (UHPC) 13

2.2.1 Mechanical properties of UHPC at elevated temperature 15

2.2.2 Transport properties of UHPC at elevated temperature 18

2.2.3 Microstructure change of concrete at elevated temperature 20

2.3 Review of explosive spalling study 21

2.4 Proposed mechanisms of explosive spalling 32

2.4.1 Pore pressure induced stress 32

2.4.2 Thermal stress induced explosive spalling 36

2.4.3 Combined thermal stress and pore pressure 39

2.5 Governing factors 41
2.5.1 Mix design parameters 42
2.5.2 Properties of concrete 50
2.5.3 Structural features related parameters 54
2.5.4 External loading parameters 55
2.6 Summary of literature review 58
Chapter 3 Identification of Mix Proportion of Ultra-high performance Concrete 60
3.1 Overview 60
3.2 Experimental program 60
3.2.1 Taguchi method and design of mixes 60
3.2.2 Materials 62
3.2.3 Preparation of the specimens 63
3.2.4 Testing procedure 64
3.3 Results and discussion 65
3.4 Confirmation of optimization result 70
3.5 Summary 71
Chapter 4 Effect of Elevated Temperature and Water Quenching on UHPC 72
4.1 Introduction 72
4.2 Materials and Experimental Methods 72
4.2.1 Materials and mix proportions 72
4.2.2 Heating and cooling regime 74
4.2.3 Experimental methods 74
4.3 Results and discussions 75
4.3.1 Compressive strength 75

4.3.2 XRD 77
4.3.3 Microstructure and discussion 79
4.4 Summary 84
Chapter 5 Effect of Factors on Flexural Behavior of UHPC 86
5.1 Overview 86
5.2 Experimental program 87
5.2.1 Materials and mix designs 87
5.2.2 Specimen preparation 89
5.2.3 Heat treatment 89
5.2.4 Compressive and flexural test 90
5.3 Compressive strength 92
5.4 Flexural hardening behavior of UHPC 94
5.4.1 Load vs. Deflection behaviors 94
5.4.2 First-crack strength and peak strength 96
5.4.3 Toughness and toughness index 99
5.5 Synergy effect of PE and steel fibers 103
5.6 Behavior of UHPC at elevated temperature 104
5.7 Summary 108
Chapter 6 Effects of Factors on the Hot Permeability of UHPC 110
6.1 Overview 110
6.2 Experimental program 110
6.2.1 Materials and mix proportions 110
6.2.2 Hot permeability test 112
6.2.3 Other measurements 115

6.3 Results and discussions 115

6.3.1 Gas permeability at elevated temperature 115

6.3.2 Microscopic investigation 119

6.3.3 Schematic illustration of influence of PP fibers and larger aggregates on permeability of UHPC at elevated temperature 124

6.4 Summary 126

Chapter 7 Effects of Geometry and Fraction of PP Fibers on Residual Permeability of UHPC and a Prediction Model 128

7.1 Overview 128

7.2 Experimental programs 129

7.2.1 Materials and mix proportions 129

7.2.2 Sample preparation 130

7.2.3 Permeability measurement, microstructure characterization, and microcracks network quantification 131

7.3 Results and discussions 134

7.3.1 Effect of PP fiber dosage and geometry on permeability 134

7.3.2 Microstructure characterization 137

7.3.3 Crack density, crack width, and crack fraction 140

7.4 Model of residual permeability of UHPC with PP 141

7.5 Summary 149

Chapter 8 Effects of Factors on Residual Permeability and Explosive Behavior of UHPC 150

8.1 Overview 150

8.2 Experimental program 150

8.2.1 Mix proportions and materials 150

8.2.2 Explosive spalling test 152
8.2.3 Experimental methods 153
8.3 Results and discussion 154
8.3.1 Extent of spalling and weight loss 154
8.3.2 Gas permeability 158
8.3.3 Microstructure investigation 160
8.4 Summary 165
Chapter 9 Conclusions and Future Work 167
9.1 Conclusions 167
9.2 Future work 169
Publications 171
References 172

List of Tables

Table 1.1 Classification of factors that influence explosive spalling

Table 2.1. Physicochemical processes in Portland cement concrete during heating (Klingsch 2014)

Table 3.1. Mix parameters and levels

Table 3.2. Mix proportions

Table 3.3. Chemical composition of cement

Table 3.4. Finesse of aggregate

Table 3.5. Test results of concrete

Table 3.6. Optimal mix design proportions for mechanical properties of UHPC

Table 3.7. Analysis of variance results of UHPC compressive strength

Table 3.8. Analysis of variance results of UHPC splitting tensile strength

Table 3.9. Analysis of variance results of UHPC uniaxial tensile strength

Table 3.10. Optimum mix-design confirmation test results

Table 4.1. Mix proportions of UHPCs

Table 4.2. Experiments conducted for each mixture

Table 5.1. Mix proportions of UHPCs and fiber volume fractions

Table 5.2. Properties of PE and steel fibers

Table 5.3. Compressive strength of specimens with different W/B ratios and AG sizes

Table 5.4. First-crack strength and peak strength of UHPC mixtures with different W/B ratios

Table 5.5. First-crack strength and peak strength of UHPC mixtures with different AG size

Table 5.6. Properties of PE10ST20 before and after exposure to 300 ℃

Table 6.1. Mix proportions and compressive strength of UHPCs

List of Tables

Table 7.1. Mix proportions of UHPC mixtures

Table 7.2. Values of parameters

Table 8.1. Mix proportions of UHPCs with PP and steel fibers

Table 8.2. Mix proportions of UHPCs

List of Figures

Fig. 1.1. Tunnel element from the Great Belt tunnel fire tested at SP Technical Research Institute of Sweden (Jansson 2013, Khoury and Anderberg 2000).

Fig. 1.2. Fire damage to concrete of Channel Tunnel between France and England indicating severe spalling of the concrete lining and exposure of the reinforcement.

Fig. 1.3. Damage to a multi-story building of the Faculty of Architecture in Delft University of Technology, Netherlands.

Fig. 1.4. To build linkages between UHPC mix design and spalling behavior.

Fig. 1.5. Layout of thesis.

Fig. 2.1. Residual compressive strength of concrete at elevated temperatures (different markers show results from different sources) (Ma, Guo, Zhao, Lin and He 2015).

Fig. 2.2. Compressive strength of concrete at elevated temperature.

Fig. 2.3. Residual splitting tensile strength of concrete at elevated temperatures (different markers show results from different sources) (Ma, Guo, Zhao, Lin and He 2015).

Fig. 2.4. Gas permeability for the mixtures at 1.5 bars after exposure to high temperatures (Liu, Ye, De Schutter, Yuan and Taerwe 2008).

Fig. 2.5. Test setup used by Bošnjak, Ožbolt and Hahn (2013) for the permeability measurements at elevated temperatures.

Fig. 2.6 (a) Water is pouring out on the cold surface of slab during a fire test (b) Thermal image showing the cracks where water reaches the surface (Jansson, Boström and Silfwerbrand 2013).

Fig. 2.7. A view of Gary's test in 1916 (Gary 1916).

Fig. 2.8. Visible saturation layer (Jansson and Boström 2009).

Fig. 2.9. Pressure cell developed by Sertmehmetoglu (Jansson, Boström and Silfwerbrand 2013).

Fig. 2.10. Pore pressure profile during heating of M100 and M30 (Kalifa, Menneteau and Quenard 2000).

Fig. 2.11. Schematic diagram of the NMR setup. The setup has a cylindrical symmetry (der Heijden, Pel and Adan 2012).

Fig. 2.12. Moisture and temperature profiles of a concrete sample with 97% RH (0.07 $m3 \cdot m^{-3}$ moisture content) heated from one side. The temperature at the boiling front is indicated by ▽ in (b). The positions of the thermocouples are indicated by •. The evolution of the profiles in time is indicated by arrows (der Heijden, Pel and Adan 2012).

Fig. 2.13. Arrangement of the HSC specimen and heating device inside the X-ray 3D-CT setup; a) Schematic arrangement; b) Photo of the installation (Stelzner, Powierza, Weise, Oesch, Dlugosch and Meng 2017).

Fig. 2.14. Experimental setup. The neutron beam enters from the right and detected by detector from the left side (Dauti, Weber, Pont, Tengattini, Toropovs and Briffaut 2017).

Fig. 2.15. Maximum vapor pressure and AE behavior of wet sample (Ozawa, Uchida, Kamada and Morimoto 2012).

Fig. 2.16. Proposed spalling risk-based approach for fire spalling design (Bischof, Borgogno and Kaufmann 2017).

Fig. 2.17. Illustration of pore pressure induced spalling of concrete according to References (Consolazio, McVay and Rish III 1997, Consolazio, McVay and Rish III 1998).

Fig. 2.18. The experimental set-up to measure pore pressure (Kalifa, Chene and Galle 2001).

Fig. 2.19. (a) Heating system and (b) insulated specimen during heating.

Fig. 2.20. (a) Temperature inside the radiant panels and in the air gap between the panel and the concrete face, and (b) scheme of the two stages of a test: heating phase and splitting (Felicetti, Lo Monte and Pimienta 2017).

Fig. 2.21. Illustration of thermal gradient induced spalling of concrete according to (Klingsch 2014).

Fig. 2.22. Temperature development at the cylinder surface, in 30 mm depth and in core of the specimen during heating (Klingsch 2014).

Fig. 2.23. Explosive spalling caused by combined thermal stresses and pore pressure (Klingsch 2014).

Fig. 2.24. Comparison of SEM observations of interfacial transition zone (ITZ) between conventional cement mortar and UHPC a. ITZ in Conventional Mortar (Shi and Xie 1998). b. ITZ in UHPC (Prabha, Dattatreya, Neelamegam and Seshagirirao 2010).

Fig. 2.25. Pressure-induced tangential space (PITS).

Fig. 2.26. Intrinsic permeability normalized to that at 80 °C (averages), versus temperature and fiber dosage (Kalifa, Chene and Galle 2001).

Fig. 2.27. Schematic of the water drop test (Kalifa, Chene and Galle 2001).

Fig. 2.28. Scanning electron microscope photos of the virgin concrete with addition of polypropylene fibers (left) and the same concrete exposed to 200 °C for 2 days (right) (Bošnjak, Ožbolt and Hahn 2013).

Fig. 2.29. Explosive spalling envelope after Christiaanse, Langhorst and Gerriste (1972).

Fig. 2.30. Explosive spalling envelope after Zhukov (1976).

Fig. 2.31. Effect of applied load on spalling time of concrete columns (Khoury and Anderberg 2000).

Fig. 2.32. Setup for slab spalling with biaxial compressive loading (Miah, Monte, Felicetti, Pimienta, Carré and Borderie 2017).

Fig. 3.1. Test setup (a). compressive and splitting tensile testing machine (b). uniaxial tensile testing machine.

Fig. 3.2. Main effect plot for compressive strength.

Fig. 3.3. Main effect plot for splitting tensile strength.

Fig. 3.4. Main effect plot for uniaxial tensile strength.

Fig. 3.5. Relationship between splitting and uniaxial tensile strength.

Fig. 4.1. Compressive strengths of UHPC mixtures after heat exposure and water quenching.

Fig. 4.2. Compressive loss rate after water quenching.

Fig. 4.3. XRD patterns of UHPC pastes after furnace cooling and water quenching.

Fig. 4.4. The SEM images of Control, PP, ST, and AG samples at ambient temperature.

Fig. 4.5. The SEM images of UHPC samples after furnace cooling and water quenching at 300 °C. (a/b) Control furnace cooling/water quenching (c/d) PP furnace cooling/water quenching (e/f) ST furnace cooling/water quenching (g/h) AG furnace cooling/water quenching.

Fig. 4.6. The SEM images of samples after furnace cooling and quenching at 600 °C. (a/b) Control furnace cooling/water quenching (c/d) PP furnace cooling/water quenching (e/f) ST furnace cooling/water quenching (g/h) ST furnace cooling/water quenching.

Fig. 4.7. The SEM images of samples after furnace cooling and quenching at 900 °C. (a/b) Control furnace cooling/water quenching (c/d) PP furnace cooling/water quenching (e/f) ST furnace cooling/water quenching (g/h) AG furnace cooling/water quenching.

Fig. 5.1. Micro steel fibers and PE fibers used in this study.

Fig. 5.2. Heating and cooling curve for the cube and prism specimens.

Fig. 5.3. Set-up for compressive test.

Fig. 5.4. Set-up for flexural test.

Fig. 5.5. Typical load–deflection response curves of FRC.

Fig. 5.6. Compressive strength of specimens with different content of PE and steel fibers.

Fig. 5.7. Load–deflection curves of specimens (a) PE00ST00, (b) PE00ST10, (c) PE00ST20, (d) PE05ST00, (e) PE05ST10, (f) PE05ST20, (g) PE10ST00, (h) PE10ST10, (i) PE10ST20, (j) PE00ST00WB03, (k) PE10ST20WB03, (l) PE00ST00AG23, (m) PE10ST20AG23.

Fig. 5.8. First-crack strength of specimens.

Fig. 5.9. Peak strength of specimens.

Fig. 5.10. Toughness at different deflections of UHPC mixtures.

Fig. 5.11. Effect of W/B ratio and larger aggregates on toughness of UHPC mixtures.

Fig. 5.12. Toughness indexes of UHPC mixtures.

Fig. 5.13. Effect of W/B ratio and larger aggregates on toughness index.

Fig. 5.14. FESEM image of steel fiber on UHPC fracture surface (a) end of steel fiber (b) lateral surface of steel fiber.

Fig. 5.15. FESEM image of PE fiber on UHPC fracture surface (a) end of PE fiber (b) lateral surface of PE fiber.

Fig. 5.16. Synergy of PE and steel fibers on toughness of mixtures.

Fig. 5.17. Spalling of UHPC samples after heated to 300 ℃ and 600 ℃.

Fig. 5.18. Cross section of UHPC samples with (a) PP and (b) PE fibers after exposure to 180 ℃.

Fig. 5.19. Cross section of UHPC with steel fiber after exposure to 300 ℃.

Fig. 6.1. Hot permeability test setup.

Fig. 6.2. Intrinsic permeability of UHPCs as functions of temperature.

Fig. 6.3. DSC thermograms of PP fibers.

Fig. 6.4. Normalized permeability relative to Control.

Fig. 6.5. Microstructure of Control (a) before and (b) after exposure to 250 °C for 4 hours.

Fig. 6.6. Microstructure of ST (a) before and (b) after exposure to 250 °C.

Fig. 6.7. Micrographs of PP (a) before and (b) after heating at 150 °C for 4 hours; (c) (e) before and (d) (f) after heating at 180 °C for 4 hours.

Fig. 6.8. FESEM photos of the microstructure of AG (a) before and (b) after exposure to 250 °C.

Fig. 6.9. FESEM photos of the microstructure of PPAG (a) before and (b) after exposure to 250 °C.

Fig. 6.10. Model of permeability of (a) normal concrete with PP fibers and larger aggregates (Mazzucco, Majorana and Salomoni 2015), (b) UHPC with PP fibers, (c) UHPC with larger aggregates, and (d) UHPC with PP fibers and larger aggregates at elevated temperature.

Fig. 7.1. Image processing procedure (a) FESEM image of an impregnated and grinded sample, (b) Montage of the Images produced by stitching, (c) Binary image after cleaning showing detectable microcracks, (d) Conversion of binary image of cracks into cracks skeleton.

Fig. 7.2. Intrinsic permeability of UHPC as a function of PP (a) fiber dosage, (b) fiber length, (c) fiber diameter, (d) fiber dosage and fiber length, and (e) fiber dosage and fiber diameter.

Fig. 7.3. Permeability of group 4 and group 5 UHPCs.

Fig. 7.4. Typical microstructure of UHPC after exposure to high temperature. (a) fiber tunnels far from each other, (b) fiber tunnels contact in parallel, and (c) fiber tunnels contact with an angle.

Fig. 7.5. Average crack width, crack fraction, and crack density.

Fig. 7.6. Schematics showing the idealization of PP fiber reinforced UHPC consisting of (a) PP fiber tunnels, (b) microcracks (black) in UHPC matrix (grey background), (c) system with PP fibers isolated, and (d) system with PP fibers connected.

Fig. 7.7. Percolation probability against fiber and crack parameters (a) *p* calibrated by groups 1 to 3, (b) *p* validated by groups 4 and 5.

Fig. 7.8. Comparison between the measured and estimated permeability of UHPC.

Fig. 7.9. Difference between the measured permeability and the permeability of matrix-microcrack phase varies with percolation probability.

Fig. 8.1. Specimens in furnace.

Fig. 8.2. Spalling extent of UHPCs with different PP and/or steel fibers after exposing to elevated temperature.

Fig. 8.3. Spalling extent of specimens with different PP fiber content and aggregate size after spalling test.

Fig. 8.4. Weight loss of UHPC specimens with (a) different PP and/or steel fibers contents (b) different PP contents and aggregate sizes after spalling test.

Fig. 8.5. Permeability of specimens after exposure to 200 ºC (a) UHPC with PP and steel fibers (b) UHPC with PP fibers and larger aggregates.

Fig. 8.6 Weight loss as a function of residual permeability of samples.

Fig. 8.7. Micrographs of UHPC with only PP fibers (P6-S0) (a) before and (b) after exposure to 200 °C.

Fig. 8.8. Micrographs of UHPC with only steel fibers (P0-S236) (a) before and (b) after exposure to 200 °C.

Fig. 8.9. Micrographs of UHPC with both PP and steel fibers (P6-S236) (a) before and (b) after exposure to 200 °C.

Fig. 8.10. Micrographs of UHPC with both PP fibers and larger aggregates after exposure to 250 °C.

Fig. 8.11 Conceptual illustration of microstructure of UHPC with (a) PP fibers, (b) steel fibers, and (c) hybrid PP and steel fibers after heating.

Chapter 1 Introduction

1.1 Research background and motivation—fire risk of ultra-high performance concrete (UHPC)

Concrete is the most widely used construction material due to its excellent strength, durability, constructability, and good fire resistance compared to steel and timber. Over the past three decades, great advances have been made in mix designs of High-Performance-Concrete (HPC). Most recently, Ultra-High Performance Concrete (UHPC) with strength greater than 150 MPa, high durability, and enhanced fracture energies was developed. With these excellent properties, UHPC can be applied in a variety of structures and buildings, such as bridges, tunnels, offshore structures, highways, and high-rise buildings (Peng 2000). UHPC has been adopted for some structures. For instance, some bridges have been designed using UHPC in United States, Europe, and China. The first UHPC simply supported bridge with two spans was built in France in 2002. Later, a pedestrian bridge spans 120 m was constructed in Seoul, Korea. The first UHPC bridge in US was built in Wapello County, Iowa in 2006. The first UHPC footbridge was constructed in Changsha, China, in 2016 (Dong 2018). UHPC was also used to build Façade of Jean Bouin Stadium in Paris, France and Pulaski Skyway in New Jersey, United States.

Fire resistance of reinforced concrete (R/C) structure mainly depends on the behavior of concrete material under fire. Compared to wood, plastic, and steel, concrete in general has superior fire resistance because of its non-combustible nature and relatively low thermal conductivity. However, UHPC structures may be more vulnerable to fire due to reduced element dimension. UHPCs are tailored at micro- and meso-scales to obtain dense microstructure. Their low permeability, however, makes UHPC more vulnerable to explosive spalling in fire conditions (Klingsch 2014). In addition, since most of the accidental fires are extinguished by hose streams, the residual mechanical strength of UHPC and the effect of rapid cooling should also be studied.

Explosive spalling is generally characterized by forcible removal of pieces or exfoliation of concrete layers from the heated surface of the structural element (Bosnjak 2014, Khoury and

Anderberg 2000). The process of spalling could be progressive, or in one shot. When explosive spalling occurs, it causes a serious effect on the fire resistance of structures, because it results in loss of structural integrity, loss of concrete cross section, and exposure of steel reinforcement to fire. The residual cross section of the concrete structure may not have sufficient load-bearing capacity to sustain imposed loads, and the unprotected steel reinforcement could reach the yield strength faster when directly exposed to fire. The accidental damage caused by spalling may lead to reduced levels of structural safety in fire conditions.

In the Great Belt Tunnel fire in Denmark in 1994, a tunnel boring machine caught fire. The primary fuel was hydraulic oil from the tunnel boring machine. The fire lasted 7 hours and the maximum temperature reached around 800 °C. The concrete of the tunnel linings had 28-day strength of 76 MPa. Spalling caused two-third loss of the 400-mm thick tunnel lining segment as shown in Fig. 1.1 (Jansson 2013, Khoury and Anderberg 2000).

Severe spalling also occurred in another well-known tunnel fire in the Channel Tunnel connecting England and France on 18th November 1996. The fire started at one end of the train with heavy goods vehicle (HGV). The fire lasted for about 2.5 hours, and the maximum temperature was estimated to be 1100 °C, resulting in severe spalling damages along 50 m length of the concrete tunnel lining (Authority and Allison 1997, Shuttleworth 1997). The mature strength of concrete at 28-day was 110 MPa. The 0.4 m thick tunnel lining was reduced to a mere mean depth of 0.17 m. The thinnest region was just 0.02 m (Fig. 1.2). Fortunately, the zone with extensive damages was in a rock layer, which prohibited water from entering the tunnel.

Fig. 1.1. Tunnel element from the Great Belt tunnel fire tested at SP Technical Research Institute of Sweden (Jansson 2013, Khoury and Anderberg 2000).

Other than infrastructure, fire also has disastrous effects for buildings. As shown in Fig. 1.3, a large-scale fire occurred in a multi-story building in Delft University of Technology on 13th May 2008. The huge fire caused part of the building to collapse as a consequence of the prolonged fire exposure (Lottman 2017). The building was demolished afterwards as the cost of repair was far too high compared to the construction cost.

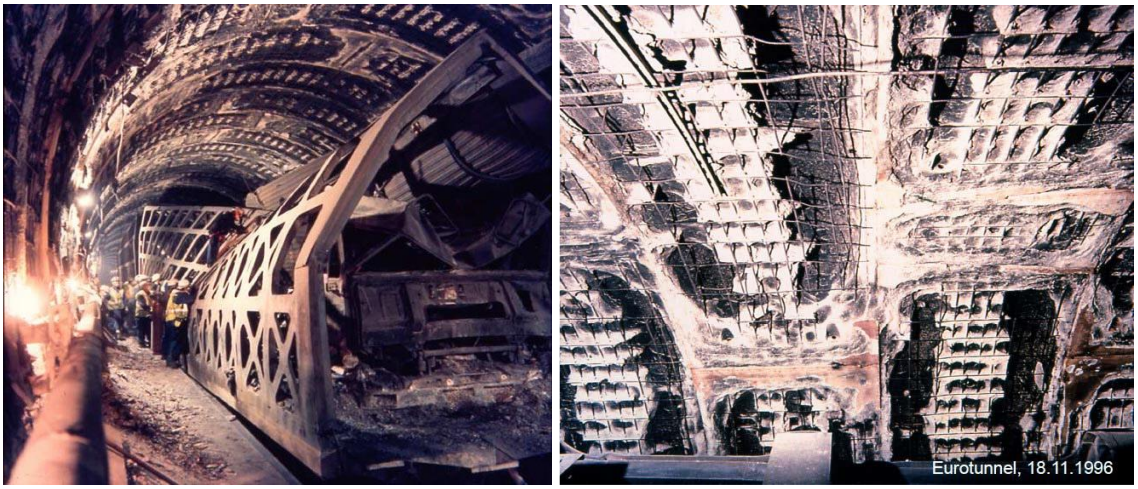

Fig. 1.2. Fire damage to concrete of Channel Tunnel between France and England indicating severe spalling of the concrete lining and exposure of the reinforcement.

Fig. 1.3. Damage to a multi-story building of the Faculty of Architecture in Delft University of Technology, Netherlands.

In the past 20 years, although extensive research has been carried out at various laboratories worldwide to determine the mechanism of explosive spalling, the structural fire engineering community has not come to a consensus on the mechanism of explosive spalling. Concrete is usually treated as a homogeneous material and spalling is analyzed at macro-scale. However, explosive spalling of concrete is a local phenomenon. The investigation should delve deeper into the physical and chemical changes in the microstructure of concrete to better understand the changes caused by aggregates, fibers, and decomposition of cement paste during and after a fire.

Although different methods have been attempted, neither engineering nor theoretical models exist to reasonably predict the risk and extent of explosive spalling. The prediction of spalling has been on an empirical basis, showing the likelihood of spalling against various parameters (i.e., moisture content, applied load level, and permeability). However, due to a large variety of concretes and the rapid development of concrete technology, the proposed empirical relationships are not widely applicable especially for UHPCs. Numerical models that try to include all the thermo-hygro-mechanical processes may be able to predict explosive spalling in idealized cases with accurate input data of material parameters. However, the parameters are not always available or can be determined through material characterization tests.

Many experimental tests have been carried out on critical factors affecting explosive spalling. Mix proportions of concrete were changed, and different admixtures were added to investigate their effects on spalling behavior of concrete on macro-scale. The conclusions of experimental and numerical studies from different sources may not be consistent and are often contradictory in some cases. This is partly due to (a) a variety of mix designs in different studies such as water-to-binder ratio, silica fume content, and fiber content, (b) heterogeneous nature of concrete materials, (c) different experimental conditions, and (d) lack of standard test method for explosive spalling. Due to the above-mentioned difficulties, it is still a challenge to understand mechanisms of explosive spalling and to find the optimized method to prevent spalling.

1.2 Research objectives and tasks

UHPC structures have smaller footprints, higher durability, and higher sustainability. Despite the great potential, performance of UHPC under fire condition must be investigated before practically designing of UHPC structures. Behavior of UHPC at elevated temperature, especially explosive spalling holds the key to the survival of a reinforced UHPC structure when subject to fire conditions. To evaluate the risk of explosive spalling, a better understanding of the spalling mechanism is the prerequisite condition. Mechanical properties of UHPC at elevated temperature is important for structure design. Since most of the

accidental fires are extinguished by hose streams, the residual mechanical strength of UHPC is crucial for the safety of post-fire structures.

From the shortcomings of previous studies on behavior of UHPC at elevated temperature, as well as from the need to further understand mechanisms of explosive spalling, a research program is designed and presented in this study. From literature review, steel fibers, PP fibers, PE fibers, and aggregate size were selected as key factors to be investigated. Measurements of permeability, strength, and spalling behavior of UHPC at elevated temperature and residual state will be carried out, together with the microstructural analysis and the development of semi-empirical model for prediction of permeability. The research is aimed at the following objectives:

1. To gain an overall understanding of UHPC behavior at elevated temperature, especially mechanisms of explosive spalling, by conducting a state-of-the-art review.
2. To evaluate the effects of steel fibers, PP fibers, PE fibers, and aggregate size on mechanical performance of UHPC at ambient and at elevated temperature.
3. To investigate the individual and combined effects of steel fibers, PP fibers, and aggregate size on transport property of UHPC at elevated temperature.
4. To fill the gap of knowledge on the effect of geometry and fraction of PP fibers and induced microcracks on permeability of UHPC when subjected to elevated temperature.
5. To investigate the individual and combined effects of steel fibers, PP fibers, PE fibers, and aggregate size on spalling behavior of UHPC, and build linkage between permeability and spalling risk.

1.3 Research scope and methodology

Factors that influence explosive spalling are summarized from previous work (Hertz 2003, Khoury and Anderberg 2000, Kodur 2000, Kodur and Phan 2007) and can be organized into four main categories as shown in Table 1.1. Parameters in each category may depended on each other. Just because of this, to investigate their effects on explosive spalling separately,

they need to be separated into different categories, in which they do not interfere with each other. For example, changing water-to-binder ratio will influence both permeability and strength of concrete etc. By changing water-to-binder ratio alone, it is impossible to distinguish the effect from permeability and strength.

The current research concentrates on the behavior of UHPC at material level. This research is mostly confined to very dense UHPCs with silica fume. Fine quartz sands (<5 mm) were selected as aggregates. Low water-to-binder ratio (lower than 0.22) was used to achieve dense microstructure. Specimens were cured in water to control the curing environment. Concrete age is fixed at 28 days. Dosage of polypropylene (PP), polyethylene (PE), and steel fibers, and aggregate size were selected as variables, since their effects on UHPC at elevated temperature are significant but their roles are not adequately understood. Since PP fibers are considered the most important factor influencing spalling, length and diameter of PP fibers were also investigated. A detailed review of the effects of these factors will be presented in Chapter 2.

Table 1.1 Classification of factors that influence explosive spalling.

Category	Mix design and curing condition	Properties of concrete	Structural features	External loading
Factor	*Aggregate size*	*Permeability*	Section size	Load intensity
	Steel fiber	*Compressive strength*	Section shape	*Heating rate*
	Polypropylene fiber	*Tensile strength*	Reinforcement ratio	Heating profile
	Polyethylene fiber	Thermal expansion	Cover to reinforcement	
	Silica fume	Porosity	Supplementary reinforcement	
	Type of aggregate	Moisture content	Degree of surrounding restraint	
	Water/binder ratio			
	Curing condition			
	Concrete age			

As mentioned in Section 1.1, conclusions of experimental and numerical studies for explosive spalling are often contradictory due to the variety of mix designs and experimental testing conditions. Fig. 1.4 shows the methodology of this study to reveal fundamental

mechanisms of explosive spalling. PP, PE, and steel fibers, and aggregate size are the key variables in UHPC mix design. Spalling extent will be evaluated by using weight loss ratio of specimens on macro scale. Instead of relating mix proportions directly to spalling behavior, intrinsic material properties such as compressive strength, tensile strength, and permeability will be measured as objective indexes to minimize influences from testing conditions and concrete mix proportions. Compressive strength is the most fundamental property of concrete for engineering practice, while tensile strength is widely considered as the governing failure criterion of spalling. Permeability is an important intrinsic material property governs moisture transport and pore pressure build-up, which will be measured at both hot and residual state. Furthermore, microstructure of UHPCs before and after exposure to elevated temperature will be analyzed to understand the mechanism behind the phenomenon. Image analysis will be used to quantify microcracks and cement paste of UHPC after heating. A model will be built to predict permeability of UHPC. Relationship between UHPC mix proportions, changes of microstructure, material properties, and spalling behavior will be studied.

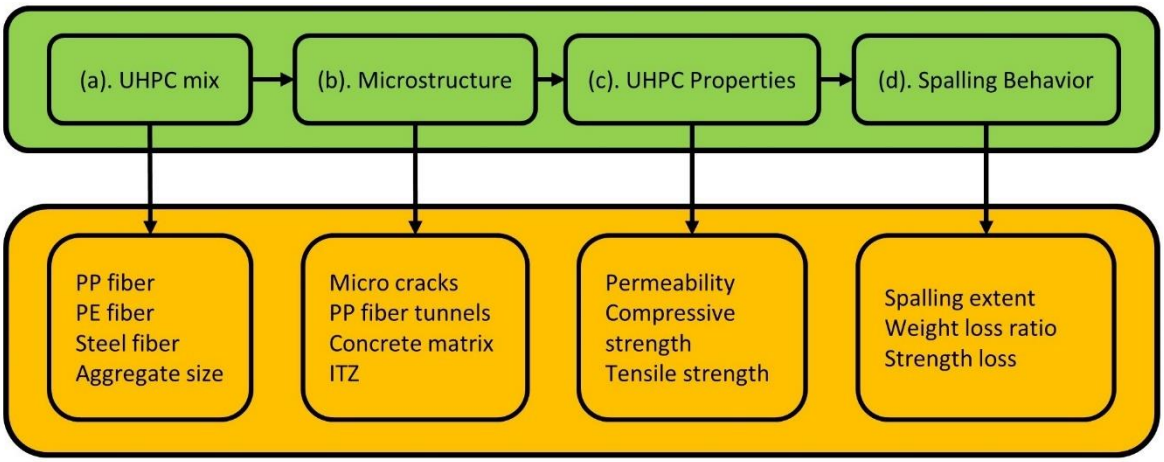

Fig. 1.4. To build linkages between UHPC mix design and spalling behavior.

1.4 Novelties

This thesis aims to investigate behavior of UHPC under elevated temperature. For this purpose, experimental studies on mechanical properties, transport properties, and spalling behavior were conducted.

- Effects of PP fiber, steel fiber, PE fiber, and aggregate size on mechanical properties of UHPC at ambient and elevated temperature were investigated, since investigations on performance of UHPC at elevated temperature are limited.
- Effects of thermal shock caused by water quenching on residual strength of UHPC were studied to provide useful information on post-fire behavior of RC structures.
- Effects of factors on spalling behavior and permeability of UHPC at both elevated temperature and residual state were investigated. Synergistic effect was found between factors on increase of permeability and spalling risk of UHPC.
- Clear correlation was identified between residual permeability and extent of spalling of UHPC mixes, which shows residual permeability can be used to evaluate risk of spalling of UHPC.
- Microstructure of UHPC before and after elevated temperature exposure were examined to reveal potential mechanisms responsible for changes in permeability. Schematic models were proposed to explain the mechanisms.
- Effects of PP fiber fraction and geometry on intrinsic residual permeability of UHPC after elevated temperature exposure were investigated, which can provide guidance for selection of PP fibers in spalling prevention.
- Quantifiable model correlating PP fibers and microcracks was proposed to estimate residual permeability of UHPC based on a newly developed method for quantification of microcrack characteristics.

1.5 Research roadmap and thesis outline

Fig. 1.5 shows the roadmap of this study. This thesis consists of four parts including nine chapters, which cover the introduction, literature review, experimental investigation, proposed model, mechanism of spalling established from the experimental work, conclusions achieved from the study, and future work. In Chapter 1, the author introduces the background, motivation, objectives, methodology, and outline of the present research. A detailed literature review on UHPC and explosive spalling of concrete at elevated temperature is given in Chapter 2. Apart from a critical overview on explosive spalling, the governing factors and mechanisms of explosive spalling are summarized.

The second part consists of the tests on mechanical and transport properties of UHPC. In Chapter 3 ((a) and (c) in Fig. 1.4), an experimental study is carried out to optimize the compressive strength, splitting tensile strength, and uniaxial tensile strength using Taguchi method. The respective contribution of each factor is identified. Attention is then given to the loss in compressive strength of UHPC after exposure to elevated temperature up to 900 ℃ and after water quenching in Chapter 4 ((a) to (c) in Fig. 1.4). The relationship between UHPC decomposition, change of microstructure, and loss in compressive strength is elaborated in Chapter 4. In Chapter 5 ((a) to (d) in Fig. 1.4), the scope is extended to the effect of polyethylene (PE)-steel fiber hybridization, water to binder ratio, and aggregate size on mechanical properties of UHPC at ambient and elevated temperature. This chapter is concluded by a discussion on the efficiency of PE fibers on preventing explosive spalling.

Permeability of UHPC is studied in Chapter 6 and Chapter 7. Chapter 6 ((a) to (c) Fig. 1.4) describes the influence of inclusion of PP fibers, steel fibers, and aggregate size on intrinsic permeability of UHPC at elevated temperature. Hot permeability measurements are performed on UHPCs subjected to elevated temperature up to 300 °C. Microstructure of UHPC samples before and after exposure to elevated temperature is studied to reveal potential mechanisms responsible for changes of permeability. A further in-depth study on effect of PP fiber fraction, geometry, and induced microcracks on the intrinsic residual permeability of UHPC is presented in Chapter 7 ((a) to (c) in Fig. 1.4). First, this investigation is based on permeability measurements and microstructure analysis. An image

analysis method for identification and quantification of microcrack characteristics in UHPC samples is elaborated. Subsequently, a semi-empirical model based on quantification of PP fiber channels and micro cracks is proposed to predict their effects on residual permeability of UHPC. The understanding gained will help to explain mechanism of permeability changes and spalling prevention.

After investigating the fundamental properties of UHPC, it is important to develop linkages between measurements of permeability and spalling extent, which is the topic of Part 3. Chapter 8 ((a) to (d) in Fig. 1.4) covers two sets of UHPC mix proportions to investigate the synergistic effects of combined PP fibers and steel fibers, and larger aggregates on explosive spalling behavior of UHPC at elevated temperature. Residual permeability of UHPC is measured at the critical temperature (200 °C) and correlated to the extent of spalling quantitatively. This will clearly highlight the contribution of vapor pressure build-up on explosive spalling and will provide a good basis to establish the spalling mechanism to be established. This chapter is concluded by microstructure of UHPC before and after elevated temperature exposure, which reveals the potential mechanisms responsible for the synergistic effect of PP fibers and steel fibers and PP fibers and larger aggregates on permeability and spalling extent.

Chapter 9 summarizes the conclusions in the preceding chapters and proposes research recommendations for future studies.

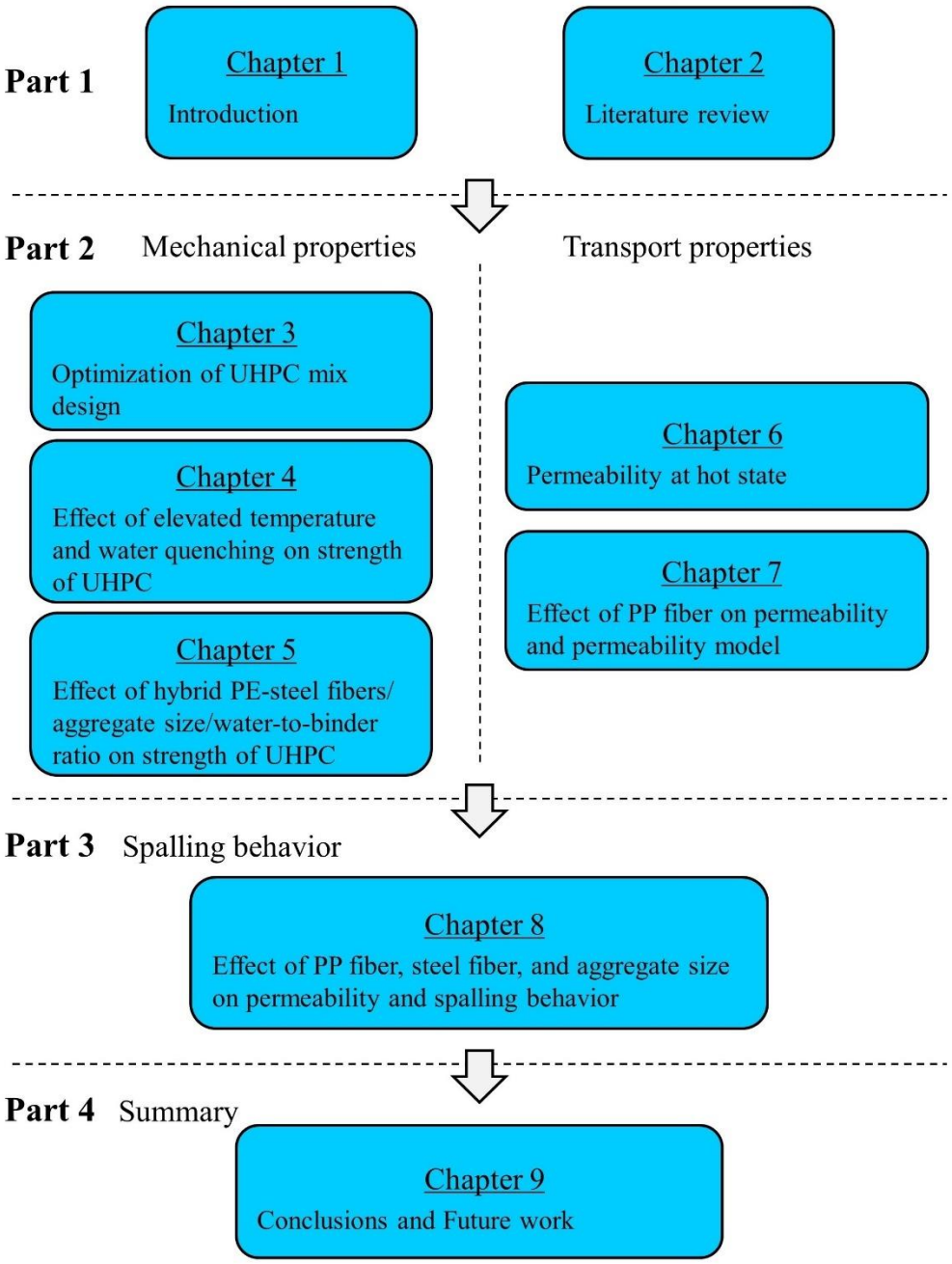

Fig. 1.5. Layout of thesis.

Chapter 2 Literature Review

2.1 Overview

In Chapter 1, the knowledge gaps of explosive spalling of UHPC are introduced. Under fire condition, UHPC undergoes severe degradation on mechanical properties and even explosive spalling. To investigate the mechanism of explosive spalling and to minimize this phenomenon, since the 1980s, both theoretical and experimental studies have been conducted. In this chapter, first a review of the development of UHPC is presented. Then a survey of experimental work regarding mechanical and transport properties of UHPC at elevated temperatures is presented. The chemical dehydration process and associated changes in microstructure are also elaborated. Thereafter, attention is given to explosive spalling study. Three main proposed mechanisms of explosive spalling are introduced and discussed. In the last section, the main factors influencing explosive spalling are divided into four categories. Their effects on spalling are illustrated.

2.2 Development of ultra-high performance concrete (UHPC)

Concrete is a composite material composed of aggregates bonded together with hardened cement paste. The first publication related to UHPC was published by (Richard and Cheyrezy) and UHPC was first published by (de Larrard and Sedran 1994). Over the past three decades, great advancement has been made in concrete technology in the design mixes of high-performance concrete (HPC) (Neville and Aitcin 1998). UHPC with high strength, high durability, high ductility, and enhanced fracture energy was also developed (Wille, El-Tawil and Naaman 2014, Wittmann, Wang, Zhang and Zhao 2015, Yoo, Shin, Yang and Yoon 2014, Yu, Spiesz and Brouwers 2014). UHPC is produced with high quality cement, low water-to-binder ratio, and different kinds of fibers to enhance ductility. The main principles for producing UHPC are reduction in porosity, enhancement in homogeneity, and improvement in microstructure. The dense and uniform microstructure of UHPC is due to the following effects: (1) closed packing of solid particles; (2) enhanced hydration and

pozzolanic reaction of cementitious materials; and (3) improvement of interfacial transition zone (ITZ) between aggregates and cement matrix (Shi, Wu, Xiao, Wang, Huang and Fang 2015).

To achieve these properties, the production of UHPC needed thermal curing at 90 °C or higher temperature with pressure. The low production efficiency and high energy consumption impeded large-scale application of UHPC. Therefore, subsequent researchers have been looking for common technology and materials to lower the cost and increase the efficiency of casting UHPC (Wang, Yang, Liu, Wan and Pu 2012, Wille, Naaman and Parra-Montesinos 2011). Conventional river sand has been used to replace refined silica sand. Incorporation of coarse aggregates also gave promising mechanical properties (Yang, Millard, Soutsos, Barnett and Le 2009).

Effects of inclusion of different fibers and admixtures on mechanical properties of concretes were investigated (Ahmed, Maalej and Paramasivam 2007, Boulay, Rossi and Tailhan 2004, Choumanidis, Badogiannis, Nomikos and Sofianos 2016, Habel, Viviani, Denarié and Brühwiler 2006, Kim, Park, Ryu and Koh 2011, Liu, Han, Cui, Zhang, Lv, Zhang and Yang 2016, Park, Kim, Ryu and Koh 2012, Richard and Cheyrezy 1995, Rossi, Arca, Parant and Fakhri 2005, Wille, Kim and Naaman 2010). Holschemacher, Mueller and Ribakov (2010) investigated the effect of steel fibers on mechanical properties of high-strength concrete. Material and bond properties of UHPC with micro steel fibers were reported by Yoo, Shin, Yang and Yoon (2014). Sanjuán, Argiz, Gálvez and Moragues (2015) and Mazloom, Ramezanianpour and Brooks (2004) studied the effect of silica fume (SF) on mechanical properties of high-strength concretes. Arunachalam and Jayakumar (2015) investigated effects of polypropylene fibers.

To further improve mechanical performance of UHPC, hybridization of fibers with different geometry and mechanical properties was investigated and showed favorable effect on mechanical properties (Ahmed, Maalej and Paramasivam 2007, Banthia and Gupta 2004, Banthia and Nandakumar 2003, Hsie, Tu and Song 2008, Qian and Stroeven 2000, Rossi, Arca, Parant and Fakhri 2005, Sivakumar and Santhanam 2007, Yao, Li and Wu 2003). Skazlić and Bjegović (2008) found that UHPC mixture with hybrid straight and hooked steel

fibers showed better flexural behavior than a mixture with only straight steel fibers for the same mass fraction. Kim, Park, Ryu and Koh (2011) found that using a mixture of micro and macro steel fibers improved the deflection capacity and toughness. Dawood and Ramli (2011) studied fibers in different materials and found that a hybrid mixture of steel, palm and barchip fibers with at least 1.5% volumetric fraction of steel fibers significantly improved compressive strength and flexural behavior of FRC. Yao, Li and Wu (2003) also found that polypropylene (PP), carbon, and steel fibers, when used in a hybrid form, could result in superior composite performance. Tensile strength of polyethylene (PE) fiber is much higher than that of PP and Polyvinyl alcohol (PVA) fiber (Choi, Lee, Ranade, Li and Lee 2016). The hydrophobic nature of PE fiber eliminates chemical bond between PE fiber and concrete matrix, which could significantly enhance the complimentary energy of fiber bridging (Ranade, Li, Stults, Heard and Rushing 2013). The use of polyethylene (PE) fibers on the development of UHPC has been documented in previous studies (Choi, Lee, Ranade, Li and Lee 2016, He, Qiu, Li and Yang 2017). However, the investigations on effects of various factors on UHPC, especially in fire condition, are still limited.

2.2.1 Mechanical properties of UHPC at elevated temperature

Under fire, concrete experiences serious damages at both micro- and meso-scales, which result in degradation of mechanical properties. Since many conditions such as specimen size, loading conditions, and hot/residual states influence the testing results of concrete, to examine the temperature effect based on a unified standard, the residual strength tested with unstressed cube specimens were studied by Ma, Guo, Zhao, Lin and He (2015). Three stages of changing in strength can be observed form Fig. 2.1:

1. From ambient temperature to 200 °C, compressive strength of concrete remained constant or even greater than the initial strength. For few concretes, this trend even continued until 300 °C.
2. From 200-800 °C, compressive strength decreased significantly.
3. Beyond 800 °C, concrete lost almost all its compressive strength.

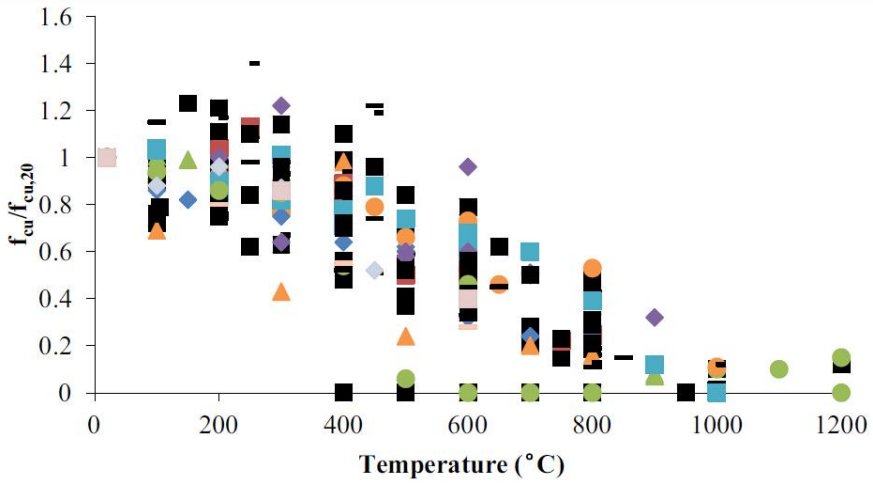

Fig. 2.1. Residual compressive strength of concrete at elevated temperatures (different markers show results from different sources) (Ma, Guo, Zhao, Lin and He 2015).

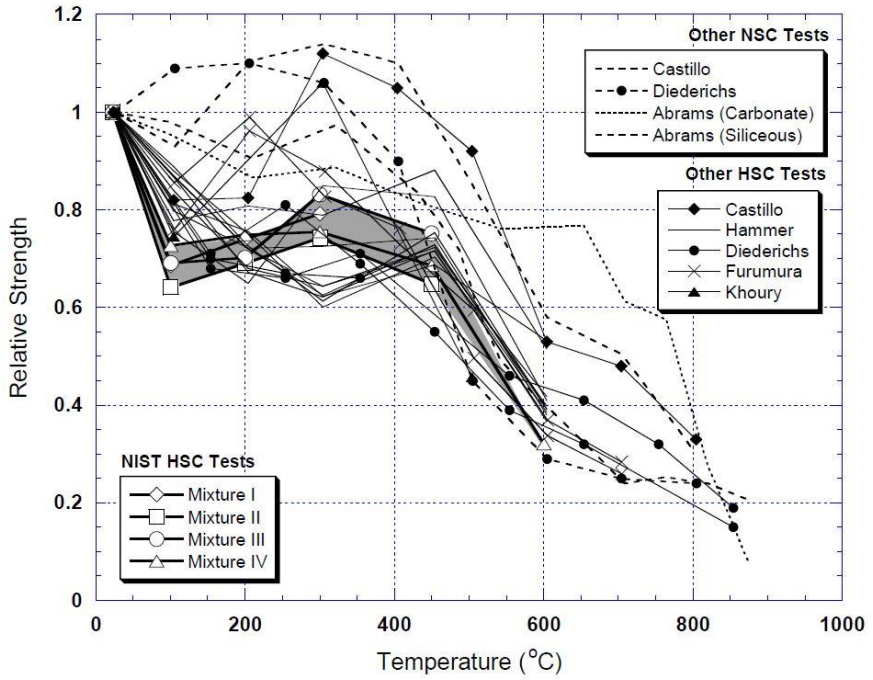

Fig. 2.2. Compressive strength of concrete at elevated temperature.

Phan (2002) summarized the results of compressive strength measurements of NSC and HSC at elevated temperature as shown in Fig. 2.2. The results have significant scatter. Compressive strength of some concretes dropped significantly after exposure to 100 °C, but recovered or even increased after heated to 300 °C. The loss of strength at 100 °C is

attributed to weakening of van der Waals' forces due to expansion of water molecules pushing apart the CSH layers further apart (Khoury 2000). Between 300 °C and 800 °C, most concretes experienced a constant strength decrease. At temperature beyond 800 °C, compressive strength almost completely lost. It was reported that the compressive strength of UHPC declined more than that of HPC with an increase in temperature but showed a higher strength at residual state. The relatively lower hot-state strength of UHPC could be attributed to higher inner vapor pressure (Khoury 2000).

Similar to compressive strength, splitting tensile strength of concretes increased before 200 °C, and then decreased with increasing temperature at nearly a linear rate (Fig. 2.3). The increasing trend before 200 °C is very clear for high strength concretes (HSC) (Chen and Liu 2004, Xiong and Richard Liew 2015, Zhao 2012). There are two prevailing hypotheses, although the exact reason is still unclear. First, the increase of strength is attributed to the increased Van der Walls forces among the gel particles due to loss of water (Behnood and Ziari 2008, Castillo and DurraniI 1990). Second, further hydration of unhydrated cement particles due to internal autoclaving condition occurs as a result of high temperature and water vapor pressure (Saad, Abo-El-Enein, Hanna and Kotkata 1996). The second explanation is particularly applicable for UHPC with silica fume as the large fraction of unhydrated cement and high vapor pressure caused by low permeability.

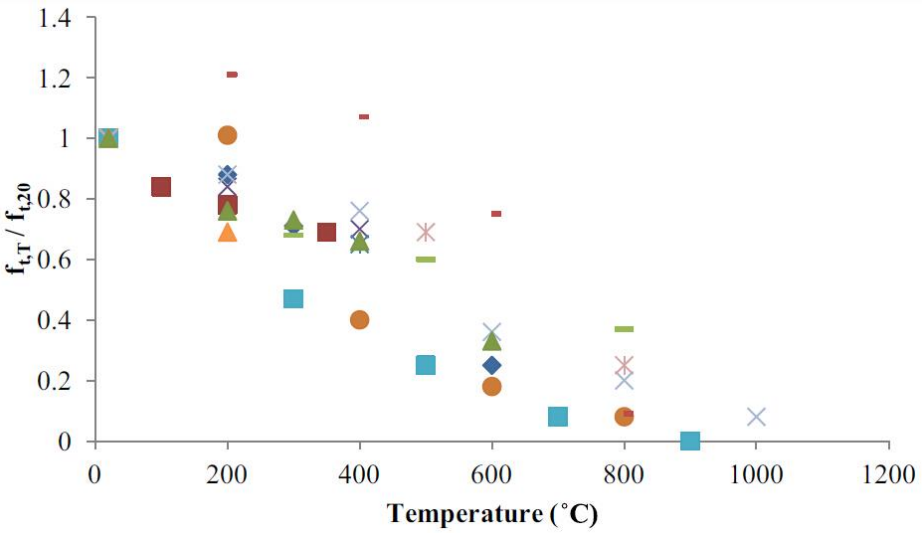

Fig. 2.3. Residual splitting tensile strength of concrete at elevated temperatures (different markers show results from different sources) (Ma, Guo, Zhao, Lin and He 2015).

2.2.2 Transport properties of UHPC at elevated temperature

Permeability is a measure of the ability of a porous material to transfer fluids under pressure gradient. For ordinary concrete the main influencing factors of permeability are the porosity and connectivity of capillary pores (Powers and Brownyard 1946). Previous studies mainly focused on the effect of elevated temperature on permeability of normal concrete and high strength concrete (Klingsch, Lu, Kässmann and Tan 2015, Loosveldt, Lafhaj and Skoczylas 2002, Noumowe, Siddique and Debicki 2009, Zeiml, Lackner, Leithner and Eberhardsteiner 2008). Investigation on intrinsic permeability of UHPC at elevated temperature was rather limited. Besides, most of the permeability measurements were performed at residual state, i.e. the permeability was measured after the heated specimens were cooled down to ambient temperature (Gawin, Alonso, Andrade, Majorana and Pesavento 2005, Kalifa, Chene and Galle 2001, Liu, Ye, De Schutter, Yuan and Taerwe 2008, Noumowe, Siddique and Debicki 2009, Zeiml, Lackner, Leithner and Eberhardsteiner 2008, Zeiml, Leithner, Lackner and Mang 2006). The results may not be the same as the permeability at hot state due to changes in microstructure after nature cooling to ambient temperature.

Noumowe, Siddique and Debicki (2009) measured the effect of elevated temperature on permeability of HPC with and without PP fibers up to 600 ℃. He found that after exposed to 200 ℃, the permeability of PP fiber reinforced HPC was greater than that of plain HPC. Liu, Ye, De Schutter, Yuan and Taerwe (2008) investigated the role of PP fibers at elevated temperature in self-compacting cement (SCC) paste samples (Fig. 2.4). Permeability increased with increasing temperature. PP fibers significantly increased permeability of both SCC and HPC. They concluded that the connectivity of pores is the major factor that determines the gas permeability below 300 °C. Since no significant increase in total pore volume was detected after the PP fibers melted, connectivity of isolated pores increased. For higher temperatures microcracks were the major factor.

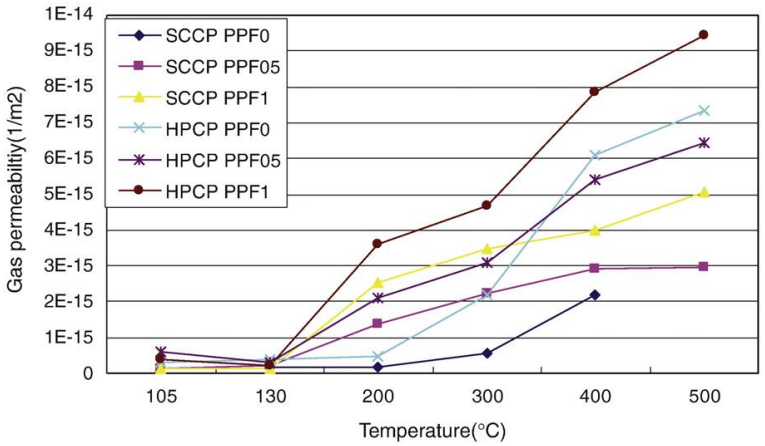

Fig. 2.4. Gas permeability for the mixtures at 1.5 bars after exposure to high temperatures (Liu, Ye, De Schutter, Yuan and Taerwe 2008).

Bošnjak, Ožbolt and Hahn (2013) developed a test setup for permeability measurements of HPC with and without PP fibers at ambient and elevated temperature (Fig. 2.5). Plain concrete showed a steady increase in permeability with increasing temperature, whereas concrete with PP fibers exhibited a sudden increase of permeability between 80 °C and 130 °C. Softening of fibers and weak concrete-fiber interface were considered the main reasons for permeability increase below the PP fiber melting point (160 to 170 °C). SEM observation suggested that it was difficult for the melted PP fibers to be absorbed by the HPC matrix. Instead, they flowed into the surrounding micro-cracks.

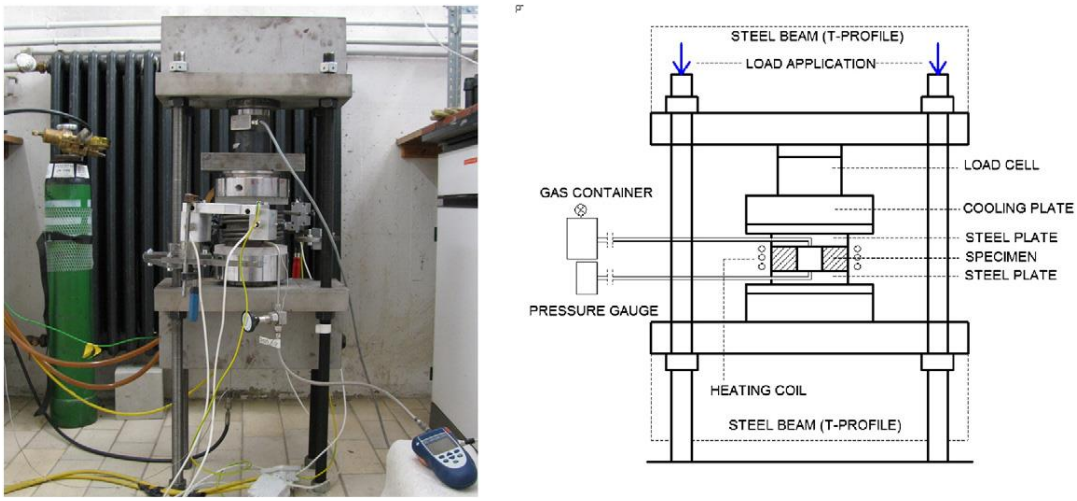

Fig. 2.5. Test setup used by Bošnjak, Ožbolt and Hahn (2013) for the permeability measurements at elevated temperatures.

Generally speaking, the measured permeability values from literatures exhibited large scatter due to vast differences in mix proportions, measurement methods, and heating curves. A significant size effect on microcracks and transport properties was found in the research from Wu, Wong and Buenfeld (2015) on the effect of drying-induced microcracking on permeability. Samples with smaller thickness/maximum aggregate size (t/MAS) ratios had more severe microcracking and higher permeability. Gas permeability decreased with increasing t/MAS. A t/MAS of at least 10 is required to obtain consistent gas permeability values. However, for permeability measurements of concrete with coarse aggregates, meeting this requirement is almost impossible. Thus, the size effect must be considered when interpreting permeability results. Moreover, although there are some studies on the microstructure change of UHPC after exposure to elevated temperature, the change on microstructure cannot be quantitatively evaluated and linkage between microstructure and permeability has not been established yet. This will be one of the objectives of current research and is described in Chapter 6 and Chapter 7.

2.2.3 Microstructure change of concrete at elevated temperature

Mechanical and transport properties are highly dependent on microstructure of concrete, which is greatly affected by elevated temperature. When concrete is heated, several physicochemical processes develop, which affect the cement paste by removal of water present in various forms in the cement paste. Thus, the porous system is subject to significant changes due to the loss of water content and decomposition of hydration products as shown in Table 2.1 (Klingsch 2014).

Another aspect is the thermal incompatibility between aggregates and cement paste at elevated temperature. This incompatibility is caused by thermal dilation of different concrete constituents. Aggregates usually expand with increasing temperature, whereas the cement paste shrinks when temperature goes beyond 150 °C (Schneider 1982). Some aggregates are unstable at elevated temperature (such as flint). Crystal phase of quartz will change at 573 °C accompanied by dilation. Thermal mismatch can cause significant micro cracks inside the concrete samples.

Table 2.1. Physicochemical processes in Portland cement concrete during heating (Klingsch 2014).

Temperature	**Physicochemical changes**
20-100 °C	Loss of free and physically bound water, concrete starts to "dry" out
105 °C	Start of hydrothermal reactions
>120 °C	Dehydration of calcium silicate hydrate (CSH)
150 °C	First peak of CSH dehydration
270 °C	Second peak of CSH dehydration (Hertz 2005)
>300 °C	Noticeable increase in porosity and micro cracking
374 °C	Evaporation of all physically bound and free water
400 °C-600 °C	Dissociation of Portlandite
535 °C	Highest peak of Portlandite decomposition (Hertz 2005)
573 °C	α-quartz to β-quartz transformation with noticeable expansion
560-1000 °C	Transformation of CSH gel into β-C_2S (Peng and Huang 2008, Stepkowska, Blanes, Franco, Real and Pérez-Rodrıguez 2004)
>700 °C	Decarbonation of calcium carbonate
710-720 °C	Third peak of decomposition of CSH phases
>800 °C	Fully evaporation of all chemically bound water
1200 °C	Melt of Concrete starts

2.3 Review of explosive spalling study

The exact mechanism of explosive spalling of concrete is still a subject of much contention. Till recently, there is no widely-held spalling model which can describe the phenomenon comprehensively. However, reviewing previous studies can help researchers to approach the essence of this phenomenon.

In 1905, Woolson (1905) first recorded the flow of moisture from the cold side of slabs during fire tests, which is a common phenomenon during fire tests of concrete (Fig. 2.6 from Jansson, Boström and Silfwerbrand (2013)). *This observation revealed that behavior of concretes under fire has strong relationship with water content inside the concrete.*

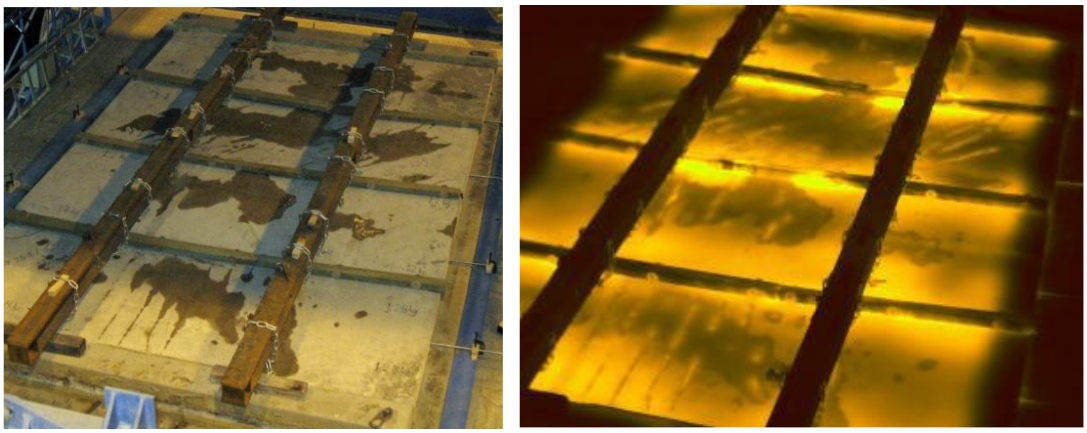

Fig. 2.6 (a) Water is pouring out on the cold surface of slab during a fire test (b) Thermal image showing the cracks where water reaches the surface (Jansson, Boström and Silfwerbrand 2013).

The first tests on spalling were carried out and presented by Gary (1916) as reported by Klingsch (2014). He conducted a series of fire tests on concrete slabs, beams, walls, and columns. It was observed that aggregates with a high coefficient of thermal expansion and a high water content increased the risk of spalling. Both 100 cm^2 and a more violent explosive spalling of concrete walls occurred with a size of about 1.0 m^2 from the concrete surface. Meyer-Ottens (1972) summarized the phenomena from Gary's tests into four categories:

- Aggregate spalling: crater-shaped spalling of aggregate grains.
- Surface-spalling: shell-shaped explosive spalling on the surface of concrete.
- Corner-spalling: explosive spalling at the corner of joints, columns, and stairs.
- Explosive spalling (Fig. 2.7): intensive explosion up to 1 m^2 wall sections.

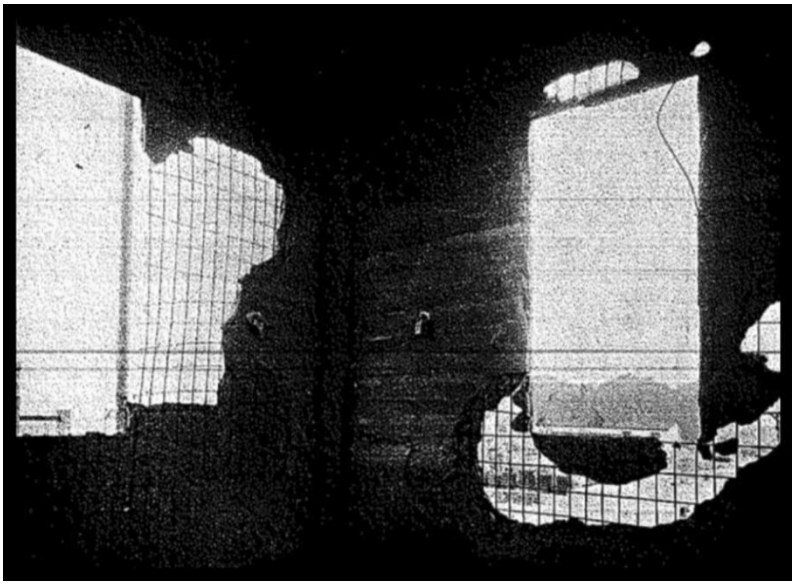

Fig. 2.7. A view of Gary's test in 1916 (Gary 1916).

This categorizing method was widely accepted by the latter researchers and engineers. However, these descriptions were generally based on the appearance of spalling. No quantitative criterion was given to evaluate the degree of violence. In actual fire scenarios, usually several of these types of spalling occur. It is very difficult to distinguish between them. On the other hand, apart from aggregate spalling, the other three categories can be attributed to two types of stresses, i.e. thermal stress and pore pressure build-up from trapped moisture in the concrete. Therefore, in the current study, surface, corner, and explosive spalling will be unified as explosive spalling.

For the build-up of pore pressure, Hermathy (1965) proposed moisture clog theory, which emphasizes migration of moisture in heated concrete. A visual observation of moisture clog is shown in Fig. 2.8 (Jansson and Boström 2009).

Fig. 2.8. Visible saturation layer (Jansson and Boström 2009).

In Hasenjäger's PhD thesis, he concluded more factors leading to explosive spalling of concrete, other than the expansion of water vapor (Hasenjäger 1935):

- Rapid heating leading to high thermal stress
- Stress perpendicular to heating surface exceeding the tensile strength of concrete
- Rapid and volumetric changes in aggregates during heating
- Build-up in pressure from liberation of water vapor and gases

Meyer-Ottens' studies in 1972 is a milestone in assessment of concrete spalling (Meyer-Ottens 1972). He conducted extensive studies on the effects of aggregate type, concrete quality, degree of reinforcement, moisture content, member shape, and compressive strength on spalling risks of concrete. A clear relationship between compressive strength and spalling extent was found. He concluded that moisture migration leads to spalling occurring close to the heated surface. Another important finding was that, both the pore size distribution and permeability of concrete influence the extent of spalling. He assumed that all pores are filled with water with different levels at the cold state. This water will migrate between large pores and cracks, while water vapor will migrate between small pores with increasing temperature, leading to different degrees of moisture saturation. This idea has been developed and widely adopted in numerical models (Bary, Ranc, Durand and Carpentier 2008, Davie, Pearce and Bićanić 2012, Gawin, Pesavento and Schrefler 2003).

Hertz's research on HSC strengthened the view of water vapor pressure. He is one of the pioneers studying the influence of silica fume on spalling of HSC. He found that some ϕ100×200 mm cylinders with 170 MPa compressive strength even spalled at a very low heating rate (1 °C/min). He concluded that the reason of intensive spalling was due to the dense microstructure, which hindered the escape of water vapor. He also believed that chemically-bound water is sufficient to cause spalling (Hertz 1984, Hertz 1985, Hertz 2003).

With the rapid development of new HPC and UHPC with inclusion of silica fume, an increased risk of spalling was noticed (Diederichs, Jumppanen and Schneider 1995, Hertz 1992). The use of polypropylene (PP) fibers to prevent concrete from spalling seemed to be a promising approach. PP fibers were first used in concrete panels at the fire research station in UK (Hannant 1978). The PP fibers then were probably thick fibers and not the fibers commonly used to prevent spalling nowadays. In 1983, the use of PP fibers with 15 μm diameter to prevent spalling in refractory materials was reported in a patent (Long and Moeller 1983). The functionality of PP fibers in concrete at elevated temperatures will be discussed in detail in Section 2.5.1.

Persson (2004) conducted many tests on fire resistance of prestressed concrete columns made of self-compacting cement (SCC) with compressive strength between 41 to 88 MPa while Boström, Wickström and Adl-Zarrabi (2007) tested different sizes of slabs and beams with compressive strength varying between 37.0 to 78.3 MPa. They found that spalling was noticed mainly on the test specimens without PP fibers. The level of preload strongly affected the extent of spalling, since applied loads caused compression stresses in the specimen, which restrained the propagation of cracks. Water vapor could not be released from the concrete surface, and thus, water vapor pressure was built up. Boström, Wickström and Adl-Zarrabi (2007) concluded that applied loads should not be neglected to achieve reliable predictions on spalling risks. One-side exposure of specimens to elevated temperature seems to be the most promising approach because external load is easier to be applied, weight loss during testing and the spalling depth can easily be measured. Considering the cost and laboratory work needed, tests on small-scale concrete specimens are acceptable to assess the general risks of spalling, even though the tests may not be sufficient to estimate the spalling behavior of concrete in real structures.

In addition to spalling behavior, research works also focused on individual parameters affecting spalling, for example, pore pressure, temperature, moisture migration, and formation of microcracks. Sertmehmetoglu (1977) first developed a test setup to evaluate the migration of moisture and build-up of pore pressure experimentally. As shown in Fig. 2.9, pressure transducers were attached at the unexposed side of the specimen.

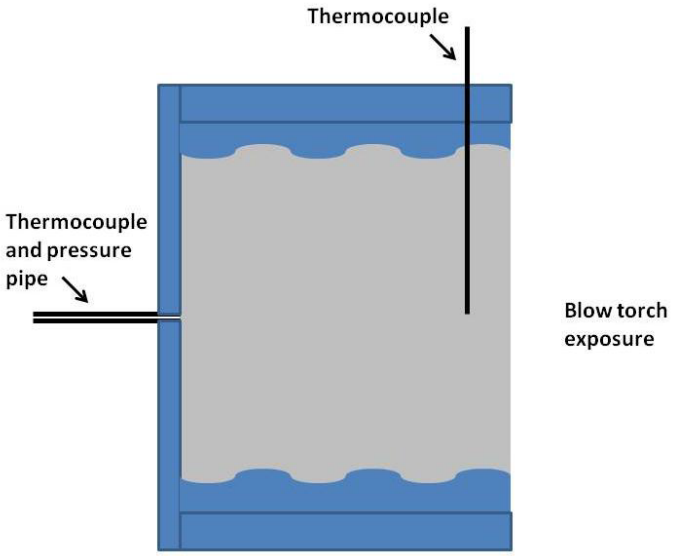

Fig. 2.9. Pressure cell developed by Sertmehmetoglu (Jansson, Boström and Silfwerbrand 2013).

In recent years, thermal couples and pressure transducers were installed inside concrete slabs and cylinders. Pore pressure and temperature were monitored at different depths from heated surfaces (Bangi and Horiguchi 2011, Bangi and Horiguchi 2012, Kalifa, Chene and Galle 2001, Kalifa, Menneteau and Quenard 2000). Kalifa, Menneteau and Quenard (2000) found that higher grade concretes (M100) experienced greater pressure and pressure gradients (Fig. 2.10).

Bangi and Horiguchi (2011) presented their studies regarding pore pressure measurements in HSC and Hybrid-Fiber-Reinforced High Strength Concrete (HFRHSC). Three types of pore pressure probes (i.e. cup with sintered metal, cup without sintered metal, and tube) were evaluated. Heating rates adopted were 5 and 10 °C/min. It was noticed that the pressure measurement technique using a cup with sintered metal and silicon oil as a medium for

pressure transfer was most effective for pore pressure measurements. A high heating rate clearly led to a higher pore pressure in deeper regions compared to slower heating. PP fibers are very effective in mitigating the pore pressure inside concrete. Addition of steel fibers reduced pore pressure slightly in deeper regions during fast heating.

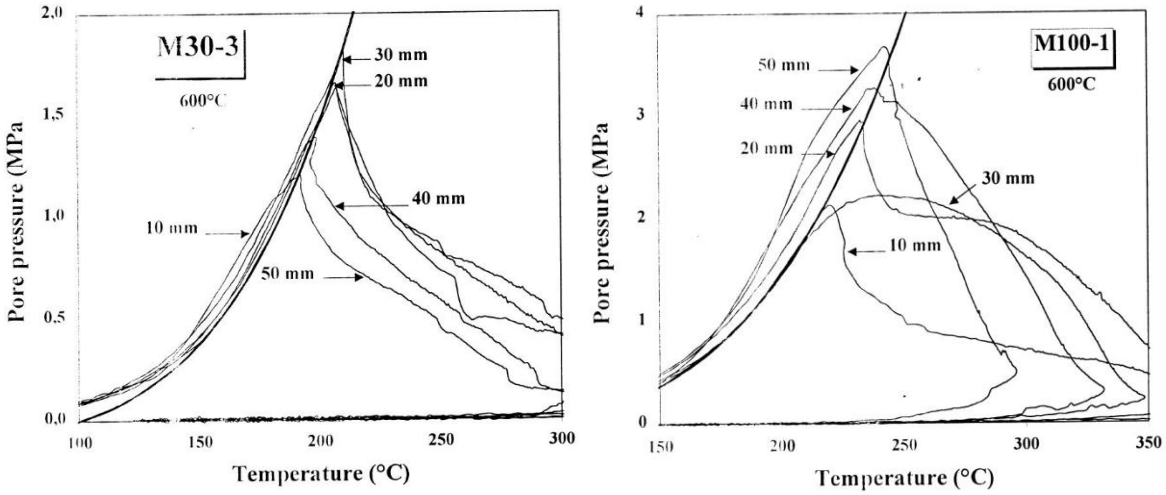

Fig. 2.10. Pore pressure profile during heating of M100 and M30 (Kalifa, Menneteau and Quenard 2000)

Sophisticated technologies used in other fields have been introduced to investigate important issues in explosive spalling, for example moisture migration and vapor movements, which were only described in spalling theory. der Heijden, Pel and Adan (2012) used nuclear magnetic resonance (NMR) to investigate moisture migration in concrete (Fig. 2.11). As shown in Fig. 2.12, *the moisture profile validated the existence of a moisture peak*, which was predicted by previous moisture transport models. Saturated regions would severely hinder the vapor transport and very high hydraulic pressure would be built up. Immediately after the heating had started, a boiling front was formed, which means that very low permeability of the concrete prevented the moisture to redistribute inwards in the time scale of the experiment. The temperatures measured at the boiling front were approximately 200 ℃ (Fig. 2.12b). This was a clear indication of increased vapor pressure at the boiling front.

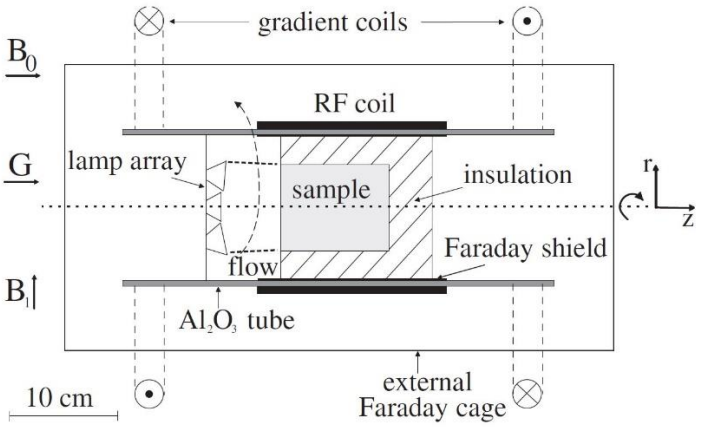

Fig. 2.11. Schematic diagram of the NMR setup. The setup has a cylindrical symmetry (der Heijden, Pel and Adan 2012).

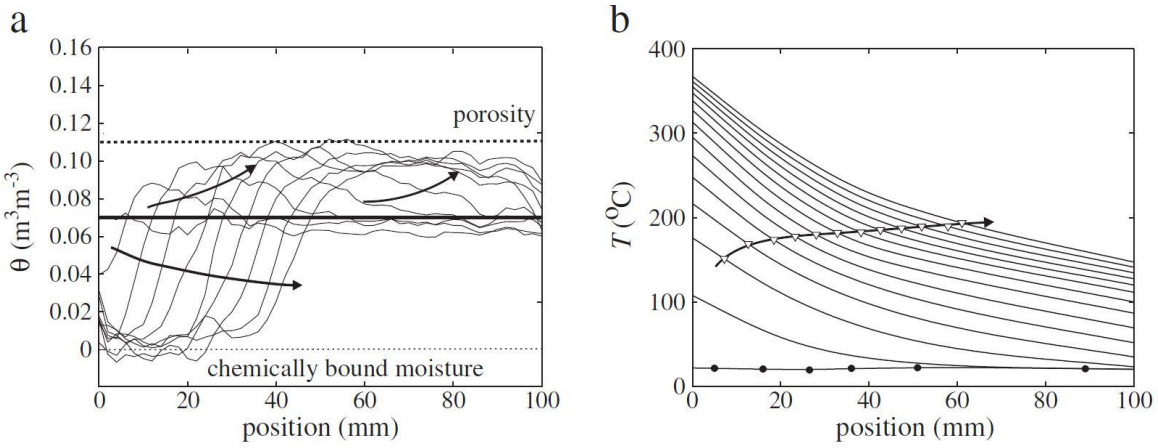

Fig. 2.12. Moisture and temperature profiles of a concrete sample with 97% RH (0.07 $m^3 \cdot m^{-3}$ moisture content) heated from one side. The temperature at the boiling front is indicated by ▽ in (b). The positions of the thermocouples are indicated by •. The evolution of the profiles in time is indicated by arrows (der Heijden, Pel and Adan 2012).

Stelzner, Powierza, Weise, Oesch, Dlugosch and Meng (2017) used X-ray 3D-computed tomography (CT) measurements to depict the moisture distribution of concrete samples during unilateral thermal exposure in three dimensions (3D), and to build linkage between pore size, concrete micro-structure, and moisture content (Fig. 2.13). One-dimensional NMR-relaxometry results were compared to X-ray 3D-CT to interpret moisture migration in 3-dimentional. The research is in progress.

The first result of fast neutron tomography with the most powerful neutron flux in the world was used to follow the dehydration process of concrete samples during heating (Dauti, Weber, Pont, Tengattini, Toropovs and Briffaut 2017) (Fig. 2.14). The results showed that the drying front moved faster in the sample with larger aggregate size. This was explained by the different thermal field caused by the presence of larger aggregates. Another reason could be that larger aggregates introduced more porous ITZ between aggregates and cement paste, which helped to release moisture. More quantitative image analysis is necessary to reveal the physical mechanism.

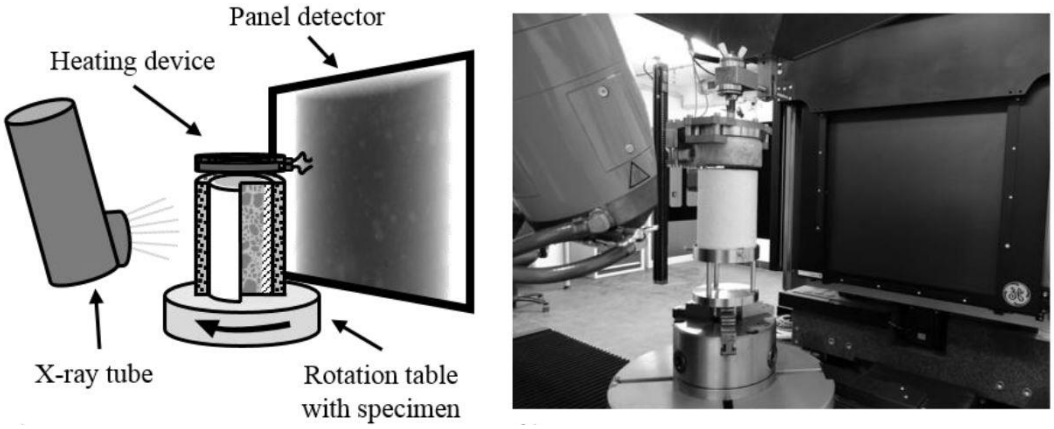

Fig. 2.13. Arrangement of the HSC specimen and heating device inside the X-ray 3D-CT setup; a) Schematic arrangement; b) Photo of the installation (Stelzner, Powierza, Weise, Oesch, Dlugosch and Meng 2017).

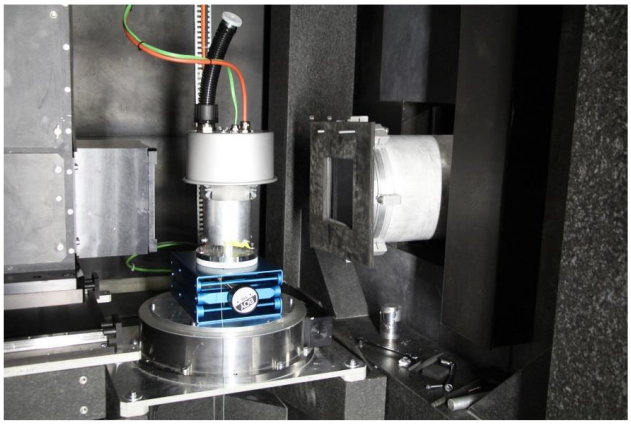

Fig. 2.14. Experimental setup. The neutron beam enters from the right and detected by detector from the left side (Dauti, Weber, Pont, Tengattini, Toropovs and Briffaut 2017).

Crack growth of concrete was detected by acoustic emission (AE) technique (Haneef, Kumari, Mukhopadhyay, Venkatachalapathy, Rao and Jayakumar 2013). With the help of AE, Kawasaki, Ozawa, Uchida and Tanibe (2015) found that more tensile cracks were formed than shear cracks at the incipient period of explosive spalling. This seems to show that pore pressure build-up contributes more to explosive spalling than thermal gradient. Fig. 2.15 shows the AE characteristics (acoustic events, cumulative acoustic events, and amplitudes) against vapor pressure and internal temperature (Ozawa, Uchida, Kamada and Morimoto 2012). A significant increase of AE events started from 100 ℃ with the increase of vapor pressure. It inferred the creation of dry, vapor, and humid zones, and the occurrence of micro-cracking was associated with thermal shrinkage and an increase of vapor pressure. The vapor pressure at the onset of spalling was 2.6–3.2 MPa with AE events having amplitudes of 90 dB or higher. *The monitored formation of microcracks implied the possible reduction of tensile strength of concrete, which may explain why the measured pore pressure at spalling is always lower than the tensile strength of concrete measured at ambient temperature.* Even Bazant (2005) claimed that pore pressure is not the dominant factor for spalling because pore pressure will decrease significantly once a crack is formed and the available volume for water vapor is increased by several orders of magnitude. However, from this research by Ozawa, Uchida, Kamada and Morimoto (2012), the *pore pressure still remained even after the creation of microcracks*.

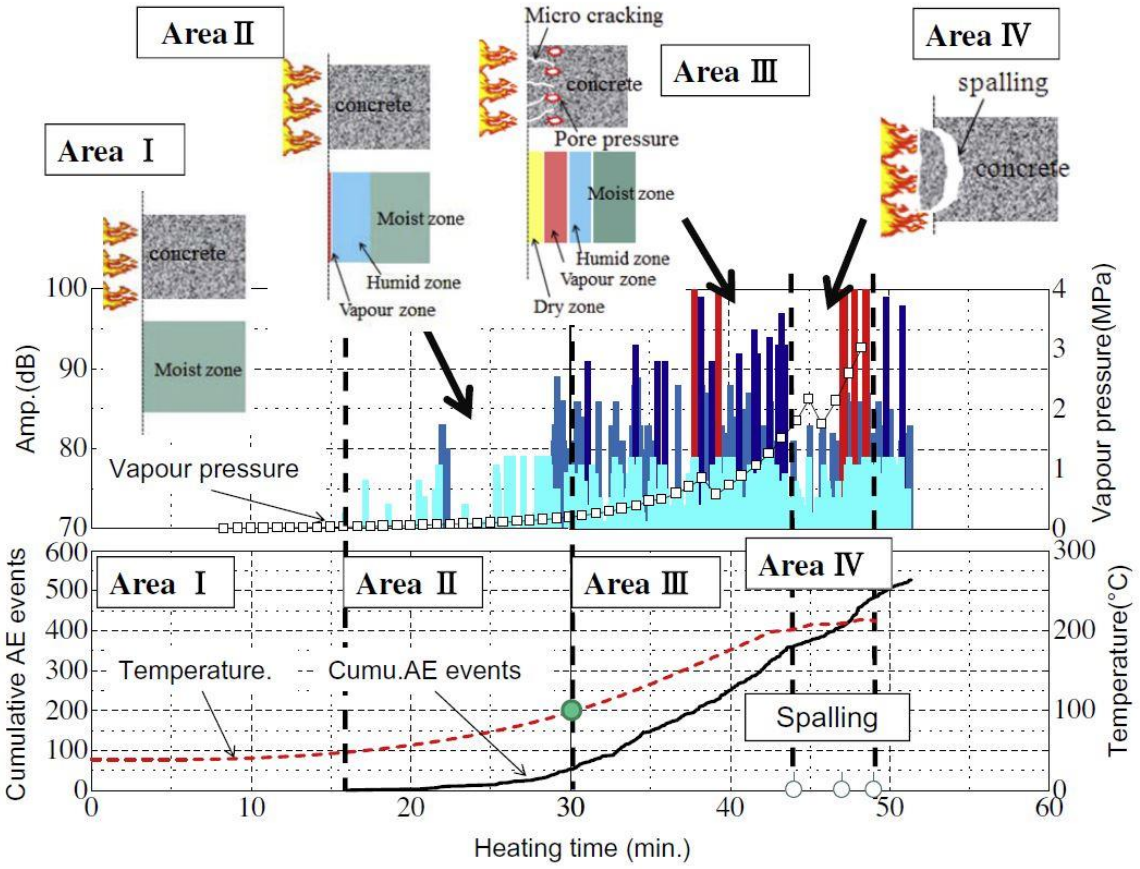

Fig. 2.15. Maximum vapor pressure and AE behavior of wet sample (Ozawa, Uchida, Kamada and Morimoto 2012).

From the aspect of engineering practice, a general risk-based spalling design approach was proposed by Bischof, Borgogno and Kaufmann (2017) (Fig. 2.16). The approach took both material behavior and structural behavior into account by means of spalling risk classification (SRC). For each SRC, methods for both spalling design and structural ultimate limit state fire design are provided. The more severe the consequences of explosive spalling are, the more precise design methods must be used.

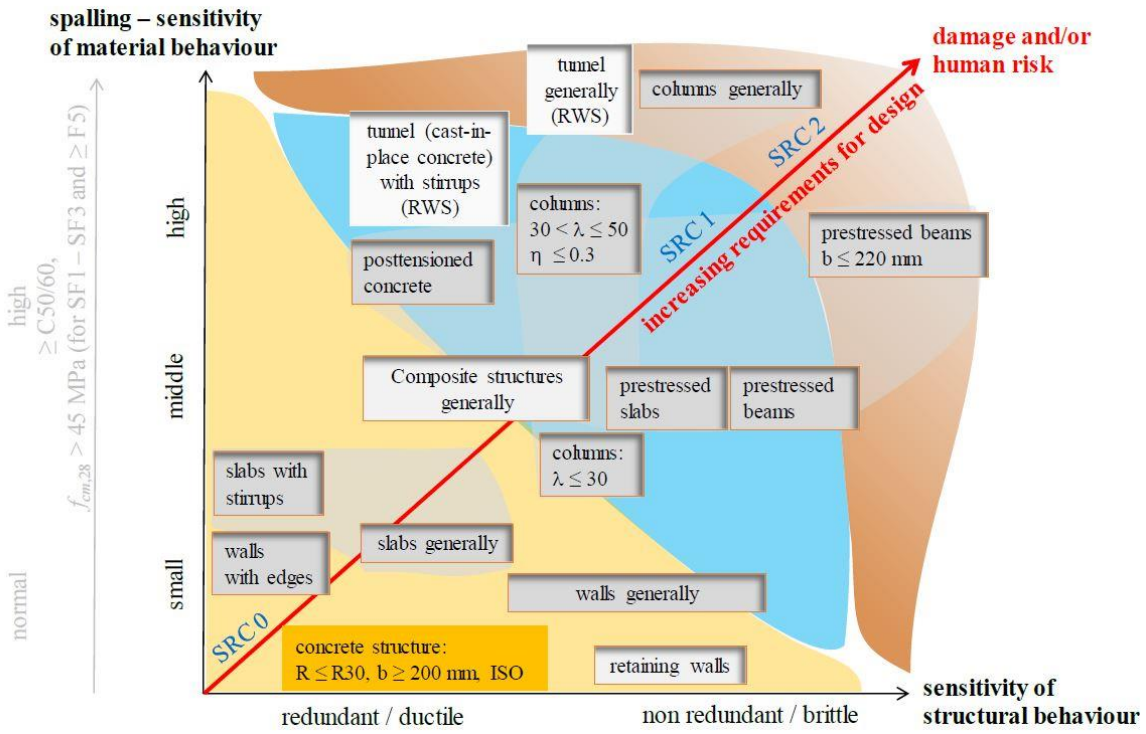

Fig. 2.16. Proposed spalling risk-based approach for fire spalling design (Bischof, Borgogno and Kaufmann 2017).

2.4 Proposed mechanisms of explosive spalling

2.4.1 Pore pressure induced stress

In this context, explosive spalling is associated with transportation of air, vapor, and liquid water in concrete. Fig. 2.17 depicts this assumption (Consolazio, McVay and Rish III 1997, Consolazio, McVay and Rish III 1998). Under the influence of high temperature, water moisture not only migrates outwards towards the heated surface, but also inwards towards the inner parts (Fig. 2.17a), where the temperature and pore pressure are lower. Moisture tends to condense again in the deeper sections, since the concrete core retains lower temperature (Fig. 2.17b). The accumulation of condensed water forms a “moisture clog” layer. Liquid water blocks the porous structure inside the concrete and further migration of gas and water vapor is prohibited as shown in Fig. 2.17c (Harmathy 1965). The air and condensed liquid water keep expanding with increasing temperature, but the concrete matrix

is relatively non-deformable. As a result, a high amount of potential energy is accumulated in the moisture layer. High pore pressure and pore pressure gradients are built up in this region. The built-up pressure may exceed the saturated vapor pressure relationship (Kalifa, Menneteau and Quenard 2000). Once the pressure reaches a certain threshold value, the concrete matrix fails, and the energy is violently released in an explosive manner (Fig. 2.17d). The lower the permeability of the material, the more severe is the build-up of pore pressure. HSC and HPC are believed to be more susceptible to spalling than NSC because of their low permeability values.

According to Khoylou (1997), if more than 32% of a closed pore is filled with water, with increasing temperature, water will expand and force the trapped air into solution, resulting in fully saturated pores. This thermal pressurization of the pore fluid is due to the discrepancy between thermal expansion coefficients of the pore fluid and of the concrete matrix. The measured value of thermal pressurization coefficient is equal to 0.6 MPa/°C (Ghabezloo, Sulem and Saint-Marc 2009). This mechanism leads to very high build-up of hydraulic pressure (liquid water transmits force to the contacting area), which is probably the cause for moisture clog. Hertz (2003) pointed out that the walls between closed pores with super-heated water and open pores with lower pressure can be destroyed by the pressure difference, which can lead to progressive breakdown of microstructure (Petrov-Denisov, Maslennikov and Pitckob 1972). This explanation is especially reasonable for UHPC, because it has very dense microstructure and more isolated pores compared to NSC. In partially water-filled porous structure of concrete, the pores are saturated with vapor particles. Thus, pore pressure relates to the saturated vapor pressure (SVP) of water. As moisture migration takes place, pressures may become hydraulic (greater than SVP) in the saturated regions, or steam pressure (less than SVP) in the dry regions. Pore pressure (pressure caused by water vapor, air, or liquid water inside concrete pores) in most experimental and numerical studies were less than the tensile strength of concrete. However, based on the hydraulic pressure theory, greater hydraulic pressure could be built up in saturated pores before explosive spalling occurs.

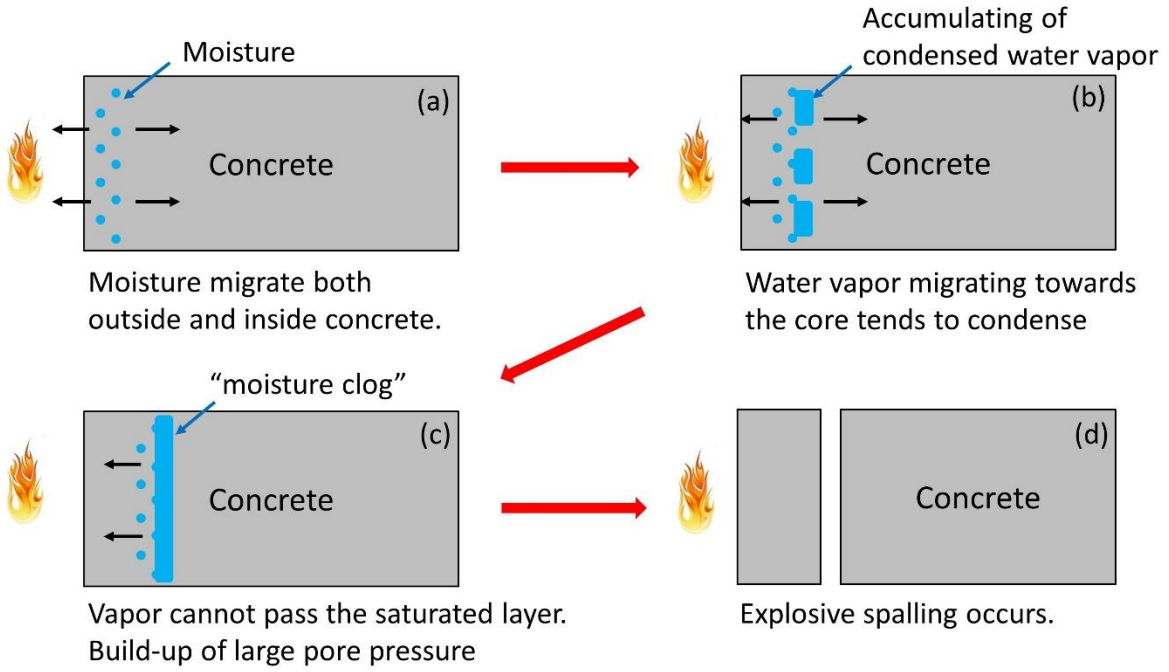

Fig. 2.17. Illustration of pore pressure induced spalling of concrete according to References (Consolazio, McVay and Rish III 1997, Consolazio, McVay and Rish III 1998)

A significant milestone in pore pressure measurement is the experimental setup as shown in Fig. 2.18 built by Kalifa, Menneteau and Quenard (2000). The results yielded important information on thermo-hygral processes: 1) HSC underwent much higher pore pressure peaks and gradients than NSC; 2) Larger pore pressure gradients were located within 20 mm from the heated face than in the deeper region, which was consistent with the spalling thickness; 3) The pore pressure build-up in HSC was attributed to a combination of saturated vapor pressure, dilation of liquid water, and partial pressure of enclosed air in the pores; and 4) The presence of PP fibers led to a large decrease in pore pressure. However, the experimental device is questionable for measuring hydraulic pressure, since hydraulic pressure is due to the discrepancy of thermal expansion coefficients between pore fluid and closed pore structures, but the pressure gauge may break the closed pores.

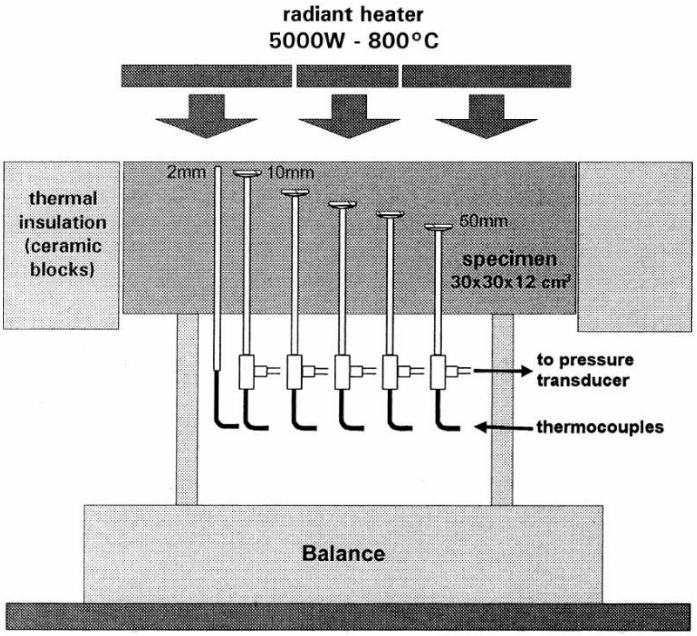

Fig. 2.18. The experimental set-up to measure pore pressure (Kalifa, Chene and Galle 2001)

The positive effect of polypropylene fibers on preventing spalling was responsible for relieving pore pressure, as evident by the increased permeability of concrete at elevated temperature (Mindeguia, Pimienta, Carré and Borderie 2013). These experimental results indirectly confirmed that vapor pressure is responsible for explosive spalling. Moisture clog was observed directly by Jansson and Boström (2009) by cutting concrete specimens. They showed that moisture clog was visible after 15 minutes of heating when subject to standard fire curve. Ichikawa (2000) argued that it is pore pressure rather than thermal stress that dominates explosive spalling. Guerrieri and Fragomeni (2016) proposed a method to isolate and quantify the spalled mass loss in terms of solid and water mass. It was found that there was a migration of water from the heated face to the nonheated face. It was postulated that this water was significantly contributed by the phase changes and chemical deterioration of concrete during heating.

Felicetti, Lo Monte and Pimienta (2017) developed a special experimental setup to measure the effect of different levels of sustained pore pressure on tensile behavior of concrete (Fig. 2.19 and Fig. 2.20). A cubic specimen was subjected to a mono-dimensional thermos-hygral

transient field. Both temperature and pressure were monitored and splitting tensile strength was measured. The results showed that pore pressure had a significant effect on tensile response of heated concrete. However, for HPC, very high pore pressure (exceeding 4 MPa) only lowered the tensile strength by less than 1 MPa. This was due to the smaller and less interconnected pores of high grade concrete. By weighing on these effects, they concluded that, pore pressure can be ruled out as the unique cause of explosive spalling. However, the hydraulic pressure caused by saturated pores was not measured.

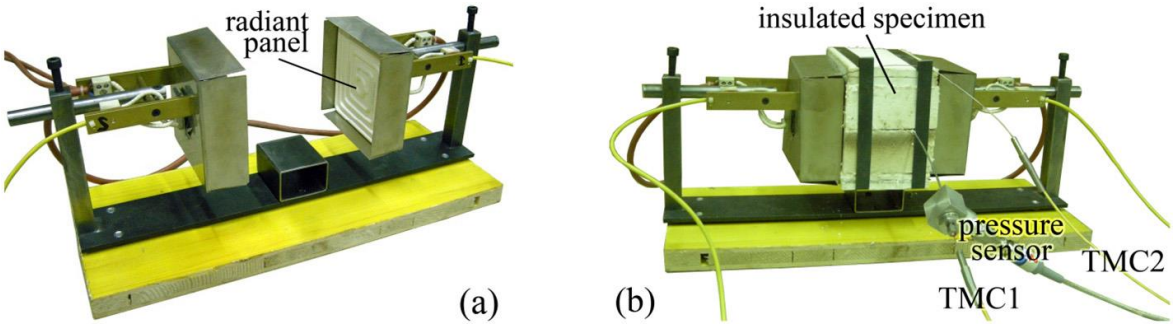

Fig. 2.19. (a) Heating system and (b) insulated specimen during heating

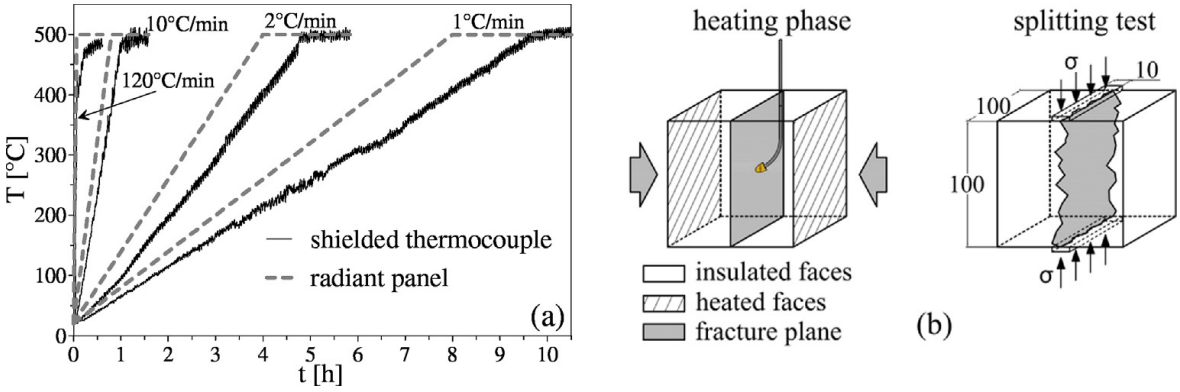

Fig. 2.20. (a) Temperature inside the radiant panels and in the air gap between the panel and the concrete face, and (b) scheme of the two stages of a test: heating phase and splitting (Felicetti, Lo Monte and Pimienta 2017).

2.4.2 Thermal stress induced explosive spalling

The second mechanism is a thermo-mechanical process. Spalling due to thermal stresses was analyzed by Saito (1966) and further explained by Dougill (1972). According to Saito's work,

spalling can be considered as concrete compression failure at the heated surface. Heated concrete generates temperature gradient, which in turn induces high compressive stresses close to the heated surface and tensile stresses in the interior regions due to restrained thermal expansion as shown in Fig. 2.21 (Bazant 1997). Higher heating rates will increase temperature gradients and thermal stress. Surface compression may be enlarged by load or confinement, which are superimposed upon the thermal stresses developed during heating. However, for UHPC, it is questionable if the thermal stresses near the heated surface exceed the compressive strength of UHPC with a cold strength of 150 MPa. Moreover, the failure plane caused by spalling is very shallow and parallel to the heated surface. Besides, the spalling failure mode of UHPC is different from compressive failure.

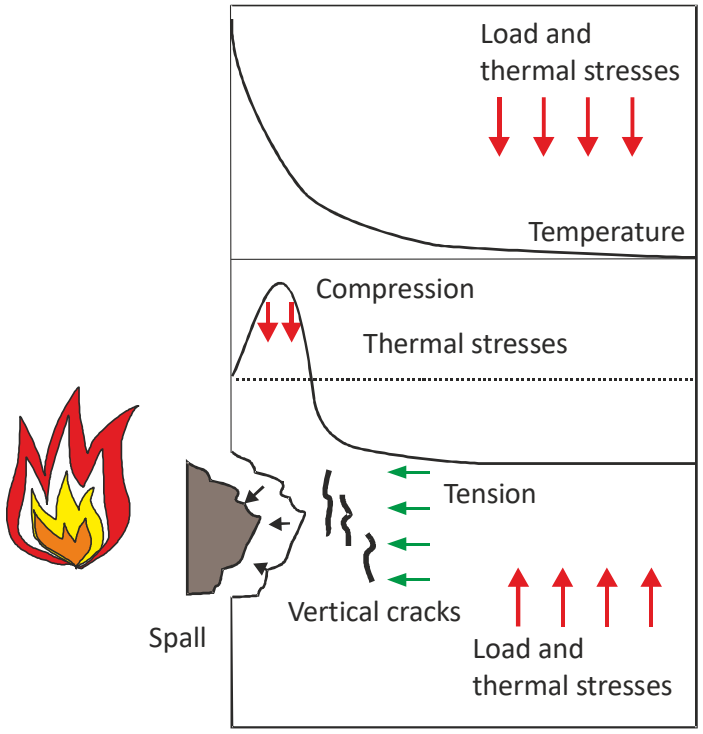

Fig. 2.21. Illustration of thermal gradient induced spalling of concrete according to (Klingsch 2014).

Klingsch (2014) reported explosive spalling in HPC with low thermal stress, when the specimen was heated under a heating rate of 1 °C/min. Fig. 2.22 shows the measured temperatures at different positions of a cylindrical sample with 150 mm diameter. It can be seen that the thermal gradient was very small, and so was the thermal stress developed.

However, spalling still occurred when the specimens were heated to 300 °C. This investigation strengthened the concept of a critical pore pressure in explosive spalling for dense concrete with a high amount of silica fume and low permeability. Additionally, the thermal stress spalling theory fails to explain the effect of moisture content on spalling risk.

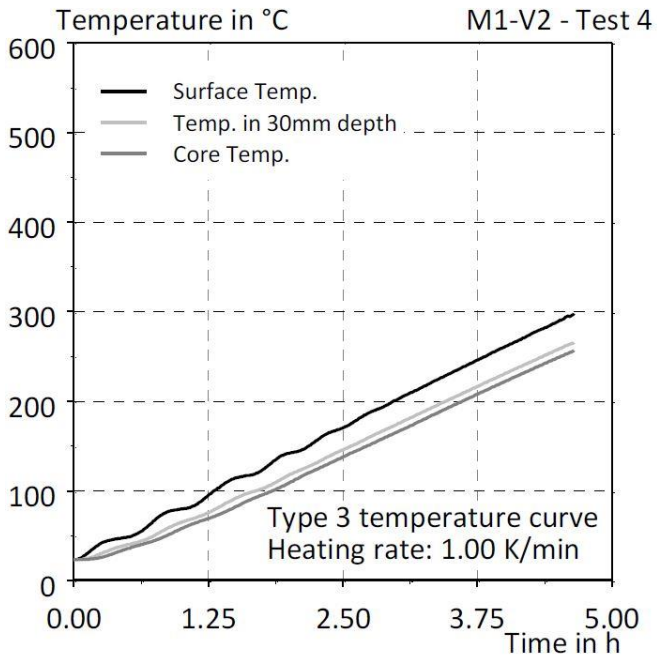

Fig. 2.22. Temperature development at the cylinder surface, in 30 mm depth and in core of the specimen during heating (Klingsch 2014).

Bazant (2005) claimed that pore pressure can serve as a trigger for the fracture leading to spalling, but thermal stresses constitute the phenomenon driving the explosion, because once a crack is formed the available volume for water vapor is increased by several orders of magnitude. However, this hypothesis has not been proved experimentally. External loading and restraint do augment the compressive stress parallel to the heating surface, but the compressive stress also hinders the expansion of microcracks perpendicular to the heated surface, which makes it difficult to release the pore pressure.

The success of including PP fibers to reduce spalling supports the theory that pore pressure is the dominant phenomenon. However, based on Kalifa, Chene and Galle (2001), PP fibers

may not only contribute to increase in permeability. Presence of PP fibers also leads to micro cracks, which may change the local stress distribution.

Thermal stress inside concrete is difficult to be measured directly. Many numerical results showed that explosive spalling of HPC specimens is mainly attributed to temperature gradient-induced thermal stress (Zhang and Davie 2013, Zhao, Zheng, Peng and van Breugel 2014). However, for the mechanical-hygral-thermal model, it is very difficult to ensure accuracy of large amount of input parameters from the same resource. At last, Khoury and Anderberg (2000) pointed out that spalling occurs due to the combined influence of pore pressure and compression in the exposed surface region.

2.4.3 Combined thermal stress and pore pressure

From the results of experimental studies of spalling carried out during the last few decades, it is almost impossible to attribute all the observed spalling failures to either build-up of high pore pressure or thermal stresses. The largely scattered results from tests and analyses also showed that it was almost impossible to assign explosive spalling to just one of the two mechanisms. The exact mechanism of explosive spalling and the effects of different mechanisms are still not comprehensively understood.

Zhukov (1976) first proposed the possibility that explosive spalling originating from superposition of pore pressure and thermal stress. He considered restrained thermal expansion and applied load acting onto the concrete as uniform stresses with a stress vector parallel to the heated surface. These stresses cause cracking in the longitudinal direction in thermally affected areas. High pore pressure was superimposed on these stresses in the direction perpendicular to the heated surface. Zhukov also proposed an empirical model to evaluate spalling risks, but his model is only limited to OPC or NSC.

Connolly (1995) developed new ideas on combined pore pressure and thermal stress spalling. The overall stress can be compared to tensile strength of concrete to identify if spalling will occur. Cracks develop parallel to the heated surface once the total stress (stress caused by pore pressure plus component of thermal stress in the direction perpendicular to the heated

surface) exceeds the tensile strength. Fig. 2.23 gives a sketch of the combined stresses acting close to the heated surface (Khoury and Anderberg 2000, Klingsch 2014).

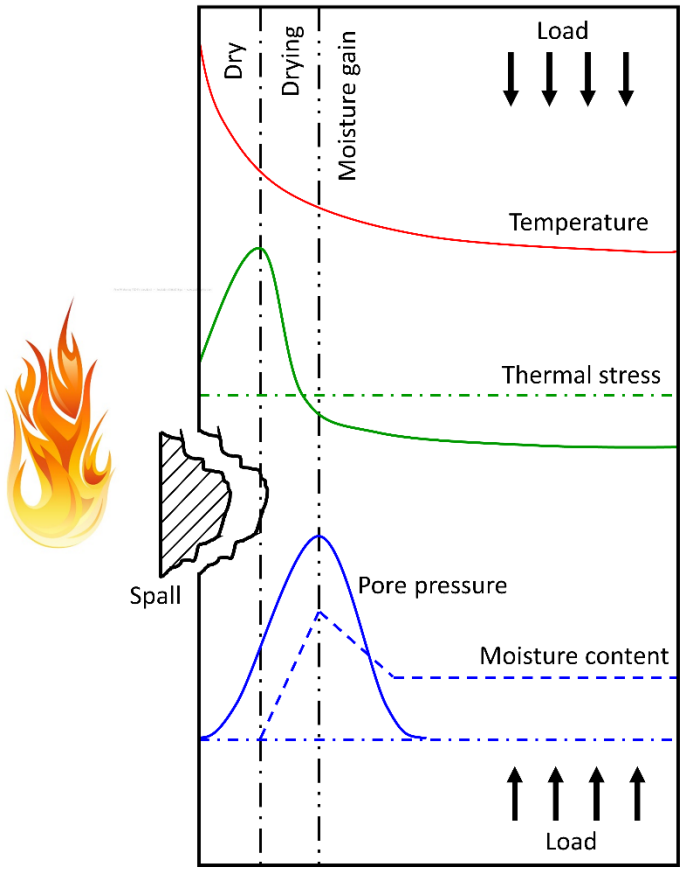

Fig. 2.23. Explosive spalling caused by combined thermal stresses and pore pressure (Klingsch 2014)

Sertmehmetoglu (1977) expanded the ideas from Dougill (1971) that thermal gradient caused compressive stress on the heated face, which in turn induced a system of cracks parallel to the heated face. As temperature rose, the cracks were filled with vapor and the vapor pressure normal to the heated surface led to spalling. Khoury (2000) also pointed out that a combination of pore pressure and thermal stress was responsible for spalling, but the importance of each mechanism may be different for different concrete strengths.

Relatively low (<2MPa) pore pressure was measured during fire test that led to explosive spalling (Mindeguia, Pimienta, Carré and Borderie 2013). This observation placed a limit to

the explanation of explosive spalling is solely due to pore pressure build-up. However, Mindeguia, Pimienta, Carré and Borderie (2013) highlighted that concrete spalling is directly linked with the transfer properties, because testing conditions resulted in a significant increase of permeability which led to lower spalling risks.

Thermal mechanical behavior of HPC cubes was studied at a meso-level by conducting thermo-chemo-hydro-mechanical numerical analysis. It was found that the spalling mechanisms are different under different heating rate. For fire heating, thermal stress plays a dominant role, but for slow heating, vapor pressure governs the mechanical behavior of the specimen (Zhao, Zheng, Peng and van Breugel 2017).

From the review of spalling mechanisms, it is challenging to define a single set of parameters that determines the occurrence of spalling. *The effect of PP fibers, moisture content, and the fact that concrete with lower permeability spalled at a low heating rate seem to indicate the major role of pore pressure in spalling phenomena. On the other hand, the numerical results, the contribution of compression loading on spalling, and the low measured pore pressure compared to the tensile strength of concrete at elevated temperature seem to support the mechanism of thermal stress. It is probable that, the dominant factors change with concrete qualities.* At least, the proposed mechanisms allow the effect of parameters to be evaluated within the assumed framework. Factors governing spalling will be reviewed in the next section.

2.5 Governing factors

Many factors have important effect on explosive spalling. However, some of them have causal relationships, such as silica fume and permeability. A clear classification between individual parameters is needed. As mentioned in Section 1.3, governing factors leading to explosive spalling have been classified into four main categories. The following is an overview of the influence of these factors on concrete spalling.

2.5.1 Mix design parameters

Water-to-binder ratio:

Concrete with low water-to-binder ratio shows a greater susceptibility towards explosive spalling (K Hertz, 1984) because the concrete matrix will be denser. Moisture cannot be released from the dense concrete matrix.

Silica Fume:

The properties of UHPC improve significantly with the use of silica fume. Silica fume mainly consists of amorphous silicon dioxide smaller than 1.0 μm. The very fine particle size of silica fume causes pozzolanic reaction. The calcium hydroxide produced in the hydration process reacts with the silica particles and creates CSH. In addition, the silica particles fill up voids and gaps inside the cement matrix and ITZ, which leads to a much denser and harder microstructure. Concrete with silica fume has much higher strength and much lower permeability (Poon, Azhar, Anson and Wong 2001), which results in higher risk of spalling due to reduced release of pore pressure (Kodur and McGrath 2006, Sanjayan, Stocks and Stocks 1993). As shown in Fig. 2.24, ITZ can hardly be observed in UHPC with silica fume. The bonding between cement matrix and aggregates is higher than that in NSC. This is one of the most important differences between UHPC and NSC.

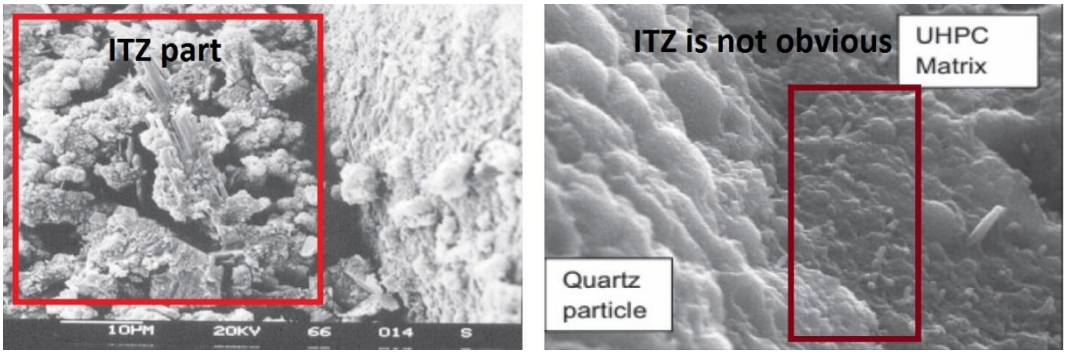

Fig. 2.24. Comparison of SEM observations of interfacial transition zone (ITZ) between conventional cement mortar and UHPC a. ITZ in Conventional Mortar (Shi and Xie 1998). b. ITZ in UHPC (Prabha, Dattatreya, Neelamegam and Seshagirirao 2010).

Limestone filler:

The effect of limestone filler can lower permeability and increases spalling risk (Boström and Jansson 2006). The concrete with more limestone filler (165 kg/m^3) spalling slightly more severe and earlier in the fire test compared to the concrete with less limestone filler (85 kg/m^3). However, it should be noted that the moisture content was less in the concrete with more filler (i.e. 4.1% compared to 4.5%) (Boström and Jansson 2007). In another tests from (Boström and Jansson 2008), it was found that the spalling depth increases with the amount of limestone filler up to 100-150 kg/m^3, and thereafter decreases. However, more tests are needed to statistically ensure the effect.

Type of aggregate:

Concretes containing high thermal expansion aggregates (e.g. gravel, siliceous) will cause greater compressive stress at the heated surface compared to concretes containing low thermal expansion aggregates (e.g. basalt, lightweight aggregate) (Khoury and Anderberg 2000). Calcareous concretes are more heat-resistant than siliceous concretes because calcareous aggregates are more stable and have less thermal expansion than siliceous aggregates at high temperature (Gales, Parker, Cree and Green 2015, Hager 2013, Li, Li, Onofrei, Ballivy and Khayat 1999). Quartz is stable up to 573 °C. At this temperature, quartz is transformed from α to β phase, which causes a significant increase in volume. This expansion leads to an increase of cracking in the concrete. However, Hertz (2003) noted that cracking would not lead to spalling, because at this temperature, most of the bound water has vaporized. In concretes with thermal sensitive aggregates, pore pressure is usually lower compared to concretes that do not contain such aggregates (Mindeguia, Pimienta, Carré and Borderie 2013). For light-weight aggregates, if the concrete is likely to be in a high moisture environment, the porous lightweight aggregates could absorb moisture, which will be released with an increase of temperature and might promote spalling (Kodur 2000). In addition, sand-stone, flint, and felspar tend to promote aggregate spalling at rather low temperatures, but they only lead to superficial spalling close to the heated surface (Connolly 1995, Hertz 2003, Meyer-Ottens 1972).

Aggregate size:

For NSC, coarse aggregates are more likely to promote aggregate spalling and the time of spalling is shorter with larger aggregates due to thermal expansion of the concrete (Connolly 1995). Kalifa, Menneteau and Quenard (2000) indicated that thermal dilation of aggregates causes local strain incompatibility between the cement paste and the aggregates and it is far too large to be accommodated by elastic strains. For concrete with denser microstructure, the expansion of aggregates and shrinkage of cement past increase micro cracks at elevated temperature, which can relieve pore pressure and reduce the risk of explosive spalling. In addition, *aggregate size also has interactive effect with PP fibers*. Heo, Sanjayan, Han and Han (2012) found a strong relationship between aggregate size, inter-aggregate spacing of coarse aggregates and PP fiber length. Therefore, aggregate size is one of the main parameters to be study in the present research.

Steel fibers:

With regard to mechanical properties, steel fibers enhance the performance of concrete under both compression and tension (Chen & Liu, 2004). The tensile strength of concrete can be increased to as high as 8-12 MPa. From this view point, higher tensile strength improves the resistance of concrete to stresses and decreases the risk of explosive spalling.

There is contradiction on effect of steel fiber on explosive spalling. Adding steel fibers was found to be beneficial in reducing spalling and enhancing fire endurance of HSC columns (Kodur, Cheng, Wang and Sultan 2003, Kodur and Phan 2007). Bonding force of steel fibers can help to withstand higher pore pressure (V. Kodur, 1998). On the contrary, in very dense silica fume concrete, more violent explosive spalling may happen because of sudden release of accumulated energy (K Hertz, 1984).

Besides, addition of steel fibers plays an important role in moisture migration. It has been reported that addition of 50 kg/m^3 of steel fibers in self-consolidating concrete could reduce pore pressure during one-dimensional heating tests (Ding, Zhang, Cao, Zhang and Azevedo 2016). It was hypothesized that steel fibers entrapped air bubbles which act as reservoirs to accommodate water vapor and the vapor pressure may be relieved through weak ITZs around the steel fibers. The mitigation of pore pressure occurs in a relatively higher-pressure zone which may due to pressure-induced tangential space (PITS) (Fig. 2.25) mechanism as a result

of poor interfacial adhesion between steel fibers and concrete matrix (Bangi & Horiguchi, 2011).

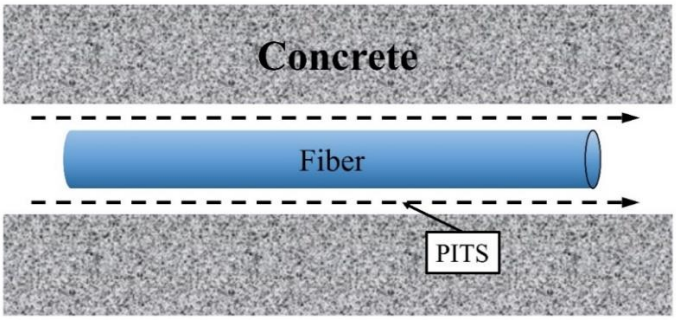

Fig. 2.25. Pressure-induced tangential space (PITS).

PP fibers:

The presence of polypropylene fibers helps to increase permeability of concrete at elevated temperature (Fig. 2.26) and mitigate pore pressure build-up. Even though *there is still a debate on the exact mechanism*, many experimental evidences show that PP fibers can help reduce the risk of explosive spalling (Bangi & Horiguchi, 2012; Bošnjak et al., 2013; Han, Hwang, Yang, & Gowripalan, 2005; Kalifa et al., 2001; Kalifa et al., 2000; Klingsch, 2014; Lee, Han, Han, Han, & Son, 2012; Zeiml et al., 2006). The use of PP fibers to prevent spalling of HPC has been included in European design standard EN 1992-1-2. It is recommended that monofilament PP fibers with a dosage higher than 2.0 kg/m^3 are needed for spalling prevention. However, this dosage may not be enough for UHPC and there is no advice on the fiber's geometry.

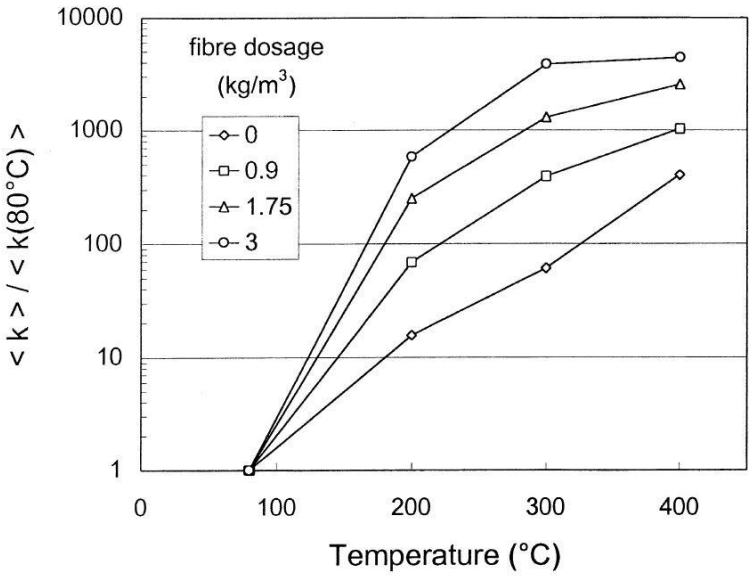

Fig. 2.26. Intrinsic permeability normalized to that at 80 °C (averages), versus temperature and fiber dosage (Kalifa, Chene and Galle 2001).

One of the theories is that, after melting at 150-175 °C, the polypropylene fibers are absorbed by the concrete matrix leaving "channels" behind for the steam to escape (V. Kodur, 2000). Khoury and Willoughby (2008) argued that the high viscosity of melted fibers makes them almost impossible to be absorbed by the surrounding cement matrix. They claimed that high vapor pressure can migrate from the Pressure-induced Tangential Space (PITS) around the fibers (Fig. 2.25) since PP fiber is hydrophobic and there is low bonding force between PP fibers and cement matrix. Kalifa, Chene and Galle (2001) confirmed that PP can be absorbed by the porous network of concrete at elevated temperature using a "water drop" test (Fig. 2.27). A layer of PP fiber was placed on a surface of concrete. The set-up was heated up to a temperature ranging between 170 °C and 200 °C. After exposure to 180 °C and above, the water drop was absorbed by the concrete penetrated by PP fibers at a much slower rate than on virgin concrete, which means that the polymer has actually penetrated into the porous network. However, whether this absorption of PP fiber is substantial enough during the fast heating during real fire exposure could not be ascertained.

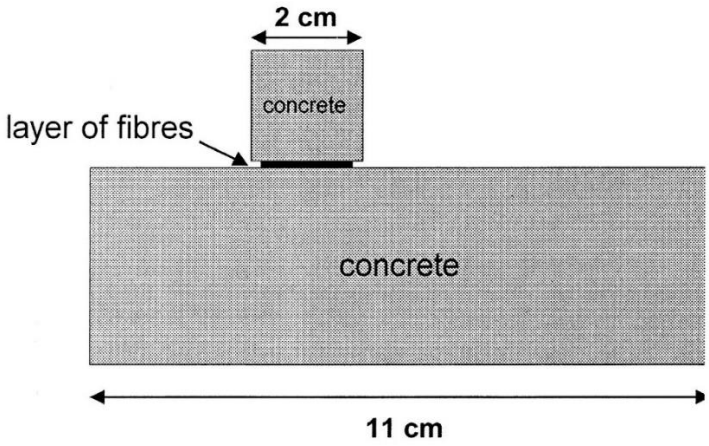

Fig. 2.27. Schematic of the water drop test (Kalifa, Chene and Galle 2001).

Bošnjak, Ožbolt and Hahn (2013) believed that softening of fibers and weak concrete-fiber interface are the main driving force for increase in permeability. From his measurements, PP fibers significantly increased the permeability of concrete between 80 °C and 130 °C, which is earlier than the melting temperature of PP fibers. Fig. 2.28 shows that, after 2 days of exposure to 200 °C, large part of melted PP fibers was still inside the channels.

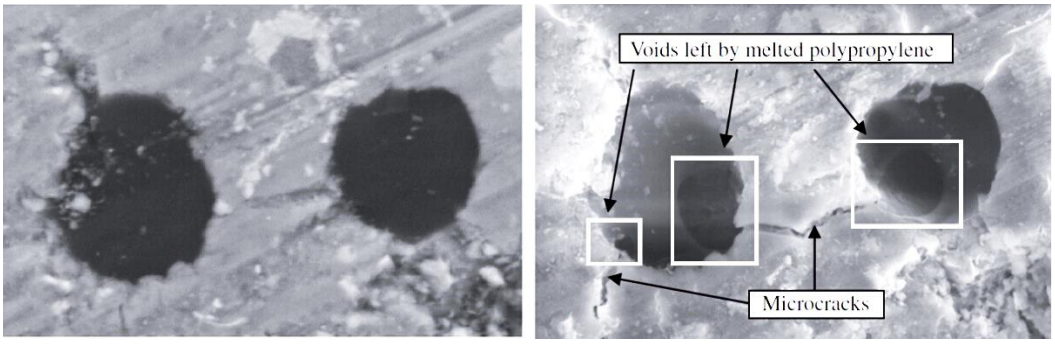

Fig. 2.28. Scanning electron microscope photos of the virgin concrete with addition of polypropylene fibers (left) and the same concrete exposed to 200 °C for 2 days (right) (Bošnjak, Ožbolt and Hahn 2013).

Bentz (2000) hypothesized that percolation of interfacial transition zones (ITZ) by PP fibers is the mechanism for improvement of permeability of concrete at high temperature. The ITZs of the fibers connect the ITZs of the aggregates creating a connected network system for moisture flow. Mazzucco, Majorana and Salomoni (2015) numerically evaluated the

mechanism of polypropylene contribution on permeability of concrete under thermal conditions through a coupled hygro-thermal–mechanical finite element formulation. The model was based on increase of porosity caused by PP fibers and ITZs at elevated temperature. The important role of PP fibers is to connect ITZs and micro pores. However, Fig. 2.24 shows that in UHPC owing to the low water-to-binder ratio and pozzolanic reaction the ITZ seems as dense as the matrix. This shows that the linkage between ITZs is unrealistic in UHPC. *Therefore, as one of the most important factors influencing explosive spalling, the effect of adding PP fibers will be studied in the current research.*

Moreover, the *combined use of PP and steel fibers* to prevent explosive spalling of fiber-reinforced self-consolidating concrete (FRSCC) and HSC subjected to elevated temperature has been investigated (Bangi and Horiguchi 2012, Ding, Zhang, Cao, Zhang and Azevedo 2016). Shallow flaking of concrete cover was observed, and release of pore pressure was reported in the literature. However, neither their effect on change of permeability, nor the micro-scale mechanism was investigated. Peng, Yang, Zhao, Liu, Bian and Zhao (2006) and Chen and Liu (2004) found the combined use of PP and steel fibers could reduce spalling. However, focus of their studies was on residual mechanical properties. Ding, Zhang, Cao, Zhang and Azevedo (2016) investigated the effect of steel, micro and macro PP fibers on the pore pressure of self-consolidating concrete under fire. The hybrid using of fibers showed positive effect on pore pressure reduction, but the mechanism was not explained clearly. More experimental results are needed to complete the empirical formula they proposed to predict the maximum pore pressure of self-consolidating concrete.

Based on Heo, Sanjayan, Han and Han (2012), *PP fiber geometry and aggregate size have strong interaction effect on spalling prevention* since they are related to inter-aggregate spacing of coarse aggregates, which is critical for the connectivity of adjacent aggregates. The larger the size of the coarse aggregate, the longer is the optimum length of fibers for spalling protection. However, the corresponding permeability was not measured, and the mechanism is not clear.

In conclusion, even though many studies have been conducted to investigate the effect of PP fibers on explosive spalling, the mechanism is still not clearly understood especially for

UHPC. Permeability should be measured at hot state to build linkage between the mix design and the spalling behavior. Besides, microstructure changes at elevated temperature should be analyzed, and quantification of effects should be carried out at micro scale. In addition, more work should be done on the combined effects of PP fibers, steel fibers, and aggregate size. This will be presented in Chapter 6 to 8.

Polyethylene fibers:

PE fibers can significantly improve mechanical strength of concrete due to their high strength can transmit large interfacial frictional stresses and the hydrophobic nature of PE fiber could significantly enhance the complimentary energy of fiber bridging (Ranade, Li, Stults, Heard and Rushing 2013). Moreover, *PE fibers have lower melting point (around 145 ℃) than PP fibers (around 165 ℃). However, studies about PE fibers on spalling prevention is rather limited.*

Nylon fibers:

Nylon fibers have been used to mitigate explosive spalling of concrete. An overall good spalling protection of HPC by combining PP and nylon fibers was shown in Lee, Han, Han, Han and Son (2012). Even though the melting point of nylon fibers is 200 °C, which is close to the critical spalling temperature (Klingsch 2014), their lower diameter and larger number of nylon fibers improved the spalling resistance by providing connections between pores.

Other types of fibers:

Ozawa and Morimoto (2014) studied the effect of polypropylene, jute, and water-soluble polyvinyl alcohol fibers on the increase in pore pressure in HPC at elevated temperatures. Permeability value were measured at 100, 200, 300, and 400 ℃. After exposure to 200 ℃, the permeability of the plain, jute, and water-soluble polyvinyl alcohol (WSPVA) specimens were four, four to nine, and three to six times higher than its permeability prior to heating, respectively. The increase in permeability of PP specimens was the highest, but it is worth noting that, the content of the jute fiber (0.075%) was only half of that of WSPVA and PP fibers (0.15%). Moreover, the length of the WSPVA fibers was shorter (4 mm) than that of PP and jute fibers (12 mm). The maximum vapor pressure measured within the jute, WSPVA,

and PP specimens were 2.5, 1.5, and 1.0 MPa. The WSPVA fibers dissolved between 50 and 90 ℃, so it was believed that pressure-induced tangential space (PITS) at the fiber-concrete interface was developed. The structure of the jute fiber was straw-like, so the vapor pressure could be released.

Air-entrainment:

The addition of air-entrainment agent can cause small air-voids inside the hardened concrete with an average size of less than 0.3 mm. The air voids help to reduce moisture content and lower the saturation level of concrete (Connolly 1995). These voids act like micro-reservoirs for moisture and permeability will also be increased. Thus, it can help to reduce pore pressure and spalling (Khoury and Anderberg 2000).

Water curing:

Water-cured specimens show increased susceptibility to explosive spalling because the oversupply of water can increase the moisture content. With increased hydration, permeability of concrete will be lower (Akhtarnrzaman & Sullivan, 1970).

Concrete age:

The age of a concrete structure is closely related to the concrete's moisture content. If fire testing of concrete is performed too soon after casting, huge quantities of water must be driven off. With increasing hydration, permeability of concrete will change with time. Hydration degree and permeability were found to be sensitive to spalling risk (Guo, Yuan and Mang 2016). However, compared to the properties that describe concrete directly and concerning the large difference between each type of concrete, concrete age is not suitable to be used as a parameter for evaluating spalling risk.

2.5.2 Properties of concrete

Moisture content:

Moisture content is usually expressed as the mass percentage of water in concrete. It defines the amount of evaporable water and therefore, has significant effect on the build-up of pore

pressure. Higher moisture content significantly increases the risk of explosive spalling, since more vapor needs to be released to mitigate pore pressure build-up. Copier (1983) concluded that moisture content is the most important parameter governing the risk of explosive spalling. Connolly (1995) showed that pre-dried concrete at 105 °C did not spall at all, whereas concretes with 4-9 % moisture content showed explosive spalling.

Meyer-Ottens (1972) studied the spalling risk of concrete with a range of moisture contents from 0.5 to 7% by mass. He found that regardless of applied heating rate, concrete members with moisture content less than 3.3% by weight did not spall. Christiaanse, Langhorst and Gerriste (1972) and Zhukov (1976) produced spalling envelopes (Fig. 2.29 and Fig. 2.30) which indicated that spalling will not occur for moisture contents below 3% by weight. However, for very dense concrete with low porosity and permeability, spalling can still occur even with moisture content between 2.3-3.0% by weight (Jumppanen 1989). Therefore, moisture content is not adequate to evaluate spalling risk. Other factors such as permeability must be considered.

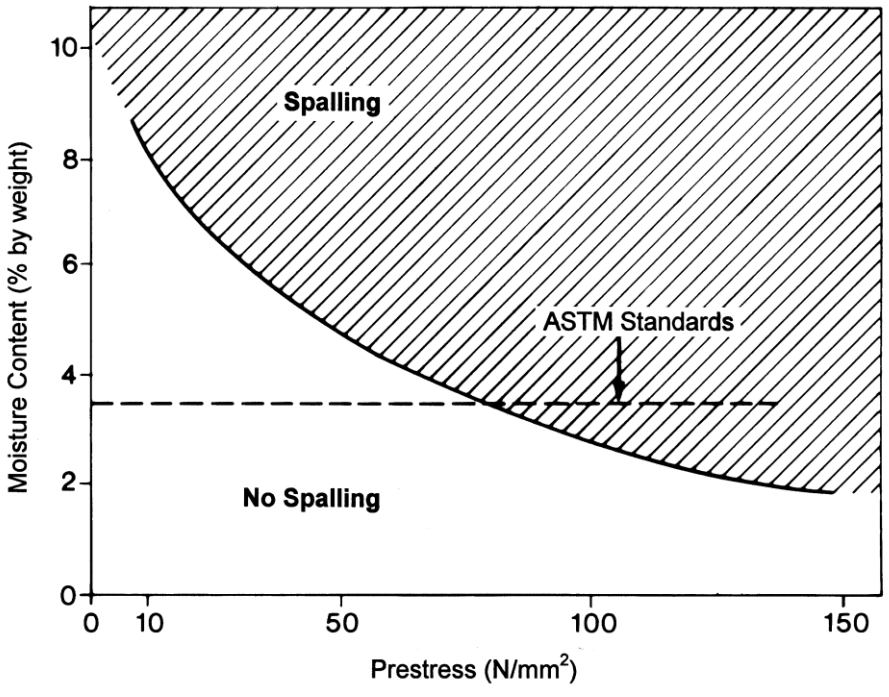

Fig. 2.29. Explosive spalling envelope after Christiaanse, Langhorst and Gerriste (1972).

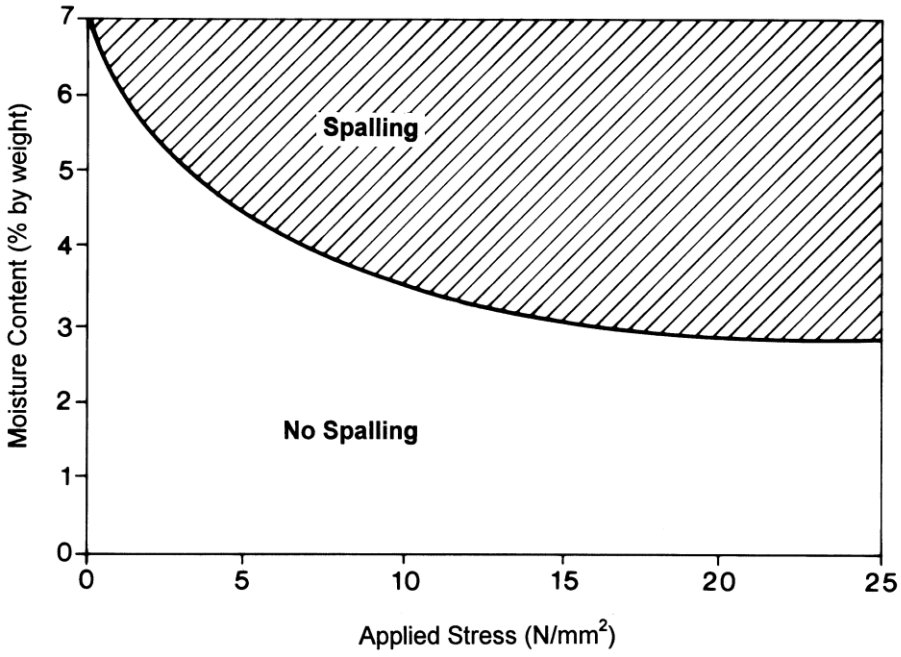

Fig. 2.30. Explosive spalling envelope after Zhukov (1976).

Moreover, moisture content also has significant influence on transport property of concrete. With a higher degree of saturation, the relative permeability of gas phase in concrete is lower (Gawin, Pesavento, & Schrefler, 2002b). It can be postulated that for concrete with high moisture content, the release of vapor pressure is more challenging from the beginning of heat exposure.

In spite of the importance of moisture content on spalling was highlighted by experimental research, from the numerical parametric study of Guo, Yuan and Mang (2016) on relative significance of material parameters for concrete exposed to fire, the saturation of concrete has only a moderate influence on the state of concrete exposed to fire.

Importance of moisture content is highlighted because it shows the contribution of pore pressure to explosive spalling and excludes the possibility that thermal stress is the only source of spalling. In summary, moisture content of concrete is an important factor affecting fire spalling resistance of concrete. However, for different experimental set-ups and concretes with different properties, the importance of moisture is hard to be quantified.

Therefore, a general fixed moisture limit for spalling risk evaluation is not adequate (Jansson, Boström and Silfwerbrand 2013).

Permeability:

Permeability is a measurement of the ability of a porous material to transfer fluids under pressure gradient. It has a significant influence on the build-up of pore pressure and thus spalling of concrete (Guo, Yuan and Mang 2016, Harmathy 1965, Kalifa, Chene and Galle 2001, Yermak, Pliya, Beaucour, Simon and Noumowé 2017). *It is one of the most important parameters bridging mix proportions and spalling behavior.*

Porosity:

Before heating up, capillary pores control the maximum water content of concrete. During heating, porosity acts as a reservoir in moisture migration and pore pressure build-up process. From the study of Guo, Yuan and Mang (2016) on relative significance of material parameters for concrete exposed to fire, porosity plays secondary role in spalling. The influence of porosity should be evaluated with other factors affecting moisture migration, such as permeability.

Compressive strength:

Many studies have demonstrated that a higher strength grade of concrete has a higher susceptibility of spalling (Khoury 2000). Even though, HPC slabs with 117 MPa compressive strength did not spall in the fire test (Khoury and Anderberg 2000). This may be due to the relatively small size of the slab specimens (900×900×104 mm). Khoury and Anderberg (2000) and Kodur and Phan (2007) concluded that HSC is usually accompanied with a compact microstructure and lower permeability. *High compressive strength is a result of the microstructure, but it is difficult to be directly related to pore pressure and thermal stress.*

Tensile strength:

Temperature-dependent tensile strength was widely considered as the failure criteria for explosive spalling. A high tensile strength is considered to lower the risk of spalling because

it offers a higher resistance to pore pressure and thermal stress (Ichikawa 2000, Kalifa, Chene and Galle 2001). It is generally assumed that once the pore pressure exceeds the tensile strength of concrete explosive, spalling will occur (Klingsch 2014). However, this conclusion is controversial because the measured pore pressure measured is much lower than the tensile strength of concrete.

Coefficient of thermal expansion:

Coefficient of thermal expansion affects thermal stress induced by temperature gradient. The expansion of the outer heated surface is restrained by the cooler inner region. Concrete with high thermal expansion rate is more likely to spall. Aggregate type and its composition influence coefficient of thermal expansion of concrete. Thermal expansion of siliceous aggregate concrete is greater than that of carbonate aggregate concrete.

2.5.3 Structural features related parameters

Cross section geometry and size:

Compared to a rectangular cross section, a circular cross section lowers the likelihood of spalling due to lower thermal gradient (Khoury & Anderberg, 2000; V. K. Kodur & McGrath, 2006). If the cross-section area is small and thin, moisture tends to escape more readily from the heated surface. Thus, no spalling could occur (Khoury and Anderberg 2000). For concrete slabs and beams, the section size on the risk of spalling is inconsistent. It is agreed that the specimen size is a secondary factor regarding the risk of spalling (Khoury and Anderberg 2000).

Cover to reinforcement:

Members with thicker concrete cover are more likely to spall, since reinforcement does not provide confinement to concrete cover (Connolly, 1995). Thickness of concrete cover is more relevant to the fire resistance of standard members but not spalling itself.

Modified structural design:

EN 1992-1-2 suggests the use of a secondary reinforcement mesh between the main reinforcement and the fire exposed concrete surface as a good way to minimize the risk of spalling. Tie spacing and configuration also have significant effect on fire performance of HSC columns (V. Kodur, 2000). In Kodur's research, HPC columns with conventional tie configurations show an increased risk of explosive spalling and lead to a total deterioration of the column. A modified tie design with 75% of the usual spacing increased the fire resistance of HPC columns significantly. Sufficient anchorage of ties can be applied by bending the ends of the ties further inwards at an angle of 135° (Kodur and McGrath 2006). The modified reinforcement layout improved the fire resistance of columns to 4 hours, even if spalling occurs on the concrete cover. Supplementary reinforcement protects concrete columns from spalling because it provides confinement.

2.5.4 External loading parameters

Applied load and restraint:

Spalling intensity increases monotonically and linearly with applied compressive stress (Boström, Wickström and Adl-Zarrabi 2007, Jumppanen 1989, Miah, Carré, Pimienta, Pinoteau and Borderie 2015). Fixed ends, eccentric axial force or bending load increase spalling risks (K. D. Hertz, 2003). End restraint will create compressive stresses during heating due to thermal expansion of concrete. It affects both stress distribution and moisture transport (Hertz 2005). Parallel cracks lying close to the heated surface may lower tensile strength of concrete. In addition, applied load restrains propagation of cracks in the direction perpendicular to the heating surface and reduces the increase in permeability (Hertz 2003). Khoury and Anderberg (2000) reported the behavior of concrete columns under different load levels and found that increasing the applied load resulted in an earlier occurrence of explosive spalling, as illustrated in Fig. 2.31. Boström, Wickström and Adl-Zarrabi (2007) investigated prestressed slabs made of HSC (from 72.9 to 106.9 MPa). The test results clearly showed increased probability and amount of spalling when applying external compressive loading.

Miah, Monte, Felicetti, Pimienta, Carré and Borderie (2017) found that biaxial compressive loading has significant influence on fire spalling of concrete (Fig. 2.32). Loaded specimens were more prone to spalling than unloaded specimens, even if the load was very small (0.5 MPa) compared to the compressive strength. Jochen and Christoph (2017) found that while spalling was not observed in slab specimens without lateral compressive load (even for very dense and high-strength concretes), 7 out of 33 concretes showed explosive spalling with lateral compressive load. It was concluded that applied compressive load is a decisive factor for the occurrence of spalling. An interesting observation was that in the cases explosive spalling occurred, very low pore pressures (less than 0.1 MPa) were measured, whereas in specimens did not spall, pore pressures up to 1.4 MPa were recorded.

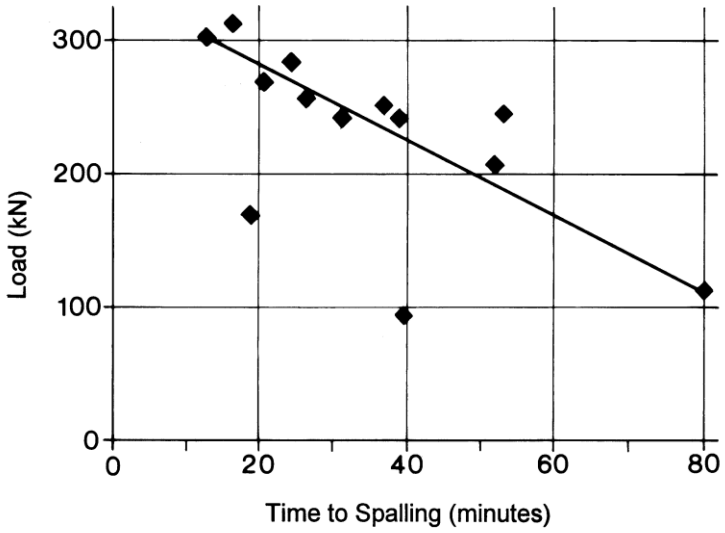

Fig. 2.31. Effect of applied load on spalling time of concrete columns (Khoury and Anderberg 2000).

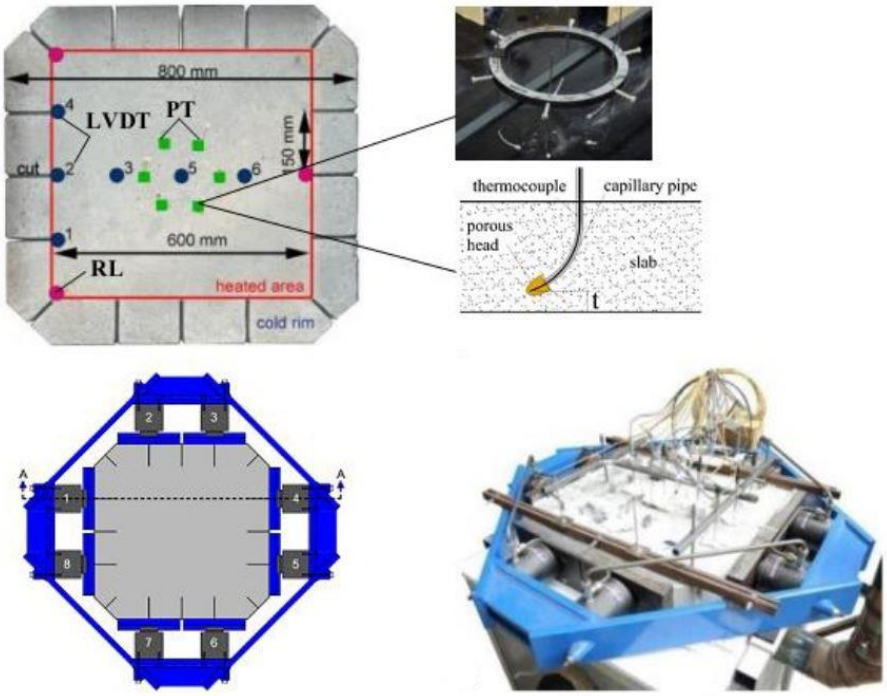

Fig. 2.32. Setup for slab spalling with biaxial compressive loading (Miah, Monte, Felicetti, Pimienta, Carré and Borderie 2017).

Heating rate:

Heating rate is closely related to thermal stress (Klingsch 2014, Kodur and Phan 2007). A higher thermal gradient quickens the pore pressure build-up. Since thermal stress and pore pressure are two main factors leading to spalling, it is expected that heating rate has pronounced effect on spalling. Even though heating rate does have an unneglectable influence on the occurrence of explosive spalling, the threshold of heating rate is highly related to the properties of concrete. Khoury and Anderberg (2000) did not encounter explosive spalling when heating 100 MPa ϕ60 mm cylindrical concrete specimens at a rate of 20-30 °C/min, but even at very slow heating rate (1.0 °C/min) explosive spalling was observed in HPC (Hertz 1984). The heating rate in the current study is chosen to either follow ISO-834 heating rate or lower than 2 °C/min to minimize thermal stress and to isolate the effect of pore pressure.

Heating profile:

Concrete slabs with sections from 20-30 mm heated from one side is less likely to spall in fire than heated from both sides because moisture can escape from the unheated rear side of the specimen (Connolly 1995). Heating on more than one surface increases thermal gradient and temperature at the corners. Therefore, it increases the spalling risk at the corners.

Cooling rate:

Reports about cooling rate on spalling of concrete are rather limited. Since most of the flames are quenched by hose streams, cooling rate was found to have significant effect on residual compressive strength of concrete (Jeyaprabha, Elangovan and Prakash 2016).

2.6 Summary of literature review

According to the literature review on experiments and analyses of UHPC and concrete spalling in this chapter, studies on behavior of UHPC at elevated temperature was outlined. Recent research programs concerning the effect of elevated temperature on mechanical properties and transport properties of UHPC were reviewed. Explosive spalling of concrete was highlighted due to severe damage to the load-bearing capacity of structures. A fairly comprehensive review of the history of explosive spalling was conducted to give an overview of this phenomenon. Three main proposed mechanisms of explosive spalling were presented viz. pore pressure induced stress, thermal gradient induced stress, and combined thermal stress and pore pressure induced stress. In the last section, the main factors influencing explosive spalling are divided into four categories. Their effects on spalling and relationship between the factors are illustrated.

As mentioned in Section 1.1, fire resistance of reinforced concrete (R/C) structures mainly depends on the behavior of concrete under fire. UHPC structures may be more vulnerable to fire due to reduced element dimension and high risk of spalling. Explosive spalling causes a serious effect on the fire resistance of structures, as it results in loss of structural integrity, loss of concrete cross section, and exposure of steel reinforcement to fire. There is still a substantial gap on the understanding of spalling mechanism. Although the effects of many factors on risk of spalling were investigated at macro scale, a holistic understanding of this

phenomenon must be based on experimental studies at the micro-scale. Microstructural changes such as degradation of UHPC matrix, physical or chemical changes of fibers, and formation of micro cracks can then be studied.

Experimental findings from different sources are not consistent. It is probable that, the dominant factors change with concrete qualities and different experimental testing conditions. Instead of relating mix proportions directly to spalling behavior, intrinsic material properties such as compressive strength, tensile strength, and permeability should be measured as objective indexes to minimize influences from testing conditions and concrete mix proportions. UHPC has a very different microstructure from NSC, so its behavior at elevated temperature needs to be investigated specially.

PP fibers are the most widely used method to prevent spalling. However, no standard is available to define the dosage, length, and diameter of PP fibers to prevent spalling. Moreover, there is no consensus on how PP fibers behave inside concrete at elevated temperature. The mechanism of PP fibers to mitigate spalling risk is not clear yet. Steel fibers are widely used to enhance mechanical properties of concrete. They have been found to be beneficial in enhancing fire endurance of HSC columns. But their effectiveness in very dense silica fume concrete has not been confirmed. PE fibers have very high strength and their hydrophobic nature could significantly enhance complimentary energy of fiber bridging. Investigation on the effect of PE fibers on mechanical properties of UHPC, especially at elevated temperature is rather limited. Moreover, PE fibers have lower melting point than that of PP fibers, but the effect of PE fibers on spalling prevention has not been investigated much. The expansion of aggregates increases micro cracks inside concrete at elevated temperature, which can relieve pore pressure and reduce the risk of explosive spalling. In summary, PP, steel, and PE fibers, and aggregate size are the key factors to be investigated in the current research. Their combined effects on mechanical properties, transport properties, and spalling prevention will also be investigated.

Chapter 3 Identification of Mix Proportion of Ultra-high performance Concrete

3.1 Overview

To find a UHPC mix proportion for further research at elevated temperature and about spalling, the effects of steel fiber content, polypropylene fiber content, silica fume content, and aggregate size on the mechanical performance of UHPC at ambient temperature are investigated. The main objective is to identify the range of UHPC mix parameters for the following chapters by optimizing the mix design parameters. The optimum mix design and the dominant parameters that have major effects on the properties of UHPC is identified by Taguchi method.

3.2 Experimental program

3.2.1 Taguchi method and design of mixes

Taguchi method is a process optimization technique developed by Genichi Taguchi during the 1950s (Roy 2010). There are three types of performance characteristics for evaluating the performance of various parameters.

- Smaller is better: choice of goal is to minimize the response.
- Larger is better: choice of goal is to maximize the target response.
- Nominal is better: choose when the goal is to target the response.

Since the aim of the present research is to determine the optimum concrete mix in order to achieve the maximum compressive and tensile strength, the ‘larger the better’ type of quality characteristic situation was evaluated in terms of signal-to-noise ratio (S/N):

$$S/N = -10 \times \log_{10}\left(\frac{1}{n}\sum_{i=1}^{n}\frac{1}{Y_i^2}\right) \quad (3.1)$$

where Y is the measured value of each response and n is the number of repetitions. Taguchi method utilizes orthogonal arrays from design of experiments (DoE) theory to study a large number of variables with the minimum number of experiments. The design of experiments is a powerful scientific statistical method for improving the quality of manufactured goods, and more recently, has been applied to engineering research. Using orthogonal arrays, the number of experimental configurations can be reduced significantly. From DoE, the present work utilized orthogonal arrays to study the following four variables: polypropylene fiber content (PP fiber), steel fiber content (ST fiber), silica fume content (SF); and aggregate size (AG). The levels for the considered parameters are shown in Table 3.1. 1, 2, and 3 kg/m^3 (corresponds to 0.11, 0.22, and 0.33% of PP fibers by volume). 78.5, 157.0, and 235.5 kg/m^3 (corresponds to 1, 2, and 3% of steel fibers by volume).

Table 3.1. Mix parameters and levels

Parameters				
Levels	PP fiber (kg/m^3)	Steel fiber (kg/m^3)	SF [a]	AG (*mm*)
1	1.0	78.5	0.1	0.6
2	3.0	157.0	0.2	2.36
3	5.0	235.5	0.3	5.0

[a] Relative mass ratio to cement

According to the parameters and their variation levels, L9 orthogonal array is used. Table 3.2 shows the defined mix proportions.

Since each mix design is a combination of different factor levels, the individual effect of independent variables needs to be segregated. This can be done by summing up the performance parameter values for the corresponding level. For example, to find out the main effect of level 78.5 kg/m^3 of the steel fiber (refer Table 3.2), sum the performance parameter values of UHPC 1, 4, and 7.

Table 3.2. Mix proportions

Mix Design	PP fiber (kg/m^3)	Steel fiber (kg/m^3)	Relative mass ratio to cement						
			SF	AG	C	FA	SP	SS	W/B
UHPC 1	**1.00**	78.5	**0.10**	**0.60**	1.00	0.15	0.03	0.25	0.20
UHPC 2	**1.00**	157.0	**0.20**	**2.36**	1.00	0.15	0.03	0.25	0.20
UHPC 3	**1.00**	235.5	**0.30**	**5.00**	1.00	0.15	0.03	0.25	0.20
UHPC 4	**3.00**	78.5	**0.20**	**5.00**	1.00	0.15	0.03	0.25	0.20
UHPC 5	**3.00**	157.0	**0.30**	**0.60**	1.00	0.15	0.03	0.25	0.20
UHPC 6	**3.00**	235.5	**0.10**	**2.36**	1.00	0.15	0.03	0.25	0.20
UHPC 7	**5.00**	78.5	**0.30**	**2.36**	1.00	0.15	0.03	0.25	0.20
UHPC 8	**5.00**	157.0	**0.10**	**5.00**	1.00	0.15	0.03	0.25	0.20
UHPC 9	**5.00**	235.5	**0.20**	**0.60**	1.00	0.15	0.03	0.25	0.20

SF: silica Fume, AG: Aggregate mass ratio to cement is fixed at 1.1, largest aggregate sizes in mm are shown in the table, C: cement, FA: fly ash, SP: superplasticizer, SS: Silica sand, W/B: water-to-binder ratio.

3.2.2 Materials

The cement used in this research was ASIA$^{@}$ CEM II 52.5 N. It has a specific gravity of 3.14 and Blaine fineness (specific surface area in square centimeters per gram) of 3860 cm^2/g. Chemical composition of the cementitious materials is given in Table 3.3. Steel fibers are supplied from Dramix$^{@}$. Their length is 13 mm and their diameter is 0.16 mm. The steel fibers have tensile strength greater than 2000 MPa. The monofilament polypropylene fibers were supplied by DFL, they have tensile strength between 550-600 MPa. Their length is 12-19 mm and their diameters are 18-40 µm. A third generation polycarboxylic type superplasticizer Sika$^{@}$ ViscoCrete$^{@}$-2044 was used in all concrete mixtures. Natural river sands were used as aggregate in the concrete mixtures. Table 3.4 presents the grading of fine aggregates.

Table 3.3. Chemical composition of cement

Chemical analyses (%)	CEM II 52.5 R
SiO2	20.7
Al2O3	3.6
Fe3O3	3.2
CaO	64.5
MgO	3.3
SO3	2.4
Na2O	0.26
K2O	0.38
TiO2	0.62
P2O5	0.12
Ignition loss	2.0

Table 3.4. Finesse of aggregate

Sieve size (mm)	% Retained
10	0.10
5.0	3.87
2.36	16.66
1.18	34.99
0.6	53.79
0.3	82.64
0.15	92.99
0	0.10
Fineness modulus	2.85

3.2.3 Preparation of the specimens

The specimens were prepared within 7 min using a rotating mixer. The binder (i.e. cement, and SF), silica sand, and fine aggregates were first mixed for 1 min without water. Afterwards, water and superplasticizer were added gradually in 30 s followed by a 1 min mixing. Then add 20 % of steel fiber and mixed for 2 min. With steel fibers, the mortar became flowable faster. At last, all the remaining fibers were added to the flowable mortar and mixed for another 2 min to get a homogeneous dispersion. Specimens were cast with vibrating.

After the mixing process was completed, specimens were cast using polyester molds with vibration. The following specimens were prepared for each mix design:

- Twenty-seven cubic specimens having dimensions 50×50×50 mm^3, three specimens for each mixture, designated for 28-day compressive strength tests.
- Twenty-seven cylindrical specimens having dimensions 50 mm in diameter and 100 mm in height, three specimens for each mixture, to be subjected to 28-day splitting tensile tests.
- Twenty-seven dog-bone specimens having dimensions 36×16 mm^2 in the middle part; three specimens for each mixture, to be subjected to uniaxial tensile tests.

After casting for 24 h, the specimens were demolded and stored in lime-saturated water at ambient temperature for 26 days. After natural drying in the air for one day, mechanical tests were conducted.

3.2.4 Testing procedure

To investigate the compressive strength, uniaxial compression tests were carried out according to ASTM C109/C109M-11. The tests were conducted by a hydraulic machine with a capacity of 3000 kN. The maximum force was recorded by a data-acquiring device (Fig. 3.1a). A constant loading rate of 100 kN/min was adopted and the maximum force was recorded automatically.

Splitting tensile strength were conducted using the same testing system for compressive strength tests. Cylindrical specimens were placed horizontally between the upper and lower bearing surfaces. Plywood bearing strips were used to distribute the load evenly along the length of the cylinder.

Uniaxial tensile strength tests were also carried out by means of an electro-mechanical testing machine with a tensile capacity of 30 kN. A personal computer was connected to the machine to acquire data. The tests were displacement-controlled, at a rate of 1 mm/min (Fig. 3.1b).

The test results on concrete is shown in Table 3.5. In which compressive strength, splitting tensile strength, and uniaxial tensile strength values were obtained from the average of three specimens.

Fig. 3.1. Test setup (a). compressive and splitting tensile testing machine (b). uniaxial tensile testing machine.

3.3 Results and discussion

Table 3.5. Test results of concrete

Mix Design	Compressive Strength (MPa)	Splitting tensile strength (MPa)	Uniaxial tensile strength (MPa)
UHPC 1	134.46	16.34	7.627
UHPC 2	151.33	19.67	9.486
UHPC 3	160.66	28.86	9.275
UHPC 4	127.48	18.29	7.222
UHPC 5	146.53	26.93	10.593
UHPC 6	149.93	27.22	12.005
UHPC 7	138.2	19.99	9.153
UHPC 8	152.33	26.17	9.097
UHPC 9	140.05	23.29	12.378

The best possible mix proportion levels were investigated for the maximum compressive strength, splitting tensile strength, and uniaxial tensile strength values by using Taguchi method. The ‘larger the better’ type of quality characteristic situation was evaluated. The commercial software JMP was adopted to conduct Taguchi method. The best possible mix

parameter combinations of the UHPC can be determined from the main effect plots for each response from Fig. 3.2 to Fig. 3.4. In the figures, the intersections of the dash lines indicate the optimal settings. Their abscissa values are the levels of parameters to choose. For example, in Fig. 3.2, maximum compressive strength is obtained at 1 kg/m^3 PP fiber, 3% steel fiber by volume, 0.3 silica fume, and aggregate with the size of 5.0 mm. The mix designs are shown in Table 3.6.

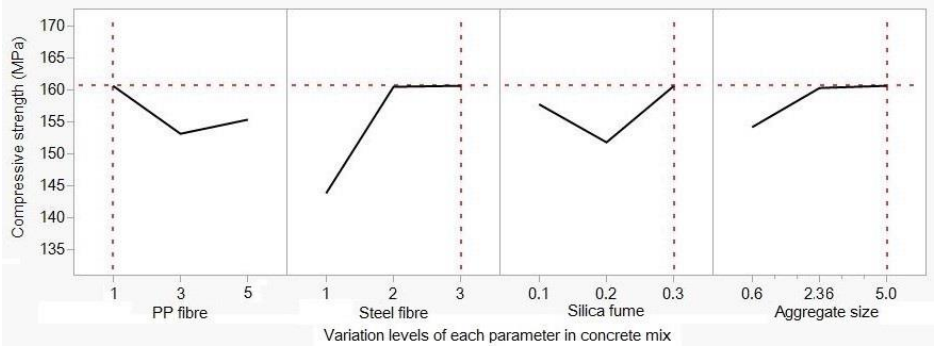

Fig. 3.2. Main effect plot for compressive strength.

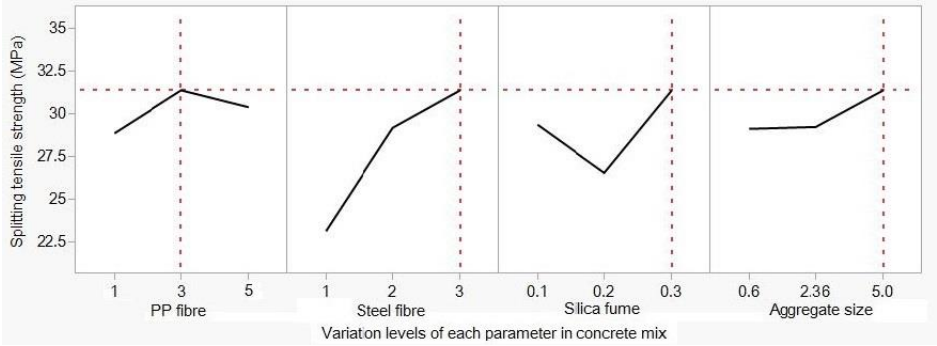

Fig. 3.3. Main effect plot for splitting tensile strength.

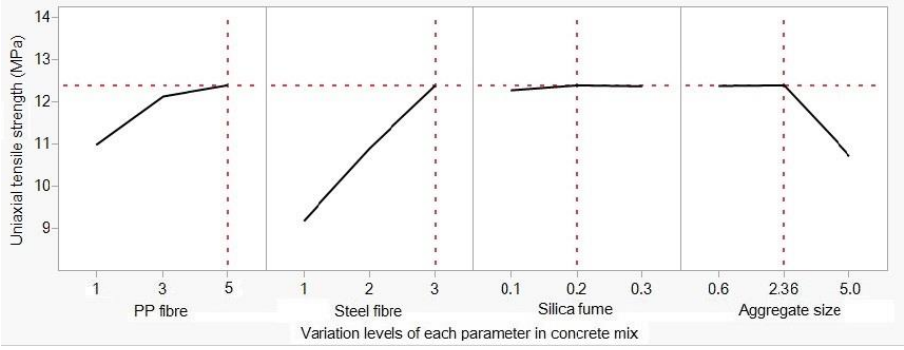

Fig. 3.4. Main effect plot for uniaxial tensile strength.

Table 3.6. Optimal mix design proportions for mechanical properties of UHPC

Optimal mix proportions	PP fiber (kg/m^3)	Steel fiber (Vol. %)	Relative mass ratio to cement	
			Silica fume	Aggregate size
Compressive strength	1	3	0.3	5.0
Splitting tensile strength	3	3	0.3	5.0
Uniaxial tensile strength	5	3	0.2	2.36

Percentage contribution of individual parameter can be well determined using analysis of variance (ANOVA). Table 3.7 to Table 3.9 present the results of ANOVA. The F-test is used for comparing the factors of the total deviation. P-value indicates the significance of parameters. The contribution percentage of factors gives an idea of the significance of factors to strength.

As shown in Fig. 3.2, increasing the steel fiber content from 1 to 2% increases the compressive strength significantly. The reason is the bonding effect of steel fibers. However, further increasing from 2 to 3% the compressive strength does not increase much. This is because with a higher amount of steel fiber, air bubbles could not escape from the steel fiber skeleton. So, more defects were formed inside the concrete. The defects compensate the enhancing effect from more fiber bonding. Research works from (Ranade, Li, Stults, Heard and Rushing 2013, Wille, Naaman, El-Tawil and Parra-Montesinos 2011, Yoo, Shin, Yang and Yoon 2014) show similar trend to the present study. In study from Wille, Naaman, El-Tawil and Parra-Montesinos (2011), the compressive strength of the UHPCs with 2 to 3.5%

steel fibers are 10 to 20 MPa higher than the UHPCs without steel fibers. In study from Ranade, Li, Stults, Heard and Rushing (2013), with increasing steel fiber content from 0 to 3.6%, the compressive strength increases from 160 MPa to 201 MPa. Yoo, Shin, Yang and Yoon (2014) has shown that increasing steel fibers from 2 to 3% the compressive strength does not show significant increase. Further increasing from 3 to 4% the compressive strength decreases about 20 MPa. The mix designs have around 150 MPa compressive strength adopt the optimal range of steel fibers (2% to 2.5%) (Hassan, Jones and Mahmud 2012, Kang and Kim 2011, Yu, Spiesz and Brouwers 2014, Yu, Spiesz and Brouwers 2015). In the present research, the compressive strength of the mix-design proportion with the finest aggregate (0.6 mm) is 4 MPa lower, which might be due to a larger specific area of fine aggregates leading to a lower flowability of concrete. In previous studies, for the UHPCs with 150 MPa compressive strength, the maximum aggregate size used was 2 mm (Klingsch 2014, Yu, Spiesz and Brouwers 2014). For the UHPCs with higher compressive strength, no aggregates larger than 0.6 mm were used. Silica fume mass ratio ranged from 0.1 to 0.4 (Ranade, Li, Stults, Heard and Rushing 2013, Sanjuán, Argiz, Gálvez and Moragues 2015, Wille, Naaman, El-Tawil and Parra-Montesinos 2011, Wille, Naaman and Parra-Montesinos 2011, Yoo, Shin, Yang and Yoon 2014). PP fibers were not the focus when strength was investigated. As a summary, steel fiber content is the most influencing factor on compressive strength of UHPC with 83.30% contribution.

Similar to compressive strength, steel fiber content made the largest contribution to both splitting and uniaxial tensile strength (83.31% and 79.07% respectively). In previous studies, the UHPCs with steel fibers show a 70 to 100% increase of uniaxial tensile strength (Hassan, Jones and Mahmud 2012, Ranade, Li, Stults, Heard and Rushing 2013, Wille, Kim and Naaman 2010, Yu, Spiesz and Brouwers 2014). With a 11.4% contribution, silica fume content plays the second role in splitting tensile strength. Larger aggregate size (13.55%) has negative contribution to uniaxial tensile strength. Induced heterogeneity is the main reason. For the mix-design parameter levels in the present work, the uniaxial tensile strength is 0.414 times of splitting tensile strength (Figure 5). In Model Code 2010-Final draft, Volume 1. fib Bulletin, 65, the data of splitting tests is not considered in order to avoid evident uncertainties resulting from indirect testing (du Béton 2012). However, it concludes that in existing codes and standards, values of uniaxial/splitting tensile strength ratio vary

from 0.67 to 0.95. For example, in EC2 the ratio adopted is 0.9. The lower uniaxial/splitting tensile strength ratio in the present study may be due to the difference between fibers reinforced UHPC and UHPCs without fibers. One possible explanation is that, steel fibers have lower effect in uniaxial tensile test. However, splitting test is affected by a strong combination effect of steel fibers and concrete matrix system.

Optimal conditions for maximum splitting and uniaxial tensile strength are obtained at 3 kg/m^3 PP fiber, 3% steel fiber, 0.3 silica fume, 5.0 mm aggregate size and 5 kg/m^3 PP fiber, 3% steel fiber, 0.2 silica fume, 2.36 mm aggregate size, respectively.

Table 3.7. Analysis of variance results of UHPC compressive strength

Parameters	Sum of squares	Degree of Freedom	Mean square	F-ratio	p-value	Contribution
PP fiber	89.27	2	44.63	0.35	0.72	5.04%
Steel fiber	561.83	2	280.92	5.79	0.040	83.30%
Silica fume	122.04	2	61.02	0.50	0.63	7.20%
Aggregate size	79.72	2	39.86	0.31	0.75	4.46%
Error	322.35	18	17.9			

Table 3.8. Analysis of variance results of UHPC splitting tensile strength

Parameters	Sum of squares	Degree of Freedom	Mean square	F-ratio	p-value	Contribution
PP fiber	9.68	2	4.84	0.19	0.83	2.64%
Steel fiber	109.50	2	54.75	5.99	0.037	83.31%
Silica fume	35.43	2	17.72	0.82	0.48	11.4%
Aggregate size	9.72	2	4.86	0.19	0.83	2.64%
Error	69.45	18	3.86			

Table 3.9. Analysis of variance results of UHPC uniaxial tensile strength

Parameters	Sum of squares	Degree of Freedom	Mean square	F-ratio	p-value	Contribution
PP fiber	3.38	2	1.69	0.48	0.64	7.32%
Steel fiber	15.57	2	7.78	5.18	0.05	79.07%
Silica fume	0.024	2	0.012	0.003	0.997	0.04%
Aggregate size	5.616	2	2.808	0.888	0.459	13.55%
Error	11.46	18	0.64			

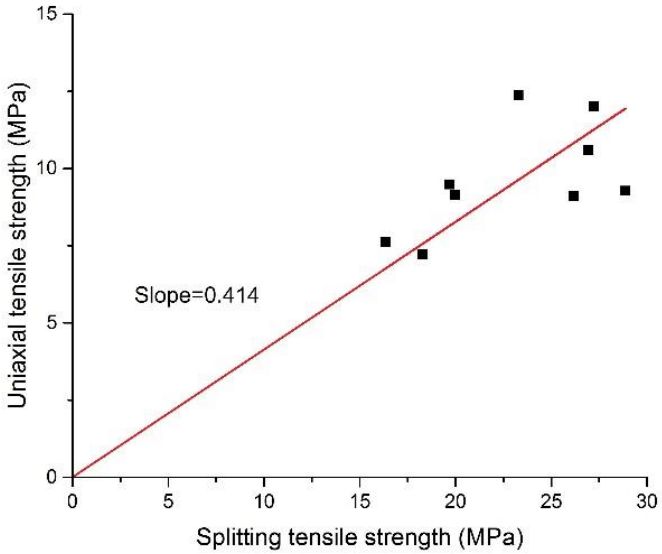

Fig. 3.5. Relationship between splitting and uniaxial tensile strength.

3.4 Confirmation of optimization result

To validate the predicted optimum mix-design proportion, a confirmation experimental study was performed. Three samples for each mechanical property at the optimal mix proportions as determined from Table 3.6 were tested. The same materials and the same loading conditions were used with the Taguchi analyses. The nine specimens were tested for compressive strength, splitting tensile strength, and uniaxial tensile strength. Table 3.10 indicates the test results. The confirmation test results show that maximum compressive

strength, splitting tensile strength, and uniaxial tensile strength could be obtained in the range of allowable error.

Table 3.10. Optimum mix-design confirmation test results

	Compressive Strength (MPa)	Splitting tensile strength (MPa)	Uniaxial tensile strength (MPa)
Optimized result	160.87	27.57	12.03

3.5 Summary

This chapter presents an experimental study to optimize the mix design proportions for UHPC so as to maximize the compressive strength, splitting tensile strength, and uniaxial tensile strength. Taguchi method with L_9 orthogonal array was used to investigate the ranking of contribution of different mix parameters. The most important parameter affecting all the three mechanical properties is steel fiber. The second influencing factor for splitting tensile strength is silica fume content. For uniaxial tensile strength, aggregate size has negative effect. PP fiber does not have significant influence on compressive and tensile strength of UHPC. Confirmation tests show the optimized mix-designs are reliable.

Chapter 4 Effect of Elevated Temperature and Water Quenching on UHPC

4.1 Introduction

Ultra-high performance concrete (UHPC) has high compressive and tensile strengths at ambient temperature. However, due to more slender design of UHPC structures, the residual strength of UHPC after exposure to elevated temperature is of great importance. Moreover, since most of the accidental fire is extinguished by hose streams, it is worthwhile to study the effect of thermal shock caused by water quenching on residual mechanical strength of UHPC. In this regard, compressive strength of UHPC after furnace cooling and water quenching are investigated in this chapter. The effects of PP fiber, steel fiber, and larger aggregate are investigated systematically. The microstructure and chemical changes of UPHCs are investigated by means of field emission scanning electron microscope (FESEM) and X-ray diffraction (XRD), which help to shed light on the deterioration mechanism of concrete at high temperature, in particular, if there are differences associated with two different means of cooling, viz. cooling slowly in furnace and rapid quenching in water. The study on high temperature effect and water quenching will not only help to obtain a better understanding of UHPC but will also provide useful information on post-fire behavior of RC structures.

4.2 Materials and Experimental Methods

4.2.1 Materials and mix proportions

Table 4.1 shows the mix proportions of 4 UHPCs and 1 UHPC cement paste (PA). A UHPC matrix was formulated and used as the control mix referring to the mix proportion in Chapter 3. PP fiber (PP), steel fiber (ST), and larger aggregate (AG) were separately added in a UHPC matrix as factors investigated. The UHPC matrix consisted of cement (C), aggregates (AG), silica sand (SS), silica fume (SF), superplasticizers (SP), and water (W). Portland cement ASIA$^{@}$ CEM I 52.5 N, natural river sand sieved to 600 μm as fine aggregate, silica

sand with a median particle size of 130 μm and Grade 940 silica fume from Elkem Microsilica@ were used. Water-to-binder ratio was kept constant at 0.2 to achieve dense packing and ultra-high strength. A third-generation polycarboxylate-based superplasticizer Sika@ ViscoCrete@-2044 superplasticizers (SP) was used in all UHPC mixtures to adjust workability in the fresh state. Monofilament cylindrical PP fibers with 12 mm length and 30 μm diameter were supplied by DFL. Micro steel fibers with a length of 13 mm and a diameter of 2.2 mm were supplied from Dramix@. The tensile strength of steel fibers is more than 2800 MPa. The mixtures were named as Control, PP (PP fiber), ST (steel fiber), AG (larger aggregate), and PA (paste). Table 4.2 shows the experiments conducted for different mixes. 3.0 kg/m^3 corresponds to 0.33% of PP fibers by volume. 157.0 kg/m^3 corresponds to 2% of steel fibers by volume. Three samples were prepared for compressive tests. After exposure to 300, 600, or 900 ℃ the samples were either slowly cooled in the furnace or rapidly quenched in water.

Table 4.1. Mix proportions of UHPCs

Mix Design	Relative mass ratio to cement						P (kg/m^3)	S (kg/m^3)
	C	AG	SS	SF	SP	W/B		
Control	1	1.1^	0.25	0.25	0.03	0.20	0	0
PP	1	1.1^	0.25	0.25	0.03	0.20	**3**	0
ST	1	1.1^	0.25	0.25	0.03	0.20	0	**157.0**
AG	1	**1.1***	0.25	0.25	0.03	0.20	0	0
PA	1	0^	0	0.25	0	0.20	0	0

C: cement, AG: aggregates, SS: silica sand, SF: silica Fume, SP: superplasticizer, W/B: water-to-binder ratio, ^ denotes aggregates with the maximum size of 600 μm, * denotes aggregates with the maximum size of 5 mm

The UHPC was mixed in a Hobart@ planetary mixer. Cement, fine aggregate, micro silica sand, and silica fume were dry-mixed for 2-5 min. Thereafter, pre-mixed water and superplasticizer were added into the dry ingredients and mixed for another 3 to 5 min until the fresh UHPC was homogenous and consistent. PP or steel fibers were then gradually added and mixed for another 2 min to achieve homogeneous distribution. The fresh UHPC mixtures were cast into 50×50×50 mm^3 cube molds with vibration to remove trapped air.

After casting, all the molded specimens were covered with plastic sheets and stored at room temperature for 24 h prior to demolding. After demolding, all the specimens were water-cured in lime-saturated water at ambient temperature for another 27 days before testing.

Table 4.2. Experiments conducted for each mixture

Mix Design	Compressive strength	XRD	SEM microstructure	SEM phase change
Control	√	√	√	
PP	√		√	
ST	√		√	
AG	√		√	
PA		√		√

4.2.2 Heating and cooling regime

At the age of 28 days, UHPC specimens were pre-heated at 105 ℃ for 2 days to dry the specimens and to prevent explosive spalling. Specimens were then exposed to elevated temperature (i.e., 300, 600, or 900 °C) in an electrical furnace. The heating rate was 1 ℃/min until reaching the pre-determined temperature. Specimens were held at that temperature for 3 h to ensure uniform temperature distribution inside the sample. After that, the specimens were either cooled down to ambient temperature inside the furnace or immediately quenched by water in a water tank. Compressive strength tests were then carried out on the samples.

4.2.3 Experimental methods

The compressive strength tests were conducted at residual state or after water quenching following ASTM C109/C109M-11 (Mater. 2011). The hydraulic compression machine had a capacity of 3,000 kN. A constant loading rate of 100 kN/min was adopted and the maximum force was recorded automatically. At least three samples were tested for each mix design (Table 4.2).

PA samples after exposure to different temperatures and after water quenching, were studied by X-ray diffraction (XRD, Bruker D8 Advance) with Cu-Ka ($\lambda = 1.5418$ Å) operating at 40 kV and 40 mA in a 2 θ range of 7–70° with a step size of 0.02 degree and a speed of 1 s per

step. Once the X-ray analysis was completed, the scans were analyzed using EVA XRD software. Peak intensities at different angles were compared with a database of different minerals and compounds. The XRD spectra were recorded and analyzed for the specimens.

The microstructure of UHPC samples was observed on polished sections. The polished samples were cut from the 50 mm cube specimens by a diamond saw to about 8×8×3 mm^3 and then grinded by emery paper to obtain the required flatness. Samples without exposing to elevated temperature were prepared by oven-drying at 105 °C for 24 hours to remove evaporable water. Finally, all samples were coated with platinum for 45 s under vacuum. The SEM examinations were performed using a field emission scanning electron microscope (FESEM, JSM-7600F, JEOL) to detect micro-structural changes.

4.3 Results and discussions

4.3.1 Compressive strength

Fig. 4.1 shows the residual compressive strengths of UHPC mixtures with different exposure temperatures subjected to cooling in a furnace (F) or water quenching (W). At ambient temperature, compressive strength of Control mix was 131.7 MPa. Inclusions of PP fibers and larger aggregates marginally increased the compressive strength by 5.0% and 5.9%, respectively. Adding steel fibers increased the compressive strength by 11.8%, as they could prevent cracks from expanding (Tai, Pan and Kung 2011).

At 300 °C, residual strength of UHPCs increased significantly without any exception. The compressive strength of ST increased to 215.6 MPa followed by Control, AG, and PP specimens to 209.8, 191.8, and 185.7 MPa, respectively. After water quenching, compressive strength of all the four UHPC mixes dropped significantly to around 150.0 MPa. Following the gain of strength at 300 °C, a lost was observed in with temperature increasing to 600 °C. Strength of ST decreased to 192.2 MPa but strength of Control sharply dropped to 144.4 MPa. PP and AG samples showed even lower compressive strength of 127.6 and 116.0 MPa, which are lower than their strength at the ambient temperature. Compressive strength of all 4 UHPCs dropped significantly after exposing to 900 °C. The residual

compressive strength of Control, PP, AG, and ST were only 55.5, 51.1, 28.7, and 55.9 MPa, which are 42.1, 37.0, 20.6, and 38.0% of their strength at the ambient temperature, respectively. At all levels of heating, residual compressive strengths of ST were higher than that of Control, PP, and AG, which indicates the ability of steel fiber to enhance UHPC.

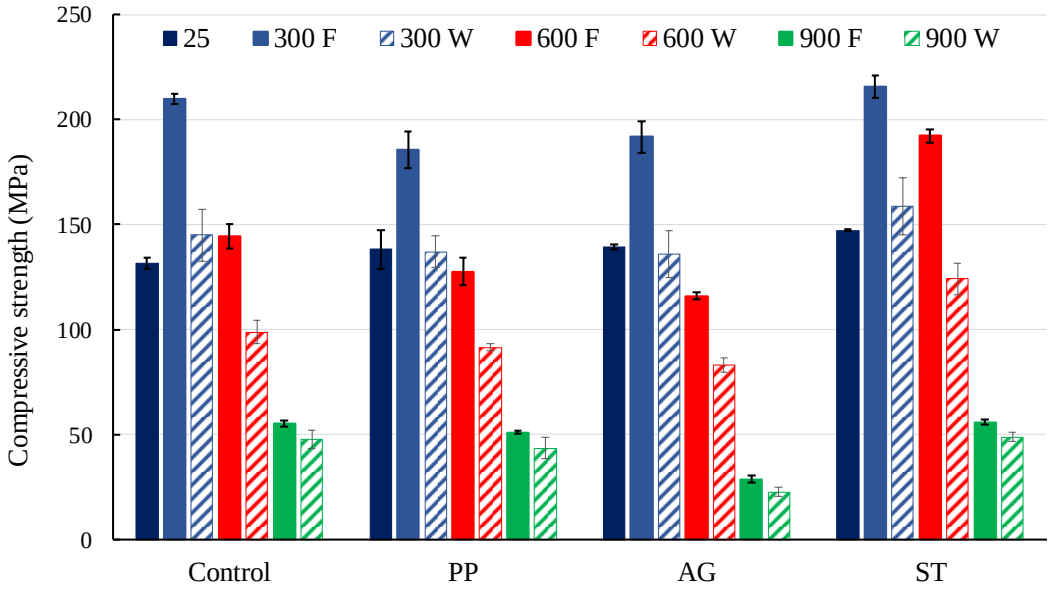

Fig. 4.1. Compressive strengths of UHPC mixtures after heat exposure and water quenching.

As shown in Fig. 4.1, water quenching (legend with "W") significantly lowers the residual compressive strength of UHPC mixtures. In Fig. 4.2, rate of compressive strength loss defined as percentage of compressive strength loss after water quenching with respect to the compressive strength after furnace cooling is illustrated. It can be seen, water quenching resulted in about 25 to 35% strength lose at 300 and 600 °C. This reduction of strength can be attributed to the thermal damage as a result of large thermal gradients within the UHPC samples. Detailed discussions on the mechanism will be presented in the following sections. The differences in mechanical strength of furnace cooled and water quenched UHPCs were more pronounced at 300 °C and 600 °C than that at 900 °C. This is because at 900 °C the samples had been severely damaged. The effect from heat exposure overshadowed the effect of water quenching on residual strength.

As shown in Fig. 4.2, the Control, ST, and AG specimens showed the highest strength loss at 300, 600, and 900 °C, respectively. In comparison, PP samples showed the lowest average strength loss. The significant strength loss of ST samples after water quenching at 600 °C implies that thermal shocking and water emerging have significant effect on steel fibers. Even so, the residual strength of ST was the highest after exposure to 600 °C.

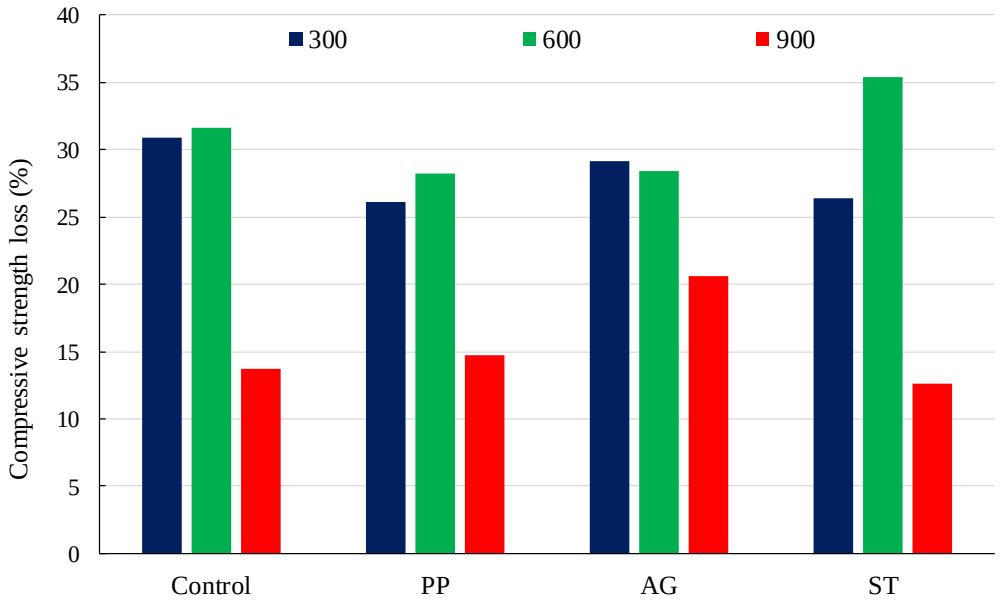

Fig. 4.2. Compressive loss rate after water quenching

4.3.2 XRD

Exposing concrete to elevated temperatures is normally associated with multiple chemo-physical transformations, which affect the microstructure of concrete and consequently, the mechanical strength. The X-ray diffractograms of the PA specimen exposed to different temperatures are shown in Fig. 4.3. As can be seen, phases of calcium hydroxide (CH peaks with label 2), ettringite (AFt peaks with label 1), and unhydrated cement clinker (alite and belite) were observed for the pristine sample without exposing to high temperature.

After 300 °C heating, AFt phase was disappeared due to decomposition of ettringite between 150 and 170 °C (Hager 2013). The intensity of CH was also found to be significantly reduced which may be attributed to conversion of CH into C-S-H due to pozzolanic reaction can be

greatly enhanced at elevated temperature (Hanehara, Tomosawa, Kobayakawa and Hwang 2001, Morsy, Alsayed and Aqel 2010, Zanni, Cheyrezy, Maret, Philippot and Nieto 1996). This process can be responsible for the increased compressive strength (Fig. 4.1). After heating to 600 °C, peaks of CH totally disappeared due to decomposition of calcium hydroxide at 450 °C (Alarcon-Ruiz, Platret, Massieu and Ehrlacher 2005, Seleem, Rashad and Elsokary 2011). Exposing the UHPC samples to 900 °C caused further decomposition of the compounds such as the CH and the C-S-H phases had fully decomposed and only Wollastonite and β-C_2S could be found, which have large crystalline particles (Zhang, Ye and Koenders 2013). Wollastonite is formed when impure $CaCO_3$ is metamorphosed or when silica-bearing fluids are introduced into calcareous sediments during metamorphism, while β-C_2S is one of the decomposition products of C-S-H at elevated temperatures (Aydın and Baradan 2007).

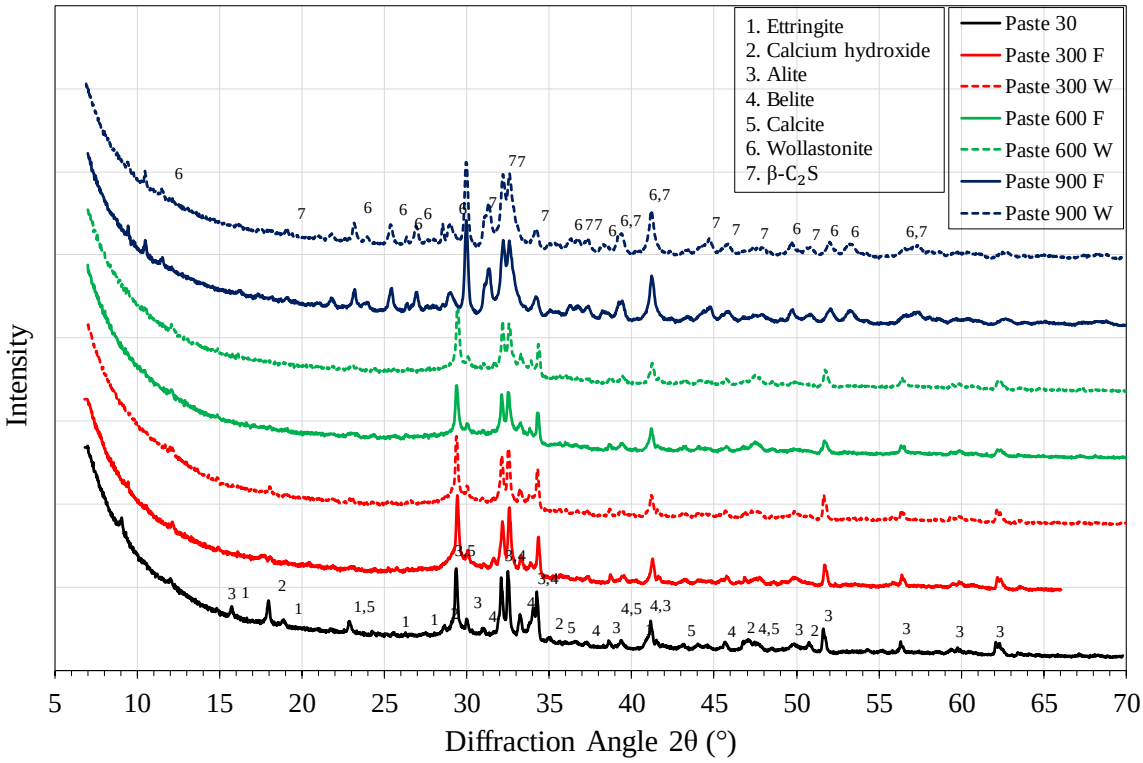

Fig. 4.3. XRD patterns of UHPC pastes after furnace cooling and water quenching.

By comparing the XRD diffractograms of different cooling methods, it seems that water quenching does not lead to significant changes in mineral phases of heated UHPC samples.

This suggests that the lower compressive strength of UHPC specimens subjected to water quenching (Fig. 4.1) was mainly attributed to damage of microstructure due to thermal shock caused, which are essentially physical changes rather than chemical changes.

4.3.3 Microstructure and discussion

The FESEM images of UHPC samples at ambient temperature are shown in Fig. 4.4. Before exposure to elevated temperatures, the samples showed dense and compact microstructure. This explains the high compressive strength of UHPC mixes in the present study (Fig. 4.1). The main hydration product of the UHPC matrix was homogeneous C–S–H gel. From Fig. 4.4, it can be seen the interfacial transitional zone (ITZ) was very compact, which can be explained by the very low water-to-binder ratio of 0.2 and pozzolanic effect of silica fume based on references (Korpa, Kowald and Trettin 2009, Wang, Shi, Wu, Xiao, Huang and Fang 2015). Large crystals of CH and ettringite were generally absent because of their low percentage (Fig. 4.4). Fine microcracks can be observed, which can be explained by expansion of unhydrated clinker and shrinkage of cement paste during the process of 105 °C drying (Piasta 1984).

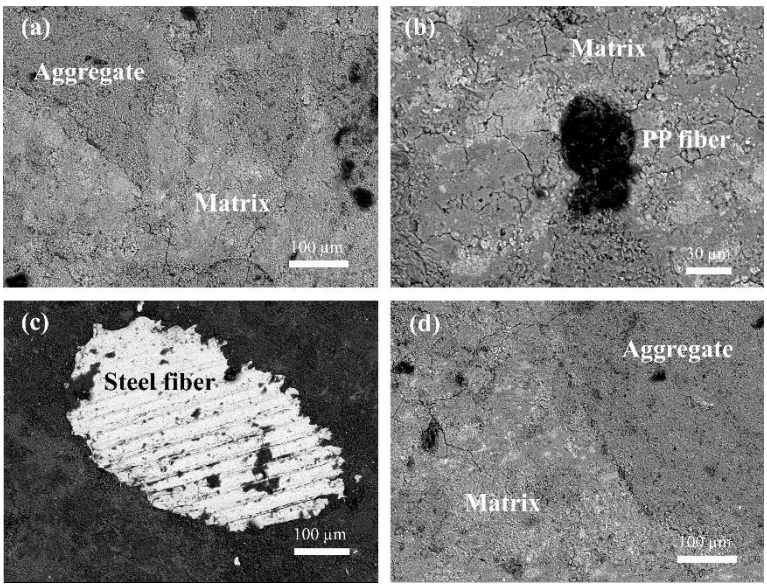

Fig. 4.4. The SEM images of Control, PP, ST, and AG samples at ambient temperature.

From Fig. 4.5, after 300 °C heating, the samples maintained a dense microstructure. Wider microcracks can be observed compared to those found in Fig. 4.4, which was at ambient temperature. For the Control sample, microcracks formed, and according to (Lau and Anson 2006) this may be explained by a further loss of physical and chemical bond water from UHPC paste. For the PP sample, the PP fibers melted and left empty fiber channels. Expansion of PP fibers at high temperature induced microcracks in the radial direction of fiber channels based on (Khoury and Willoughby 2008), which combined with the empty fiber channels accounted for the lower compressive strength of PP samples compared to other UHPC mixtures. Thermal incompatibility between larger aggregates and UHPC matrix also caused microcracks (Fu, Wong, Tang and Poon 2004, Mehta and Monteiro 2006, Sellevold and Bjøntegaard 2006, Zunino, Castro and Lopez 2015), which explains lower compressive strength of AG mix compared to that of Control mix. On the contrary, due to the bonding effect of steel fibers, ST mix showed higher compressive strength than that of Control mix (Fig. 4.1).

In general, even there seemed to be more microcracks at 300 °C than that at the ambient temperature, the compressive strength of the samples increased significantly, which is likely attributed to the enhanced UHPC matrix by further hydration of unhydrated cement clinkers as a result of increased pozzolanic reaction of silica fume. It is worth noting that, approximately a w/c ratio of 0.38 by mass is needed for full hydration of clinker minerals (Oertel, Hutter, Helbig and Sextl 2014), which is much higher than the w/b ratio of 0.2 (w/c=0.25) used in the present UHPC mixtures.

As an evidence, XRD results in Fig. 4.3 showed the reduced peak of CH at 300 °C. Conversion of CH into C-S-H due to pozzolanic reaction can be greatly enhanced at elevated temperature (Hanehara, Tomosawa, Kobayakawa and Hwang 2001, Morsy, Alsayed and Aqel 2010, Zanni, Cheyrezy, Maret, Philippot and Nieto 1996). From Fig. 4.5b, d, f, and h, the microcracks after water quenching seemed to be wider than those after furnace cooling. This was caused by thermal shock from water quenching and it accounted for the significantly lower strength of water quenched samples. However, quantitatively analysis of cracks still needs much more effort.

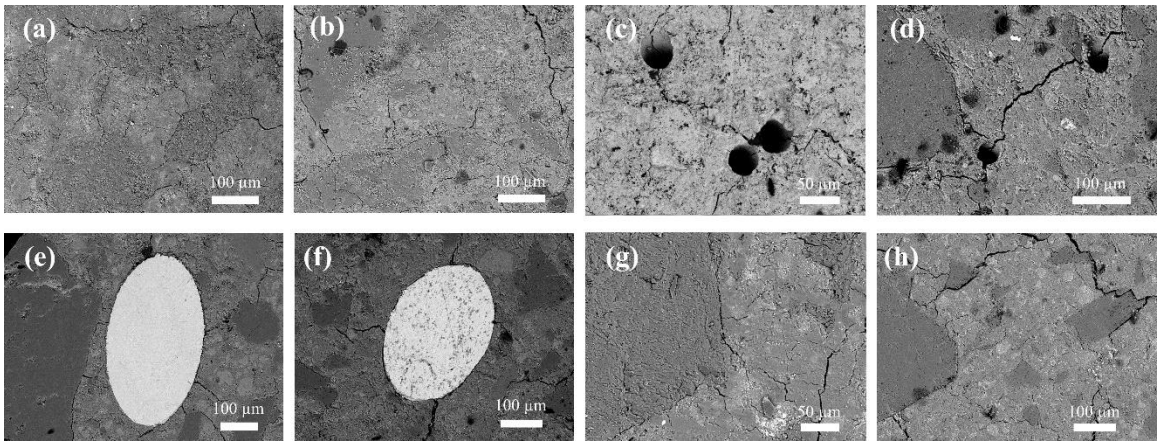

Fig. 4.5. The SEM images of UHPC samples after furnace cooling and water quenching at 300 °C. (a/b) Control furnace cooling/water quenching (c/d) PP furnace cooling/water quenching (e/f) ST furnace cooling/water quenching (g/h) AG furnace cooling/water quenching.

Fig. 4.1 demonstrates that the UHPC samples deteriorated at 600 °C. From Fig. 4.6, further increasing temperature up to 600 °C resulted in wider microcracks than that at 300 °C. The XRD results show that the crystalline compositions of UHPC paste were generally kept constant from ambient to 600 °C (Fig. 4.3), except for totally dehydration of calcium hydroxide (CH). However, for amorphous C–S–H, it is believed that dehydration and recrystallization of C–S–H compound starts from 450 to 500 °C (Piasta 1984, Zhang, Ye and Koenders 2013) accompanied with volume reduction. On the other hand, the unhydrated clinker particles, which were surrounded by C-S-H, expanded due to thermal dilation. Thus, thermal strain mismatch between shrinking hydration products and expanding clinker led to micro-cracking and microstructural changes. Coarsening of pore structure is another reason for significantly loss of strength at 600 °C (Poon, Azhar, Anson and Wong 2001).

The AG mix had the lowest compressive strength after heated to 600 °C, which corresponds to its widest cracks along the aggregates as shown in Fig. 4.6g. This is due to expansion of quartz caused by α to β phase transformation at 573 °C (Seleem, Rashad and Elsokary 2011). With larger aggregate diameter, more severe cracks will be formed in AG specimens according to (Grassl, Wong and Buenfeld 2010). The very high remaining strength of ST mix (192.2 MPa) at 600 °C was attributed to bonding effect of steel fibers. 600 °C is still far

below the melting point of the steel fiber (around 1370 °C). From Fig. 4.6e, the steel fiber did not detach from UHPC matrix significantly, which implies a good contact between the fiber and the UHPC matrix. On the other hand, melting of PP fibers is irreversible. Therefore, mechanical strength of PP samples was compromised.

After water quenching, thermal shock caused about 30% strength loss of UHPC mixes (Fig. 4.2). From Fig. 4.6b, d, f, and h, $CaCO_3$ crystals can be observed on the surface of the water-quenched samples. The $CaCO_3$ crystals were from carbonation of $Ca(OH)_2$ (Papadakis, Fardis and Vayenas 1992), which is a result of hydration of unhydrated clinkers or CaO caused by dehydration of C-S-H. Volume change of crystals during this process is postulated to be another reason for the loss of compressive strength.

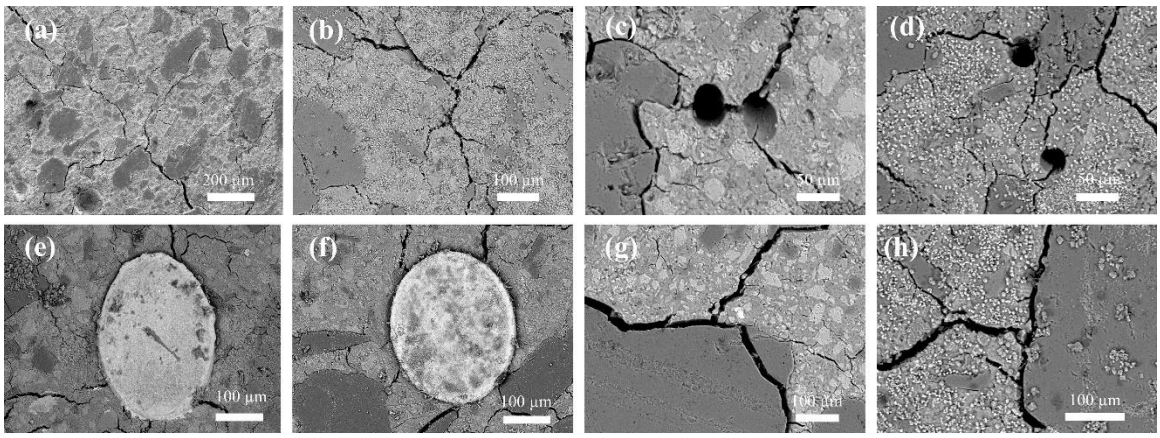

Fig. 4.6. The SEM images of samples after furnace cooling and quenching at 600 °C. (a/b) Control furnace cooling/water quenching (c/d) PP furnace cooling/water quenching (e/f) ST furnace cooling/water quenching (g/h) ST furnace cooling/water quenching.

After heated to 900 °C, the Control, PP, and ST mixes had residual compressive strength dropped to about 40 MPa and the AG mix only remained 20 MPa of compressive strength. Fig. 4.7 illustrates the microstructure of UHPCs at this temperature level. As can be seen, all the main hydrated phases appeared as very loose and porous formation. The coarsening of the pore structure is a main reason for the reduction of mechanical properties (Ma, Guo, Zhao, Lin and He 2015).

Exposing the UHPC samples to 900 °C caused further decomposition of the hydration compounds. From the XRD results (Fig. 4.3), the CH and the C-S-H phases had fully decomposed and only Wollastonite and β-C_2S could be observed. Wollastonite is formed when impure $CaCO_3$ is metamorphosed or when silica-bearing fluids are introduced into calcareous sediments during metamorphism, while β-C_2S is one of the decomposition products of C-S-H at elevated temperatures based on (Aydın and Baradan 2007). According to (Zhang, Ye and Koenders 2013), the C-S-H transformed to β-C_2S in the form of particles and then merged into large β-C_2S particles accompanied by large volume change. Thus, the UHPC paste tended to separate from the aggregates at ITZ area thereby creating wider cracks. It seems that deterioration of UHPC matrix dominated the decrease of compressive strength of the UHPC mixtures.

Water quenching also caused loss of compressive strength at 900 °C. Large thermal gradients within the UHPC samples is a main reason for reduction of strength. Potential reaction of decomposed hydration products with water could change the volume of UHPC matrix (Aydın and Baradan 2007, Jeyaprabha, Elangovan and Prakash 2016). At last, another potential mechanism is that quenching water may penetrate the matrix and act as lubricant between failure planes.

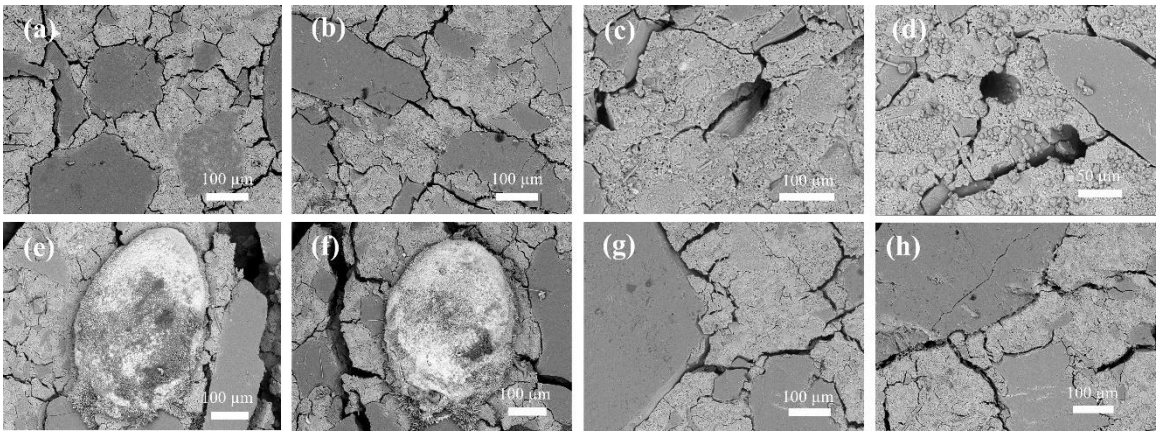

Fig. 4.7. The SEM images of samples after furnace cooling and quenching at 900 °C. (a/b) Control furnace cooling/water quenching (c/d) PP furnace cooling/water quenching (e/f) ST furnace cooling/water quenching (g/h) AG furnace cooling/water quenching.

Considering the porous microstructure and the formed microcracks, the UHPCs at high temperature may absorb more water during the quenching process. However, from the XRD results, sudden contact with water did not affect the hydration products of UHPCs (Fig. 4.3). Therefore, the loss of compressive strength due to water quenching is mainly attributed to the formation of microcracks due to larger thermal stresses in the samples. Besides the soaked water behaves as a lubricant between failure planes.

4.4 Summary

The slenderer cross section of UHPC structures compared to normal strength concrete structures makes post-fire properties of UHPC more crucial. Most of the accidental fire is extinguished by hose streams. Therefore, the compressive strength of UHPC with PP fibers, steel fibers, and larger aggregates after exposure to elevated temperature from 300 ℃ to 900 ℃ and after water quenching were investigated in this chapter. The microstructures of UPHCs were investigated by means of field emission scanning electron microscope (FESEM) and X-ray diffraction (XRD).

At ambient temperature, adding PP fiber, larger aggregate, and steel fiber increased the compressive strength by 5.0%, 5.9%, and 11.8%, respectively. At 300 °C, the average residual strength of UHPC mixtures after furnace cooling increased by 44.4%, which was attributed to hydration of unhydrated cement clinkers. There was evidence of pozzolanic reaction by the reduced CH peak from the XRD analysis. All samples showed dense microstructures, and thin microcracks could be observed.

A sharp loss of compressive strength was observed with temperature increasing to 600 °C. Microcracks widened due to decomposition of cementitious compound C-S-H (from 450 to 500 °C) and α to β-phase transformation of quartz sand. Steel fibers still enhanced compressive strength but adding PP fibers and larger aggregates caused more cracks and decreased the compressive strength.

At 900 °C, the residual compressive strength was only 34.4% of that at the ambient temperature. The hydration products showed significant decomposition. The UHPC paste

appeared as very loose and porous formations. The peaks of C-S-H and clinkers merged into one peak in the gray-scale histogram. Wollastonite and β-C_2S with large crystalline particles were observed from XRD analysis. The Control, PP, and ST samples had similar residual compressive strengths. On the other hand, the AG samples had lower compressive strength probably due to more extensive cracking.

At all temperature levels the compressive strength of all the UHPC mixtures cooled rapidly by water quenching decreased significantly. The compressive strength decreased by 28.1, 30.9, and 15.4% at 300, 600, and 900 °C, respectively. From XRD analysis, water soaking did not show any effect on hydration products of UHPCs. The reduction of strength is mainly attributed to physical formation of microcracks as a result of thermal shock to the samples and the lubrication effect of water between failure planes.

Chapter 5 Effect of Factors on Flexural Behavior of UHPC

5.1 Overview

This chapter aims to investigate effects of polyethylene fibers and steel fibers on mechanical properties of UHPC. The effect of combined use of PE and steel fibers is investigated since 1). hybridization of fibers showed favorable effect on mechanical properties, especially tensile and flexural performance (Ahmed, Maalej and Paramasivam 2007, Banthia and Gupta 2004, Banthia and Nandakumar 2003, Hsie, Tu and Song 2008, Qian and Stroeven 2000, Sivakumar and Santhanam 2007, Yao, Li and Wu 2003); 2). Polyethylene (PE) fiber has much higher tensile strength than that of PP and Polyvinyl alcohol (PVA) fiber (Choi, Lee, Ranade, Li and Lee 2016). The high strength can transmit large interfacial frictional stresses generated by the densely-packed UHPC matrix without rupturing. And 3). the hydrophobic nature of PE fiber could significantly enhance the complimentary energy of fiber bridging (Ranade, Li, Stults, Heard and Rushing 2013). However, investigation on hybrid combination of PE and steel fibers on flexural performance of UHPC is limited, even the fibers can provide potential improvement in mechanical properties of concrete separately. Moreover, the effects of aggregate size and water-to-binder ratio are also investigated. The parameters to evaluate mechanical performances are compressive strength, flexural tensile strength, toughness, toughness index, and synergistic index at ambient and elevated temperatures.

Beyond mechanical properties, the possibility of PE fiber to prevent explosive spalling is also investigated. Differences between PE fiber and PP fiber on UHPC microstructure is analyzed by FESEM.

5.2 Experimental program

5.2.1 Materials and mix designs

Table 5.1 shows mix proportions of UHPCs. The control mix used in this chapter followed the mix proportion used in Chapter 3 and Chapter 4, which consisted of cement, fine aggregate (less than 0.6 mm), micro silica sand, and silica fume, with a water-to-binder ratio of 0.2. Binder comprised cement (C) and silica fume (SF). The cement used was ASIA@ CEM I 52.5 N Portland cement. Natural river sands were used as fine aggregate in the concrete mixtures. Silica sand (SS) with a median particle size of 130 μm was used as a filler material. The silica fume used was Grade 940 from Elkem Microsilica@, which is a highly reactive pozzolan. A third generation polycarboxylate-based superplasticizer (SP) Sika@ ViscoCrete@-2044 was used in the design mix to achieve desired consistency and workability.

Table 5.1. Mix proportions of UHPCs and fiber volume fractions

Mix Design	Relative mass ratio to cement						PE fiber (vol.%)	Steel fiber (vol.%)
	C	AG	SS	SF	SP	W/B		
PE00ST00	1.0	1.1^	0.25	0.25	0.04	0.2	0.0	0.0
PE00ST10	1.0	1.1^	0.25	0.25	0.04	0.2	0.0	1.0
PE00ST20	1.0	1.1^	0.25	0.25	0.04	0.2	0.0	2.0
PE05ST00	1.0	1.1^	0.25	0.25	0.04	0.2	0.5	0.0
PE05ST10	1.0	1.1^	0.25	0.25	0.04	0.2	0.5	1.0
PE05ST20	1.0	1.1^	0.25	0.25	0.04	0.2	0.5	2.0
PE10ST00	1.0	1.1^	0.25	0.25	0.04	0.2	1.0	0.0
PE10ST10	1.0	1.1^	0.25	0.25	0.04	0.2	1.0	1.0
PE10ST20	1.0	1.1^	0.25	0.25	0.04	0.2	1.0	2.0
PE00ST00WB03	1.0	1.1^	0.25	0.25	0.04	**0.3**	0.0	0.0
PE10ST20WB03	1.0	1.1^	0.25	0.25	0.04	**0.3**	1.0	2.0
PE00ST00AG23	1.0	**1.1***	0.25	0.25	0.04	0.2	0.0	0.0
PE10ST20AG23	1.0	**1.1***	0.25	0.25	0.04	0.2	1.0	2.0

C: cement, AG: aggregates, SS: silica sand, SF: silica Fume, SP: superplasticizer, W/B: water-to-binder ratio, ^ denotes aggregates with the maximum size of 0.6 mm, * denotes aggregates with maximum size of 2.3 mm.

To investigate the hybridization effect of PE and steel fiber on flexural performance of UHPC, 0.0, 0.5, and 1.0% (corresponds to 9.6 kg/m^3) of PE fibers, and 0.0, 1.0, and 2.0% (157.0 kg/m^3) of steel fibers were added in UHPC mixes, respectively. The combinations led to nine mix designs as summarized in Table 5.1. The letters PE, ST, WB, and AG indicate the PE fiber, steel fiber, water-to-binder ratio, and aggregate size, respectively. Subsequent numbers denote the fiber volume fraction, water to binder ratio, and aggregate size. For example, PE05ST10 represents a UHPC containing 0.5% volume of PE fibers and 1.0% volume of steel fibers. PE00ST00WB03 and PE10ST20WB03 contained higher water-to-binder ratio of 0.3 while PE00ST00AG23 and PE10ST20AG23 have larger aggregates (2.3 mm).

Fig. 5.1 shows the type of steel fibers and PE fibers used. To achieve high ductility, 19 mm long high-strength high-modulus PE fibers (Spectra® 1000, Honeywell) with a diameter of 23 μm were used. Steel fibers with a length of 13 mm and a diameter of 220 μm were supplied from Dramix$^{@}$. Table 5.2 summarizes the mechanical properties and geometry of PE and steel fibers used in this study. As can be seen, the tensile strength of the Dramix$^{@}$ steel fibers is above 2,800 MPa and the Spectra® 1000 PE fiber has a very high tensile strength of 3250 MPa due to the use of ultra-high-molecular-weight PE resin for the production of fibers through a gel-spinning process.

Fig. 5.1. Micro steel fibers and PE fibers used in this study.

Table 5.2. Properties of PE and steel fibers

	Diameter (μm)	Length (mm)	Tensile strength (MPa)	Elastic modulus (GPa)	Density (kg/m^3)
PE fiber	23	19	3250	113	960
Steel fiber	220	13	>2800	200	7850

5.2.2 Specimen preparation

The UHPC samples were prepared by using the same procedure described in Section 0.

From each mix design, 3 cubes (50×50×50 mm^3) were cast for compression tests and 3 prisms (50×50×350 mm^3) for flexural tests.

5.2.3 Heat treatment

For flexural behavior after exposure to elevated temperature, the samples were subjected to 300 and 600 ℃ in an electrical heating furnace. All the specimens were heated at a heating rate of 1 ℃/min and the target temperatures were maintained for 3 h to ensure uniform temperature distribution within the sample volume. After heating, the specimens were cooled down to the room temperature within the furnace. Then flexural tests were carried out the next day.

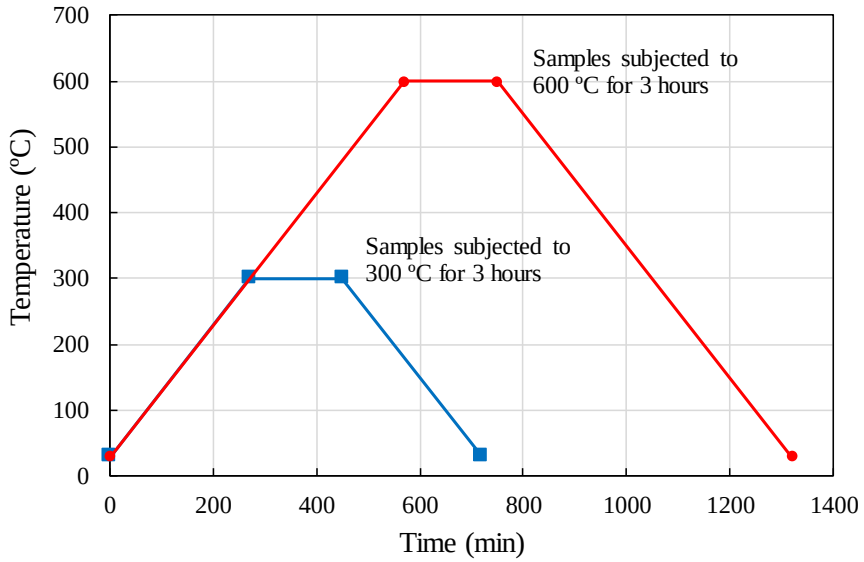

Fig. 5.2. Heating and cooling curve for the cube and prism specimens.

5.2.4 Compressive and flexural test

To investigate the compressive strength after heating, uniaxial compression test was carried out on the cubes. The compressive strength tests were conducted following ASTM C109/C109M-11 (Mater. 2011). A hydraulic compression machine of 3,000 kN capacity driven by a servo-hydraulic control unit was used for the load-control compression tests (Fig. 5.3). A constant loading rate of 100 kN/min was adopted and the maximum force was recorded.

Fig. 5.3. Set-up for compressive test.

The geometry of flexural specimen (50×50×350 mm^3) and the test set-up are shown in Fig. 5.4. A universal testing machine was used to conduct displacement-controlled bending tests under third-point flexural loading, and a uniaxial load was monotonically applied to the beams at a rate of 0.2 mm/min to obtain the load-deflection curve. The clear span length was 300 mm. Two frames equipped with linear variable differential transducers (LVDT) at both faces of the specimen were installed to measure the mid-span deflection. The applied load was measured from the load cell. Three beams were used for each mix design to obtain an average value, and they were tested according to standard ASTM C1609/C1609M (Mater. 2012).

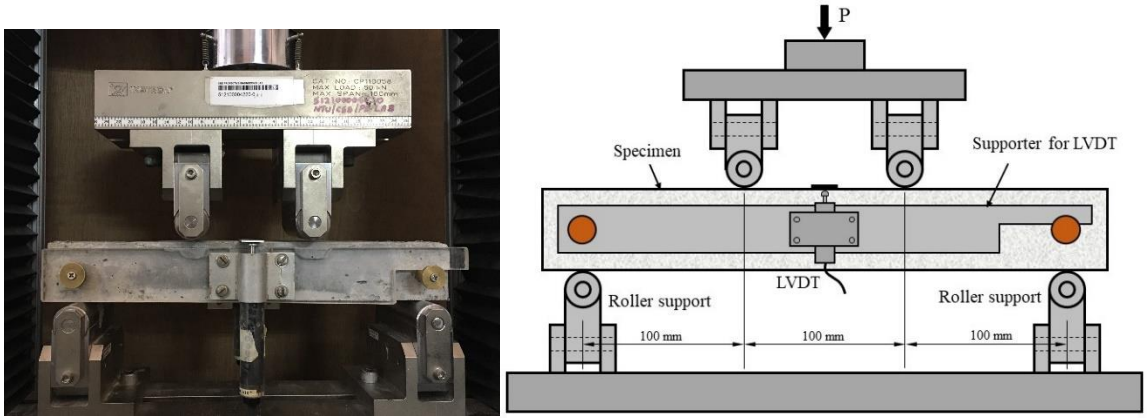

Fig. 5.4. Set-up for flexural test.

Flexural behavior of UHPC can be categorized into deflection hardening and softening behaviors as shown in Fig. 5.5. Following ASTM C1609/C1609M (Mater. 2012) and ASTM C1018 (Mater. 1997), parameters describing flexural behavior of UHPC were used in this study. The first-crack strength f_1 which characterizes flexural behavior of the fiber-reinforced concrete specimen up to the onset of cracking, is defined as the stress value corresponding to the first-crack load:

$$f = \frac{PL}{bd^2} \tag{5.1}$$

where P is the total load (Fig. 5.4), L is the clear span length of 300 mm, b is the width of specimen, and d is the full depth of specimen. The first-crack load P_1 is the load value at the first point on the load-deflection curve when there is a change in gradient. The peak strength f_P is the stress corresponding to the peak load P_p (Fig. 5.5) in Eq. 5.1. It is noted that toughness is a measure of the energy absorption capacity of the test specimen. It is the energy equivalent to the area under the load-deflection curve up to a specified deflection. The specimen toughness T_{150}^{D} refers to toughness of beam of nominal depth D at a deflection of L/150. As in ASTM C1609/C1609M, total applied loads P corresponding to a deflection of L/600 and L/150 were measured (Fig. 5.5). Two additional deflections of L/100 and L/75 were measured because UHPC exhibited an excellent load-carrying capacity even at larger deflections. Toughness values are directly dependent upon geometrical variables of the

specimen and the loading arrangement, and toughness index reflects the degree of member ductility. According to ASTM C1018 (Mater. 1997), toughness indexes I_5, I_{10}, and I_{20} are respectively the ratios of the area under the load–deflection curve (up to 3.0, 5.5, and 10.5 times the first-crack deflection δ) to the triangular area up to the first-crack deflection δ (Fig. 5.5). For brittle materials, toughness index equals to 1. Due to high ductility of UHPC, I_{30} at the deflection of 15.5δ could still be measured.

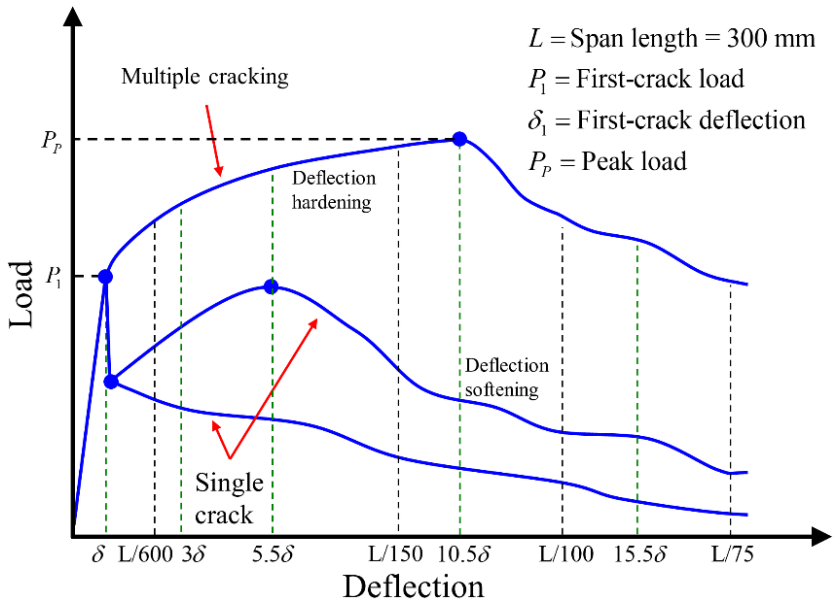

Fig. 5.5. Typical load–deflection response curves of FRC.

5.3 Compressive strength

The compressive strength of all UHPC mixtures after 28 days are illustrated in Fig. 5.6. As can be seen, PE fibers have slightly negative effect on compressive strength. For the PExST00 (x=0, 05, 10) with PE fiber increased from 0 to 1%, the compressive strength reduced 6.6% from 145.1 MPa to 134.9 MPa. This may be that the PE fibers with 640 aspect ratio trapped more air bubbles during mixing (Wille, Naaman, El-Tawil and Parra-Montesinos 2011). In contrast, adding steel fibers from 0 to 2% increased the compressive strength. Moreover, the inclusion of PE fibers in UHPC somewhat negated the beneficial effect from steel fibers. For example, the compressive strength of PE00ST20 was 17.1 MPa

(11.8%) higher than that of PE00ST00. However, PE10ST20 only increased 12.1 MPa (9.0%) compared to that of PE10ST00.

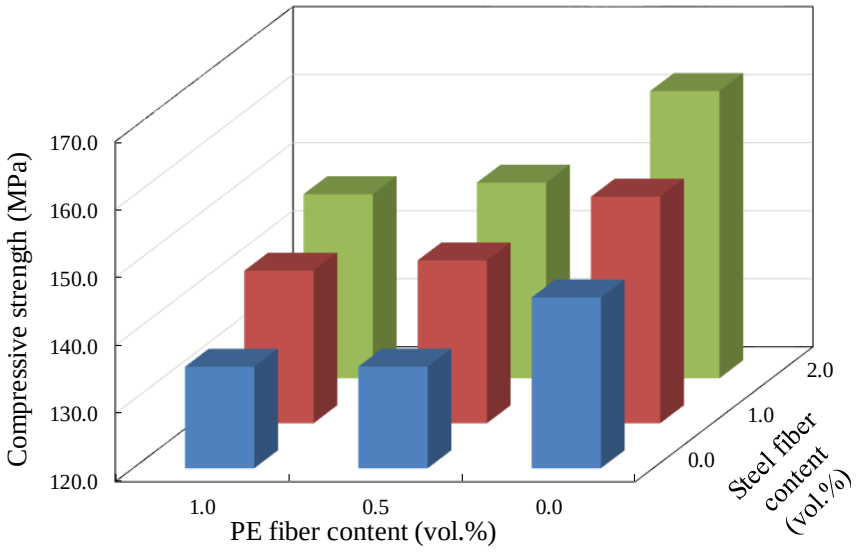

Fig. 5.6. Compressive strength of specimens with different content of PE and steel fibers.

Table 5.3 shows the effect of W/B ratio and aggregate size on compressive strength of UHPC. Each value is an average of three samples and the "±" indicates the standard deviation for each mix design. For PE00ST00, increasing W/B ratio from 0.2 to 0.3 only led to a slight reduction of compressive strength. However, at W/B=0.3 PE10ST20 showed 14.2 MPa lower compressive strength compared to that of PE00ST00. This is because at W/B=0.3, the concrete matrix as well as the bond between UHPC matrix and the fibers were weaker. Instead of providing enhancement to the matrix, the fibers lowered the compressive strength of UHPC. Increasing aggregate size from 0.6 mm to 2.3 mm only led to 3.3 MPa reduction of compressive strength to PE00ST00. However, for PE10ST20AG23 with both fibers, an increase of 6.7 MPa was observed. This is probably because the cement paste was not weakened by the inclusion of larger aggregates. In addition, better interlocking action between fibers and larger aggregates was obtained (Liu, Han, Cui, Zhang, Lv, Zhang and Yang 2016).

Table 5.3. Compressive strength of specimens with different W/B ratios and AG sizes

Compressive strength		
Mix design	W/B ratio	
	0.2	0.3
PE00ST00(WB02/03)	145.1±5.5 MPa	141.8±4.6 MPa
PE10ST20(WB02/03)	147.1±2.5 MPa	127.6±2.9 MPa
Mix design	AG size	
	0.6 mm	2.3 mm
PE00ST00(AG06/23)	145.1±5.5 MPa	141.8±4.0 MPa
PE10ST20(AG06/23)	147.1±2.5 MPa	153.8±2.5 MPa

5.4 Flexural hardening behavior of UHPC

5.4.1 Load vs. Deflection behaviors

Typical flexural responses of all test series are illustrated by respective load–deflection curves in Fig. 5.7. The load after cracking of PE00ST00 drops directly (Fig. 5.7a). For UHPC with steel fibers alone (Fig. 5.7b and c), their strength increased with increasing fiber content. However, earlier and steeper decrease in the post-peak flexural load was observed as compared to those with combined fibers. Post cracking strength of PE05ST00 (Fig. 5.7d) was less than its first crack load since the total force held by PE fibers was not sufficient to form new cracks, so the initial crack widened and localized. Increasing the PE fiber dosage to 1% (Fig. 5.7g), PE10ST00 had sufficient PE fibers between the crack surfaces to sustain an ultimate load more than the first crack load. Therefore, PE10ST00 showed flexural hardening. As shown in Fig. 5.7e to i, combined use of PE and steel fibers significantly improved the maximum load and flexural hardening behavior. Increased water-to-binder ratio to 0.3 significantly decreased the maximum load but increased aggregate size to 2.3 mm seemed to improve the flexural behavior of UHPC (Fig. 5.7j to m). The results of toughness and toughness index will be further discussed in the following sections.

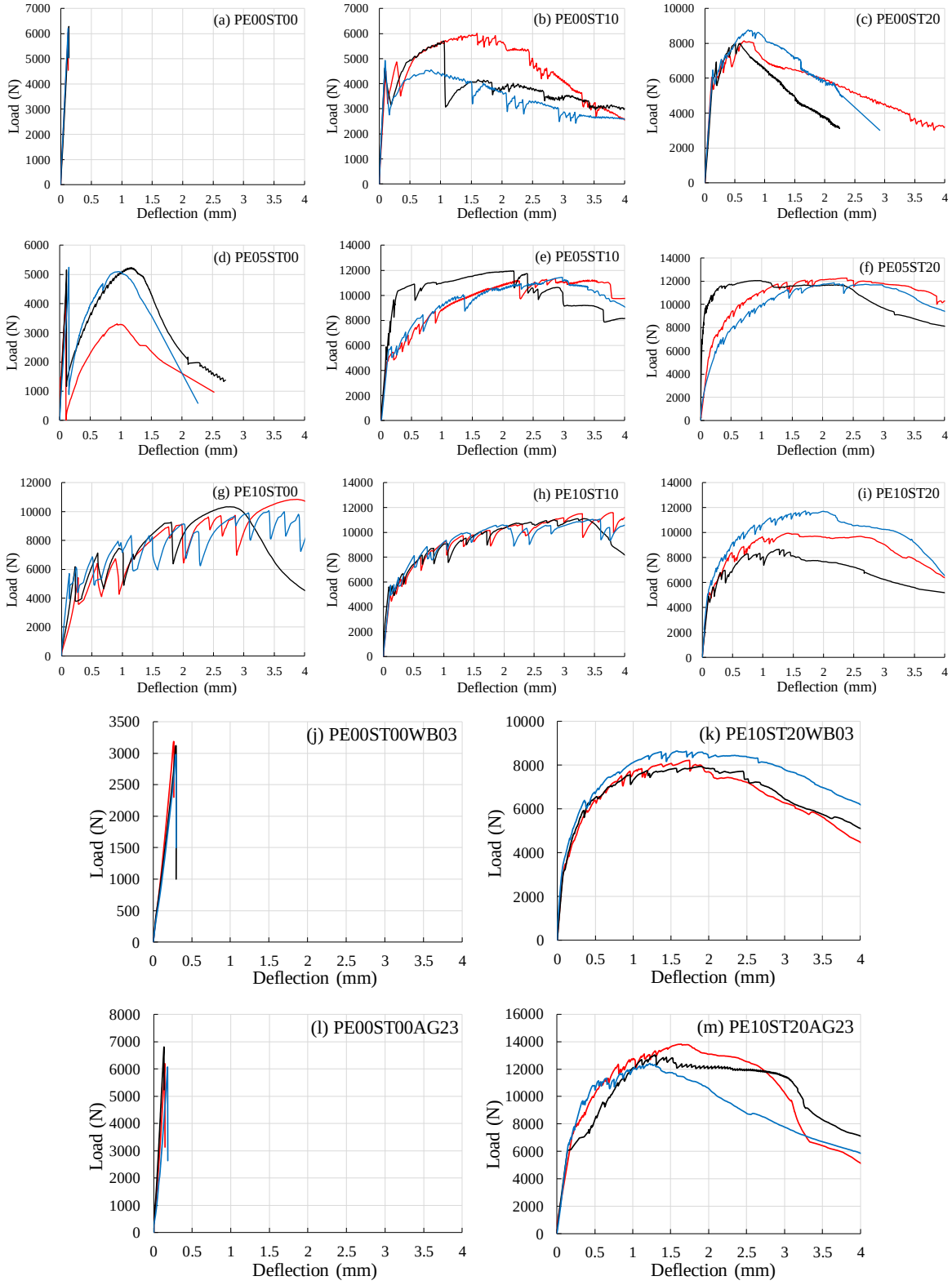

Fig. 5.7. Load–deflection curves of specimens (a) PE00ST00, (b) PE00ST10, (c) PE00ST20, (d) PE05ST00, (e) PE05ST10, (f) PE05ST20, (g) PE10ST00, (h) PE10ST10,

(i) PE10ST20, (j) PE00ST00WB03, (k) PE10ST20WB03, (l) PE00ST00AG23, (m) PE10ST20AG23.

5.4.2 First-crack strength and peak strength

Due to deflection-hardening response, flexural properties at the first-crack and the peak load points were separately investigated. Fig. 5.8 and Fig. 5.9 show combined effects of PE and steel fibers on first-crack strength and peak strength, respectively. From Fig. 5.8, fiber volume fraction did not show obvious effect on first-crack strength. The largest discrepancy between the highest and the lowest first-crack strength according to fiber fraction was 3.61 MPa. This is because first-crack strength is more closely influenced by UHPC matrix rather than fiber bridging capacity, which is only mobilized after cracking has taken place (Li and Leung 1992, Yoo, Kang, Banthia and Yoon 2016). The average first-crack strength of all UHPC specimens was 13.25 MPa.

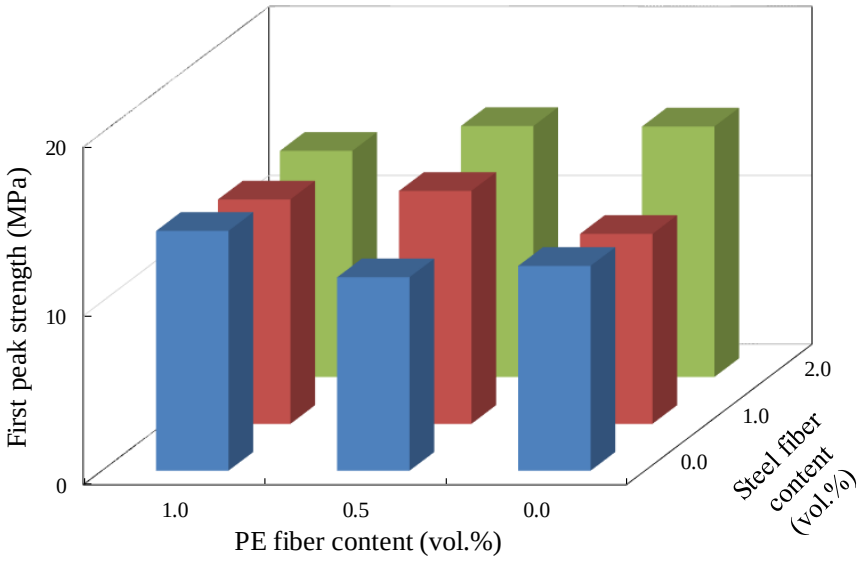

Fig. 5.8. First-crack strength of specimens.

Unlike the first-crack strength, peak strength was significantly improved by adding PE and/or steel fibers, and it was greatly influenced by fiber hybridization. For PE00ST00 and PE05ST00 with no flexural hardening (Fig. 5.7a and d), the peak strength was equal to the first-crack strength. Other mix designs (PE10ST00 and PE00/05/10ST10/20) showed

flexural hardening. From Fig. 5.9, the peak strength increased with increasing fiber fraction due to more fibers provided bridging force. Inclusion of PE or steel fibers alone only showed obvious effect at high volume fraction, i.e. for PE fibers only, minimum content should be 1% and for steel fibers only, this value is 2%. Adding either 1.0% PE fibers or 2% steel fibers led to 125.8% and 49.5% increase of peak strength, respectively, compared to the control specimen PE00ST00.

Hybrid use of PE and steel fibers exhibited much greater peak strength. For example, PE05ST10 with totally 1.5% fibers showed 16.08 MPa (140.4%) and 14.25 MPa (107.2%) higher peak strength than those of PE05ST00 and PE00ST10, respectively. However, doubling the fiber fraction to PE10ST20 decreased the peak strength slightly. One possible explanation is that the very high bond strength between fibers and UHPC matrix caused cracking in surrounding matrix when fibers were pulled out (Wille, Xu, El-Tawil and Naaman 2016). The splitting cracks weakened the pullout capacity of adjacent fibers when they were in lumps (Yoo, Kim, Park, Park and Kim 2017). Another plausible reason is that more trapped air voids by higher fraction of fibers reduced the mechanical properties of UHPC matrix and reduced the bonding force between the matrix and the fibers (Wille, Naaman, El-Tawil and Parra-Montesinos 2011).

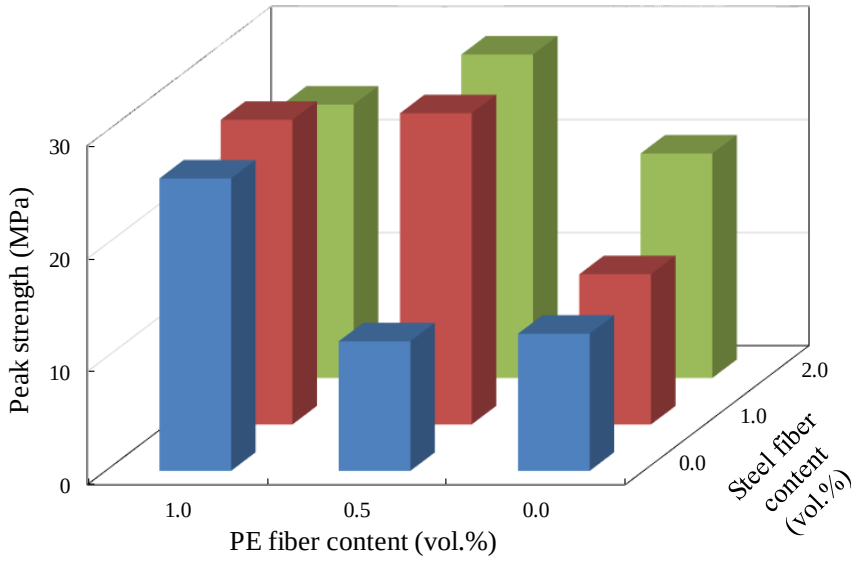

Fig. 5.9. Peak strength of specimens.

Table 5.4 shows the effect of W/B ratio on first-crack strength and peak strength of UHPC mixes. Increasing W/B ratio will lower both the mechanical properties of UHPC matrix and the bond strength between fibers and matrix (Ahmed, Maalej and Paramasivam 2007). Therefore, increasing the W/B ratio from 0.2 to 0.3 reduced the first-crack strength of both the PE00ST00 and the PE10ST20 significantly. For the peak strength, the reduction of PE10ST20 was 18.0%, smaller than that of PE00ST00 (39.4%).

From Table 5.5, increasing the aggregate size from 0.6 mm to 2.3 mm enhanced the first-crack strength of PE00ST00 by 25.8%. For PE10ST20, the first-crack strength increased 19.0% while the peak strength increased 28.6%. Larger aggregates of 2.3 mm have smaller specific surface area, which led to better workability and compactness of fresh concrete. Moreover, the rigid quartz sands will increase friction between fibers and larger aggregates (Liu, Han, Cui, Zhang, Lv, Zhang and Yang 2016). Although some previous studies showed larger aggregates would negate mechanical properties of UHPC (Liu, Li, Liu, Cui and Yang 2013, Yoo, Kang, Lee and Yoon 2013), the aggregate used in the present study is quite small (smaller than 2.3 mm) and the rigidity of quartz sands is much higher than that of crushed stones.

Table 5.4. First-crack strength and peak strength of UHPC mixtures with different W/B ratios

First-crack strength		
Mix design	W/B ratio	
	0.2	0.3
PE00ST00(WB02/03)	12.13±0.02 MPa	7.36±0.23 MPa
PE10ST20(WB02/03)	13.39±0.82 MPa	8.05±0.69 MPa
Peak strength		
Mix design	W/B ratio	
	0.2	0.3
PE00ST00(WB02/03)	12.13±0.02 MPa	7.36±0.23 MPa
PE10ST20(WB02/03)	24.19±3.00 MPa	19.83±0.70 MPa

Table 5.5. First-crack strength and peak strength of UHPC mixtures with different AG size

First-crack strength		
Mix design	AG size	
	0.6 mm	2.3 mm
PE00ST00(AG06/23)	12.13±0.02 MPa	15.26±0.77 MPa
PE10ST20(AG06/23)	13.39±0.82 MPa	15.94±1.16 MPa
Peak strength		
Mix design	AG size	
	0.6 mm	2.3 mm
PE00ST00(AG06/23)	12.13±0.02 MPa	15.26±0.77 MPa
PE10ST20(AG06/23)	24.19±3.00 MPa	31.11±1.61 MPa

5.4.3 Toughness and toughness index

The energy absorption capacity of UHPC was investigated according to toughness. The toughness values at four different deflection points (*L*/600, *L*/150, *L*/100, and *L*/75) were analyzed, where *L*=300 mm is the clear span length. The average toughness at different deflections are shown in Fig. 5.10. PE00ST00 failed before *L*/600 (0.5 mm), so no toughness was recorded.

Hybrid use of PE and steel fibers exhibited superior toughness compared to mono-fiber reinforced specimens. Take the toughness at *L*/75 as an example, PE05ST10 with totally 1.5 vol.% of PE and steel fibers had 38.90 N·m and 23.33 N·m greater toughness than those of PE05ST00 and PE00ST10, respectively. However, further increasing PE fiber content actually decreased the toughness possibly due to the high aspect ratio of PE fibers led to more trapped air voids and presence of splitting cracks (Wille, Naaman, El-Tawil and Parra-Montesinos 2011, Wille, Xu, El-Tawil and Naaman 2016, Yoo, Kim, Park, Park and Kim 2017).

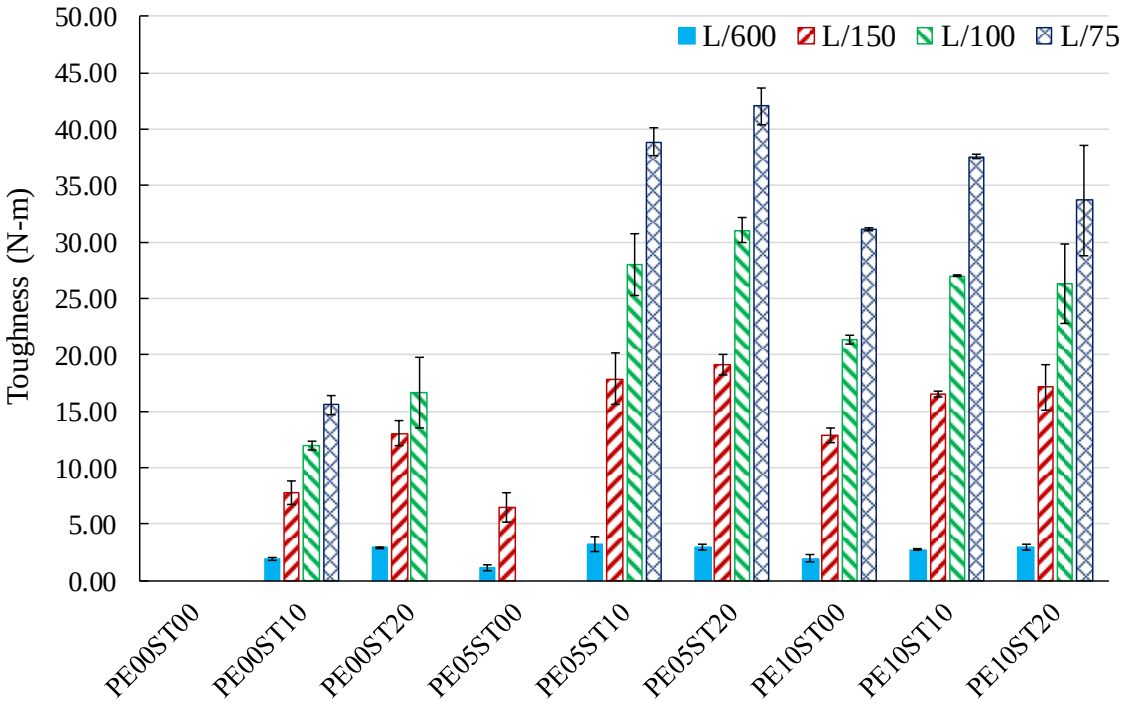

Fig. 5.10. Toughness at different deflections of UHPC mixtures.

Fig. 5.11 shows the effect of W/B ratio and larger aggregates on toughness of UHPC at each deflection. The increase of W/B ratio to 0.3 reduced toughness, while larger aggregates (0.6 to 2.3 mm) actually improved toughness.

Since toughness is directly dependent on the size of specimens, toughness index is adopted to classify the ductility of UHPC mixes. Naaman (1996) pointed out that fiber reinforced composites having toughness indexes $I_i > i$ (i =5, 10, 20, and 30) can be classified as flexural hardening composites. From Fig. 5.12, except for PE00ST00 and PE05ST00, all composites met this criterion. It is worth noting that, I_{30} of all the four UHPC with hybrid fiber (PE05ST10, PE05ST20, PE10ST10, and PE10ST20) reached nearly or even beyond 50. This shows that the combined use of PE and steel fiber has significant effect on improving flexural hardening behavior of UHPC. Compared to roughness indexes at higher deflection, differences of I_5 among the different UHPC specimens are smaller, since at the onset of post-cracking stage (just after the first crack) the mechanism of fiber bridging had

not been fully activated. But at larger deflections, more cracks began to form and expand. The effect of crack-arresting mechanism started to show.

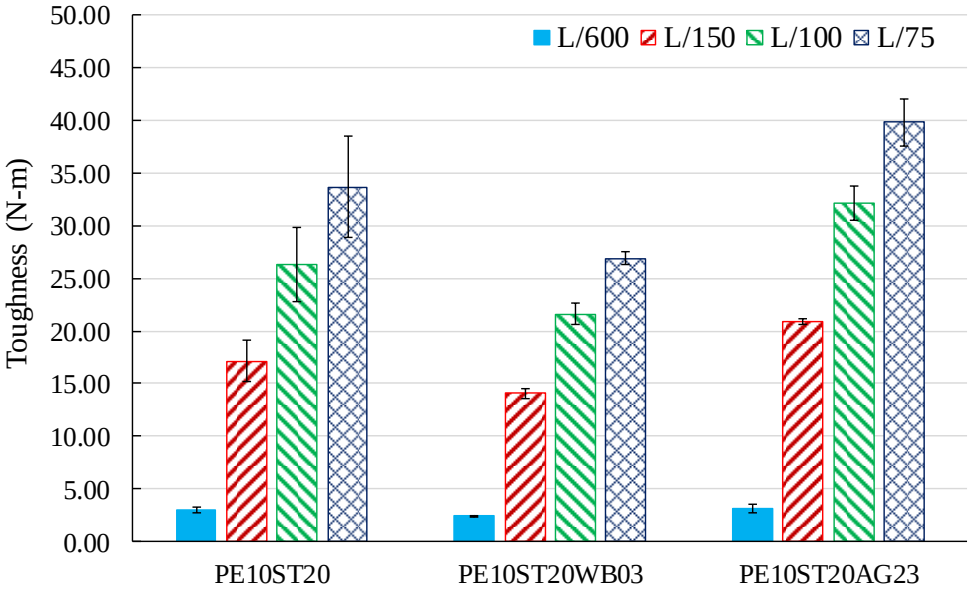

Fig. 5.11. Effect of W/B ratio and larger aggregates on toughness of UHPC mixtures.

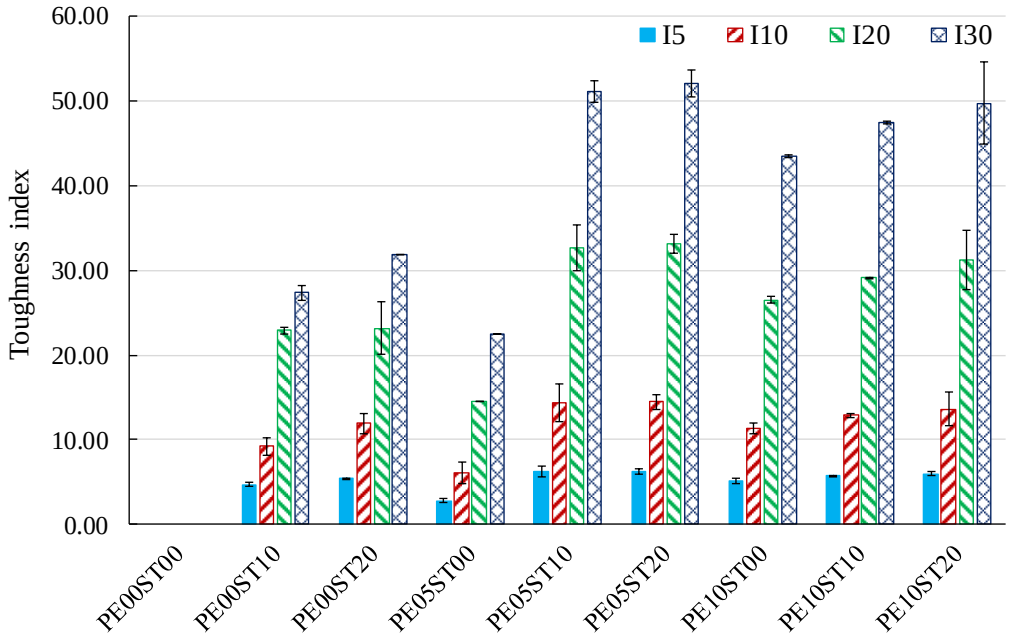

Fig. 5.12. Toughness indexes of UHPC mixtures.

Fig. 5.13 shows the effect of W/B ratio and larger aggregates on toughness index of UHPC. Although increasing W/B ratio decreased the first-crack strength, peak strength (Table 5.4), and toughness of UHPC mixes (Fig. 5.11), it actually increased the toughness index of PE10ST20WB03. This is probably because cracks were easier to form in weaker concrete matrix. In the same vein, stronger UHPC matrix led to lower flexural hardening behavior of PE10ST20AG23 compared to that of PE10ST20.

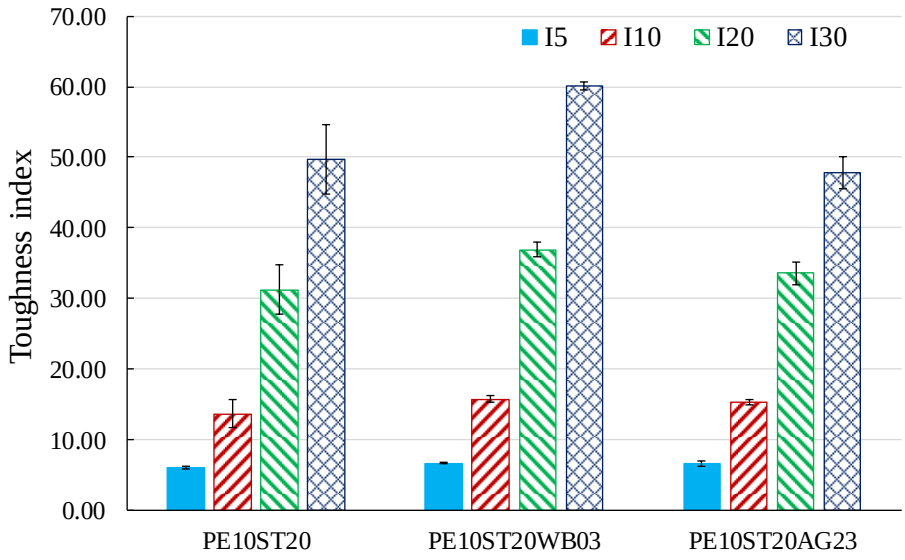

Fig. 5.13. Effect of W/B ratio and larger aggregates on toughness index.

Fig. 5.14 and Fig. 5.15 show the FESEM images of steel and PE fibers on the fractured surface of UHPC samples. The steel fiber was pulled out from UHPC matrix before it reached full capacity (Fig. 5.14 a), while the PE fiber was partially pulled out but ruptured due to attaining the tensile strength (Fig. 5.15 a). Although the PE fiber has greater tensile strength, compared to steel fiber, the former has smaller diameter (23 μm) compared to the latter (220 μm). From Fig. 5.14 b and Fig. 5.15 b, the surfaces of the steel and the PE fibers were damaged by UHPC matrix during the pull-out process, which shows the presence of strong bonding force between the UHPC matrix and the fibers.

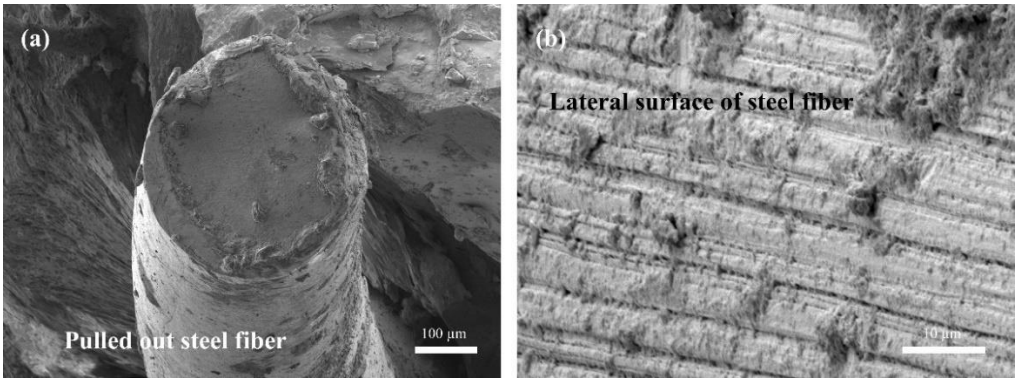

Fig. 5.14. FESEM image of steel fiber on UHPC fracture surface (a) end of steel fiber (b) lateral surface of steel fiber.

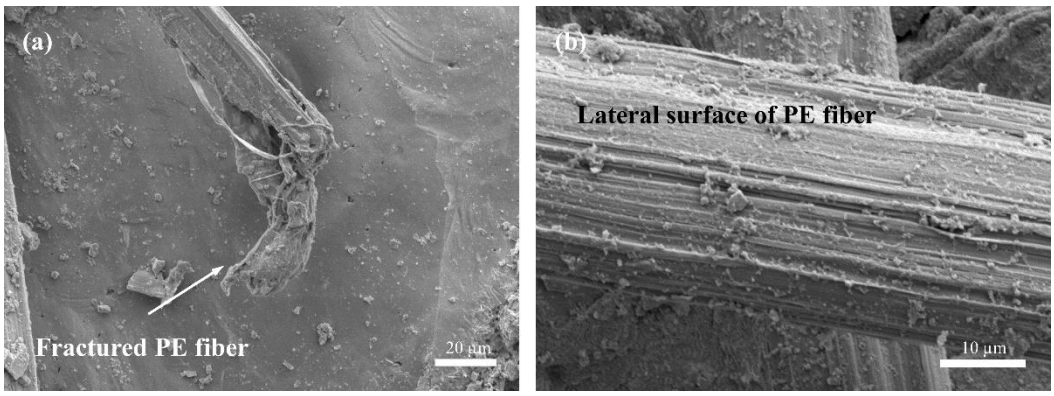

Fig. 5.15. FESEM image of PE fiber on UHPC fracture surface (a) end of PE fiber (b) lateral surface of PE fiber.

5.5 Synergy effect of PE and steel fibers

To examine the effectiveness of fiber hybridization quantitatively, an equation to evaluate the synergy of combined use of PE and steel fibers on energy absorption capacity was adopted as follows (Banthia, Majdzadeh, Wu and Bindiganavile 2014):

$$Synergy = \frac{PCT_{hybrid,a+b}}{PCT_a + PCT_b} - 1 \tag{5.2}$$

where *PCT* is the toughness at a certain deflection under flexure (energy equivalent to the area under the load-deflection curve up to a specified deflection). It was obtained by

subtracting it from the toughness of the matrix. PCT_a and PCT_b are the toughness of UHPC with only PE or steel fibers.

Fig. 5.16 summarizes the synergy in toughness for PE05ST10, PE05ST20, PE10ST10, and PE10ST20. The synergy showed an increasing trend with increasing deflection. The synergy of PE05ST10 showed positive values at all the four deflections and increased with increasing deflection. For PE05ST20, the synergy was -0.23 at *L*/600, but it turned positive at *L*/100 and increased significantly with increasing deflection. Since the PE05ST00 and PE00ST20 did not survive deflection of *L*/75, based on Eq. 5.2, the synergy of PE05ST20 showed infinite value at *L*/75. It should be noted that, PE10ST10 exhibited negative synergy regardless of the deflection and PE10ST20 only showed positive synergy at L/75. Thus, based on Banthia's definition PE05ST10 and PE05ST20 yielded the best combination of fibers.

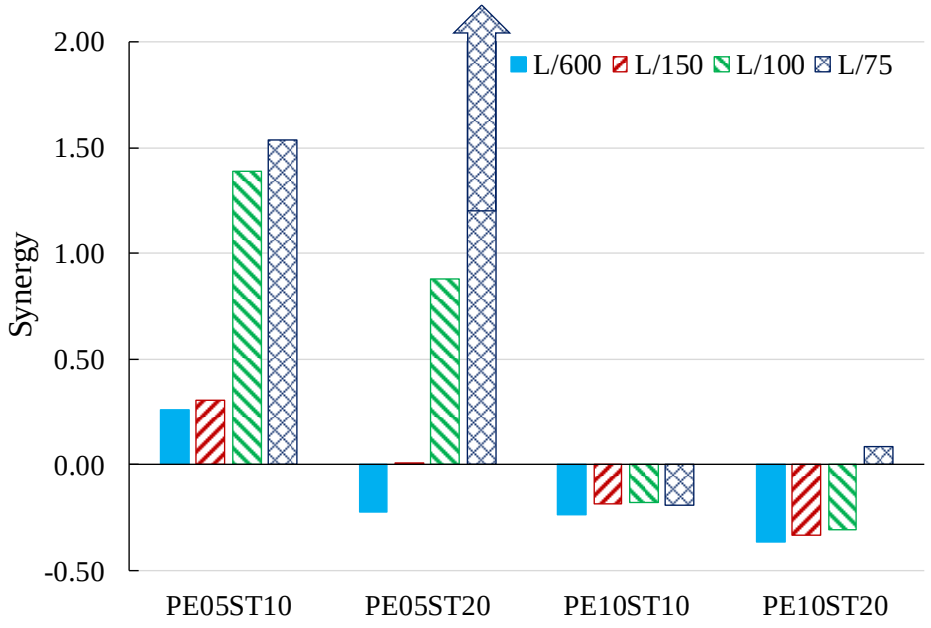

Fig. 5.16. Synergy of PE and steel fibers on toughness of mixtures.

5.6 Behavior of UHPC at elevated temperature

Residual flexural performance of UHPC with hybrid PE and steel fibers after heat exposure will be evaluated in this section. However, as can be seen in Fig. 5.17, the specimens spalled

even at very low heating rate (1 ℃/min), which is a rare occurrence for normal concrete or even HPC with compressive strength lower than 60 MPa. Therefore, it can be concluded that thermal stress is not the main reason for spalling of this UHPC mix design at very low heating rate. For PE00ST20 with only steel fibers, the samples spalled severely at both 300 ℃ and 600 ℃. This suggests that greater bonding force provided by steel fibers is not enough to prevent spalling. For PE10ST20 samples with 1% PE fibers, spalling did not happen at temperature below 300 ℃, but when heated to 600 ℃, samples spalled. Compared to PE00ST20, it can be concluded that PE fibers could help to mitigate spalling, but the effect is limited.

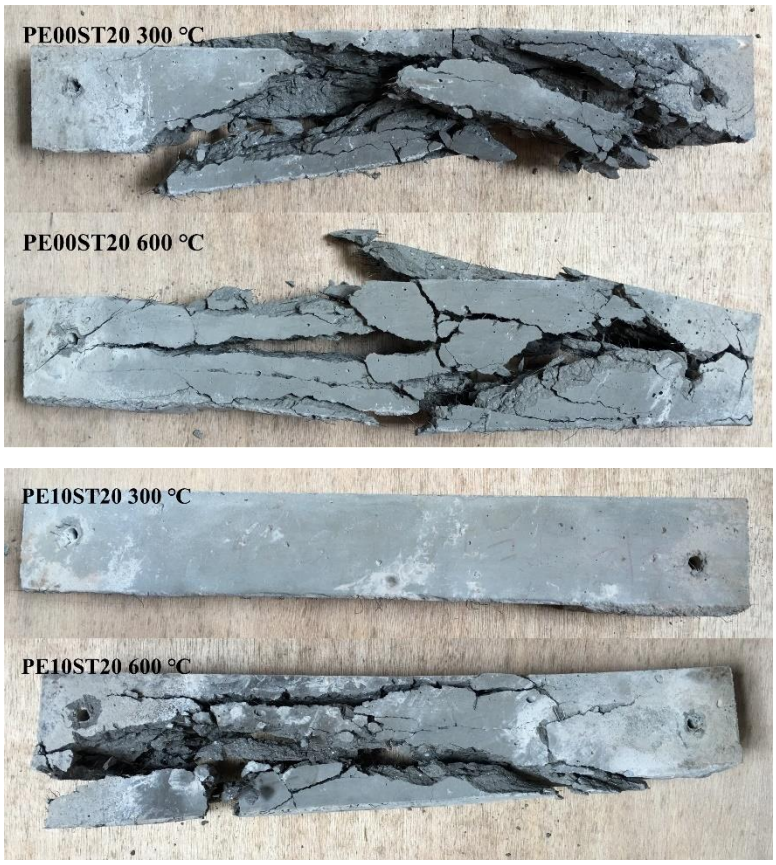

Fig. 5.17. Spalling of UHPC samples after heated to 300 ℃ and 600 ℃.

The flexural behavior of PE10ST20 before and after exposure to 300 ℃ is shown in Table 5.6. After exposure to 300 ℃, all the measured properties decreased significantly. The first-crack strength and the peak strength dropped by 21.0% and 27.0%, respectively. The samples failed before attaining *L/150*, so toughness and toughness index at larger deflection were not

available. At $L/150$, T_{600}^{D} decreased by 54.8% and I_5 decreased by 58.8%. The significant degradation of mechanical properties was attributed to the melting of PE fibers. Another reason is the loss of bond between the steel fibers and the UHPC matrix.

Table 5.6. Properties of PE10ST20 before and after exposure to 300 ℃

Properties of PE10ST20		Ambient temperature	300 ℃
First-crack strength (MPa)		13.39±0.82	10.45±2.30
Peak strength (MPa)		24.19±3.00	17.67±3.53
Toughness (N·m)	T_{600}^{D}	3.03±0.25	1.37±0.75
	T_{150}^{D}	17.15±2.01	-
	T_{100}^{D}	26.29±3.51	-
	T_{75}^{D}	33.71±4.88	-
Toughness index	I_5	6.00±0.29	2.47±0.83
	I_{10}	13.61±0.59	-
	I_{20}	31.18±0.91	-
	I_{30}	49.73±1.59	-

It is widely reported that 0.5 to 3.0 kg/m^3 (<0.35 vol.%) PP fibers can prevent explosive spalling of concrete at elevated temperature even at a high heating rate (Bangi and Horiguchi 2012, Ding, Zhang, Cao, Zhang and Azevedo 2016, Kodur, Cheng, Wang and Sultan 2003, Peng, Yang, Zhao, Liu, Bian and Zhao 2006). Compared to PP fibers (melting point around 165 ℃), PE fibers actually have lower melting point (around 145 ℃) (Khoury and Willoughby 2008, Smith and Lemstra 1980), but PE fibers did not prevent spalling (Fig. 5.17). To reveal the difference between PP and PE fibers, UHPC matrix with PP and PE fibers were analyzed by FESEM after exposure to 180 ℃. From Fig. 5.18, the melted fibers left empty tunnels in the UHPC samples. Micro cracks can be observed in radial direction of the fiber tunnels due to the thermal expansion of fibers at elevated temperature could cause significant tensile stress build-up in the tangential direction along the fiber-matrix interface (Khoury and Willoughby 2008). The micro cracks and the empty fiber tunnels could form an inter-connected micro-cracks-fiber-tunnel network, which helps to release trapped vapor pressure and mitigate spalling. From Fig. 5.18a, the width of micro cracks around PP fiber

tunnel was about 5 μm. On the contrary, PE fiber only caused very thin micro cracks narrower than 1 μm (Fig. 5.18b). The coefficient of thermal expansion (CTE) perpendicular to the axial direction of PP fiber is greater than 21×10^{-5}/℃ at temperature above 100 ℃ (Khoury and Willoughby 2008). However, the CTE of normal ultra-high molecular weight polyethylene is only half as much (10×10^{-5}/℃) (Peters 2013). With narrower micro cracks it is more difficult for fiber tunnels to be percolated and thus trapped vapor pressure cannot be released. This explains the lower efficiency of PE fiber for preventing spalling. Another explanation is that probably although PE fibers have lower melting point than PP fibers, their viscosity several times greater than that of PP fibers (Khoury and Willoughby 2008, Knack 2011, Martienssen and Warlimont 2006). Taking the thinner micro cracks into consideration, the fiber tunnels may not be emptied in a short period of time to create an interconnected network for water vapor to be released.

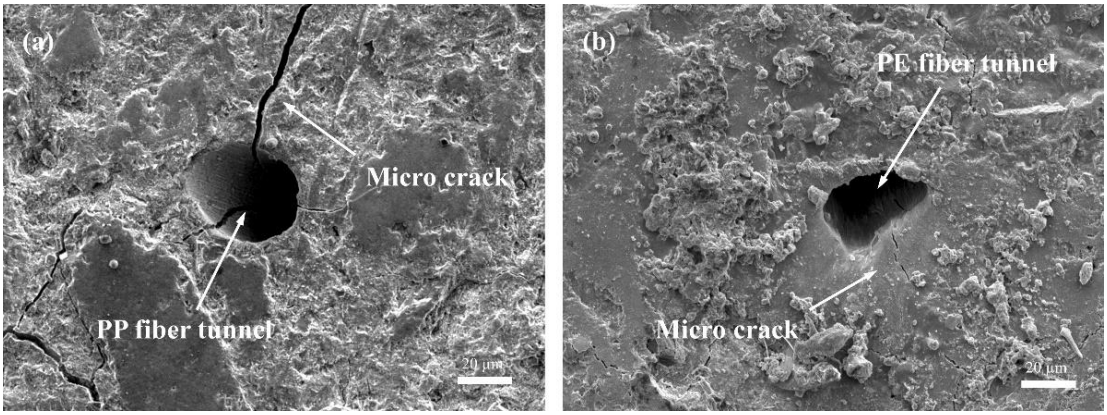

Fig. 5.18. Cross section of UHPC samples with (a) PP and (b) PE fibers after exposure to 180 ℃

Fig. 5.19 shows the cross section of UHPC with steel fiber after exposure to 300 ℃. Micro cracks with width ranging from 1 to 5 μm around the embedded steel fibers can be observed. The steel fiber was detached from the concrete matrix due to thermal incompatibility between the steel fibers and the matrix (Zunino, Castro and Lopez 2015). Micro cracks and separation between the steel fiber and the matrix negated bond behavior. Moreover, at 300 ℃, PE fibers had already melted. Therefore, at elevated temperature, flexural behavior of PE10ST20 dropped significantly (Table 5.6).

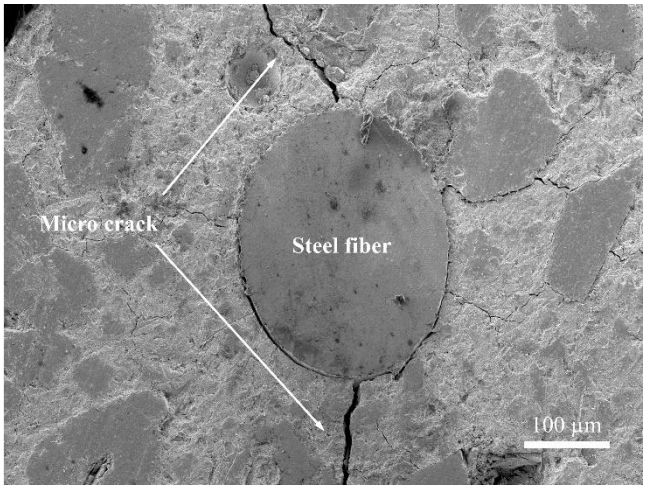

Fig. 5.19. Cross section of UHPC with steel fiber after exposure to 300 ℃.

5.7 Summary

This study investigated the effect of polyethylene (PE)-steel fiber hybridization, water to binder ratio, and larger aggregate on flexural performance, including load-deflection relationship, first-crack strength, peak strength, toughness, and toughness index on UHPC at ambient and elevated temperature.

Inclusion of steel fibers enhanced the compressive strength of UHPC but increasing PE fibers from 0.5% to 1% volume fraction has negative effect on compressive strength. Apart from PE00ST00 and PE05ST00, all UHPC specimens are classified as flexural hardening composites. For addition of PE or steel fibers alone, flexural performance only increases beyond a relatively higher fiber fraction (0.5% for PE fiber and 1.0% for steel fiber).

Hybrid PE and steel fibers effectively improve the flexural performance compared to UHPC with mono fiber, but the first-crack strength is only marginally affected by the fiber type and volume fraction. PE05ST10 and PE05ST20 were found to be the favorable PE and steel fiber fractions for flexural performance of UHPC. Further increasing the PE fiber fraction to 1% deteriorated flexural performance. The synergy value clearly shows the effectiveness of fiber hybridization and it increases with increasing deflection.

Increasing water-to-binder ratio from 0.2 to 0.3 resulted in a significant reduction of compressive strength, first-crack strength, peak strength, as well as toughness. However, toughness index increases due to easier crack formation in weaker UHPC matrix. In contrast, although larger aggregates significantly improved flexural performance, it resulted in slightly lower flexural hardening behavior.

After being heated to 300 ℃, all the flexural performance decreased significantly due to melting of PE fibers and lower bond strength between steel fibers and UHPC matrix. Compared to PP fiber, the effect of PE fiber on spalling prevention is negligible. From microstructural analysis, micro cracks formed by PE fiber are much narrower than that caused by PP fiber. Therefore, it is more difficult for the interconnected network of PE fiber to be percolated.

Chapter 6 Effects of Factors on the Hot Permeability of UHPC

6.1 Overview

Permeability of concrete at elevated temperature is the governing factor for moisture transport and pore pressure build-up inside concrete (Khoury 2000, Klingsch 2014, Kodur and Phan 2007, Ozawa and Morimoto 2014). It is also an essential input parameter for modelling of spalling behavior. Investigation on intrinsic permeability of UHPC at elevated temperature was rather limited. Besides, most of the permeability measurements were performed either at ambient temperature or in residual state, i.e. after cooling the specimens from the target temperature to ambient condition (Gawin, Alonso, Andrade, Majorana and Pesavento 2005, Kalifa, Chene and Galle 2001, Liu, Ye, De Schutter, Yuan and Taerwe 2008, Noumowe, Siddique and Debicki 2009, Zeiml, Lackner, Leithner and Eberhardsteiner 2008, Zeiml, Leithner, Lackner and Mang 2006), which may not be the same as the permeability at hot state due to physical changes in microstructure during the cooling process.

This chapter reports the influence of PP fiber, steel fiber, and aggregate size on the intrinsic permeability of UHPC at elevated temperature. The general principle of the experimental setup followed the RILEM-CEMBUREAU method (Kollek 1989) and the intrinsic gas permeability was calculated by adopting Klinkenberg method (Klinkenberg 1941). Hot permeability measurements were performed on five UHPC mixes subjected to elevated temperature in the range between ambient temperature and 300 °C. Microscopic investigations were performed on UHPC samples before and after the exposure to elevated temperature to reveal potential mechanisms responsible for the increase in permeability.

6.2 Experimental program

6.2.1 Materials and mix proportions

A UHPC matrix with compressive strength of 150 MPa was formulated and used as the control mix shown in Table 6.1. The control mix consisted of cement, fine aggregates (less

than 600 μm), micro silica sand, and silica fume and had a water-to-cement ratio of 0.22. Superplasticizers were used in the mix to achieve sufficient consistency and workability. To investigate the influence of fiber addition, 3.0 kg/m^3 of PP fibers were added in the PP mix, while ST mix had 196.3 kg/m^3 (2.5% by volume) of steel fibers. Larger aggregates with the maximum size of 5 mm were used in the AG mix to study the effect of aggregate size. PPAG mix contained both PP fibers and larger aggregates of 5 mm to investigate the combined effects of the two factors.

Table 6.1. Mix proportions and compressive strength of UHPCs

Mix Design	Relative mass ratio to cement						PP fiber (kg/m^3)	Steel fiber (kg/m^3)	f_c (MPa)
	C	AG	SS	SF	SP	W/B			
Control	1.0	1.1$^{\wedge}$	0.25	0.25	0.03	0.22	0.0	0.0	149.6±4.78
PP	1.0	1.1$^{\wedge}$	0.25	0.25	0.03	0.22	**3.0**	0.0	159.7±5.70
ST	1.0	1.1$^{\wedge}$	0.25	0.25	0.03	0.22	0.0	**196.3**	172.1±3.66
AG	1.0	**1.1***	0.25	0.25	0.03	0.22	0.0	0.0	145.0±4.14
PPAG	1.0	**1.1***	0.25	0.25	0.03	0.22	**3.0**	0.0	147.7±1.49

C: cement, AG: aggregates, SS: silica sand, SF: silica Fume, SP: superplasticizer, W/B: water-to-binder ratio, f_c : Compressive strength at age of 28 days, $^{\wedge}$ denotes aggregates with the maximum size of 600 μm, * denotes aggregates with the maximum size of 5 mm

The cement used in this research was ASIA$^{@}$ CEM I 52.5 N. The silica fume used was Grade 940 from Elkem Microsilica$^{@}$, which is a high reactive pozzolan. Natural river sands were used as aggregate in the concrete mixtures. For UHPC mixes with fine aggregates, the aggregates were sieved to 600 μm. The silica sand used had a median particle size of 130 μm. Steel fibers with a length of 13 mm and a diameter of 160 μm were supplied from Dramix$^{@}$. The tensile strength of the steel fibers is about 2,000 MPa. Monofilament PP fibers with a length of 12 mm and a diameter of 40 to 60 μm were supplied by DFL. A third generation polycarboxylate-based superplasticizer Sika$^{@}$ ViscoCrete$^{@}$-2044 was used in all UHPC mixtures to increase workability in the fresh state.

The mixing and curing procedure was shown in Section 0. The fresh UHPC mixtures were then cast into cube (50×50×50 mm^3) and cylindrical disc (Ø150 mm×48 mm) molds for the compressive strength and hot permeability tests, respectively. After curing, the surfaces of

cylindrical discs were smoothened by grinding from two ends to 40 mm thick to ensure good contact with the permeability measurement device and to eliminate possible effects from the mold.

6.2.2 Hot permeability test

Apparent gas permeability was determined by means of the RILEM-CEMBUREAU method, which is easy to perform and reasonably accurate at the same time (Kollek 1989). The apparent gas permeability was determined based on the Darcy's law which was later modified by the Hagen-Poiseuille relationship (Gallé and Sercombe 2001):

$$k_a = \frac{Q}{A}\frac{2\mu L p_{atm}}{\left(p_i^2 - p_{atm}^2\right)} \tag{6.1}$$

where k_a [m^2] is the apparent gas permeability, Q [m^3/s] is the gas flow rate, A [m^2] is the specimen cross sectional area, p_i [Pa] is the inlet pressure, p_{atm} [Pa] is the outlet pressure which is atmosphere pressure, L [m] is the thickness of the specimen, and μ [Pa·s] is the dynamic viscosity of the gas used.

Viscous flow and slip flow (Knudsen diffusion) occur during gas percolation through a porous media, where viscous flow generated from collisions between gas molecules and slip flow generated from collisions between gas molecules and the pore walls (Sun, Yao, Fan, Wang and Sun 2015). When the average pore diameter is large compared to the mean free path of gas molecules (average distance between collisions), the probability of collisions between gas molecules is higher than collisions between gas molecules and the pore walls, thus viscous flow dominates the gas transport. However, in a tight porous media, when the average pore size is of the same order of magnitude as the mean free path of gas molecules, the collisions between molecules and the pore walls become more important and the slip flow cannot be neglected (Sun, Yao, Fan, Wang and Sun 2015). This is especially true in the case of UHPC, where a very dense microstructure is expected. The mean free path of gas molecules and gas transport are influenced by the pore pressure, which is affected by the applied inlet pressure during the test. As a result, the apparent gas permeability changes at

different inlet pressures. Klinkenberg (Klinkenberg 1941) suggested adopting intrinsic gas permeability, which only relates to viscous flow, to correct the apparent gas permeability. The intrinsic gas permeability is regarded as an independent property from the inlet gas pressure as follows.

$$k_a = k_{\text{int}}\left(1+\frac{b}{p_m}\right) \tag{6.2}$$

where k_{int} [m^2] is the intrinsic gas permeability when the mean pressure p_m approaches infinity, b [Pa] is the Klinkenberg constant, and $p_m = \left(p_i + p_{\text{atm}}\right)/2$ [Pa] is the average value of the inlet and outlet pressures (atmospheric pressure) on the two sides of the specimen.

The general principle of the measurement is to carry out a continuous gas flow through the sample under steady air pressures (Loosveldt, Lafhaj and Skoczylas 2002). Fig. 6.1 shows the experimental setup used for measuring permeability at the hot state (Klingsch, Lu, Kässmann and Tan 2015). The device was designed to subject the specimens to a constant gas pressure p_i in the upper chamber and atmospheric pressure p_{atm} in the lower chamber. The device consisted of two symmetric lids. Each of the lids had an inner and an outer sealing ring. The specimen was secured in a pipe segment sandwiched between the two lids. High temperature silicone, which could withstand up to 315 °C, was applied between the sealing rings and the specimen. The lateral surfaces of the discs were also sealed with high temperature silicone to ensure one-dimensional airflow from the top to the bottom surface of the disc during the hot permeability tests. The two lids were fixed and clamped by twelve bolts all around the flange. The entire device was placed inside an electrical furnace. Compressed air was supplied into the upper chamber through an aluminum tube by a compressor. The air can be preheated by pathing through the tube. The pressure was adjusted via a gas pressure regulator. The velocity of air flowing through the specimen was measured from the outlet.

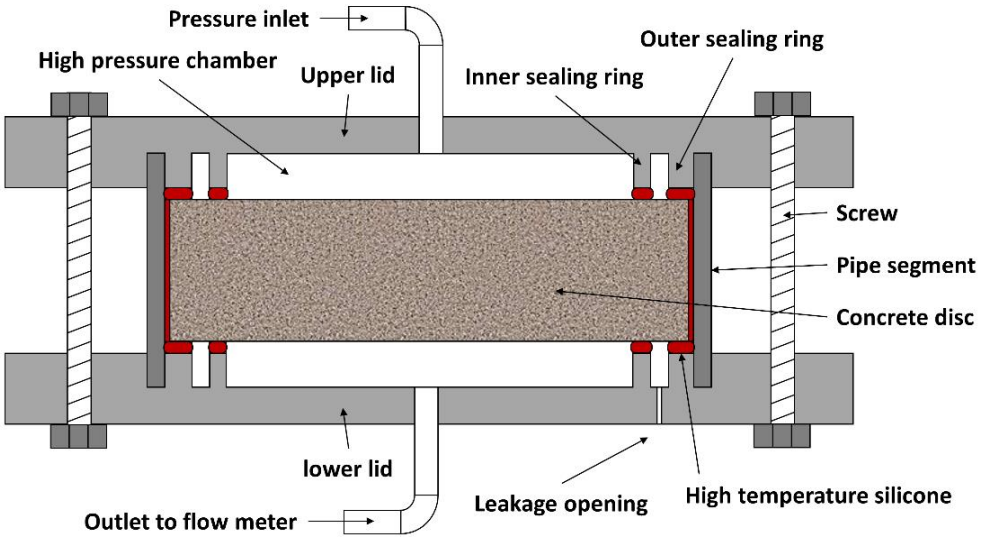

Fig. 6.1. Hot permeability test setup.

It has been reported that the degree of saturation of concrete specimen can significantly influence the measured permeability (Abbas, Carcasses and Ollivier 1999, Jacobs 1998, Picandet, Khelidj and Bastian 2001). To determine the intrinsic permeability of UHPC, cylindrical disc specimens were pre-conditioned in oven at 105 °C until they reached a constant weight. By then, all evaporable water was removed, and moisture clogging was minimized. To perform the hot permeability test, specimens were heated to predetermined temperatures of 30, 105, 150, 175, 200, 250, and 300 °C, as spalling is most pronounced within this range of temperature (Klingsch 2014, Mindeguia, Pimienta, Noumowé and Kanema 2010). The heating rate was lower than 1 °C/min to prevent undesirable temperature gradients and thermal stress developed inside the specimens, which could introduce micro-damages to the samples and influence the test results. After the target temperature was reached, the specimens were kept in the furnace for 2 hours before the permeability tests. For temperature below 150 °C, three pressure levels were applied, i.e. 3 bars, 6 bars, and 9 bars (1 bar = 1 atmospheric pressure) to determine the intrinsic gas permeability of the specimens. For higher temperature levels, lower gas pressure was used to maintain gas flux within the measurable range of the equipment. The airflow rate was measured and recorded until it reached steady state. This condition was identified by taking three consecutive measurements at a 30-minute interval.

6.2.3 Other measurements

The compression tests were conducted following ASTM C109/C109M-11 (Mater. 2011). The hydraulic compression machine had a capacity of 3,000 kN. A constant loading rate of 100 kN/min was adopted and the maximum force was recorded. Three samples were tested for each mixture.

Differential scanning calorimetry (DSC) monitors the amount of heat required to increase the temperature of samples and therefore indicates when the sample undergoes a physical transformation. DSC/TGA instrument Q10 apparatus was used to measure the melting point of PP fibers. In DSC, 5 mg PP fiber sample was exposed to the heating rate of 2 °C/min in a nitrogen atmosphere.

Change of microstructure before and after heating at residual state was studied by means of field emission scanning electron microscope (FESEM). All specimens were oven-dried at 105°C for 24 hours to remove evaporable water. Micrographs were taken from the broken cube specimens to observe the morphology of the fracture surface and from the cutting surface of cube specimens to examine the fiber cross section and micro cracks before and after heating. PP specimens were heated to 150 °C and 180 °C to investigate the melting and decomposition of PP fibers, respectively. Other UHPC mixes were heated to 250 °C to observe changes of microstructures. The heating rate was 1 °C/min for all specimens.

6.3 Results and discussions

6.3.1 Gas permeability at elevated temperature

Fig. 6.2 shows the intrinsic gas permeability as a function of temperature for the five UHPC mixes. The general trend shows that gas permeability remains largely unchanged from ambient temperature to 105 °C. This is mainly because the specimens were pre-conditioned in oven at 105 °C prior to the gas permeability test so that the permeability at the ambient temperature is was the residual state of 105 °C. Afterwards, the intrinsic gas permeability increases continuously with increasing temperature. Other research works reported

oscillation of permeability with temperature below 200 °C, which might be caused by the moisture clogging effect of undried samples (Klingsch, Lu, Kässmann and Tan 2015, Zeiml, Lackner, Leithner and Eberhardsteiner 2008). This highlights the importance of sample pre-conditioning for the hot state permeability test. The intrinsic gas permeability of the five UHPCs at ambient temperature, i.e. initial gas permeability, are quite similar and in the range between 1.2×10^{-18} and 2.6×10^{-18} m^2, which is lower than that of normal fiber-reinforced concrete (FRC) or high performance concrete (from 10^{-17} to 10^{-16} m^2) reported in other studies (Noumowe, Siddique and Debicki 2009, Picandet, Khelidj and Bellegou 2009, Zeiml, Lackner, Leithner and Eberhardsteiner 2008). This could be attributed to the low water-to-binder ratio and the denser microstructure of UHPC matrix. In normal FRC, the ITZ between fiber and matrix occupies a significant fraction of total cement paste volume and the inclusion of fibers could increases the permeability. However, in UHPC matrix, the ITZ area shows very dense microstructure at the fiber-matrix interface, or the aggregate-matrix interface (Shi, Wu, Xiao, Wang, Huang and Fang 2015, Wang, Jacobsen, He, Zhang, Lee and Lein 2009). Therefore, the permeability of UHPC is not dominated by the ITZ introduced by the inclusion of aggregates and fibers.

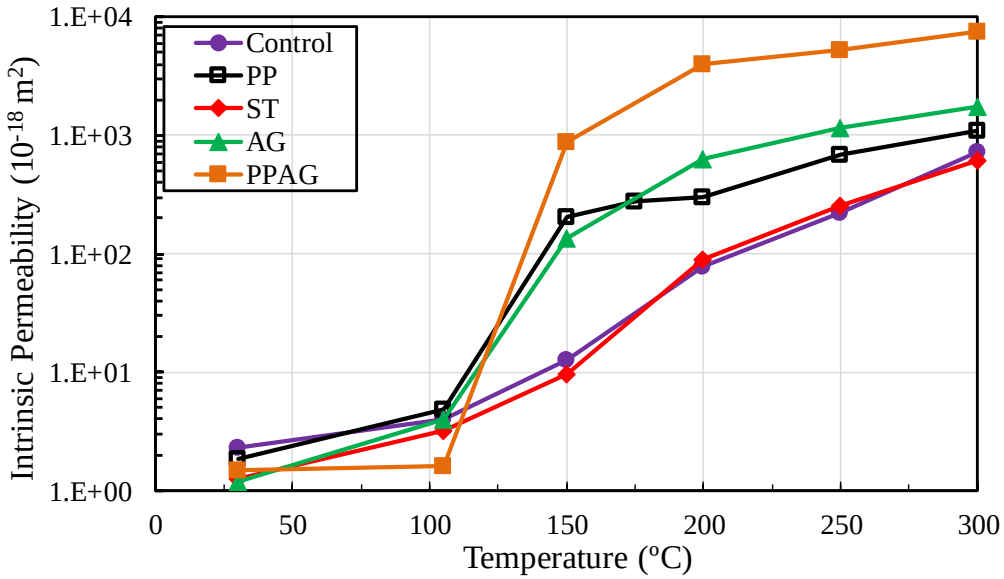

Fig. 6.2. Intrinsic permeability of UHPCs as functions of temperature.

For the control mix, the intrinsic gas permeability increases almost linearly with increasing temperature at the semi-log scale. At 300 °C, the gas permeability increases by about three

orders of magnitude as compared to the permeability at ambient temperature. The addition of steel fibers (ST) does not lead to significant change of gas permeability at elevated temperature. The increase of permeability of the Control and ST is primarily due to the formation of micro cracks and the dehydration of hydrated products which makes the microstructure more porous (Lin, Lin and Powers-Couche 1996).

The initial gas permeability of UHPC with the addition of PP fibers (PP) is similar to that of Control. At 150 °C, however, a sudden increase in permeability of almost two orders of magnitude can be observed in PP. This was generally explained by the formation of micro cracks and softening of PP fibers, followed by partial transport of PP fibers into surrounding concrete matrix (Bošnjak, Ožbolt and Hahn 2013). It is worth noting that the temperature corresponding to the sudden increase of permeability (105-150 °C) is lower than the melting temperature of PP fibers (150 to 175 °C). Similar phenomenon was observed and reported in reference (Bošnjak, Ožbolt and Hahn 2013) as well. Fig. 6.3 shows the DSC thermogram of PP fibers used in the current study. As can be seen, while the PP fibers possess an exothermic peak at 166.5 °C which represents the melting point of the fibers, the onset of melting starts at a much lower temperature of around 125 °C.

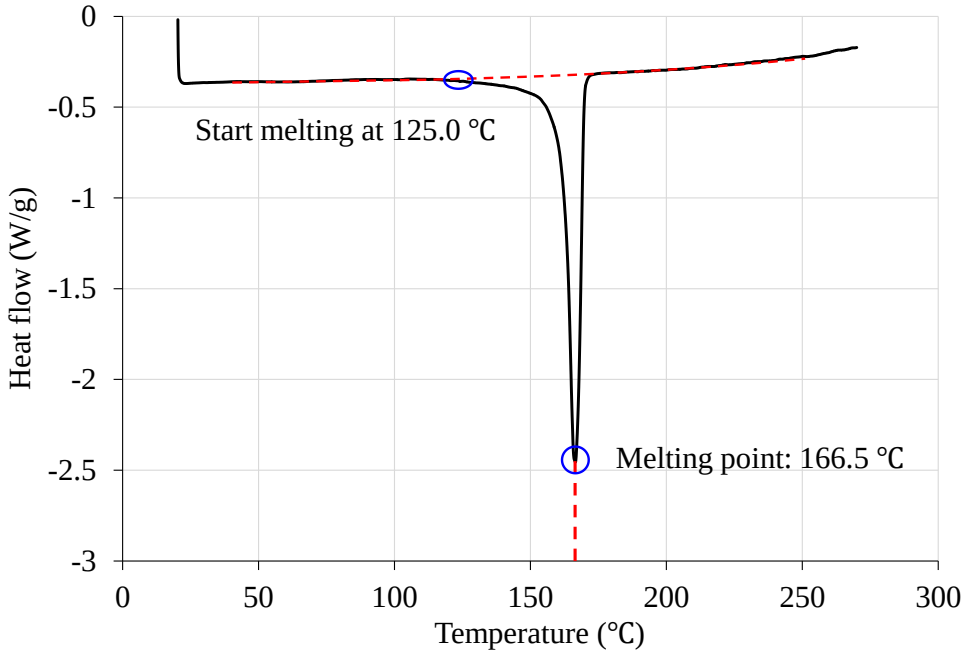

Fig. 6.3. DSC thermograms of PP fibers

It is plausible that the softened and partially melted PP fibers are deformed from their original locations due to externally applied air pressure during the hot permeability test, which could create pressure-induced tangential space (PITS) (Ozawa and Morimoto 2014), leaving gaps at the fiber-matrix interface and causing an increase of permeability at the hot state. Beyond 150 °C, the increasing rate of permeability reduces and the difference in permeability between PP and the control sample becomes smaller. This is probably due to the PP fibers has melted and formation of micro-cracks is almost completed, further changes of UHPC at higher temperature mainly come from the degradation of the cement matrix.

The presence of larger aggregates (5 mm) is another significant factor contributing to the increase of permeability (Fig. 6.2). Probably, this is attributed to the formation of micro-cracks resulting from incompatible thermal expansion between the cement paste and the larger aggregates at elevated temperature. Such incompatible deformation causes bond failure between the aggregate and the matrix interface due to tension and/or shear, which is largely influenced by the size of aggregate. (Idiart, Bisschop, Caballero and Lura 2012) reported a critical aggregate size of 1.0 mm will lead to shrinkage cracking. No micro cracks wider than 0.5 μm were observed when smaller aggregates were used in that particular study.

The combined use of PP fibers and larger aggregates increased the intrinsic permeability of UHPC significantly. At 150 °C, the intrinsic permeability of PPAG is nearly two orders of magnitude higher than that of Control and one order of magnitude higher than that of PP and AG. This highlights the synergistic effect of the combined uses of PP fibers and larger aggregates on increasing permeability. From 150 to 300 °C, the permeability of PPAG remained the highest among all the UHPC mixes.

For the UHPCs with PP fibers and/or larger aggregates, the increase in permeability at temperature above 150 °C is moderate. Similar results were also reported in other studies (Gallé and Sercombe 2001, Liu, Ye, De Schutter, Yuan and Taerwe 2008). It can be concluded that at 150 °C, the damage induced by PP fibers and larger aggregates is the dominant factor responsible for the increase of permeability, which overshadows the effect from dehydration of cement matrix. However, at higher temperature up to 300 °C, continuous damage of the cement matrix is the main cause.

Fig. 6.4 shows the normalized intrinsic permeability relative to Control. The effect of PP fibers and larger aggregates is shown. For PP, AG, and PPAG, the effects of PP fibers and larger aggregates can be seen clearly at 150 °C. No significant difference between Control and ST can be observed. The contribution of larger aggregates to the increase of permeability is less than that of PP fibers at 150 °C, but a reverse trend is observed at higher temperature. The inclusion of both PP fibers and larger aggregates significantly increases the permeability. It can be concluded that the damage caused by the thermal incompatibility between larger aggregates and UHPC matrix and the expansion and partial melting of PP fibers are the major reasons for the increase of permeability at 150 °C. Above 200 °C, the PP fibers had already melted. Therefore, they lost the ability to continuously affect permeability significantly. The effect of larger aggregates decreased gradually from 200 °C to 300 °C. Expansion of unhydrated clinker and shrinkage of hydration products can cause damage to the cement matrix (Piasta 1984). It is plausible the effect from larger aggregates was overshadowed by the changes in the cement matrix.

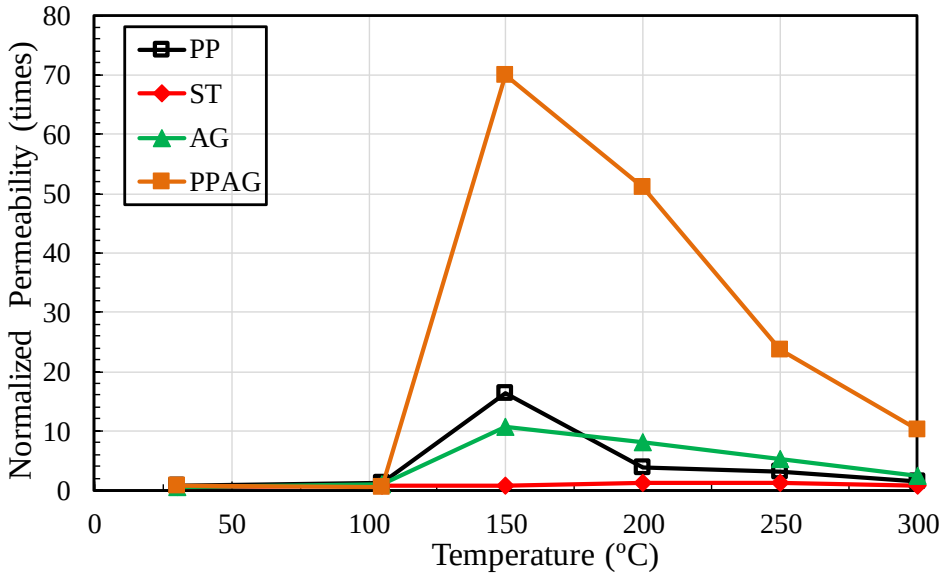

Fig. 6.4. Normalized permeability relative to Control.

6.3.2 Microscopic investigation

Fig. 6.5 shows the FESEM micrographs of Control before and after heating at 250 °C for 4 hours. As can be seen, the UHPC matrix used in this study has a very dense microstructure

owing to low water-to-cement ratio and the inclusion of silica fume. After heating at 250 °C for 4 hours, micro-cracks can be observed in the matrix as shown in Fig. 5 (b). The formation of micro-cracks together with dehydration and decomposition of hydration products increases the porosity of the matrix and contributes to the moderate increase of permeability at elevated temperature of Control. It is worth mentioning that the micro-cracks were only present in the matrix and not along the aggregate-matrix interface. This observation is in agreement with the findings in the literature that very small aggregate particles (less than 1 mm) cause negligible bond failure between the aggregate and matrix interface (Idiart, Bisschop, Caballero and Lura 2012).

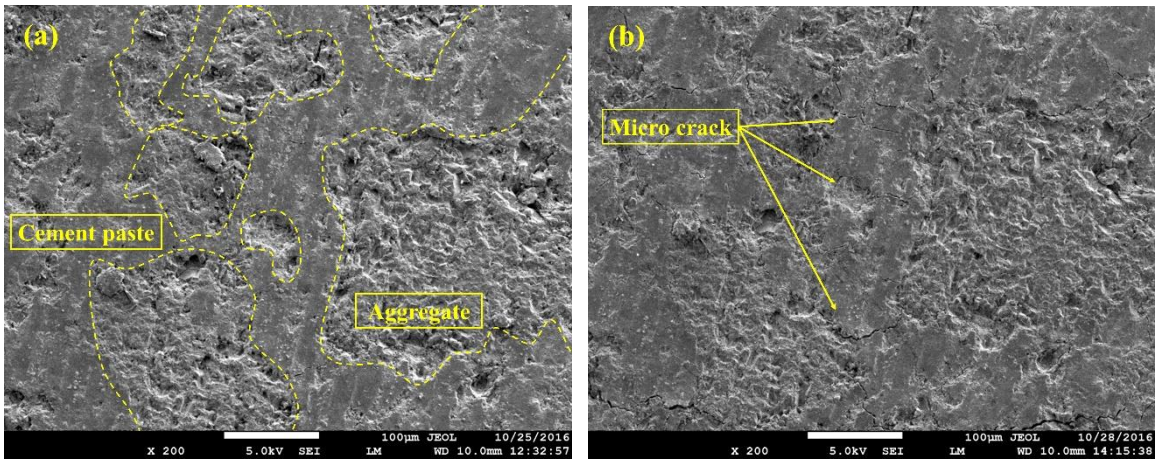

Fig. 6.5. Microstructure of Control (a) before and (b) after exposure to 250 °C for 4 hours.

Fig. 6.6 shows the cross section of ST before and after exposure to 250 °C for 4 hours. Steel fibers remain in the matrix after heating because the melting temperature of steel is much higher than 250 °C. However, radial micro-cracks with crack width ranging from 1 to 5 µm around the embedded steel fibers were observed. This is attributed to thermal incompatibility between steel fibers and UHPC matrix. The formation of radial cracks is due to larger thermal expansion of the steel fibers compared to that in the UHPC matrix (Zunino, Castro and Lopez 2015). However, the formation of these micro-cracks, does not lead to significant increase of permeability of the ST specimen as compared to Control (Fig. 6.2). It has been reported that if the micro-crack network is not percolated, permeability of concrete is governed by the transport property of the cement paste (Abyaneh, Wong and Buenfeld 2016).

This suggests that the micro-cracks introduced by the expansion of steel fibers in the present study are not percolated.

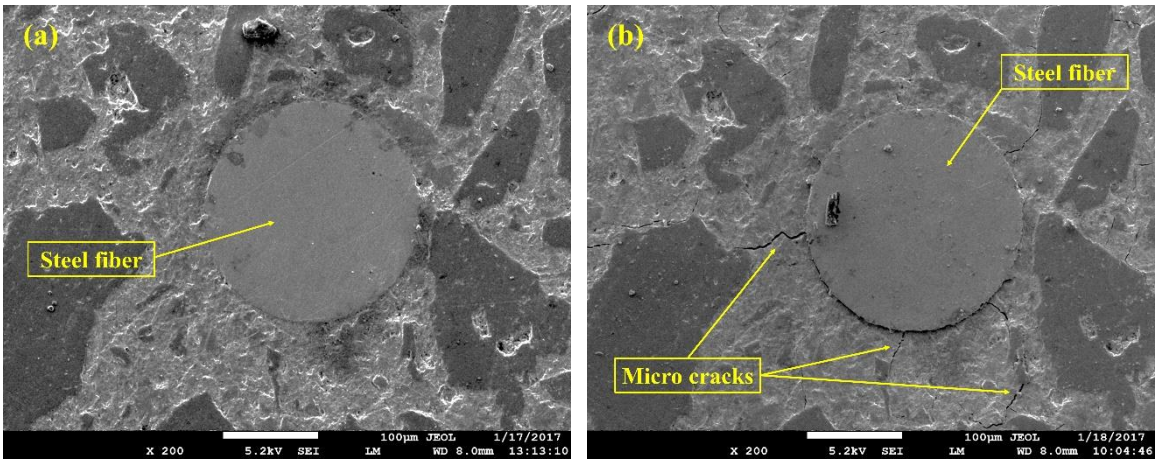

Fig. 6.6. Microstructure of ST (a) before and (b) after exposure to 250 °C.

Fig. 6.7 shows the micrograph of PP before and after heating at elevated temperatures (150 °C or 180 °C) for 4 hours. As can be observed in Fig. 6.7 (a) and (b), the PP fiber has largely disappeared and only a small amount of residue is attached to the fiber tunnel after heating at 150 °C. While the heating temperature is below the melting point (166.5 °C) of PP fibers, it is well above the onset of melting (125 °C) as in Fig. 6.3. This shows that the function of PP fibers against spalling under elevated temperature may be activated as soon as the temperature is above the onset of melting of fibers (125 °C). At higher temperature (180 °C), PP fibers disappear completely as shown in Fig. 6.7 (c) to (d).

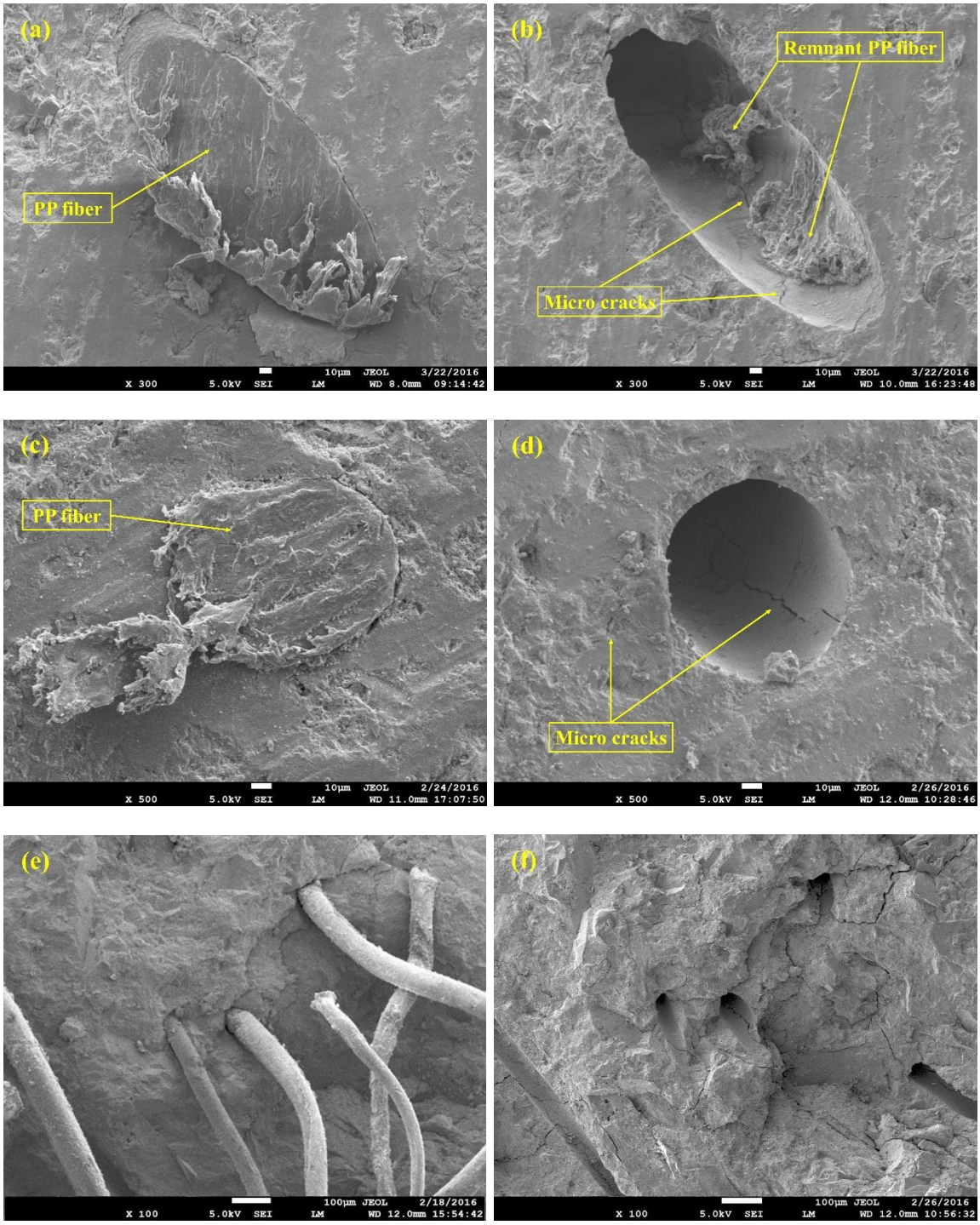

Fig. 6.7. Micrographs of PP (a) before and (b) after heating at 150 °C for 4 hours; (c) (e) before and (d) (f) after heating at 180 °C for 4 hours.

The coefficient of thermal expansion (CTE) of polypropylene at ambient temperature is about ten times greater than that of concrete and the ratio is even higher at elevated

temperature (Khoury and Willoughby 2008). The expansion of PP fibers at elevated temperature therefore could cause significant tensile stress build-up in the tangential direction along the fiber-matrix interface. As can be seen in Fig. 6.7 (b) and (d), several micro cracks formed in the radial direction of the fiber tunnel. The width of such micro cracks was smaller than 5 μm. From Fig. 6.7 (e) and (f), the inclusion of PP fibers facilitates the formation of an inter-connected micro-cracks and fiber tunnel network, which is responsible for the increase of permeability at elevated temperature.

Fig. 6.8 shows the AG before and after exposure to 250 °C for 4 hours. As can be seen, aggregates debond from the matrix after heating, which is distinct from Control where only very fine sand (< 600 μm) is used in the mix (Fig. 6.5). Since CTE of aggregates are generally lower than that of cement paste (Mehta and Monteiro 2006, Sellevold and Bjøntegaard 2006, Shui, Zhang, Chen and Xuan 2010, Zunino, Castro and Lopez 2015), the maximum principal stress along the aggregate-matrix interface occurs in the radial direction of the aggregates. As a result, cracks propagate primarily in the tangential direction along the aggregate-matrix interface (Fu, Wong, Tang and Poon 2004, Zunino, Castro and Lopez 2015) and may branch out into matrix as shown in Fig. 6.8 (b). Therefore, the inclusion of larger aggregates also facilitates the formation of an inter-connected micro-cracks network, which is responsible for the increase of permeability of AG at elevated temperature. The width of such cracks is around 5 μm in current study.

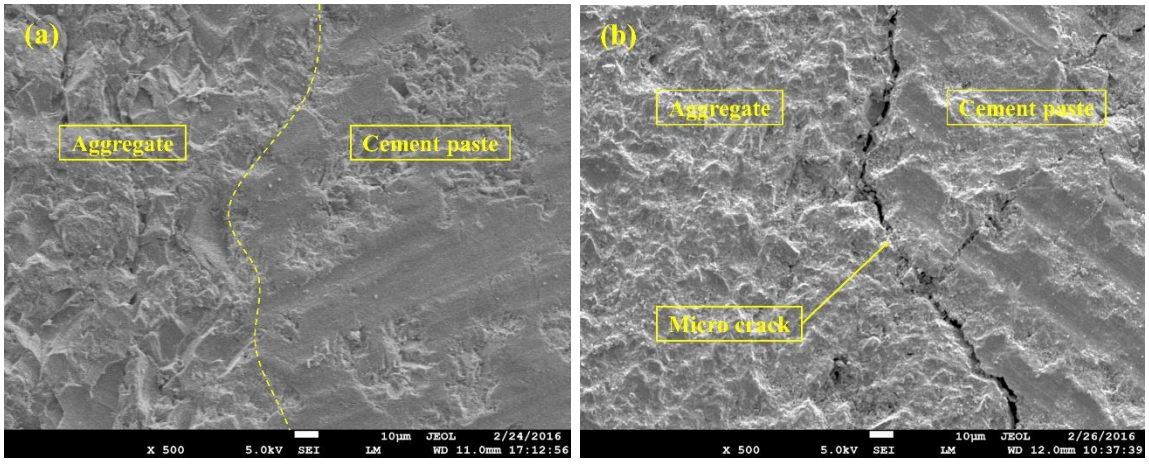

Fig. 6.8. FESEM photos of the microstructure of AG (a) before and (b) after exposure to 250 °C.

Fig. 6.9 shows the PPAG before and after exposure to 250 °C for 4 hours. As can be seen, many micro-cracks were generated due to thermal expansion and mismatch between fiber/aggregate and matrix. The radial micro cracks formed around PP fibers are attributed to the larger CTE of PP fibers compared to that of concrete matrix. The "bond cracks" at the aggregate-paste interface are attributed to the smaller CTE of aggregates. The micro-cracks are interconnected, which could lead to a higher connectivity between empty fiber tunnels and bond cracks along aggregate-matrix interface, resulting in a higher permeability of UHPC at elevated temperature. The permeability measurement shows that the combined effect of PP fibers and larger aggregates could significantly increase the permeability of PPAG at high temperature.

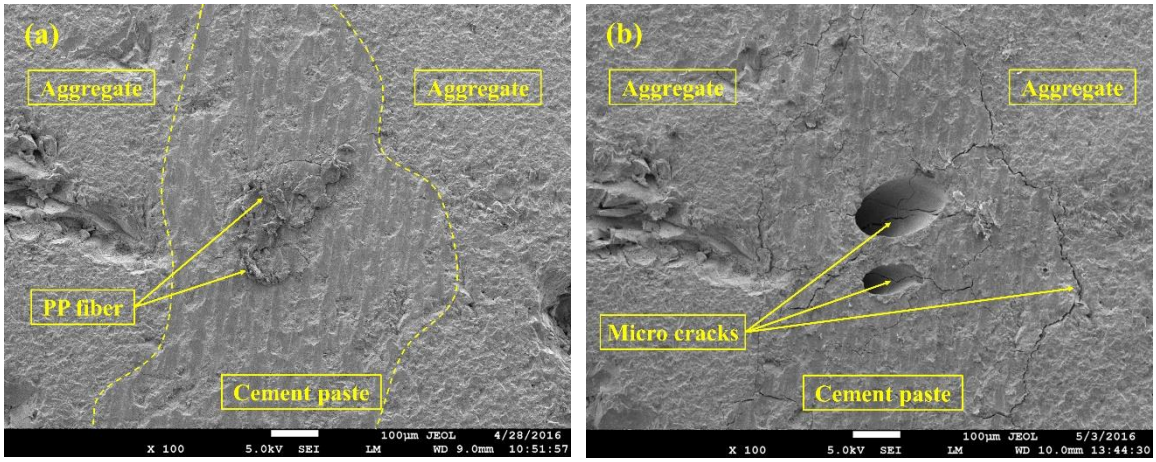

Fig. 6.9. FESEM photos of the microstructure of PPAG (a) before and (b) after exposure to 250 °C.

6.3.3 Schematic illustration of influence of PP fibers and larger aggregates on permeability of UHPC at elevated temperature

It has been reported that the inclusion of PP fibers greatly enhanced the spalling resistance of high strength concrete at elevated temperature. It was generally believed that the melting of PP fibers creates pathway by connecting the porous ITZs between the aggregates and the matrix, thus increasing the permeability of concrete at elevated temperature as illustrated in Fig. 6.10 (a) (Mazzucco, Majorana and Salomoni 2015). In normal mortars and concretes, ITZ occupies a significant fraction of the total paste volume. However, in UHPC, no

significant porous ITZ was observed between the aggregates and the matrix interface or the fibers and the matrix interface (Shi, Wu, Xiao, Wang, Huang and Fang 2015, Wang, Yang, Liu, Wan and Pu 2012). This can be attributed to the very low water-to-binder ratio and the presence of silica fume. The low water-to-binder ratio led to a compact cement paste, and the very fine particle size of silica fume caused pozzolanic reaction. The calcium hydroxide produced in the hydration process reacted with the silica particles and created CSH (Korpa, Kowald and Trettin 2009, Wang, Shi, Wu, Xiao, Huang and Fang 2015). In addition, the silica particles filled up voids and gaps inside the cement matrix and ITZs, which led to a much denser microstructure. Based on the microstructure investigation above, new observations are made, and new models are proposed in current study to capture the influence of PP fibers and larger aggregates on permeability of UHPC at elevated temperature.

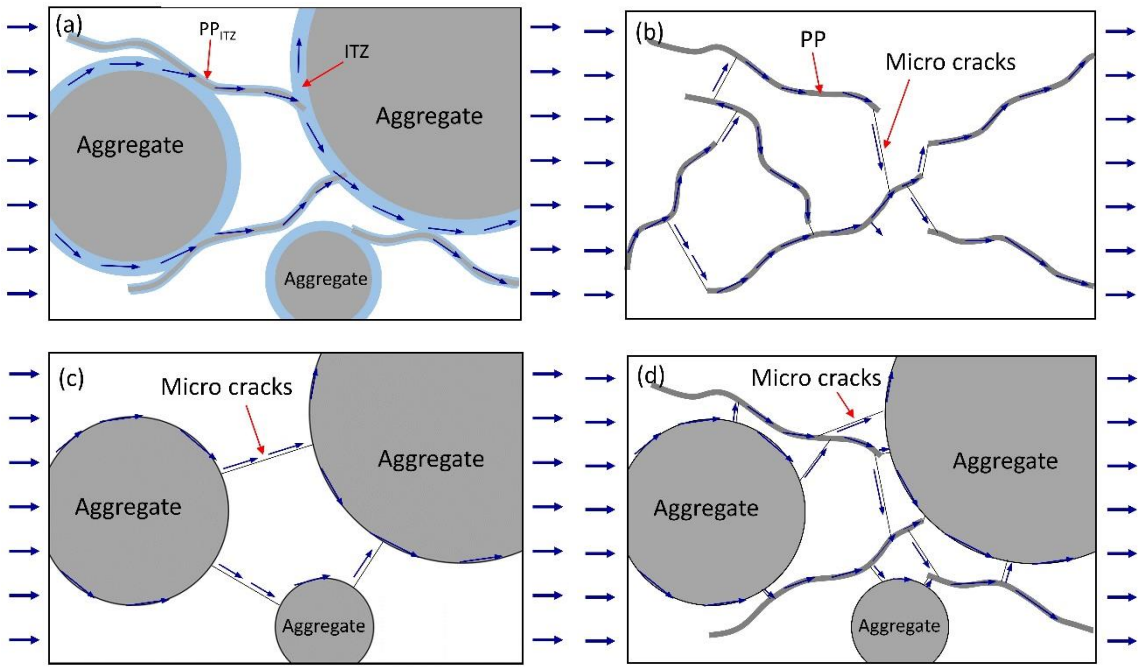

Fig. 6.10. Model of permeability of (a) normal concrete with PP fibers and larger aggregates (Mazzucco, Majorana and Salomoni 2015), (b) UHPC with PP fibers, (c) UHPC with larger aggregates, and (d) UHPC with PP fibers and larger aggregates at elevated temperature.

As discussed in the previous section, micro-cracks can be formed by PP fibers and/or larger aggregates in the UHPC samples, due to thermal expansion and mismatch between the fiber/aggregate and the matrix. Micro-cracks tend to initiate in the high stress region and propagate along the weakest area to release stresses (Abyaneh, Wong and Buenfeld 2016). Therefore, at elevated temperature, these micro-cracks provide connectivity between empty PP fiber tunnels in PP as Fig. 6.10 (b), bond cracks along aggregates in AG as Fig. 6.10 (c), or both in PPAG as Fig. 6.10 (d) at elevated temperature. The formation of such micro-cracks network is responsible for the increase of UHPC permeability. It is worth noting that, the matrix cracks are generated by the combined effects of PP fibers and larger aggregates (Fig. 6.10 (d)). In PPAG, it is expected that the volume fraction, number of micro cracks, and specific surface area of matrix cracks would be larger, which account for the higher intrinsic permeability at elevated temperature. Further study on the characterization of micro-crack networks is needed in order to provide quantitative analysis.

6.4 Summary

This chapter investigates the influence of aggregate size and inclusion of PP and steel fibers on the intrinsic permeability of UHPC at elevated temperature. Hot permeability measurements were performed on UHPCs subjected to elevated temperature up to 300 °C. Microstructure of UHPC samples before and after the exposure to elevated temperature was studied to reveal potential mechanisms responsible for the change of permeability.

It was found that the inclusion of either PP fibers or larger aggregates significantly increases hot permeability, while the addition of steel fiber does not contribute to the enhancement of permeability of UHPC at elevated temperature. The combined use of PP fibers and larger aggregates in UHPC showed synergistic effect and resulted in a significant increase of permeability at elevated temperature. This is mainly attributed to the formation of interconnected micro-crack networks at elevated temperature due to melting of PP fiber and thermal expansion and mismatch between the aggregate/fiber and matrix. Radial micro cracks formed around PP fibers, while the “bond cracks” formed alone the aggregate-matrix interface. In addition, the function of PP fibers against spalling under elevated temperature

may be activated once the temperature is above the onset of melting of fiber at about 125 °C, which is much lower than the melting point of 165 °C.

Chapter 7 Effects of Geometry and Fraction of PP Fibers on Residual Permeability of UHPC and a Prediction Model

7.1 Overview

From Chapter 2 and microstructural observation in Chapter 6, the increase of permeability is not only due to empty fiber tunnels but also tied to the formation of microcracks instead of porous ITZs. The literature contains very few studies that have directly characterized thin microcracks (< 5 μm) and correlated the microcrack-fiber tunnel network to permeability of UHPC. This chapter aims to provide a better understanding of the influence of PP fiber fraction and geometry and microcracks on the intrinsic residual permeability of UHPC after elevated temperature exposure.

To achieve this aim, the residual permeability and the characteristics of microcracks of 5 groups of UHPC mixes with PP fibers were measured. The general principle of the permeability measurement setup followed the RILEM-CEMBUREAU method (Kollek 1989). Klinkenberg method was adopted to calculate the intrinsic permeability of the samples (Klinkenberg 1941).

Microcracks of UHPC specimens were observed by field emission scanning electron microscope (FESEM) under backscattered electron (BSE) mode and were characterized by using image analysis method. The geometry of formed microcracks network was quantified for microcrack density, average crack width, and crack fraction. Based on the quantification of microcracks, a quantifiable model correlating PP fiber and microcracks was proposed to analyze the effect of PP fiber tunnels and microcracks on residual permeability. The probability of percolation of PP fiber tunnels was calibrated by the first 3 groups of the UHPC mixes and then validated by the last 2 groups. The understanding gained will help in the interpretation of permeability changes which can be used as a spalling indicator. It will also facilitate modeling of explosive spalling on microstructural level.

7.2 Experimental programs

7.2.1 Materials and mix proportions

Portland cement (ASIA@ CEM I 52.5 N), fine aggregates (natural river sands sieved to 0.6 mm), micro silica sands (median particle size of 130 μm), a highly reactive silica fume (Grade 940 from Elkem Microsilica@), the 3rd generation polycarboxylate-based superplasticizer (Sika@ ViscoCrete@-2044), and monofilament cylindrical PP fibers with different geometries supplied by DFL, were used to prepare the UHPC mixes. Water-to-binder ratio was 0.2 to realize dense packing.

Five groups UHPC mixes were prepared as shown in Table 7.1. The first group investigated the effects of PP fiber dosage (1.0 to 5.0 kg/m^3) and the second and the third groups studied the influences of fiber length (6, 12, 18 mm) and fiber diameter (30, 50, 60 μm), respectively. The fourth group examined the combined effects of fiber length and fiber dosage, where fiber length increased proportionally with fiber dosage according to the following equation so that the number of fibers per unit volume N remained unchanged.

$$N = 4\phi_m / \pi\rho l d^2 \tag{7.1}$$

where ϕ_m is fiber dosage (mass fraction), ρ is the density of PP fibers, l is fiber length, and d is fiber diameter. Similarly, the fifth group examined the combined effects of fiber diameter and fiber dosage, where fiber diameter increased proportionally with fiber dosage according to Eq. 7.1 so that N is constant.

Table 7.1. Mix proportions of UHPC mixtures

Group	Mix		Relative mass ratio to cement						PP fibers		
	No.	Designation	C	AG	SS	SF	SP	W/B	Length (mm)	Diameter (μm)	Fraction (kg/m^3)
1	1	L12D30M1	1.0	1.1	0.25	0.25	0.04	0.2	12	30	**1**
	2	L12D30M3	1.0	1.1	0.25	0.25	0.04	0.2	12	30	**3**
	3	L12D30M5	1.0	1.1	0.25	0.25	0.04	0.2	12	30	**5**
2	4	L6D30M3	1.0	1.1	0.25	0.25	0.04	0.2	**6**	30	3
	5	L12D30M3	1.0	1.1	0.25	0.25	0.04	0.2	**12**	30	3
	6	L18D30M3	1.0	1.1	0.25	0.25	0.04	0.2	**18**	30	3
3	7	L12D30M3	1.0	1.1	0.25	0.25	0.04	0.2	12	**30**	3
	8	L12D50M3	1.0	1.1	0.25	0.25	0.04	0.2	12	**50**	3
	9	L12D60M3	1.0	1.1	0.25	0.25	0.04	0.2	12	**60**	3
4	10	L6D30M1.5	1.0	1.1	0.25	0.25	0.04	0.2	**6**	30	**1.5**
	11	L12D30M3	1.0	1.1	0.25	0.25	0.04	0.2	**12**	30	**3**
	12	L18D30M4.5	1.0	1.1	0.25	0.25	0.04	0.2	**18**	30	**4.5**
5	13	L12D30M3	1.0	1.1	0.25	0.25	0.04	0.2	12	**30**	**3**
	14	L12D50M8.3	1.0	1.1	0.25	0.25	0.04	0.2	12	**50**	**8.3**
	15	L12D60M12	1.0	1.1	0.25	0.25	0.04	0.2	12	**60**	**12**

C: cement, AG: aggregates, SS: silica sand, SF: silica Fume, SP: superplasticizer, W/B: water-to-binder ratio

7.2.2 Sample preparation

Raw materials were mixed in a Hobart[@] planetary mixer. Cement, fine aggregates, micro silica sands, and silica fume were dry-mixed for 2 minutes. Thereafter, premixed water and superplasticizer were added and mixed for another 3 to 5 minutes until the fresh mortar is homogenous and consistent. Fibers were then slowly added into the mixture and mixed for another 2 minutes. The fresh UHPC mixtures were then cast into cylindrical (Ø150 mm×48 mm) and cubical (50×50×50 mm^3) molds for permeability tests and microstructural study, respectively. Specimens were covered with a plastic sheet at room temperature for the first 24 h. Afterwards, specimens were demolded and stored in lime-saturated water at room temperature for another 27 days before testing.

7.2.3 Permeability measurement, microstructure characterization, and microcracks network quantification

After curing, cylindrical samples were ground from two ends until the thickness of the disc reduced to 40 mm. Surfaces of the discs were fine polished to ensure good contact with the permeability measuring device. Please refer to Section 6.2.2 about the method to measure and calculate permeability.

To quantify the microcracks generated in UHPC samples after exposure to elevated temperature, 20×20×5 mm^3 samples were heated to 200 °C for 24 hours and then cooled down to ambient temperature. The heating rate was 1 °C/min for all specimens to minimize thermal stress. The samples were then impregnated and fixed with epoxy after heating. The impregnated samples were cured at room temperature for 1 day followed by grinding to remove epoxy on the top surface (~300 μm in thickness) and to expose impregnated microcracks. The sample surface was further polished with silicon carbide paper of grit size ranging from P320 to P1200 to reduce the surface roughness.

Backscattered electron (BSE) imaging of sample was captured by FESEM with 15.0 kV beam energy. The brightness setting was calibrated so that the brightness histogram of the recorded image spans the entire range of available grey scale. The same setting was applied to all images for consistency. A magnification of 200× was used to obtain the details of micro cracks. The resolution of images was 271 dpi and the width of each pixel was smaller than 0.5 μm, which is a sharper resolution than published literature (1.5 to 20 μm) (Homand, Hoxha, Belem, Pons and Hoteit 2000, Landis, Zhang, Nagy, Nagy and Franklin 2006, Zhou, Li and Pang 2012). For each sample, micrographs were taken at three random locations. For each location, 3×3 continuous images were taken, aligned and stitched together by ImageJ to produce a larger montage, which covered an area of 1.6×1.25 mm^2 (Fig. 7.1). The images were used to analyze the microcrack networks in 2-dimension.

The images imported into ImageJ were in a 256-gray level (as shown in Fig. 7.1b). The images were first processed with an “Isotropic Diffusion 2D” filter to reduce noise. All detectable microcracks were then segmented by using “Triangle” method of thresholding on

the montage to obtain a binary image that consisted of cracks (Fig. 7.1c). After which, the 'crack' pixels were defined as 1 (black) and the 'concrete matrix' pixels were assigned as 0 (white). The accuracy of segmentation was checked by cross-referencing with actual micrograph. The 'crack' pixels caused by defects in aggregates or fiber tunnels were cleared manually. At last, particles with circularity ($4\pi\times$area/perimeter^2) larger than 0.5 were excluded to ensure only microcracks were counted. "Analyze Particles" function was used to measure the area of each microcrack. After skeletonizing, "Analyze Skeleton" function was used to measure the lengths of each microcrack.

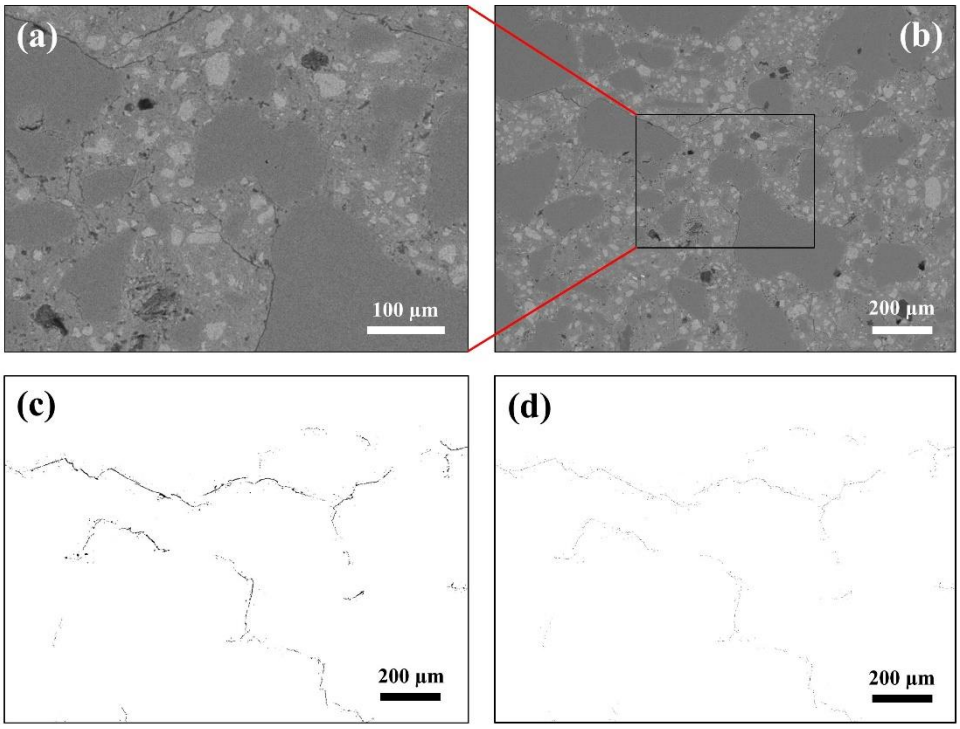

Fig. 7.1. Image processing procedure (a) FESEM image of an impregnated and grinded sample, (b) Montage of the Images produced by stitching, (c) Binary image after cleaning showing detectable microcracks, (d) Conversion of binary image of cracks into cracks skeleton.

The crack density L_s from 2D microcrack images, which is commonly adopted in stereological study of crack geometry (Litorowicz 2006, Samaha and Hover 1992, Zhou, Li

and Pang 2012), is defined as the arithmetic addition of crack lengths l_i $(i=1,n)$ divided by surface area *A*.

$$L_s = \frac{1}{A}\sum_{i=1}^{n} l_i \tag{7.2}$$

The average microcrack width is defined as the arithmetic addition of 2D microcrack areas a_i $(i=1,n)$ divided by the arithmetic addition of crack lengths l_i $(i=1,n)$ in Eq. 7.3. Since a 2D image samples the microcracks at an arbitrary plane (Wong, Zimmerman and Buenfeld 2012) and the imaging plane intersects the microcrack plane at a random angle (not perpendicular to the crack plane). Thus, the crack area determined from the 2D images is larger than the actual values. It has been reported that the stereology parameters can be extracted from the 2D microcrack image and used to interpret the 3D crack pattern (Mouton 2002), which have been applied to describe the crack networks in concrete (Ammouche, Riss, Breysse and Marchand 2001, Litorowicz 2006). In the current study, a stereological correction factor $\eta_w = 2/\pi$ was adopted by averaging the overestimation in the crack width for all possible angles (Nemati 1994).

$$w = \eta_w \sum_{i=1}^{n} a_i / \sum_{i=1}^{n} l_i \tag{7.3}$$

In the current study, crack density was used as an indicator of crack connectivity because the two have strong correlation. Crack fraction in Eq. 7.4 was defined as the arithmetic

addition of crack areas $a_i\,(i=1,n)$ of microcracks divided by surface area *A*. It represents the fraction of crack areas in the concrete matrix in a 2D plane.

$$V(\%)=\sum_{i=1}^{n} a_i / A\times 100 \tag{7.4}$$

7.3 Results and discussions

7.3.1 Effect of PP fiber dosage and geometry on permeability

The influence of PP fiber fraction and geometry on intrinsic permeability is shown in Fig. 7.2. Each value is an average of three specimens. The intrinsic permeability increased from 2.18×10^{-18} to 3.44×10^{-17} m^2 with increasing PP fiber dosage from 1.0 to 5.0 kg/m^3 (Fig. 7.2a). This is expected because more fiber tunnels are available when higher dosage of PP fiber was used. Furthermore, increase of fiber length also led to an increase of intrinsic permeability (Fig. 7.2b), e.g. the permeability of UHPC with 18 mm PP fibers was up to 18 times that with 6 mm PP fibers. This is mainly attributed to enhanced connectivity when longer fiber is used in UHPC. On the contrary, as shown in Fig. 7.2c, the permeability decreased from 1.42×10^{-17} to 2.07×10^{-18} m^2 with increasing fiber diameter from 30 to 60 μm. This can be attributed to the significantly reduced number and total length of fiber in UHPC with larger diameter. While the total volume fraction of fiber tunnels remained the same, the connectivity of fiber tunnels has decreased due to a reduction of number and total length of fibers.

Fig. 7.2d shows that permeability of UHPC increased with proportionally increasing fiber length and fiber fraction while the diameter of fiber remained unchanged (and thus the number of fibers per unit volume). As can be seen, the residual permeability of L18D30M4.5 is about 40 times that of L6D30M1.5. The increase of permeability of group 4 is more than that of group 1 (solo increase of fiber dosage) and group 2 (solo increase of fiber length). As the fiber diameter and fiber fraction increased proportionally while the length of fiber remained unchanged (and thus the number of fibers per unit volume, group 5), the

permeability of UHPC slightly increased from 1.42×10^{-17} to 2.37×10^{-17} m^2 (Fig. 7.2e). This may be because the effects of the two factors, e.g. increase of fiber fraction and fiber diameter, on permeability of UHPC cancelled each other.

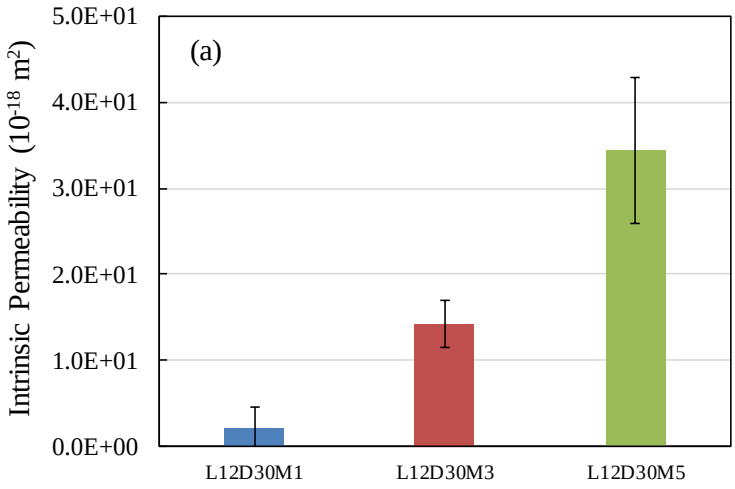

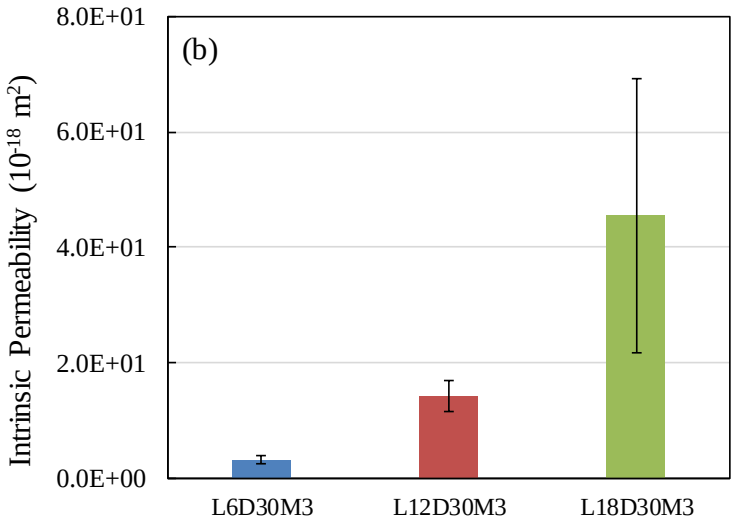

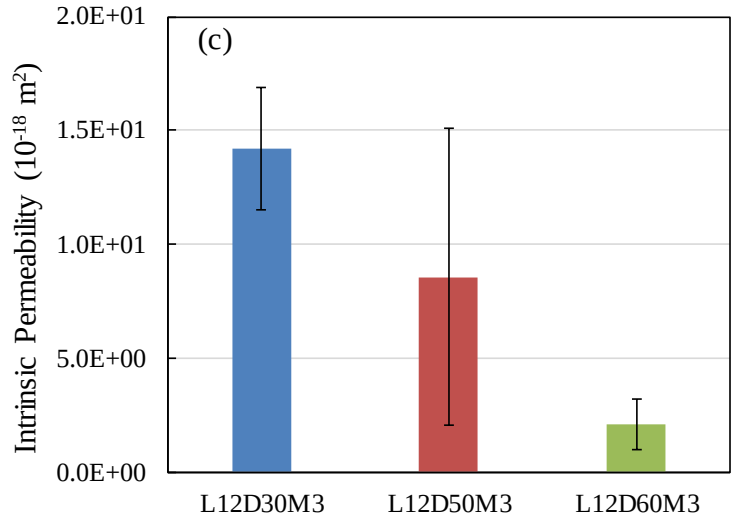
(c)
Intrinsic Permeability (10-18 m2)
2.0E+01
1.5E+01
1.0E+01
5.0E+00
0.0E+00
L12D30M3
L12D50M3
L12D60M3

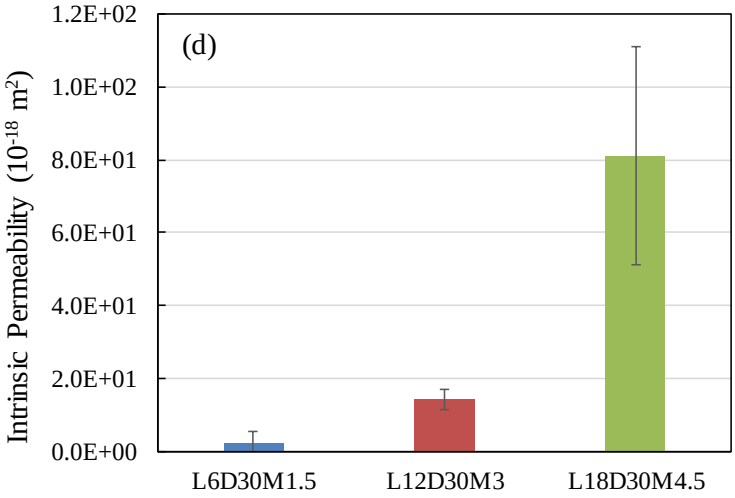
(d)
Intrinsic Permeability (10-18 m2)
1.2E+02
1.0E+02
8.0E+01
6.0E+01
4.0E+01
2.0E+01
0.0E+00
L6D30M1.5
L12D30M3
L18D30M4.5

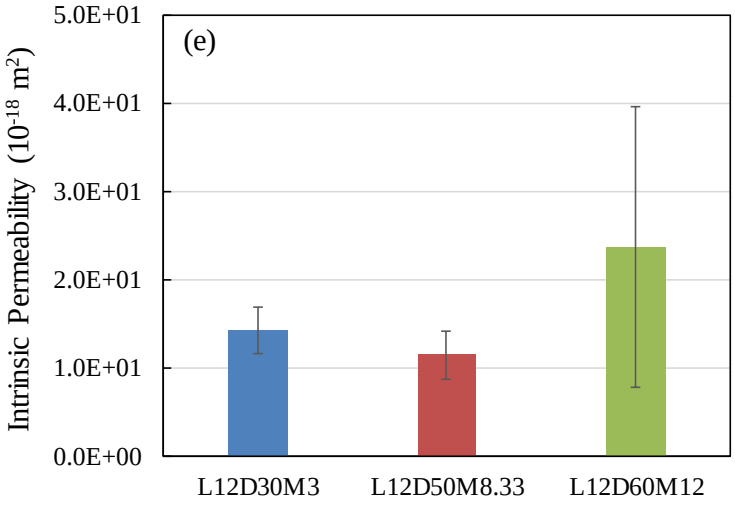
(e)
Intrinsic Permeability (10-18 m2)
5.0E+01
4.0E+01
3.0E+01
2.0E+01
1.0E+01
0.0E+00
L12D30M3
L12D50M8.33
L12D60M12

Fig. 7.2. Intrinsic permeability of UHPC as a function of PP (a) fiber dosage, (b) fiber length, (c) fiber diameter, (d) fiber dosage and fiber length, and (e) fiber dosage and fiber diameter.

Fig. 7.3 compares the permeability of group 4 (Fig. 7.2d) and group 5 (Fig. 7.2e) UHPCs, where PP fiber dosage increases through increasing the fiber length (group 4) or the fiber diameter (group 5) given that both groups have the same number of fibers per unit volume. As can be seen, increasing PP fiber dosage through increasing the fiber length has much stronger effect than that through increasing the fiber diameter on enhancing residual permeability of UHPC. This may be attributed to that longer fiber greatly enhanced the percolation of fiber tunnels and thus increasing fiber length is more effective.

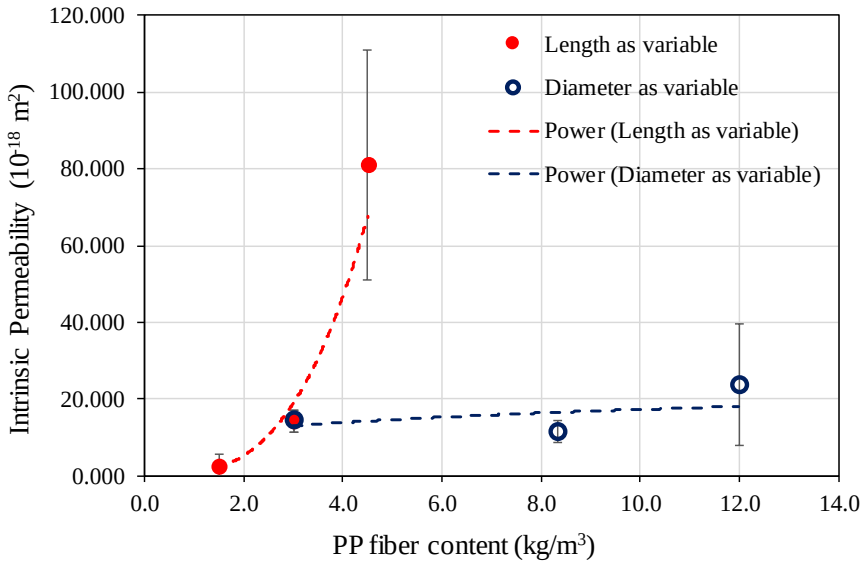

Fig. 7.3. Permeability of group 4 and group 5 UHPCs.

7.3.2 Microstructure characterization

As shown in Fig. 5.5, the UHPC matrix is dense and no obvious porous ITZs, which are distinct from the 'bulk paste' can be observed. The exposed surfaces of oven-heated samples show empty fiber tunnels and microcracks formed in the radial direction of fiber tunnels. This is because coefficient of thermal expansion (CTE) of polypropylene at ambient

temperature is ten times greater than that of concrete matrix and this ratio is even higher at elevated temperature (Khoury and Willoughby 2008). Expansion of PP fibers at elevated temperature thus causes significant tensile stresses in the tangential direction along the fiber-matrix interface. Inclusion of PP fibers facilitates the formation of an inter-connected fiber-tunnel-microcrack network (Fig. 5.5), which provides pathways for gaseous transport and therefore increases the permeability. It is expected that the narrow microcracks provide higher resistance to gas than the wide empty fiber tunnels.

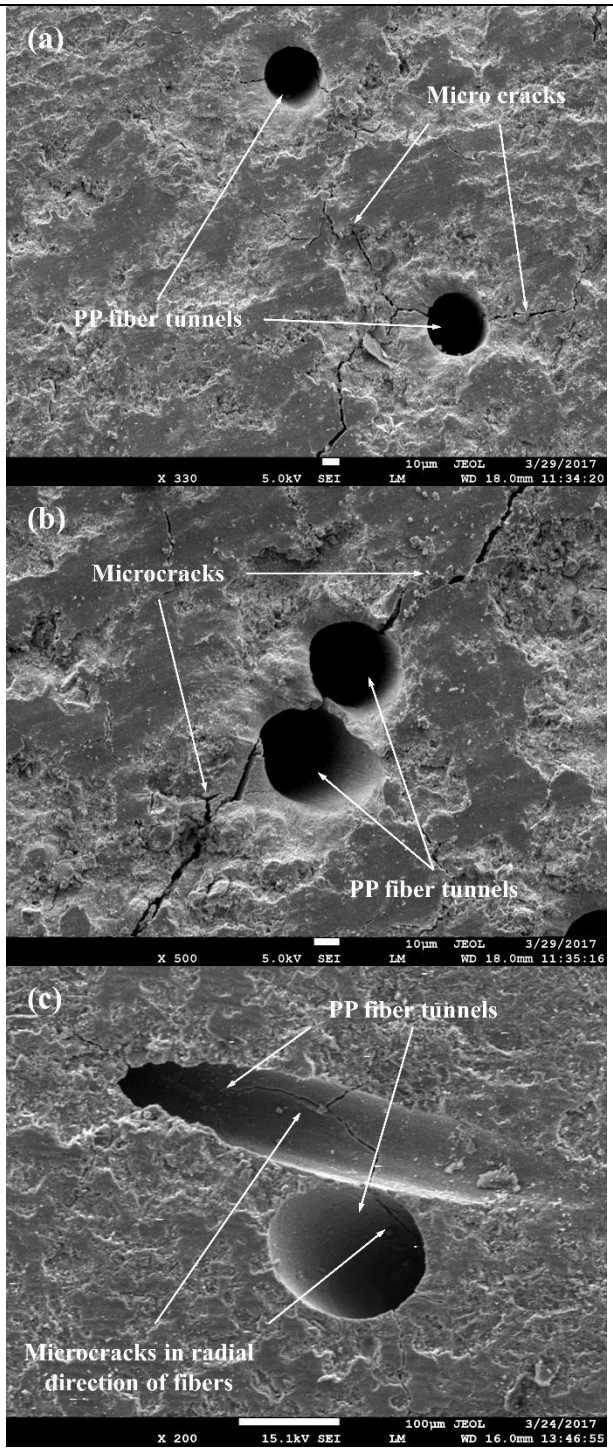

Fig. 7.4. Typical microstructure of UHPC after exposure to high temperature. (a) fiber tunnels far from each other, (b) fiber tunnels contact in parallel, and (c) fiber tunnels contact with an angle.

7.3.3 Crack density, crack width, and crack fraction

Fig. 7.5 summarizes the crack fraction, crack density, and average crack width from image analysis. Each data point is an average of three replicates. The detectable microcracks have crack widths between 1.16 and 2.05 μm. As can be seen, crack width increases with increasing fiber length (Fig. 7.5b, group 2) and reduces with increasing fiber diameter (Fig. 7.5c, group 3). Trend between crack width and fiber fraction is not significant. For the crack density, the results collectively show that increase of fiber dosage or fiber length induces more microcracks leading to higher crack density (Fig. 7.5a and b). On the contrary, increase of fiber diameter lowers crack density (Fig. 7.5c). The same trend can be found for crack fraction. As microcracks are induced by thermal expansion of PP fibers, which can be considered as nucleation sites of microcracks. Increase of fiber dosage leads to more potential nucleation sites of microcracks, and thus crack fraction and crack density increase with increasing fiber dosage. Increase of fiber diameter; on the contrary, lead to reduced number of fibers, result in lower crack density and crack fraction.

Combined effect of increasing fiber length and fiber fraction proportionally (group 4) is evaluated in Fig. 7.5d. By comparing Fig. 7.5a, b, and d, it seems that their effects superimposed upon each other. In general, crack fraction, crack density, and crack width increased with proportionally increasing fiber length and fraction (Fig. 7.5d). However, since increasing fiber fraction did not show significant trend (Fig. 7.5a), the three parameters increased slower in Fig. 7.5d than that in Fig. 7.5b. By comparing Fig. 7.5a, c, and e, it seemed that increasing fiber diameter dominated the effect of proportionally increasing fiber diameter and fraction proportionally (group 5). As shown in Fig. 7.5e, crack fraction, crack density, and crack width showed a decreasing trend.

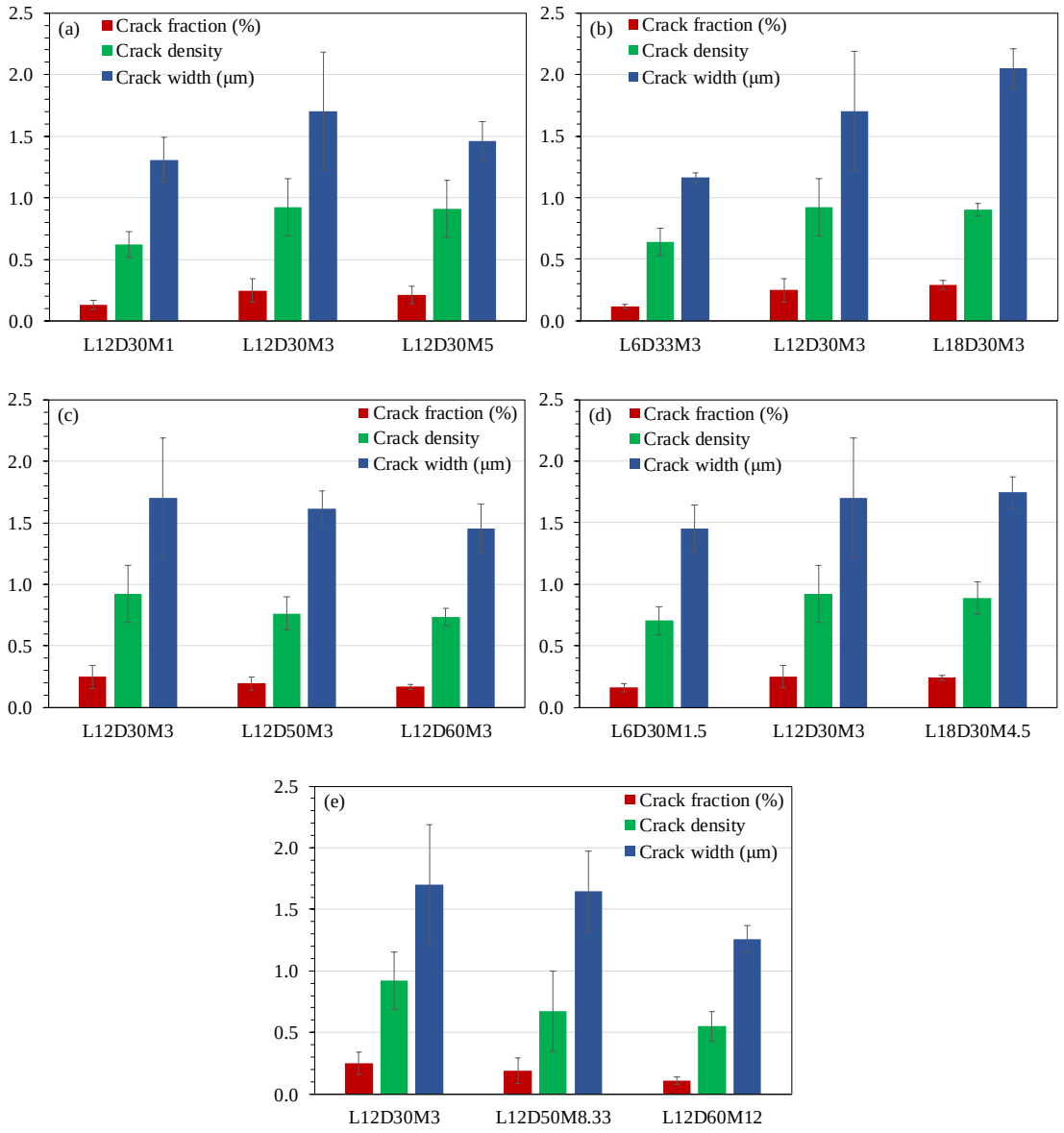

Fig. 7.5. Average crack width, crack fraction, and crack density.

7.4 Model of residual permeability of UHPC with PP

Previous studies have attempted to model the permeability of cement-based materials (Abyaneh, Wong and Buenfeld 2016, Li, Stroeven, Stroeven and Sluys 2016, Mazzucco, Majorana and Salomoni 2015, Neithalath, Sumanasooriya and Deo 2010, Song, Pack, Nam, Jang and Saraswathy 2010, Tran, Meftah, Izoret and Behloul 2013). The well-known

Kozeny-Carman model is a function of porosity and specific surface area of a homogeneous percolated porous media (Chandrappa and Biligiri 2016). The pore structure was idealized as a network of tubes arranged in a simple cubic lattice. Each pore was assumed to have the same cross-sectional size and shape (Wong, Zimmerman and Buenfeld 2012). Clearly, this assumption is not applicable for the fiber tunnel-microcrack network in the present study, which is highly heterogeneous. To quantitatively evaluate the relative contribution of PP fiber tunnels and microcracks on permeability, a new model was developed based on a limited set of input parameters, i.e. fiber fraction, fiber geometry, and microcrack width and length. The model was built in three stages as shown in Fig. 7.6, where the fibers and microcracks were considered randomly distributed and oriented in the samples. The fiber tunnels and microcracks were idealized as a network of tubes and cracks. To determine the permeability of this network, the volumetric flow rate through the tunnels and microcracks and the pattern of connectivity between fiber tunnels and microcracks were proposed.

In the first step (Fig. 7.6a), permeability of individual fiber tunnel can be described by the directional Poiseuille transport (Kaviany 2012, Lock, Jing, Zimmerman and Schlueter 2002)

$$k_f = \eta_{\theta f} \tau_f \frac{d^2}{32} \tag{7.5}$$

where k_f is the permeability of a single fiber tunnel, and d is the diameter of PP fiber, $\eta_{\theta f} = 0.5$ is the stereological correction considering the random orientation of fiber axis (Bentur and Mindess 2006), and $\tau_f = 0.5$ is the tortuosity of fiber tunnels. It can be expected that k_f only changes with variation in fiber diameter.

The second step is to determine the permeability of UHPC matrix (Fig. 7.6b). It is assumed in this study that the permeability of UHPC matrix is dominated by the characteristics of microcracks (Fig. 7.5) due to dense microstructure of UHPC matrix. The permeability of the cracked UHPC matrix can be derived as (Akhavan, Shafaatian and Rajabipour 2012, Grassl, Wong and Buenfeld 2010):

$$k_m = \frac{\eta_{\theta c}\tau_c w^3 l_c}{12\left(1+8.8R_r^{1.5}\right)A_m} \tag{7.6}$$

where k_m is the permeability of cracked UHPC matrix, w is the width of microcracks, l_c is the total length of microcracks; and $\tau_c = \left(X_{\max}/L_e\right)^2$ is the tortuosity of cracks defined by the effective crack length (L_e) and the nominal crack length ($X_{\max}$) (Bear 2013), which is assumed to be 0.18 according to (Akhavan, Shafaatian and Rajabipour 2012, Grassl and Bolander 2016). A_m is the cross sectional area, R_r is the relative surface roughness of microcracks (Akhavan, Shafaatian and Rajabipour 2012), and $\eta_{\theta c}$ accounts for the randomness of microcracks. In the current study, the microcracks are assumed to be randomly distributed and fully percolated, and thus $\eta_{\theta c} = 2/\pi$ is adopted (Bentur and Mindess 2006). k_m can be derived as long as the width and length of the microcracks can be experimentally determined as shown in Fig. 7.5.

In the third step (Fig. 7.6c and d), UHPC with PP fibers is considered as a binary composite, i.e. PP fiber tunnels embedded in cracked UHPC matrix. For two-component composites, the consideration would be that the components are arranged in either parallel or series with respect to fluid flow, which give the upper or lower bounds of permeability k_{fm}. When the fiber tunnels are totally percolated ($p=1$) as shown in Fig. 7.6d, k_{fm}^{p} corresponds to the situation that the fiber tunnels and UHPC matrix are in parallel (Kumlutaş, Tavman and Çoban 2003, Progelhof, Throne and Ruetsch 1976):

$$k_{fm}^{p} = \phi k_f + \left(1-\phi\right)k_m \tag{7.7}$$

where ϕ is the volume fraction of PP fibers. k_{fm}^{p} is mainly controlled by k_f and ϕ. When the fibers tunnels are not percolated at all $p=0$ as shown in Fig. 7.6c, k_{fm}^{np} corresponds to the situation that the fiber tunnels and UHPC matrix are in series. Thus, gas transfers through

fiber tunnels and microcracks (Kumlutaş, Tavman and Çoban 2003, Progelhof, Throne and Ruetsch 1976):

$$k_{fm}^{np} = \left(\phi k_f^{-1} + (1-\phi) k_m^{-1}\right)^{-1} \tag{7.8}$$

The permeability k_{fm} of the composite is determined using the upper and lower bounds of k_{fm}^{p} and k_{fm}^{np} (Tran, Meftah, Izoret and Behloul 2013),

$$k_{fm} = p k_{fm}^{p} + (1-p) k_{fm}^{np} \tag{7.9}$$

where *p* is the probability of percolation of fiber tunnels.

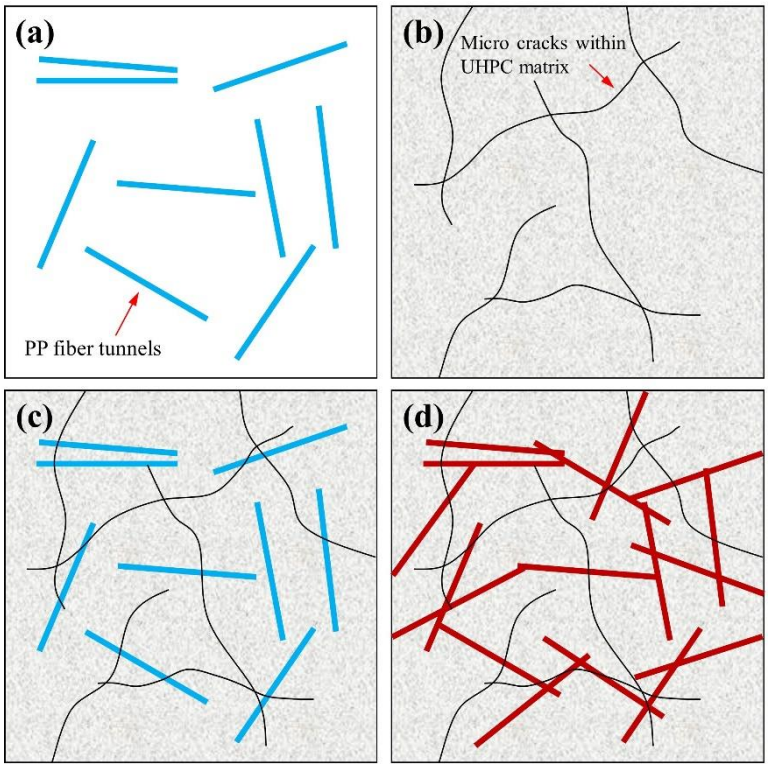

Fig. 7.6. Schematics showing the idealization of PP fiber reinforced UHPC consisting of (a) PP fiber tunnels, (b) microcracks (black) in UHPC matrix (grey background), (c) system with PP fibers isolated, and (d) system with PP fibers connected.

In the current problem, it is challenging to determine the percolation percentage *p*. In the similar problem for predicting electrical conductivity or heat conductivity of polymer matrix composites filled with conductive fibers (Berhan and Sastry 2007, Ma and Gao 2008), the conductive fillers were modeled as a 3-D network of finite sites that are randomly positioned. In these models (Gu 2016, Ma and Gao 2008, Natsuki, Endo and Takahashi 2005, Ogale and Wang 1993), the fibers were considered percolated when the shortest distance between two axes of fibers is smaller than their diameters. This implies fibers can overlap and penetrate with one another, which is not true in reality. In the current study, a correlation between the factor *p* and fibers dosage, average crack width, fiber length, and fiber diameter was established (Eqs. 7.12-7.14) and calibrated with experimental results of groups 1 to 3. The model was then validated by comparing the model results to the experimental results of UHPCs in groups 4 and 5.

For each mix design, the factor *p* can be determined as:

$$p = \min_{p} \left(k_{fm} - k_{test} \right)^2 = \min_{p} \left(p k_{fm}^{p} + \left(1 - p\right) k_{fm}^{np} - k_{test} \right)^2 \tag{7.10}$$

where k_{test} is the measured permeability. *p* can then be determined by solving the following equation

$$\frac{d\left(p k_{fm}^{p} + \left(1 - p\right) k_{fm}^{np} - k_{test} \right)^2}{dp} = 0 \tag{7.11}$$

Thus, *p* can be explicitly obtained as

$$p = \frac{k_{test} - k_{fm}^{np}}{k_{fm}^{p} - k_{fm}^{np}} \tag{7.12}$$

The parameters calculated including *p* are summarized in Table 7.2. The percolation probability *p* significantly increased with increasing fiber dosage (group 1) and length (group 2) but decreased with increasing fiber diameter (group 3). For group 4, the effect of increasing fiber dosage and length superimposed, and *p* increased faster than that in the first

two groups. For the 5th group, even the total number of PP fibers remained constant with proportionally increased fiber diameter and dosage according to Eq. 7.1, p value still decreased. This is because the effect of increasing fiber dosage is canceled by increasing fiber diameter. In addition, as shown in Fig. 7.5, the width of micro cracks decreased. Therefore, fewer fibers were percolated.

Table 7.2. Values of parameters

Mix No.		ϕ (%)	p (%)	k_f (m^2)	k_m (m^2)	k_{fm}^{p} (m^2)	k_{fm}^{np} (m^2)	$k_{fm} = k_{test}$ (m^2)
1	L12D30M1	0.11	0.014	7.03E-12	1.07E-18	7.64E-15	1.07E-18	2.14E-18
	L12D30M3	0.33	0.043	7.03E-12	4.42E-18	2.29E-14	4.44E-18	1.43E-17
	L12D30M5	0.54	0.084	7.03E-12	2.41E-18	3.82E-14	2.43E-18	3.45E-17
2	L6D30M3	0.33	0.011	7.03E-12	6.88E-19	2.29E-14	6.9E-19	3.21E-18
	L12D30M3	0.33	0.043	7.03E-12	4.42E-18	2.29E-14	4.44E-18	1.43E-17
	L18D30M3	0.33	0.16	7.03E-12	8.76E-18	2.29E-14	8.79E-18	4.55E-17
3	L12D30M3	0.33	0.043	7.03E-12	4.42E-18	2.29E-14	4.44E-18	1.43E-17
	L12D50M3	0.33	0.0087	1.95E-11	2.98E-18	6.36E-14	2.99E-18	8.54E-18
	L12D60M3	0.33	0.00016	2.81E-11	1.91E-18	9.17E-14	1.92E-18	2.06E-18
4	L6D30M1.5	0.16	0.0045	7.03E-12	1.82E-18	1.15E-14	1.83E-18	2.34E-18
	L12D30M3	0.33	0.043	7.03E-12	4.42E-18	2.29E-14	4.44E-18	1.43E-17
	L18D30M4.5	0.49	0.22	7.03E-12	4.67E-18	3.44E-14	4.69E-18	8.04E-17
5	L12D30M3	0.33	0.043	7.03E-12	4.42E-18	2.29E-14	4.44E-18	1.43E-17
	L12D50M8.33	0.91	0.0048	1.95E-11	2.85E-18	1.77E-13	2.88E-18	1.18E-17
	L12D60M12	1.30	0.0062	2.81E-11	8.12E-19	3.67E-13	8.22E-19	2.38E-17

The percolation of fibers is strongly dependent on the aspect ratio (l/d) of fibers (Ma and Gao 2008). From Table 7.2, the percolation probability p is also affected by the fiber fraction and the relative permeability of microcracks and fiber tunnels (w^2/d^2). Here we assume fibers with larger diameter can only be considered percolated with wider microcracks. Thus, the following relationship is proposed:

$$p = \alpha\phi(\frac{l}{d})^2(\frac{w^2}{d^2}) = \alpha\phi\frac{w^2l^2}{d^4} \tag{7.13}$$

where α is a constant, ϕ is the fraction of PP fibers, w, l, and d are average crack width, fiber length and fiber diameter, respectively. The coefficient α can be determined by solving the following optimization problem:

$$\alpha = \min_{\alpha} \sum_{i=1}^{7} \left(p_i - p_i' \right)^2 \tag{7.14}$$

By using MATLAB optimization toolbox (The MathWorks 2015), after calibrated by groups 1 to 3 the value of α is 5.82×10^{-4} in this study. Fig. 7.7a shows the correlation between proposed relationship Eq. 7.13 and value of p from experiments. It should be noted that the y axis is in logarithmic scale. The R^2 value is 0.989. Fig. 7.7b shows the validation of Eq. 7.13 by experimental results of groups 4 and 5. A very strong relationship is indicated by R^2 value of 0.992. Fig. 7.8 shows the estimated k_{fm} in Eq. 7.9 against the measured permeability by using the proposed p. The R^2 value is 0.88.

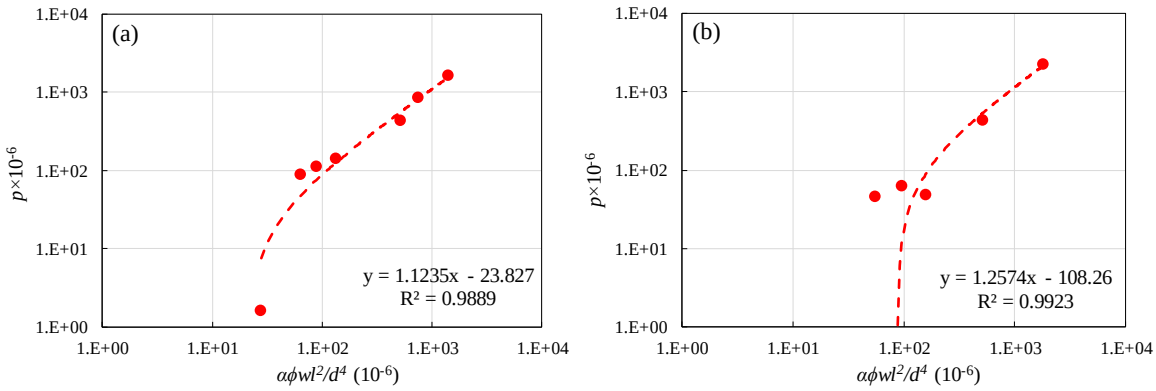

Fig. 7.7. Percolation probability against fiber and crack parameters (a) p calibrated by groups 1 to 3, (b) p validated by groups 4 and 5.

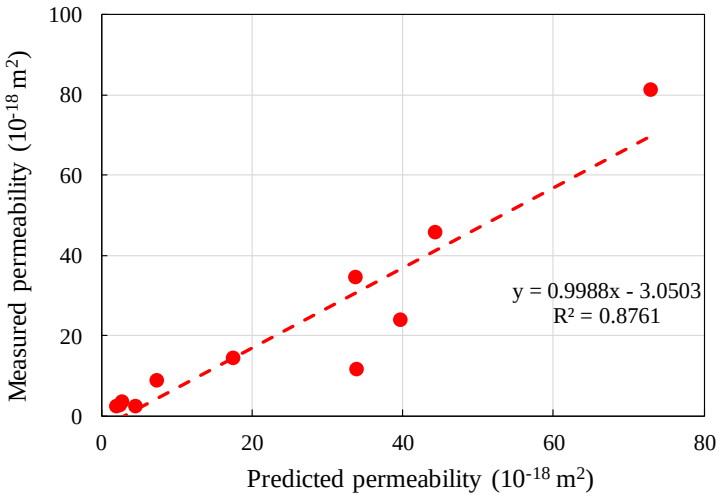

Fig. 7.8. Comparison between the measured and estimated permeability of UHPC.

Another important conclusion can be drawn from the results is that when connectivity of PP fibers is low, the residual permeability of UHPC is determined by the permeability of the cracked UHPC matrix. For example, L12D60M3 with very small percolation probability of 0.00016% from Table 7.2, the measured permeability $k_{test} = 2.06\times10^{-18}$ approached to the permeability of the cracked UHPC matrix ($k_m = 1.91\times10^{-18}$). As shown in Fig. 7.9, with the percolation probability p approaches zero, the difference between the measured permeability and the permeability of the cracked UHPC matrix k_m approaches 0.

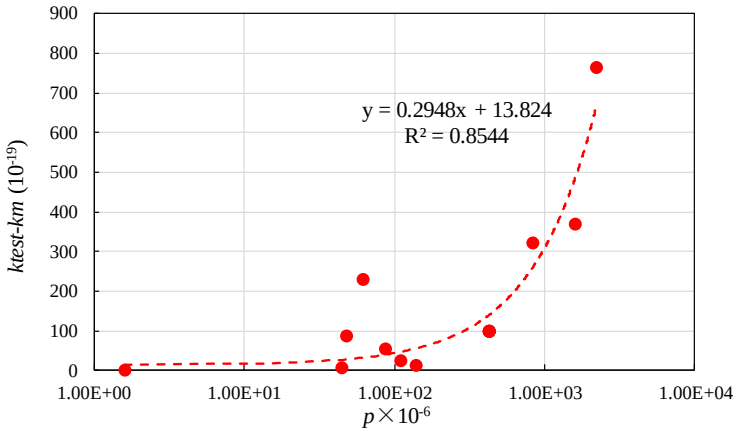

Fig. 7.9. Difference between the measured permeability and the permeability of matrix-microcrack phase varies with percolation probability.

Clearly, to estimate the permeability of UHPC, more work is needed to characterize the way in which fiber tunnels and microcracks in UHPC are connected. Better estimations of the void distribution can be obtained by using advanced three-dimensional imaging techniques such as FIB-Nano tomography, synchrotron computed tomography or confocal microscopy (Wong, Zimmerman and Buenfeld 2012). With the help of 3D microtomographic images, the skeleton of voids can be extracted, and 3D model can be built to simulate the permeation of liquid through the microstructure of UHPC. However, currently FESEM is the most practical method to obtain high resolution images for a relatively large sample. Besides, the simplicity and efficiency of FESEM is much greater compared to three-dimensional imaging techniques.

7.5 Summary

The effect of fiber fraction, geometry, and induced microcracks on the intrinsic residual permeability of UHPC after exposure to 200 °C were investigated based on permeability measurements, microstructure analysis, and image processing. A method for identification and quantification of microcrack characteristics in epoxy impregnated UHPC samples was elaborated. Microcracks of 0.5 μm width can be detected. The proposed method provides a quantitative determination of the microcrack density, average crack width, and crack volume fraction. A model based on fiber parameters and microcrack parameters was proposed to predict residual permeability of UHPC.

Permeability of UHPC was significantly influenced by fiber fraction and geometry of PP fiber. The measured permeability spanned from 2.06×10^{-18} to 80.40×10^{-18} m^2 (almost 40 times). Increasing the fiber length has greater beneficial effect on permeability compared to increasing fiber diameter. Longer PP fibers will result in a higher probability of percolation. From the permeability model, probability of percolation of fiber tunnels is a key parameter for permeability of UHPC. When the percolation probability approaches zero, the residual permeability of UHPC is mainly determined by the permeability of the matrix-microcrack phase in UHPC.

Chapter 8 Effects of Factors on Residual Permeability and Explosive Behavior of UHPC

8.1 Overview

Permeability is an important factor influencing spalling, which is a measure of the ability of a porous material to transfer fluids under pressure gradient. This chapter proves the correlation between permeability of UHPC and extent of explosive spalling through experiments. Independent and synergistic effects of PP and steel fibers, and PP fibers and larger aggregates on residual intrinsic permeability, spalling extent, weight loss, tensile strength, and compressive strength of UHPC are investigated. Spalling resistance of 16 UHPCs with the addition of PP and/or steel fibers and 9 UHPCs with addition of PP fibers and larger aggregates was tested under 1-hour ISO 834 fire. Intrinsic permeability of UHPC was measured by RILEM-CEMBUREAU method (Kollek 1989) and calculated by adopting Klinkenberg method (Klinkenberg 1941) at residual state. Microstructures of UHPCs before and after elevated temperature exposure were investigated to reveal potential mechanisms responsible for changes in permeability and differences in spalling extent.

8.2 Experimental program

8.2.1 Mix proportions and materials

Table 8.1 and Table 8.2 summarize the mix proportions for investigating different combinations of PP and/or steel fibers and PP fibers and/or larger aggregates on spalling protection, respectively. The UHPC matrix consisted of cement, silica fume, fine aggregate, and micro silica sand. A water-to-binder (W/B) ratio of 0.2 was used to achieve dense packing and high strength. Superplasticizers were used to achieve adequate workability. The 16 UHPC mix designs in Table 8.1 were named as UHPC Px-Sy, where x and y indicate the respective content of PP and steel fibers. The 9 UHPCs in Table 8.2 were named as UHPC Px-Ay, where x and y indicate the content of PP fibers in kg/m^3 and aggregate size in mm, respectively.

Table 8.1. Mix proportions of UHPCs with PP and steel fibers

UHPC	Relative mass ratio to cement						PP (kg/m^3)	S (kg/m^3)	f'_c (MPa)	f'_t (MPa)
	C[a]	AG	SS	SF	SP	W/B				
P0-S0	1.0	1.1	0.25	0.25	0.04	0.20	0	0	147.0±4.3	8.5±3.0
P0-S79	1.0	1.1	0.25	0.25	0.04	0.20	0	79	145.5±5.0	10.6±1.6
P0-S157	1.0	1.1	0.25	0.25	0.04	0.20	0	157	147.5±3.4	10.4±2.0
P0-S236	1.0	1.1	0.25	0.25	0.04	0.20	0	236	165.7±1.9	9.8±1.2
P2-S0	1.0	1.1	0.25	0.25	0.04	0.20	2	0	147.2±4.9	8.7±1.1
P2-S79	1.0	1.1	0.25	0.25	0.04	0.20	2	79	150.5±5.0	10.5±0.2
P2-S157	1.0	1.1	0.25	0.25	0.04	0.20	2	157	142.2±4.2	10.4±1.3
P2-S236	1.0	1.1	0.25	0.25	0.04	0.20	2	236	160.4±2.7	11.0±0.2
P4-S0	1.0	1.1	0.25	0.25	0.04	0.20	4	0	141.2±5.4	10.8±1.7
P4-S79	1.0	1.1	0.25	0.25	0.04	0.20	4	79	145.9±4.5	10.7±0.1
P4-S157	1.0	1.1	0.25	0.25	0.04	0.20	4	157	150.6±1.0	9.7±0.8
P4-S236	1.0	1.1	0.25	0.25	0.04	0.20	4	236	155.9±1.3	11.2±0.8
P6-S0	1.0	1.1	0.25	0.25	0.04	0.20	6	0	139.0±2.1	10.7±0.8
P6-S79	1.0	1.1	0.25	0.25	0.04	0.20	6	79	146.2±8.2	10.2±1.8
P6-S157	1.0	1.1	0.25	0.25	0.04	0.20	6	157	146.8±1.2	10.1±0.7
P6-S236	1.0	1.1	0.25	0.25	0.04	0.20	6	236	160.2±1.5	10.7±0.3

Table 8.2. Mix proportions of UHPCs with PP fibers and larger aggregates

UHPC	Relative mass ratio to cement						PP fiber (kg/m^3)	Aggregate size (mm)	f_c (MPa)
	C[a]	AG	SS	SF	SP	W/B			
P0-A0.6	1.0	1.1	0.25	0.25	0.04	0.20	0	0.6	126.2
P0-A2.3	1.0	1.1	0.25	0.25	0.04	0.20	0	2.3	126.8
P0-A5.0	1.0	1.1	0.25	0.25	0.04	0.20	0	5.0	124.3
P2-A0.6	1.0	1.1	0.25	0.25	0.04	0.20	2	0.6	121.1
P2-A2.3	1.0	1.1	0.25	0.25	0.04	0.20	2	2.3	121.4
P2-A5.0	1.0	1.1	0.25	0.25	0.04	0.20	2	5.0	140.0
P4-A0.6	1.0	1.1	0.25	0.25	0.04	0.20	4	0.6	123.3
P4-A2.3	1.0	1.1	0.25	0.25	0.04	0.20	4	2.3	126.6
P4-A5.0	1.0	1.1	0.25	0.25	0.04	0.20	4	5.0	135.1

[a] C: cement, AG: aggregates, SS: silica sands, SF: silica fume, SP: superplasticizer, W/B: water-to-binder ratio, PP: polypropylene fibers, S: steel fibers. Binder consists of cement and silica fume.

Portland cement, fine aggregate, silica sand, silica fume, and superplasticizer were described in Section 0. Monofilament cylindrical PP fibers with a length of 12 mm and a diameter of

30 μm were supplied by DFL. Micro steel fibers with a length of 13 mm and a diameter of 2.2 mm were supplied from Dramix@.

The mixing and curing procedure was shown in Section 0. The fresh UHPC mixtures were then cast into cubes (50×50×50 mm^3), dog bones (36×18 mm^2 cross section), cylinders (Ø75 mm×150 mm), and discs (Ø150 mm×48 mm) for compressive strength, uniaxial tensile, spalling, and permeability tests, respectively. After curing, the surfaces of cylindrical discs (Ø150 mm×48 mm) were smoothened by grinding from two ends to 40 mm thick.

8.2.2 Explosive spalling test

UHPC specimens were subjected to the standard heating curve of ISO-834 produced by an electrical heating furnace. After 1-hour spalling test, the cylinders were cooled down to ambient temperature inside the furnace. The surfaces of specimens were observed, and weights of specimens were recorded before and after heating. At least three specimens were tested for each mix. In real situations, heating rate might be different from ISO-834 heating and structures are often under restraint, which will change the development of mechanical properties and permeability. However, the furnace heating provides a controllable approach for comparison purpose of concrete materials. Mechanisms of spalling are easier to be analyzed in this situation.

Fig. 8.1. Specimens in furnace.

8.2.3 Experimental methods

The device and method to measure permeability was shown in Section 6.2.2. 200 °C was chosen as the temperature to identify the effect of permeability on spalling resistance because Kalifa, Chene and Galle (2001) noticed that main change of permeability is between 80 °C and 200 °C. Specimens were heated to 200 °C and kept for 48 hours to remove free water from the specimens. The heating rate was lower than 1 °C/min to prevent undesirable temperature gradients inside the specimens. After heating, the specimens were cooled down naturally within the furnace. At least three specimens were tested for each mix and the average value and the standard deviation were reported.

The method to test compressive strength was shown in Section 3.2.4. Uniaxial tensile strength tests were carried out by means of an electro-mechanical testing machine with a tensile capacity of 30 kN. A personal computer was connected to the testing machine to acquire the test data. The tests were displacement-controlled at a rate of 0.2 mm/min. The compressive and tensile strength are shown in Table 8.1 and Table 8.2. The inclusion of PP fibers did not enhance the tensile and compressive strength of UHPC. Addition of steel fibers only marginally increased the tensile strength but improved the compressive strength of UHPC significantly.

Microstructures of UHPC samples before and after elevated temperature exposure were examined by means of a field emission scanning electron microscope (FESEM, JSM-7600F, JEOL). Samples were cut from cube specimens by a diamond saw to about 10×10×3 mm^3 and ground with emery papers. Samples were heated to 200 °C at a heating rate of 1 °C/min. The targeted temperature was held for 10 hours. Control samples (without exposing to elevated temperature) were prepared by oven-drying the samples at 105 °C for 24 hours to remove evaporable water. All samples were coated with platinum for 30 s under vacuum. Secondary electron imaging (SEI) was used to probe surface morphology and backscattered electron imaging (BEI) was used to reveal micro cracks.

8.3 Results and discussion

8.3.1 Extent of spalling and weight loss

Fig. 8.2 shows the spalling extent of UHPC specimens with different PP and steel fiber contents after ISO 834 heating. The control specimen P0-S0 suffered severe spalling. The debris were flake-like and the size of debris was smaller than 2 cm with thickness smaller than 5 mm indicating shallow spalling. The addition of steel fibers (up to 236 kg/m^3) alone did not provide protection from explosive spalling, even as shown in Fig. 4.1, steel fibers increased the tensile strength of UHPC to more than 200 MPa after heated to 300 °C. As shown in Fig. 8.2, UHPCs with only steel fibers (i.e. P0-Sy, y=0-236) completely disintegrated into small pieces.

The addition of PP fibers alone is moderately effective. As can be seen, extent of spalling of UHPC decreased with increasing PP fiber content (up to 6 kg/m^3). Debris of P2-S0 was larger than the debris of control (P0-S0), which indicates that addition of PP fibers helps to reduce pore pressure by releasing internally trapped moisture and vapor. However, 2 kg/m^3 of PP fibers was not sufficient to prevent explosive spalling. With higher dosage of PP fibers, P4-S0 and P6-S0 did not show spalling. Instead, macrocracks were observed in the radial direction of the cylinders and the specimens disintegrated into several sections. Formation of these macro cracks created free surfaces for water vapor to release. Besides, PP fibers induced micro channels, and these channels also helped to release trapped vapor and enhanced spalling resistance. The critical PP fiber content to completely prevent spalling is 4 kg/m^3 in the present study, much higher than the recommended content for 80 MPa in HSC (1 kg/m^3) (Debicki, Haniche and Delhomme 2012). The higher dosage of PP fibers is probably due to the denser matrix of UHPC, which does not contain much porous interface transition zone (ITZ) (Wang, Jacobsen, He, Zhang, Lee and Lein 2009). It is worth noting that, as shown in Table 3.9 and Table 8.1, PP fibers did not increase tensile strength of UHCP significantly. Therefore, this is not the main function of inclusion of PP fibers.

The combined use of PP and steel fibers effectively prevented spalling and enhanced integrity of UHPC specimens, even the mechanical properties were not enhanced significantly. For P2-S79, spalling occurred on the surface and the core of the specimens

remained intact. For P2-S157 and P2-S236, minor spalling was observed only at the corner. The spalled pieces did not fall off from the specimen due to bridging effect of steel fibers, which prevented further spalling and maintained specimen integrity. For other specimens with higher PP and steel fiber dosage (Px-Sy; x = 4, 6; y = 79, 157, 236), explosive spalling was completely avoided, and the specimens remained intact after heating.

Fig. 8.2. Spalling extent of UHPCs with different PP and/or steel fibers after exposing to elevated temperature.

Fig. 8.3 shows the spalling behavior of UHPC samples with various PP fiber fractions and aggregate sizes after subjected to ISO 834 fire. As shown, the control specimen P0-A0 suffered severe spalling. The debris were flake-like and the size was smaller than 5 cm. The increase of aggregate size to 5 mm alone did not decrease the extent of spalling. UHPC mixtures with only increasing aggregate size (i.e. P0-Ay, y=0.6-5)) completely disintegrated

into small pieces. On the contrary, the addition of PP fibers alone is effective for preventing spalling. The observation is similar to the phenomenon shown in Fig. 8.2. The combined use of PP fibers and larger aggregates is beneficial for preventing spalling. As can be seen, debris left by P2-A2.3 were larger than the debris of P0-A2.3 and P2-A0.6, which indicates that addition of both PP fibers and larger aggregates helps to mitigate spalling. For other samples with higher PP fiber contents and larger aggregate sizes i.e. P2-A5, P4-A2.3, and P4-A5, explosive spalling was completed prevented and the samples remained intact.

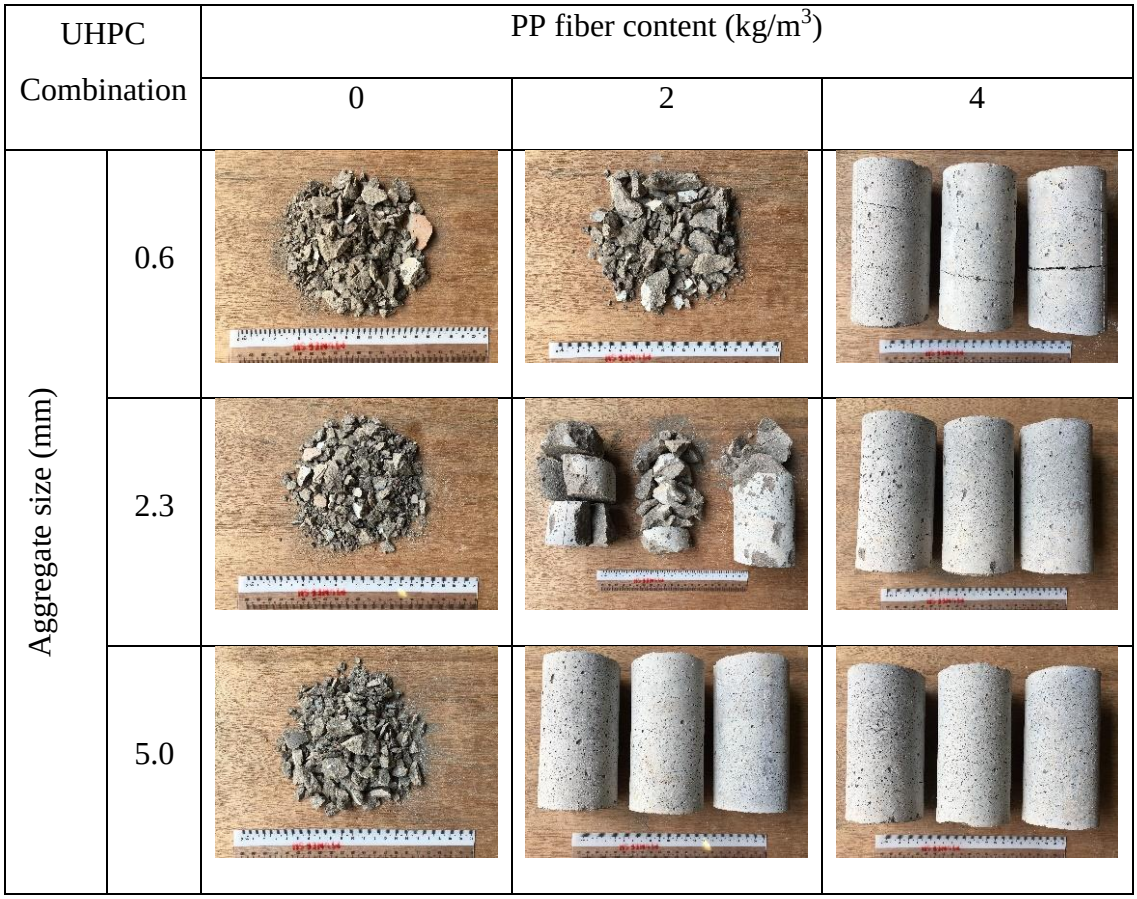

Fig. 8.3. Spalling extent of specimens with different PP fiber content and aggregate size after spalling test.

After spalling tests, weights of the largest remaining parts of UHPC specimens were measured to calculate weight loss ratio (Fig. 8.4). Clearly, weight loss is proportional to the extent of spalling (Fig. 8.2 and Fig. 8.3). According to Heo et al. (Heo, Sanjayan, Han and Han 2010), 20% weight loss (inclusive of moisture loss) was taken as the threshold for severe spalling of UHPC. For Px-Sy, the highest weight loss was found in control specimens (P0-

S0) with weight loss of nearly 100%, followed by UHPCs with only steel fibers with weight loss more than 80%. For UHPCs containing only PP fibers, weight loss reduced with increasing fiber dosage. At a PP fiber content of 6 kg/m^3 (P6-S0), the residual weight of specimens was 60.3%. As can be seen, weight loss of UHPCs with hybrid PP and steel fibers was dramatically reduced. At the lowest content of hybrid fibers, the weight loss of P2-S79 was 28.6%. At higher combination dosage, spalling was totally suppressed with a weight loss of 11.1 to 15.5%, which was mainly attributed to the loss of moisture and decomposition of hydration products.

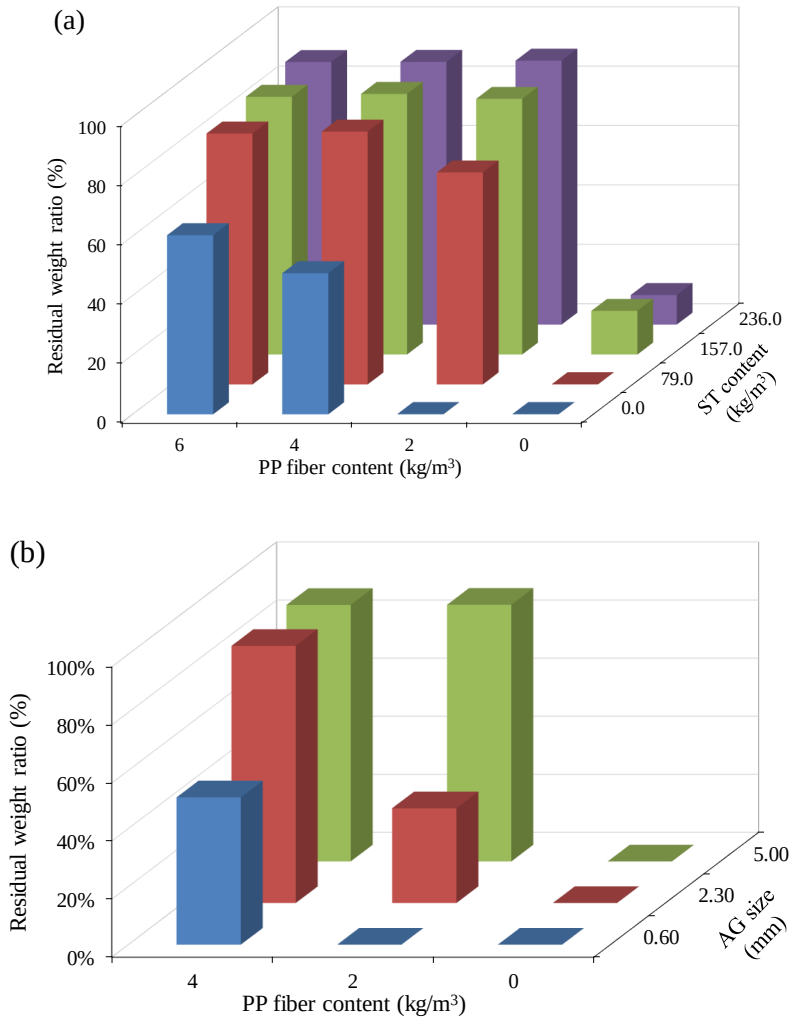

Fig. 8.4. Weight loss of UHPC specimens with (a) different PP and/or steel fibers contents (b) different PP contents and aggregate sizes after spalling test.

From Fig. 8.4b, for P0-A0.6/2.3/5.0, the remnant weights were found to be nearly 0%. For P2-A0.6, the spalling was also severe and almost no weight remained. For UHPCs contained 4 kg/m^3 PP fibers but the smallest aggregates (P4-A0.6), spalling was prevented but only 50.7% weight remained, which is due to the samples disintegrate into several sections. As shown, the remnant weight of the samples with both PP fibers and larger aggregates was dramatically increased. For P2-A2.3, the residual weight was 32.7%. At higher PP fiber content and aggregate size, spalling was totally suppressed with a remnant mass ratio of 88.3 to 88.6%.

8.3.2 Gas permeability

Fig. 8.5 shows the results of intrinsic residual permeability (in logarithmic scale) of UHPC mixes. As can be seen, sole addition of PP fibers significantly increased permeability of UHPC. Permeability increased almost linearly from around 7.3×10^{-19} to 4.9×10^{-17} m^2 with increasing PP fiber content from 0 to 6 kg/m^3. At 4 kg/m^3 PP fiber addition, spalling was prevented (Fig. 8.2) and the resulting UHPC has a residual intrinsic permeability of 1.89×10^{-17} m^2 (Fig. 8.5). However, addition of steel fibers alone reduced the intrinsic permeability. As shown in Fig. 8.5a, the permeability of P0-Sy (y = 79, 157, 236) was lower than that of P0-S0. This may be attributed to the reduction of shrinkage-induced cracking during curing stage in UHPC samples because of the addition of steel fibers (Sun, Chen, Luo and Qian 2001, Wong, Zobel, Buenfeld and Zimmerman 2009). The permeability of P0-Sy (y = 79, 157, 236) increased slightly with increasing steel fiber dosage. This may be caused by more entrapped air voids due to lower workability (Wille, Naaman, El-Tawil and Parra-Montesinos 2011). The combined use of PP and steel fibers in UHPC resulted in a significant increase of permeability. As can be seen, the intrinsic permeabilities of UHPCs with hybrid PP and steel fibers (Px-Sy; x = 2, 4, 6; y = 79, 157, 236) are at least three orders greater than that of UHPC with only steel fibers (P0-Sy; y = 79, 157, 236) and one order higher than that of UHPC with only PP fibers (Px-S0; x = 2, 4, 6).

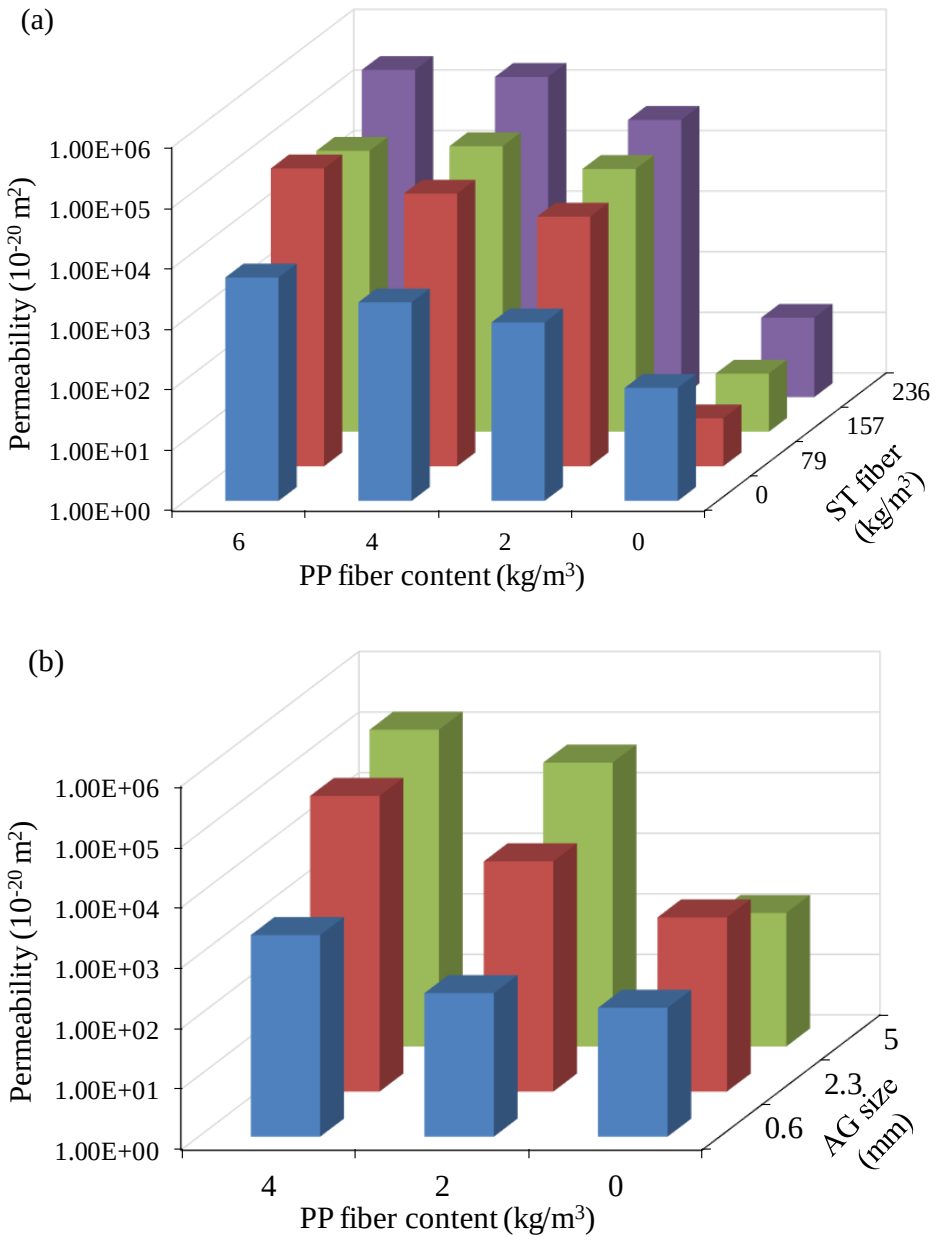

Fig. 8.5. Permeability of specimens after exposure to 200 ºC (a) UHPC with PP and steel fibers (b) UHPC with PP fibers and larger aggregates.

Fig. 8.5b shows the results of residual permeability (in logarithmic scale) of UHPC mixtures with PP fibers and larger aggregates. Only increasing aggregate size did not increase the intrinsic permeability significantly. The combined use of PP fibers and larger aggregates in UHPC resulted in significant increase of permeability. The intrinsic permeability of UHPCs

with both PP fibers and larger aggregates (Px-Ay; x=2, 4; y=2.3, 5.0) are much greater than that of UHPC with only PP fibers or larger aggregates.

Combining the two sets of tests together, Fig. 8.6 plots the weight loss of UHPC specimens against the residual permeability. It can be clearly seen that UHPCs in this study spalled completely when the permeability was lower than 1.0×10^{-17} m^2. Weight loss reduced with increasing residual permeability from 1.0×10^{-17} to about 1.7×10^{-16} m^2. At higher permeability beyond 2.2×10^{-16} m^2, spalling was completely prevented. This indicates permeability of material governs performance of UHPC against explosive spalling and it is an objective parameter to study spalling behavior of material at elevated temperature.

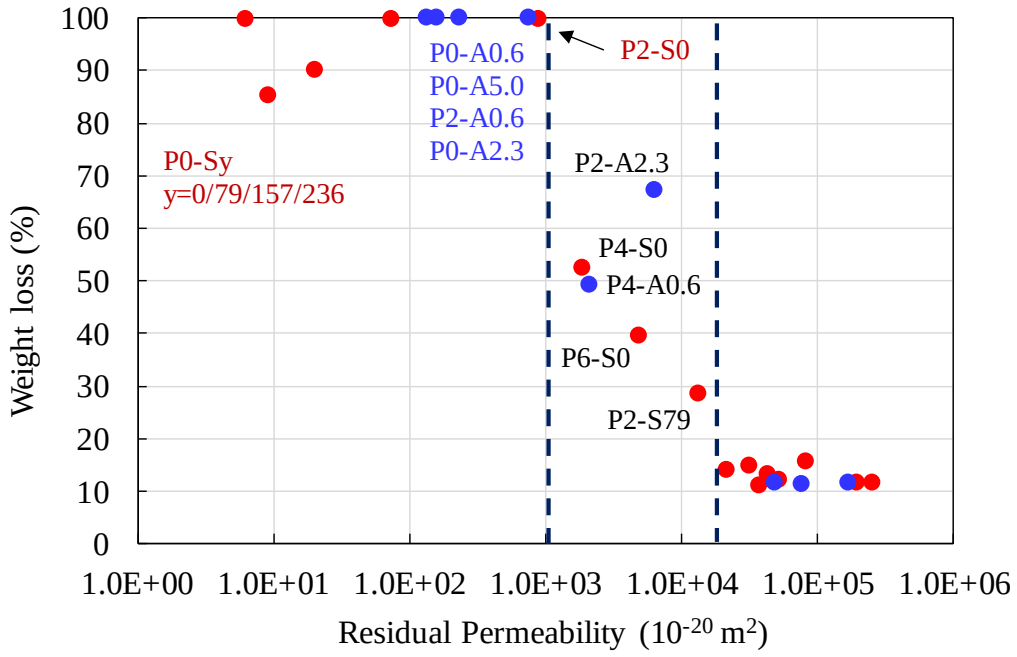

Fig. 8.6 Weight loss as a function of residual permeability of samples.

8.3.3 Microstructure investigation

Fig. 8.7 shows the micrograph of UHPC with only PP fibers (P6-S0) before and after heating at 200 °C. As can be seen, after 200 °C heating, PP fibers disappeared completely (leaving behind fiber tunnels) and microcracks were formed in the radial direction of the fiber tunnel

(Fig. 8.7 b). This is mainly attributed to melting of PP fibers and expansion of polypropylene at elevated temperature. Coefficient of thermal expansion (CTE) of polypropylene is 210×10^{-6}/°C at 100 to 140 °C, which is more than 10 times greater than that of concrete (Khoury and Willoughby 2008). In addition, UHPC matrix will shrink with losing of humidity. Expansion of PP fibers caused significant tensile stress in the tangential direction along the fiber/matrix interface and thus microcracks were formed along the radial direction of fiber tunnel. Microcracks with width of 5 μm can be observed, and they were wide enough to let water vapor path through. These microcracks connected fiber tunnels and created an inter-connected network, which increased permeability of UHPC at elevated temperature.

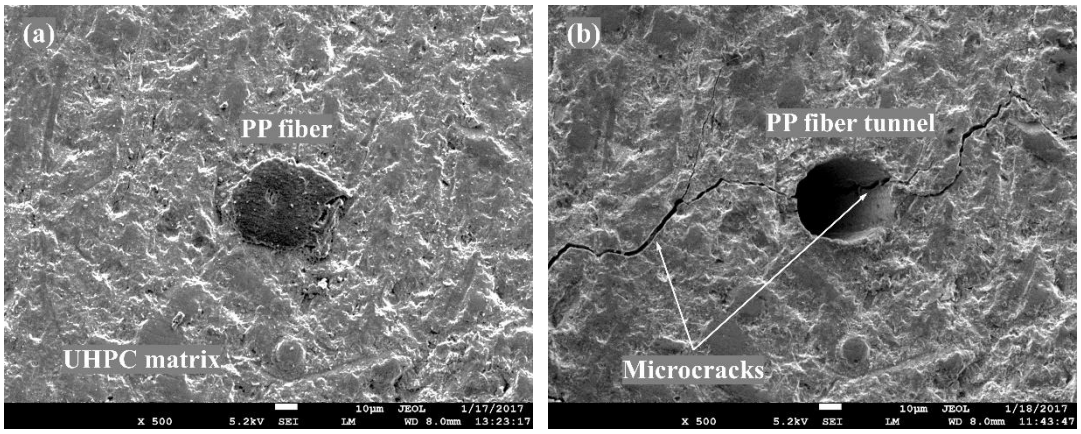

Fig. 8.7. Micrographs of UHPC with only PP fibers (P6-S0) (a) before and (b) after exposure to 200 °C.

Fig. 8.8a shows the cross section of UHPC with only steel fibers (P0-S236) before and after exposure to 200 °C. As can be seen, steel fibers remained in the UHPC matrix after heating. Microcracks resulting from thermal incompatibility between steel fiber and UHPC matrix were observed along the radial direction of the embedded steel fibers (Fig. 8.8 b). Formation of microcracks, however, did not increase permeability of UHPC significantly as compared to that of control (P0-S0, Fig. 8.5). This may be due to the microcracks were not well percolated, and besides, steel fibers could not melt and there was no formation of fiber tunnels in these specimens. Thus permeability was governed by the transport properties of the UHPC matrix (Abyaneh, Wong and Buenfeld 2016).

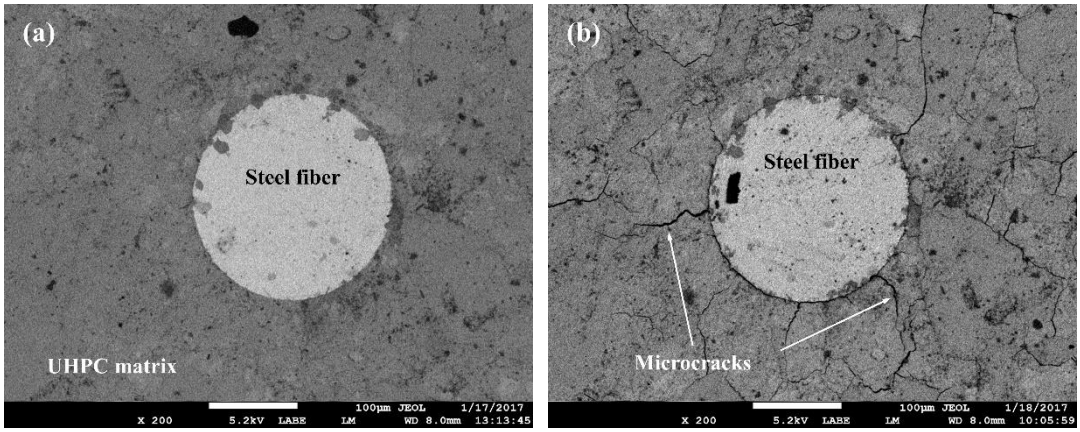

Fig. 8.8. Micrographs of UHPC with only steel fibers (P0-S236) (a) before and (b) after exposure to 200 °C.

Fig. 8.9 shows UHPC with both PP and steel fibers (P6-S236) before and after exposure to 200 °C. As can be seen, fiber tunnels (due to melting of PP fibers) were well connected by multiple microcracks (along the radial direction of fiber/matrix interface due to thermal expansion of PP fibers and incompatibility between steel fibers and UHPC matrix), which results in higher permeability of UHPC at elevated temperature (Fig. 8.5). This highlights the synergistic effect of hybrid PP and steel fibers, which significantly increased the permeability of UHPC at elevated temperature as compared to UHPCs with only PP or steel fibers.

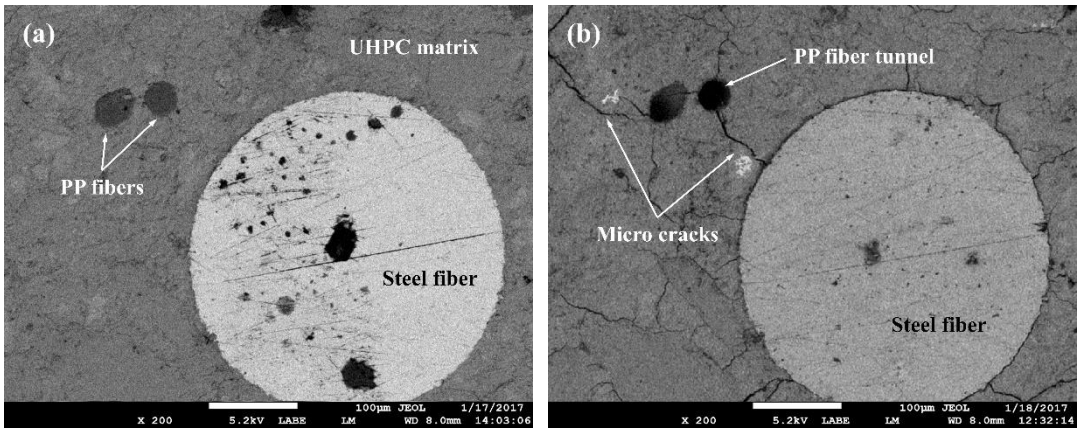

Fig. 8.9. Micrographs of UHPC with both PP and steel fibers (P6-S236) (a) before and (b) after exposure to 200 °C.

Fig. 8.10 shows the synergistic effect of PP fibers and larger aggregates. The large aggregate debond from the matrix after heating due to CTE of aggregates are generally lower than that of cement paste (Mehta and Monteiro 2006, Sellevold and Bjøntegaard 2006, Shui, Zhang, Chen and Xuan 2010, Zunino, Castro and Lopez 2015). However, no micro cracks were observed alone the small aggregates-cement paste interface. This observation is in agreement with the previous findings that very small aggregate particles (less than 1 mm) cause negligible bond failure between the aggregate and the matrix (Idiart, Bisschop, Caballero and Lura 2012). The inclusion of larger aggregates facilitates the formation of micro cracks. Therefore, fiber tunnels were well connected by multiple micro cracks, which results in higher permeability of UHPC. This highlights the synergistic effect of combined used of PP fibers and larger aggregates.

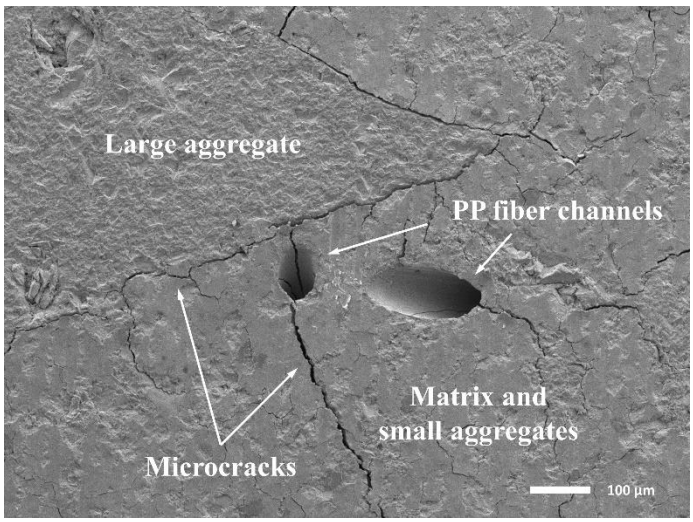

Fig. 8.10. Micrographs of UHPC with both PP fibers and larger aggregates after exposure to 250 °C.

Fig. 8.11 illustrates conceptually the microstructure of UHPCs with PP fibers, steel fibers, and larger aggregates after elevated temperature according to the SEM findings. As discussed above, microcracks were formed due to larger thermal expansion of PP fiber and thermal incompatibility between steel fiber/aggregates and hardened UHPC matrix. Microcracks initiated in the high stress region and propagated into UHPC matrix to release stresses (Abyaneh, Wong and Buenfeld 2016). For UHPC with only PP fibers, microcracks and fiber tunnels formed inter-connected network (Fig. 8.11a). For UHPC with only steel

fibers or larger aggregates, the thin microcracks were not so well percolated (Fig. 8.11b), and the residual permeability did not significantly increase since it was governed by that of UHPC matrix (Abyaneh, Wong and Buenfeld 2016). When both PP and steel fibers or PP fibers and larger aggregates were used together, as shown in Fig. 8.11c, empty PP fiber tunnels were well connected by microcracks. The enhanced connectivity of fiber tunnel by multiple microcracks significantly increased permeability of UHPC and released trapped vapor pressure, which highlighted the synergistic effect of hybrid PP and steel fibers and PP fibers and larger aggregates in UHPC at elevated temperature.

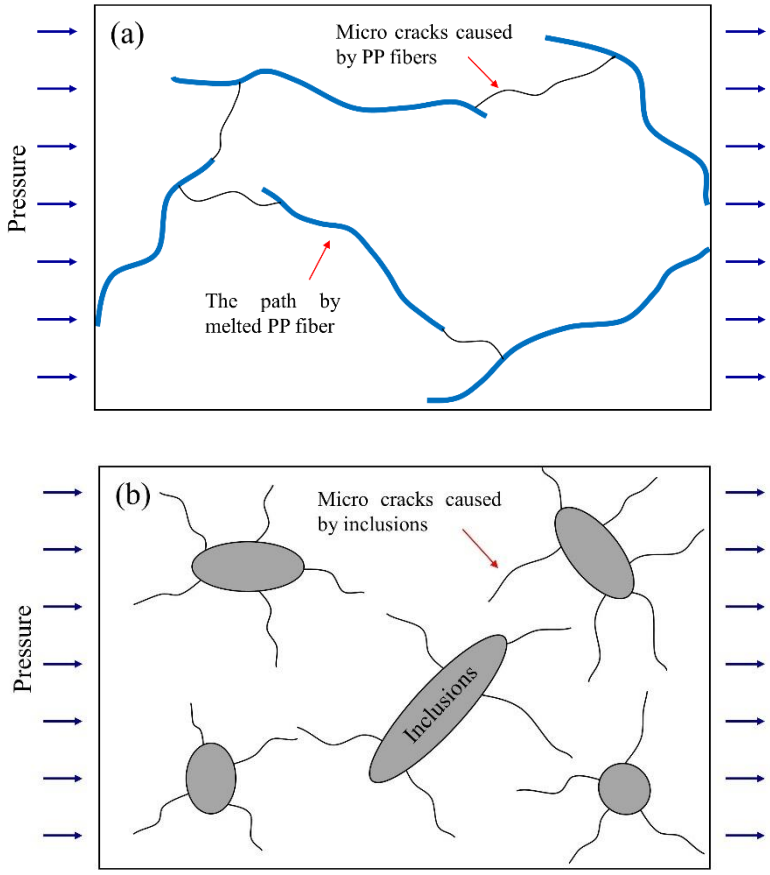

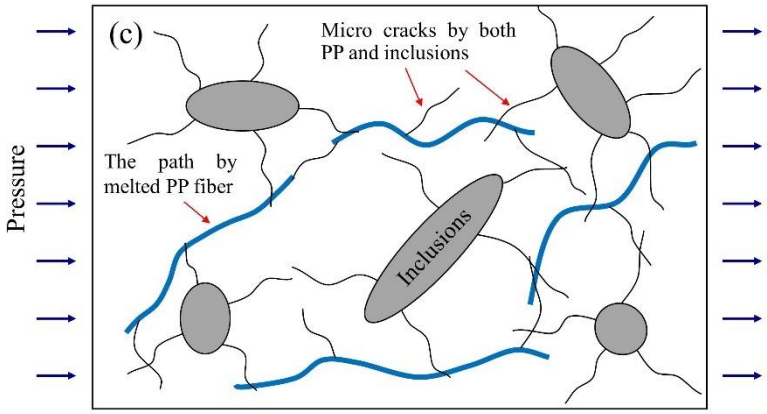

Fig. 8.11 Conceptual illustration of microstructure of UHPC with (a) PP fibers, (b) steel fibers, and (c) hybrid PP and steel fibers after heating.

8.4 Summary

In this chapter, permeability of UHPC was measured and quantitatively correlated to the extent of spalling. Synergistic effects between PP and steel fibers, and PP fibers and larger aggregates on explosive spalling prevention of UHPC were found for the first time to the author's best knowledge. Microstructure of UHPC before and after elevated temperature exposure were examined to reveal potential mechanisms responsible for changes in permeability. Results showed that control specimen suffered severe explosive spalling due to its dense microstructure. The addition of steel fiber or larger aggregate on their own did not provide any protection against explosive spalling, while the inclusion of 4 kg/m^3 of PP fiber suppressed explosive spalling of UHPC, which is higher than the dosage required in Eurocode 2 (2 kg/m^3). The use of hybrid PP and steel fibers, and combined PP fibers and larger aggregates completely prevented explosive spalling even at low fiber dosage due to a significant increase in permeability. Weight loss due to spalling reduces proportionally with increasing permeability of UHPC. Thus, permeability of material was proven governs performance of UHPC against explosive spalling. UHPC samples spalled completely with permeability lower than 1.0×10^{-17} m^2. In contrast, explosive spalling was prevented when residual permeability exceeded 2.2×10^{-16} m^2, which is in the same order of magnitude with that of normal concrete. These values can provide references for evaluation of spalling risk

of concrete. Microstructural analyses revealed that such synergistic effect on increased permeability was attributed to enhanced connectivity of empty PP fiber tunnels by multiple microcracks generated from thermal expansion and incompatibility of PP fiber, steel fibers, and larger aggregates.

Chapter 9 Conclusions and Future Work

9.1 Conclusions

Although UHPC has exceptional mechanical properties and durability at ambient temperature, the slenderer design of UHPC structural members and higher susceptibility of explosive spalling highlight the necessity to investigate UHPC under fire condition. This thesis aims to investigate the behavior of UHPC under elevated temperature. For this purpose, experimental studies on mechanical properties, transport properties, and spalling behavior were conducted. The main conclusions of the study are summarized below, reflecting the objectives and scope of work presented in Chapter 1:

Effects of steel fibers, PP fibers, PE fibers, aggregate size on mechanical performance of UHPC at ambient and at elevated temperature (Chapter 3 to Chapter 5).

- Among the factors investigated, the most important parameter affecting mechanical properties of UHPC is steel fiber.
- The average residual strength of UHPC mixtures increased significantly after exposure to 300 °C, which was attributed to further hydration of unhydrated cement clinkers. After increasing the temperature to 600 °C and 900 °C, a sharp loss of compressive strength was observed due to decomposition of cementitious compound C-S-H (from 450 to 500 °C) and α to β-phase transformation of quartz sand.
- The effect of water quenching on compressive strength of all the UHPC mixtures was significant at all temperature levels. The reduction of strength was mainly attributed to physical formation of further microcracks as a result of thermal shock to the samples but not change of hydration products.
- Hybrid PE fibers and steel fibers effectively improved flexural performance of UHPC. Increasing water-to-binder ratio from 0.2 to 0.3 resulted in a significant reduction of mechanical properties. In contrast, larger aggregates significantly improved first-crack strength, peak strength, and toughness.

Effects of steel fiber, PP fiber, and aggregate size on permeability of UHPC (Chapter 6 and Chapter 7).

- Inclusion of PP fibers significantly increased permeability of UHPC.
- Permeability of UHPC was significantly influenced by fraction and geometry of PP fibers. The increase of fiber fraction led to an increase in permeability. Increasing the fiber length had greater beneficial effect on the increase of permeability compared to increasing the fiber diameter.
- The combined use of PP fibers and larger aggregates and PP fibers and steel fibers showed synergistic effect and resulted in significant increase of permeability at elevated temperature. This is mainly attributed to the formation of interconnected micro-crack networks.
- A method was developed for identification and quantification of microcracks in heated UHPC samples. Probability of percolation of fiber tunnels was found to be a key parameter for residual permeability of UHPC. Longer PP fibers and higher fiber fraction will result in a higher probability of percolation.

Spalling behavior of UHPC with individual and combined PP fibers, steel fibers, PE fibers, and larger aggregates (Chapter 5 and Chapter 8).

- The addition of steel fibers or larger aggregates alone did not provide protection against explosive spalling, while the inclusion of 4 kg/m^3 of PP fibers suppressed explosive spalling of UHPC.
- The use of hybrid PP fibers and steel fibers and PP fibers and larger aggregates completely prevented explosive spalling even at low fiber dosage due to a significant increase in permeability.

- Residual permeability was found have direct relationship with spalling extent. The limits of completed spall and no spalling are 1.0×10^{-17} m^2 and 2.2×10^{-16} m^2, respectively.
- PE fibers cannot prevent spalling, due to micro cracks formed by PE fibers are much narrower than those caused by PP fibers. Moreover, viscosity of PE fibers is higher than that of PP fibers at elevated temperature. Therefore, it is more difficult for the interconnected network to be percolated.

9.2 Future work

While the research work in this thesis reduced the knowledge gaps identified in Chapter 2, based on the experimental findings, the following items are to be studied further:

1. Currently, the spalling results of concrete from specially designed test setups cannot directly represent fire resistance of concrete structures. It is promising to develop a standard test setup to include important factors. A "non-dimensional spalling index" evaluating the spalling risks of concrete based on quantifiable factors is needed.

2. Continuation of the research on explosive spalling of UHPC should rely on both numerical and experimental studies. Numerical investigations should be developed considering the coupled thermo-hygral-mechanical problem. The saturated zone in concrete during the heating process should be considered. Failure criterion for explosive spalling should be defined, since fracture of concrete is not controlled by a simple strength criterion. Simultaneous measurements of temperature, pore pressure, and thermal stress during fire exposure should be conducted to validate the numerical model.

3. Almost none of the pore pressure measurement was conducted on UHPC including silica fume, which is known to decrease permeability of concrete significantly. It would be interesting to analyze the pore pressure development within UHPC with

extremely low permeability. The capability of the current experimental device for measuring the pressure in the region of moisture clog needs to be analyzed.

4. Permeability of concrete needs to be further studied at both residual and hot state with a standard testing method. Current permeability measurements at hot state need very long duration to reach a stable state. It is inconvenient for large batch measurements. Explosive spalling occurs within several minutes of heating. Actual permeability in heated UHPCs may not be the same with the data measured from the long duration tests conducted in this research program.

Publications

- **Li, Y.**, K. H. Tan and E.-H. Yang (2018). Influence of aggregate size and inclusion of polypropylene and steel fibers on the hot permeability of ultra-high performance concrete (UHPC) at elevated temperature. Construction and Building Materials 169: 629-637.
- **Li, Y.**, Tan, K. H., Zhang, D. (2016). Optimization of Compressive Strength and Tensile Strength of Ultra-High Performance Concrete. In Proceedings of 4th International Symposium on Ultra-High Performance Concrete and High Performance Materials.
- **Li, Y.**, Tan, K. H. (2016). Effects of polypropylene and steel fibers on permeability of Ultra-high performance concrete at hot state. In Proceedings of 9TH INTERNATIONAL CONFERENCE ON STRUCTURES IN FIRE.
- **Li, Y.**, Yang, E-H., Tan, K. H. Synergistic effect of polypropylene and steel fibers on spalling protection of ultra-high performance concrete in fire. (under review)
- **Li, Y.**, Yang, E-H., Zhang, Y., Tan, K. H. Effects of heating followed by water quenching on strength and microstructure of ultra-high performance concrete (UHPC). (under review)
- **Li, Y.**, Yang, E-H., Tan, K. H. Effects of elevated temperature and water quenching on strength and microstructure of ultra-high performance concrete (UHPC) with larger aggregate, polypropylene and steel fibers. (under review)
- **Li, Y.**, Pimienta, P., Pinoteau, N., Tan, K. H. Effect of aggregate size and inclusion of polypropylene and steel fibers on explosive spalling and pore pressure in ultra-high-performance concrete (UHPC) at elevated temperature. (under review)

References

Abbas, A., M. Carcasses and J.-P. Ollivier (1999). "Gas permeability of concrete in relation to its degree of saturation." Materials and Structures **32**(1): 3-8.

Abyaneh, S. D., H. S. Wong and N. R. Buenfeld (2016). "Simulating the effect of microcracks on the diffusivity and permeability of concrete using a three-dimensional model." Computational Materials Science **119**: 130-143.

Ahmed, S. F. U., M. Maalej and P. Paramasivam (2007). "Flexural responses of hybrid steel–polyethylene fiber reinforced cement composites containing high volume fly ash." Construction and Building Materials **21**(5): 1088-1097.

Akhavan, A., S.-M.-H. Shafaatian and F. Rajabipour (2012). "Quantifying the effects of crack width, tortuosity, and roughness on water permeability of cracked mortars." Cement and concrete research **42**(2): 313-320.

Alarcon-Ruiz, L., G. Platret, E. Massieu and A. Ehrlacher (2005). "The use of thermal analysis in assessing the effect of temperature on a cement paste." Cement and concrete research **35**(3): 609-613.

Ammouche, A., J. Riss, D. Breysse and J. Marchand (2001). "Image analysis for the automated study of microcracks in concrete." Cement and Concrete Composites **23**(2): 267-278.

Arunachalam, A. and K. Jayakumar (2015). "Performance of polypropylene fibre in high-performance concrete." Proceedings of the ICE - Construction Materials: 1-4.

Authority, C. T. S. and R. Allison (1997). Inquiry into the fire on heavy goods vehicle shuttle 7539 on 18 November 1996, Stationery Office.

Aydın, S. and B. Baradan (2007). "Effect of pumice and fly ash incorporation on high temperature resistance of cement based mortars." Cement and concrete research **37**(6): 988-995.

Bangi, M. R. and T. Horiguchi (2011). "Pore pressure development in hybrid fibre-reinforced high strength concrete at elevated temperatures." Cement and concrete research **41**(11): 1150-1156.

Bangi, M. R. and T. Horiguchi (2012). "Effect of fibre type and geometry on maximum pore pressures in fibre-reinforced high strength concrete at elevated temperatures." Cement and concrete research **42**(2): 459-466.

References

Banthia, N. and R. Gupta (2004). "Hybrid fiber reinforced concrete (HyFRC): fiber synergy in high strength matrices." Materials and Structures **37**(10): 707-716.

Banthia, N., F. Majdzadeh, J. Wu and V. Bindiganavile (2014). "Fiber synergy in Hybrid Fiber Reinforced Concrete (HyFRC) in flexure and direct shear." Cement and Concrete Composites **48**: 91-97.

Banthia, N. and N. Nandakumar (2003). "Crack growth resistance of hybrid fiber reinforced cement composites." Cement and Concrete Composites **25**(1): 3-9.

Bary, B., G. Ranc, S. Durand and O. Carpentier (2008). "A coupled thermo-hydro-mechanical-damage model for concrete subjected to moderate temperatures." International Journal of Heat and Mass Transfer **51**(11-12): 2847-2862.

Bazant, Z. (2005). Concrete creep at high temperature and its interaction with fracture: recent progress. Concreep-7 conference: creep. Shrinkage and durability of concrete and concrete structures.

Bazant, Z. P. (1997). Analysis of pore pressure, thermal stress and fracture in rapidly heated concrete. International workshop on fire performance of high-strength concrete.

Bear, J. (2013). Dynamics of fluids in porous media, Courier Corporation.

Behnood, A. and H. Ziari (2008). "Effects of silica fume addition and water to cement ratio on the properties of high-strength concrete after exposure to high temperatures." Cement and Concrete Composites **30**(2): 106-112.

Bentur, A. and S. Mindess (2006). Fibre reinforced cementitious composites, CRC Press.

Bentz, D. P. (2000). "Fibers, percolation, and spalling of high-performance concrete." ACI Materials Journal-American Concrete Institute **97**(3): 351-359.

Berhan, L. and A. Sastry (2007). "Modeling percolation in high-aspect-ratio fiber systems. I. Soft-core versus hard-core models." Physical Review E **75**(4): 041120.

Bischof, P., W. Borgogno and W. Kaufmann (2017). Risk-Based Design for Fire Spalling of ConcreteRISK-BASED DESIGN FOR FIRE SPALLING OF CONCRETE. 5th International Workshop on Concrete Spalling due to Fire Exposure, RISE Research Institutes of Sweden.

References

Bosnjak, J. (2014). "Explosive spalling and permeability of high performance concrete under fire: numerical and experimental investigations."

Bošnjak, J., J. Ožbolt and R. Hahn (2013). "Permeability measurement on high strength concrete without and with polypropylene fibers at elevated temperatures using a new test setup." Cement and concrete research **53**: 104-111.

Boström, L. and R. Jansson (2006). Spalling of self compacting concrete. 4th International Workshop on Structures in Fire. Averio, Portugal. 2006, Universidade de Averio.

Boström, L. and R. Jansson (2007). Fire Spalling of Self-compacting Concrete. 5th International RILEM Symposium on Self-Compacting Concrete. Ghent, Belgium**:** 741-745.

Boström, L. and R. Jansson (2008). Self-compacting concrete exposed to fire.

Boström, L., U. Wickström and B. Adl-Zarrabi (2007). "Effect of specimen size and loading conditions on spalling of concrete." Fire and Materials **31**(3): 173-186.

Boulay, C., P. Rossi and J.-L. Tailhan (2004). Uniaxial tensile test on a new cement composite having a hardening behaviour. 6th International RILEM symposium on fibre-reinforced concretes (BEFIB'2004), RILEM, Varenna, Italy.

Castillo, C. and A. DurraniI (1990). "Effect of transient high temperature on high-strength concrete." ACI Materials Journal **87**(1).

Chandrappa, A. K. and K. P. Biligiri (2016). "Comprehensive investigation of permeability characteristics of pervious concrete: A hydrodynamic approach." Construction and Building Materials **123**: 627-637.

Chen, B. and J. Liu (2004). "Residual strength of hybrid-fiber-reinforced high-strength concrete after exposure to high temperatures." Cement and concrete research **34**(6): 1065-1069.

Choi, J.-I., B. Y. Lee, R. Ranade, V. C. Li and Y. Lee (2016). "Ultra-high-ductile behavior of a polyethylene fiber-reinforced alkali-activated slag-based composite." Cement and Concrete Composites **70**: 153-158.

Choumanidis, D., E. Badogiannis, P. Nomikos and A. Sofianos (2016). "The effect of different fibres on the flexural behaviour of concrete exposed to normal and elevated temperatures." Construction and Building Materials.

References

Christiaanse, A., A. Langhorst and A. Gerriste (1972). "Discussion of fire resistance of lightweight concrete and spalling." Dutch Society of Engineers (STUVO), Report **12**.

Connolly, R. J. (1995). The spalling of concrete in fires, Aston University.

Consolazio, G. R., M. McVay and J. Rish III (1997). Measurement and prediction of pore pressure in cement mortar subjected to elevated temperature. Proceedings of the International Workshop on Fire Performance of High-Strength Concrete, NIST, Gaithersburg, Maryland.

Consolazio, G. R., M. C. McVay and J. W. Rish III (1998). "Measurement and prediction of pore pressures in saturated cement mortar subjected to radiant heating." ACI Materials Journal **95**(5).

Copier, W. (1983). "The spalling of normal weight and lightweight concrete exposed to fire." Special Publication **80**: 219-236.

Dauti, D., B. Weber, S. D. Pont, A. Tengattini, N. Toropovs and M. Briffaut (2017). First results on fast neutron tomography of heated concrete. 5th International Workshop on Concrete Spalling due to Fire Exposure, RISE Research Institutes of Sweden.

Davie, C. T., C. J. Pearce and N. Bićanić (2012). "Aspects of Permeability in Modelling of Concrete Exposed to High Temperatures." Transport in porous media **95**(3): 627-646.

Dawood, E. T. and M. Ramli (2011). "High strength characteristics of cement mortar reinforced with hybrid fibres." Construction and Building Materials **25**(5): 2240-2247.

de Larrard, F. and T. Sedran (1994). "Optimization of ultra-high-performance concrete by the use of a packing model." Cement and concrete research **24**(6): 997-1009.

Debicki, G., R. Haniche and F. Delhomme (2012). "An experimental method for assessing the spalling sensitivity of concrete mixture submitted to high temperature." Cement and Concrete Composites **34**(8): 958-963.

der Heijden, G. H. A. v., L. Pel and O. C. G. Adan (2012). "Fire spalling of concrete, as studied by NMR." Cement and concrete research **42**(2): 265-271.

Diederichs, U., U. Jumppanen and U. Schneider (1995). High temperature properties and spalling behaviour of high strength concrete. Proceedings of Fourth Weimar workshop on high performance concrete, HAB Weimar, Germany.

References

Ding, Y., C. Zhang, M. Cao, Y. Zhang and C. Azevedo (2016). "Influence of different fibers on the change of pore pressure of self-consolidating concrete exposed to fire." Construction and Building Materials **113**: 456-469.

Dong, Y. (2018). "Performance assessment and design of ultra-high performance concrete (UHPC) structures incorporating life-cycle cost and environmental impacts." Construction and Building Materials **167**: 414-425.

Dougill, J. (1971). The effect of high temperature on concrete with reference to thermal spalling, PhD Thesis. Imperial College, London.

Dougill, J. (1972). "Modes of failure of concrete panels exposed to high temperatures." Magazine of Concrete Research **24**(79): 71-76.

du Béton, F. I. (2012). "Model Code 2010-Final draft, Volume 1. fib Bulletin, 65." Lausanne, Switzerland.

Felicetti, R., F. Lo Monte and P. Pimienta (2017). "A new test method to study the influence of pore pressure on fracture behaviour of concrete during heating." Cement and concrete research **94**: 13-23.

Fu, Y., Y. Wong, C. Tang and C. Poon (2004). "Thermal induced stress and associated cracking in cement-based composite at elevated temperatures—Part I: Thermal cracking around single inclusion." Cement and Concrete Composites **26**(2): 99-111.

Gales, J., T. Parker, D. Cree and M. Green (2015). "Fire Performance of Sustainable Recycled Concrete Aggregates: Mechanical Properties at Elevated Temperatures and Current Research Needs." Fire Technology.

Gallé, C. and J. Sercombe (2001). "Permeability and pore structure evolution of silicocalcareous and hematite high-strength concretes submitted to high temperatures." Materials and Structures **34**(10): 619-628.

Gary, M. (1916). Brandproben an Eisenbetonbauten: Ausgeführt im königl. Materialprüfungsamt zu Berlin-Lichterfelde-West in d. Jahren 1914 u. 1915 - Deutscher Ausschuss für Eisenbeton Heft 33. 1916, W. Ernst und Sohn.

Gawin, D., C. Alonso, C. Andrade, C. E. Majorana and F. Pesavento (2005). "Effect of damage on permeability and hygro-thermal behaviour of HPCs at elevated temperatures: Part 1. Experimental results." Computers and Concrete **2**(3): 189-202.

References

Gawin, D., F. Pesavento and B. A. Schrefler (2003). "Modelling of hygro-thermal behaviour of concrete at high temperature with thermo-chemical and mechanical material degradation." Computer methods in applied mechanics and engineering **192**(13-14): 1731-1771.

Ghabezloo, S., J. Sulem and J. Saint-Marc (2009). "The effect of undrained heating on a fluid-saturated hardened cement paste." Cement and concrete research **39**(1): 54-64.

Grassl, P. and J. Bolander (2016). "Three-Dimensional Network Model for Coupling of Fracture and Mass Transport in Quasi-Brittle Geomaterials." Materials **9**(9): 782.

Grassl, P., H. S. Wong and N. R. Buenfeld (2010). "Influence of aggregate size and volume fraction on shrinkage induced micro-cracking of concrete and mortar." Cement and concrete research **40**(1): 85-93.

Gu, H. (2016). Three-dimensional modeling of percolation behavior of electrical conductivity in segregated network polymer nanocomposites using Monte Carlo method. 2016 International Symposium on Materials Science and Engineering.

Guerrieri, M. and S. Fragomeni (2016). "Mechanisms of Spalling of Concrete Panels of Different Geometry in Hydrocarbon Fire." Journal of Materials in Civil Engineering: 04016164.

Guo, F., Y. Yuan and H. A. Mang (2016). "Determination of the relative significance of material parameters for concrete exposed to fire." International Journal of Heat and Mass Transfer **100**: 191-198.

Habel, K., M. Viviani, E. Denarié and E. Brühwiler (2006). "Development of the mechanical properties of an Ultra-High Performance Fiber Reinforced Concrete (UHPFRC)." Cement and concrete research **36**(7): 1362-1370.

Hager, I. (2013). "Behaviour of cement concrete at high temperature." Bulletin of the Polish Academy of Sciences: Technical Sciences **61**(1): 145-154.

Haneef, T. K., K. Kumari, C. K. Mukhopadhyay, Venkatachalapathy, B. P. Rao and T. Jayakumar (2013). "Influence of fly ash and curing on cracking behavior of concrete by acoustic emission technique." Construction and Building Materials **44**: 342-350.

Hanehara, S., F. Tomosawa, M. Kobayakawa and K. Hwang (2001). "Effects of water/powder ratio, mixing ratio of fly ash, and curing temperature on pozzolanic reaction of fly ash in cement paste." Cement and concrete research **31**(1): 31-39.

References

Hannant, P. (1978). Fibre cements and fibre concretes.

Harmathy, T. Z. (1965). "Effect of moisture on the fire endurance of building elements." ASTM special technical publication(385): 74-95.

Hasenjäger, S. (1935). Ueber das Verhalten des Betons und Eisenbetons im Feuer und die Ausbildung von Dehnungsfugen im Eisenbetonbau.

Hassan, A. M. T., S. W. Jones and G. H. Mahmud (2012). "Experimental test methods to determine the uniaxial tensile and compressive behaviour of ultra high performance fibre reinforced concrete (UHPFRC)." Construction and Building Materials **37**: 874-882.

He, S., J. Qiu, J. Li and E.-H. Yang (2017). "Strain hardening ultra-high performance concrete (SHUHPC) incorporating CNF-coated polyethylene fibers." Cement and concrete research **98**: 50-60.

Heo, Y.-S., J. G. Sanjayan, C.-G. Han and M.-C. Han (2010). "Synergistic effect of combined fibers for spalling protection of concrete in fire." Cement and concrete research **40**(10): 1547-1554.

Heo, Y.-S., J. G. Sanjayan, C.-G. Han and M.-C. Han (2012). "Relationship between inter-aggregate spacing and the optimum fiber length for spalling protection of concrete in fire." Cement and concrete research **42**(3): 549-557.

Hermathy, T. (1965). "Effect of moisture on the fire endurance of building materials. Moisture in Relation to Fire Tests." ASTM special technical publication(385): 74-95.

Hertz, K. (1984). "Explosion of silica-fume concrete." Fire Safety Journal **8**(1): 77.

Hertz, K. (1985). Analyses of prestressed concrete structures exposed to fire, Technical University of Denmark.

Hertz, K. D. (1992). "Danish investigations on silica fume concretes at elevated temperatures." ACI Materials Journal **89**(4).

Hertz, K. D. (2003). "Limits of spalling of fire-exposed concrete." Fire Safety Journal **38**(2): 103-116.

Hertz, K. D. (2005). "Concrete strength for fire safety design." Magazine of Concrete Research **57**(8): 445-453.

Holschemacher, K., T. Mueller and Y. Ribakov (2010). "Effect of steel fibres on mechanical properties of high-strength concrete." Materials & Design **31**(5): 2604-2615.

Homand, F., D. Hoxha, T. Belem, M.-N. Pons and N. Hoteit (2000). "Geometric analysis of damaged microcracking in granites." Mechanics of Materials **32**(6): 361-376.

Hsie, M., C. Tu and P. S. Song (2008). "Mechanical properties of polypropylene hybrid fiber-reinforced concrete." Materials Science and Engineering: A **494**(1-2): 153-157.

Ichikawa, Y. (2000). Prediction of pore pressures, heat and moisture transfer leading to spalling of concrete during fire, Imperial College London (University of London).

Idiart, A., J. Bisschop, A. Caballero and P. Lura (2012). "A numerical and experimental study of aggregate-induced shrinkage cracking in cementitious composites." Cement and concrete research **42**(2): 272-281.

Jacobs, F. (1998). "Permeability to gas of partially saturated concrete." Magazine of Concrete Research **50**(2).

Jansson, R. (2013). Fire spalling of concrete–A historical overview. MATEC Web of Conferences, EDP Sciences.

Jansson, R. and L. Boström (2009). Fire spalling—the moisture effect. 1st international workshop on concrete spalling due to fire exposure—from real life experiences and practical applications to lab-scale investigations and numerical modelling. MFPA Institute Leipzig, Germany.

Jansson, R., L. Boström and J. Silfwerbrand (2013). "Fire spalling of concrete."

Jeyaprabha, B., G. Elangovan and P. Prakash (2016). "Effects of elevated temperature and water quenching on strength and microstructure of mortars with river sand substitutes." Construction and Building Materials **114**: 688-698.

Jochen, R. and M. Christoph (2017). The influence of the pore size distribution and the chemical composition of cement paste on the explosive spalling of concrete. 5th International Workshop on Concrete Spalling due to Fire Exposure, RISE Research Institutes of Sweden.

Jumppanen, U.-M. (1989). "Effect of strength on fire behaviour of concrete." Nordic concrete research(8): 116-127.

Kalifa, P., G. Chene and C. Galle (2001). "High-temperature behaviour of HPC with polypropylene fibres: From spalling to microstructure." Cement and concrete research **31**(10): 1487-1499.

Kalifa, P., F.-D. Menneteau and D. Quenard (2000). "Spalling and pore pressure in HPC at high temperatures." Cement and concrete research **30**(12): 1915-1927.

Kang, S.-T. and J.-K. Kim (2011). "The relation between fiber orientation and tensile behavior in an Ultra High Performance Fiber Reinforced Cementitious Composites (UHPFRCC)." Cement and concrete research **41**(10): 1001-1014.

Kaviany, M. (2012). Principles of heat transfer in porous media, Springer Science & Business Media.

Kawasaki, Y., M. Ozawa, S. Uchida and T. Tanibe (2015). Basic study on evaluation for explosive spalling process in concrete by acoustic emission methods. 4th International Workshop on Concrete Spalling due to Fire Exposure.

Khoury, G. A. (2000). "Effect of fire on concrete and concrete structures." Progress in Structural Engineering and Materials **2**(4): 429-447.

Khoury, G. A. and Y. Anderberg (2000). "Concrete spalling review." Fire Safety Design: 1-60.

Khoury, G. A. and B. Willoughby (2008). "Polypropylene fibres in heated concrete. Part 1: Molecular structure and materials behaviour." Magazine of Concrete Research **60**(2): 125-136.

Khoylou, N. (1997). Modelling of moisture migration and spalling behaviour in non-uniformly heated concrete, Imperial College London (University of London).

Kim, D. J., S. H. Park, G. S. Ryu and K. T. Koh (2011). "Comparative flexural behavior of Hybrid Ultra High Performance Fiber Reinforced Concrete with different macro fibers." Construction and Building Materials **25**(11): 4144-4155.

Klingsch, E. W., F. Lu, R. Kässmann and K. H. Tan (2015). Tests on the hot and residual permeability of concrete at high temperatures. 4th International Workshop on Concrete Spalling due to Fire Exposure. F. Dehn. Leipzig, MFPA Leipzig**:** 65-75.

Klingsch, E. W. H. (2014). EXPLOSIVE SPALLING OF CONCRETE IN FIRE. Zurich, ETH. **Doctor of Sciences**.

References

Klinkenberg, L. (1941). The permeability of porous media to liquids and gases. Drilling and production practice, American Petroleum Institute.

Knack, I. (2011). The use of PP fibres in tunnel construction to avoid explosive concrete spalling in case of fire. New test results for the clarification of the mode of action. Proceedings of the 2nd International RILEM Workshop on Concrete Spalling due to Fire Exposure, Delft, The Netherlands.

Kodur, V. (2000). Spalling in high strength concrete exposed to fire—concerns, causes, critical parameters and cures. Proceedings, ASCE Structures Congress, Philadelphia, PA.

Kodur, V., F.-P. Cheng, T.-C. Wang and M. Sultan (2003). "Effect of strength and fiber reinforcement on fire resistance of high-strength concrete columns." Journal of Structural Engineering **129**(2): 253-259.

Kodur, V. and L. Phan (2007). "Critical factors governing the fire performance of high strength concrete systems." Fire Safety Journal **42**(6): 482-488.

Kodur, V. K. and R. McGrath (2006). "Effect of silica fume and lateral confinement on fire endurance of high strength concrete columns." Canadian Journal of Civil Engineering **33**(1): 93-102.

Kodur, V. K. R. and L. Phan (2007). "Critical factors governing the fire performance of high strength concrete systems." Fire Safety Journal **42**(6-7): 482-488.

Kollek, J. (1989). "The determination of the permeability of concrete to oxygen by the Cembureau method—a recommendation." Materials and Structures **22**(3): 225-230.

Korpa, A., T. Kowald and R. Trettin (2009). "Phase development in normal and ultra high performance cementitious systems by quantitative X-ray analysis and thermoanalytical methods." Cement and concrete research **39**(2): 69-76.

Kumlutaş, D., I. H. Tavman and M. T. Çoban (2003). "Thermal conductivity of particle filled polyethylene composite materials." Composites Science and Technology **63**(1): 113-117.

Landis, E. N., T. Zhang, E. N. Nagy, G. Nagy and W. R. Franklin (2006). "Cracking, damage and fracture in four dimensions." Materials and Structures **40**(4): 357-364.

Lau, A. and M. Anson (2006). "Effect of high temperatures on high performance steel fibre reinforced concrete." Cement and concrete research **36**(9): 1698-1707.

References

Lee, G., D. Han, M.-C. Han, C.-G. Han and H.-J. Son (2012). "Combining polypropylene and nylon fibers to optimize fiber addition for spalling protection of high-strength concrete." Construction and Building Materials **34**: 313-320.

Li, K., P. Stroeven, M. Stroeven and L. J. Sluys (2016). "Estimating permeability of cement paste using pore characteristics obtained from DEM-based modelling." Construction and Building Materials **126**: 740-746.

Li, V. C. and C. K. Leung (1992). "Steady-state and multiple cracking of short random fiber composites." Journal of Engineering Mechanics **118**(11): 2246-2264.

Li, X., Z. Li, M. Onofrei, G. Ballivy and K. Khayat (1999). "Microstructural characteristics of HPC under different thermo-mechanical and thermo-hydraulic conditions." Materials and Structures **32**(10): 727-733.

Lin, W.-M., T. Lin and L. Powers-Couche (1996). "Microstructures of fire-damaged concrete." ACI Materials Journal **93**(3).

Litorowicz, A. (2006). "Identification and quantification of cracks in concrete by optical fluorescent microscopy." Cement and concrete research **36**(8): 1508-1515.

Liu, J., F. Han, G. Cui, Q. Zhang, J. Lv, L. Zhang and Z. Yang (2016). "Combined effect of coarse aggregate and fiber on tensile behavior of ultra-high performance concrete." Construction and Building Materials **121**: 310-318.

Liu, J., C. Li, J. Liu, G. Cui and Z. Yang (2013). "Study on 3D spatial distribution of steel fibers in fiber reinforced cementitious composites through micro-CT technique." Construction and Building Materials **48**: 656-661.

Liu, X., G. Ye, G. De Schutter, Y. Yuan and L. Taerwe (2008). "On the mechanism of polypropylene fibres in preventing fire spalling in self-compacting and high-performance cement paste." Cement and concrete research **38**(4): 487-499.

Lock, P. A., X. Jing, R. W. Zimmerman and E. M. Schlueter (2002). "Predicting the permeability of sandstone from image analysis of pore structure." Journal of Applied Physics **92**(10): 6311.

Long, W. G. and H. H. Moeller (1983). Rapid-fire refractories, Google Patents.

Loosveldt, H., Z. Lafhaj and F. Skoczylas (2002). "Experimental study of gas and liquid permeability of a mortar." Cement and concrete research **32**(9): 1357-1363.

Lottman, B. B. G. (2017). "The spalling mechanism of fire exposed concrete."

Ma, H. M. and X. L. Gao (2008). "A three-dimensional Monte Carlo model for electrically conductive polymer matrix composites filled with curved fibers." Polymer **49**(19): 4230-4238.

Ma, Q., R. Guo, Z. Zhao, Z. Lin and K. He (2015). "Mechanical properties of concrete at high temperature—A review." Construction and Building Materials **93**: 371-383.

Martienssen, W. and H. Warlimont (2006). Springer handbook of condensed matter and materials data, Springer Science & Business Media.

Mater., A. S. T. (1997). ASTM C 1018-97, Standard Test Method for Flexural Toughness and First-Crack Strength of Fiber-Reinforced Concrete (Using Beam With Third-Point Loading).

Mater., A. S. T. (2011). ASTM C 109/C 109 M-11, Standard Test Method for Compressive Strength of Hydraulic Cement Mortars (Using 2-in. or 50-mm Cube Specimens).

Mater., A. S. T. (2012). ASTM C 1609/C 1609 M-12, Standard Test Method for Flexural Performance of Fiber-Reinforced Concrete (Using Beam With Third-Point Loading).

Mazloom, M., A. A. Ramezanianpour and J. J. Brooks (2004). "Effect of silica fume on mechanical properties of high-strength concrete." Cement and Concrete Composites **26**(4): 347-357.

Mazzucco, G., C. E. Majorana and V. A. Salomoni (2015). "Numerical simulation of polypropylene fibres in concrete materials under fire conditions." Computers & Structures **154**: 17-28.

Mehta, P. K. and P. J. Monteiro (2006). Concrete: Microstructure, Properties and Materials. , McGraw-Hill.

Meyer-Ottens, C. (1972). Zur Frage der Abplatzungen an Betonbauteilen aus Normalbeton bei Brandbeanspruchung, na.

Miah, M. J., H. Carré, P. Pimienta, N. Pinoteau and C. L. Borderie (2015). Effect of uniaxial mechanical loading on fire spalling of concrete. 4th International Workshop on Concrete Spalling due to Fire Exposure.

Miah, M. J., F. L. Monte, R. Felicetti, P. Pimienta, H. Carré and C. l. Borderie (2017). Experimental Investigation on Fire Spalling Behaviour of Concrete: Effect of Biaxial Compressive Loading and

References

Cement Type. 5th International Workshop on Concrete Spalling due to Fire Exposure, RISE Research Institutes of Sweden.

Mindeguia, J.-C., P. Pimienta, H. Carré and C. L. Borderie (2013). "Experimental analysis of concrete spalling due to fire exposure." European Journal of Environmental and Civil Engineering **17**(6): 453-466.

Mindeguia, J.-C., P. Pimienta, A. Noumowé and M. Kanema (2010). "Temperature, pore pressure and mass variation of concrete subjected to high temperature — Experimental and numerical discussion on spalling risk." Cement and concrete research **40**(3): 477-487.

Morsy, M., S. Alsayed and M. Aqel (2010). "Effect of elevated temperature on mechanical properties and microstructure of silica flour concrete." International journal of civil & environmental engineering **10**(1): 1-6.

Mouton, P. R. (2002). Principles and practices of unbiased stereology: an introduction for bioscientists, JHU Press.

Naaman, A. (1996). Characterization of high performance fiber reinforced cement composites-HPFRCC. High performance fiber reinforced cement composites.

Natsuki, T., M. Endo and T. Takahashi (2005). "Percolation study of orientated short-fiber composites by a continuum model." Physica A: Statistical Mechanics and its Applications **352**(2): 498-508.

Neithalath, N., M. S. Sumanasooriya and O. Deo (2010). "Characterizing pore volume, sizes, and connectivity in pervious concretes for permeability prediction." Materials Characterization **61**(8): 802-813.

Nemati, K. M. (1994). Generation and Interaction of Compressive Stress-Induced Microcracks in Concrete. Department of Civil Engineering, University of California at Berkeley. **Ph.D.**

Neville, A. and P.-C. Aitcin (1998). "High performance concrete—an overview." Materials and Structures **31**(2): 111-117.

Noumowe, A. N., R. Siddique and G. Debicki (2009). "Permeability of high-performance concrete subjected to elevated temperature (600°C)." Construction and Building Materials **23**(5): 1855-1861.

Oertel, T., F. Hutter, U. Helbig and G. Sextl (2014). "Amorphous silica in ultra-high performance concrete: First hour of hydration." Cement and concrete research **58**: 131-142.

Ogale, A. and S. Wang (1993). "Simulation of the percolation behavior of quasi-and transversely isotropic short-fiber composites with a continuum model." Composites Science and Technology **46**(4): 379-388.

Ozawa, M. and H. Morimoto (2014). "Effects of various fibres on high-temperature spalling in high-performance concrete." Construction and Building Materials **71**: 83-92.

Ozawa, M., S. Uchida, T. Kamada and H. Morimoto (2012). "Study of mechanisms of explosive spalling in high-strength concrete at high temperatures using acoustic emission." Construction and Building Materials **37**: 621-628.

Papadakis, V., M. Fardis and C. Vayenas (1992). "Effect of composition, environmental factors and cement-lime mortar coating on concrete carbonation." Materials and Structures **25**(5): 293-304.

Park, S. H., D. J. Kim, G. S. Ryu and K. T. Koh (2012). "Tensile behavior of Ultra High Performance Hybrid Fiber Reinforced Concrete." Cement and Concrete Composites **34**(2): 172-184.

Peng, G.-F. and Z.-S. Huang (2008). "Change in microstructure of hardened cement paste subjected to elevated temperatures." Construction and Building Materials **22**(4): 593-599.

Peng, G.-F., W.-W. Yang, J. Zhao, Y.-F. Liu, S.-H. Bian and L.-H. Zhao (2006). "Explosive spalling and residual mechanical properties of fiber-toughened high-performance concrete subjected to high temperatures." Cement and concrete research **36**(4): 723-727.

Peng, G. F. (2000). Evaluation of fire damage to high performance concrete. Hong Kong, Hong Kong Polytechnic University. **Doctor**.

Persson, B. (2004). "Fire resistance of self-compacting concrete, SCC." Materials and Structures **37**(9): 575-584.

Peters, S. T. (2013). Handbook of composites, Springer Science & Business Media.

Petrov-Denisov, V., L. Maslennikov and A. Pitckob (1972). "Heat-and moisture transport during drying and first heating of heat resistant concrete." Concrete and Reinforced Concrete **2**: 17-18.

Phan, L. T. (2002). "High-strength concrete at high temperature-An overview." Proceedings of 6th International Symposiumon Utilization of High Strength/High Performance Concrete, Leipzig, Germany: 501-518.

Piasta, J. (1984). "Heat deformations of cement paste phases and the microstructure of cement paste." Materials and Structures **17**(6): 415-420.

Picandet, V., A. Khelidj and G. Bastian (2001). "Effect of axial compressive damage on gas permeability of ordinary and high-performance concrete." Cement and concrete research **31**(11): 1525-1532.

Picandet, V., A. Khelidj and H. Bellegou (2009). "Crack effects on gas and water permeability of concretes." Cement and concrete research **39**(6): 537-547.

Poon, C.-S., S. Azhar, M. Anson and Y.-L. Wong (2001). "Comparison of the strength and durability performance of normal-and high-strength pozzolanic concretes at elevated temperatures." Cement and concrete research **31**(9): 1291-1300.

Powers, T. C. and T. L. Brownyard (1946). Studies of the physical properties of hardened Portland cement paste. Journal Proceedings.

Prabha, S. L., J. Dattatreya, M. Neelamegam and M. Seshagirirao (2010). "Study on Stress-Strain Properties of Reactive Powder Concrete under Uniaxial Compression." International Journal of Engineering Science and Technology **2**(11): 6408-6416.

Progelhof, R., J. Throne and R. Ruetsch (1976). "Methods for predicting the thermal conductivity of composite systems: a review." Polymer Engineering & Science **16**(9): 615-625.

Qian, C. and P. Stroeven (2000). "Development of hybrid polypropylene-steel fibre-reinforced concrete." Cement and concrete research **30**(1): 63-69.

Ranade, R., V. C. Li, M. D. Stults, W. F. Heard and T. S. Rushing (2013). "Composite Properties of High-Strength, High-Ductility Concrete." ACI Materials Journal **110**(4).

Richard, P. and M. Cheyrezy (1994). Reactive Powder Concrete with high ductility and 200-800 MPa compressive strength. ACI Spring Convention, Concrete Technology: Past, Present, and Future. San Francisco, Special Publication. **144:** 507-518.

Richard, P. and M. Cheyrezy (1995). "Composition of reactive powder concretes." Cement and concrete research **25**(7): 1501-1511.

Rossi, P., A. Arca, E. Parant and P. Fakhri (2005). "Bending and compressive behaviours of a new cement composite." Cement and concrete research **35**(1): 27-33.

Roy, R. K. (2010). A primer on the Taguchi method, Society of Manufacturing Engineers.

Saad, M., S. Abo-El-Enein, G. Hanna and M. Kotkata (1996). "Effect of temperature on physical and mechanical properties of concrete containing silica fume." Cement and concrete research **26**(5): 669-675.

Saito, H. (1966). "Explosive spalling of prestressed concrete in fire." Bulletin of Japan Association for Fire Science and Engineering **15**(2): 23-30.

Samaha, H. R. and K. C. Hover (1992). "Influence of microcracking on the mass transport properties of concrete." Materials Journal **89**(4): 416-424.

Sanjayan, G., L. Stocks and L. Stocks (1993). "Spalling of high-strength silica fume concrete in fire." ACI Materials Journal **90**(2).

Sanjuán, M. Á., C. Argiz, J. C. Gálvez and A. Moragues (2015). "Effect of silica fume fineness on the improvement of Portland cement strength performance." Construction and Building Materials **96**: 55-64.

Schneider, U. (1982). Verhalten von Beton bei hohen Temperaturen, Ernst.

Seleem, H. E. D. H., A. M. Rashad and T. Elsokary (2011). "Effect of elevated temperature on physico-mechanical properties of blended cement concrete." Construction and Building Materials **25**(2): 1009-1017.

Sellevold, E. and Ø. Bjøntegaard (2006). "Coefficient of thermal expansion of cement paste and concrete: mechanisms of moisture interaction." Materials and Structures **39**(9): 809-815.

Sertmehmetoglu, Y. (1977). On a mechanism of spalling of concrete under fire conditions, University of London.

Shi, C., Z. Wu, J. Xiao, D. Wang, Z. Huang and Z. Fang (2015). "A review on ultra high performance concrete: Part I. Raw materials and mixture design." Construction and Building Materials **101**: 741-751.

Shi, C. and P. Xie (1998). "Interface between cement paste and quartz sand in alkali-activated slag mortars." Cement and concrete research **28**(6): 887-896.

References

Shui, Z.-h., R. Zhang, W. Chen and D.-x. Xuan (2010). "Effects of mineral admixtures on the thermal expansion properties of hardened cement paste." Construction and Building Materials **24**(9): 1761-1767.

Shuttleworth, P. (1997). "Fire Performance of Concrete for Tunnel Linings." Channel Tunnel Rail Link Technical Report, ARUP.

Sivakumar, A. and M. Santhanam (2007). "Mechanical properties of high strength concrete reinforced with metallic and non-metallic fibres." Cement and Concrete Composites **29**(8): 603-608.

Skazlić, M. and D. Bjegović (2008). "Toughness testing of ultra high performance fibre reinforced concrete." Materials and Structures **42**(8): 1025-1038.

Smith, P. and P. J. Lemstra (1980). "Ultra-high-strength polyethylene filaments by solution spinning/drawing." Journal of Materials Science **15**(2): 505-514.

Song, H.-W., S.-W. Pack, S.-H. Nam, J.-C. Jang and V. Saraswathy (2010). "Estimation of the permeability of silica fume cement concrete." Construction and Building Materials **24**(3): 315-321.

Stelzner, L., B. Powierza, F. Weise, T. Oesch, R. Dlugosch and B. Meng (2017). Analysis of moisture transport in unilateral-heated dense high-strength concrete. 5th International Workshop on Concrete Spalling due to Fire Exposure, RISE Research Institutes of Sweden.

Stepkowska, E., J. Blanes, F. Franco, C. Real and J. Pérez-Rodrıguez (2004). "Phase transformation on heating of an aged cement paste." Thermochimica acta **420**(1): 79-87.

Sun, H., J. Yao, D.-y. Fan, C.-c. Wang and Z.-x. Sun (2015). "Gas transport mode criteria in ultra-tight porous media." International Journal of Heat and Mass Transfer **83**: 192-199.

Sun, W., H. Chen, X. Luo and H. Qian (2001). "The effect of hybrid fibers and expansive agent on the shrinkage and permeability of high-performance concrete." Cement and concrete research **31**(4): 595-601.

Tai, Y.-S., H.-H. Pan and Y.-N. Kung (2011). "Mechanical properties of steel fiber reinforced reactive powder concrete following exposure to high temperature reaching 800°C." Nuclear Engineering and Design **241**(7): 2416-2424.

The MathWorks, I. (2015). MATLAB and Optimization Toolbox Release 2015a. Natick, Massachusetts, United States, The MathWorks, Inc.

References

Tran, V. H., F. Meftah, L. Izoret and M. Behloul (2013). On explicit modeling of polypropylene fiber effects on hydro-thermal behavior of heated concrete. MATEC Web of Conferences. **6:** 05007.

Wang, C., C. Yang, F. Liu, C. Wan and X. Pu (2012). "Preparation of Ultra-High Performance Concrete with common technology and materials." Cement and Concrete Composites **34**(4): 538-544.

Wang, D., C. Shi, Z. Wu, J. Xiao, Z. Huang and Z. Fang (2015). "A review on ultra high performance concrete: Part II. Hydration, microstructure and properties." Construction and Building Materials **96**: 368-377.

Wang, X. H., S. Jacobsen, J. Y. He, Z. L. Zhang, S. F. Lee and H. L. Lein (2009). "Application of nanoindentation testing to study of the interfacial transition zone in steel fiber reinforced mortar." Cement and concrete research **39**(8): 701-715.

Wille, K., S. El-Tawil and A. E. Naaman (2014). "Properties of strain hardening ultra high performance fiber reinforced concrete (UHP-FRC) under direct tensile loading." Cement and Concrete Composites **48**: 53-66.

Wille, K., D. J. Kim and A. E. Naaman (2010). "Strain-hardening UHP-FRC with low fiber contents." Materials and Structures **44**(3): 583-598.

Wille, K., A. E. Naaman, S. El-Tawil and G. J. Parra-Montesinos (2011). "Ultra-high performance concrete and fiber reinforced concrete: achieving strength and ductility without heat curing." Materials and Structures **45**(3): 309-324.

Wille, K., A. E. Naaman and G. J. Parra-Montesinos (2011). "Ultra-high performance concrete with compressive strength exceeding 150 MPa (22 ksi): A simpler way." ACI Materials Journal **108**(1).

Wille, K., M. Xu, S. El-Tawil and A. Naaman (2016). "Dynamic impact factors of strain hardening UHP-FRC under direct tensile loading at low strain rates." Materials and Structures **49**(4): 1351-1365.

Wittmann, F. H., P. Wang, P. Zhang and T. Zhao (2015). "Capillary Absorption and Chloride Penetration into High-Performance Fiber-Reinforced Cement-Based Composites (HPFRCC) as Influenced by Tensile Stress and Self-Healing." Restoration of Buildings and Monuments **21**(2-3).

Wong, H. S., R. W. Zimmerman and N. R. Buenfeld (2012). "Estimating the permeability of cement pastes and mortars using image analysis and effective medium theory." Cement and concrete research **42**(2): 476-483.

References

Wong, H. S., M. Zobel, N. R. Buenfeld and R. W. Zimmerman (2009). "Influence of the interfacial transition zone and microcracking on the diffusivity, permeability and sorptivity of cement-based materials after drying." Magazine of Concrete Research **61**(8): 571-589.

Woolson, I. (1905). Investigation of the Effect of Heat Upon the Crushing Strength and Elastic Properties of Concrete. Proceedings of the American Society for Testing Materials.

Wu, Z., H. S. Wong and N. R. Buenfeld (2015). "Influence of drying-induced microcracking and related size effects on mass transport properties of concrete." Cement and concrete research **68**: 35-48.

Xiong, M.-X. and J. Richard Liew (2015). "Spalling behavior and residual resistance of fibre reinforced Ultra-High performance concrete after exposure to high temperatures." Materiales de Construcción **65**(320): e071.

Yang, S., S. Millard, M. Soutsos, S. Barnett and T. Le (2009). "Influence of aggregate and curing regime on the mechanical properties of ultra-high performance fibre reinforced concrete (UHPFRC)." Construction and Building Materials **23**(6): 2291-2298.

Yao, W., J. Li and K. Wu (2003). "Mechanical properties of hybrid fiber-reinforced concrete at low fiber volume fraction." Cement and concrete research **33**(1): 27-30.

Yermak, N., P. Pliya, A. L. Beaucour, A. Simon and A. Noumowé (2017). "Influence of steel and/or polypropylene fibres on the behaviour of concrete at high temperature: Spalling, transfer and mechanical properties." Construction and Building Materials **132**: 240-250.

Yoo, D.-Y., S.-T. Kang, N. Banthia and Y.-S. Yoon (2016). "Nonlinear finite element analysis of ultra-high-performance fiber-reinforced concrete beams." International Journal of Damage Mechanics: 1056789515612559.

Yoo, D.-Y., S.-T. Kang, J.-H. Lee and Y.-S. Yoon (2013). "Effect of shrinkage reducing admixture on tensile and flexural behaviors of UHPFRC considering fiber distribution characteristics." Cement and concrete research **54**: 180-190.

Yoo, D.-Y., S. Kim, G.-J. Park, J.-J. Park and S.-W. Kim (2017). "Effects of fiber shape, aspect ratio, and volume fraction on flexural behavior of ultra-high-performance fiber-reinforced cement composites." Composite Structures.

Yoo, D.-Y., H.-O. Shin, J.-M. Yang and Y.-S. Yoon (2014). "Material and bond properties of ultra high performance fiber reinforced concrete with micro steel fibers." Composites Part B: Engineering **58**: 122-133.

Yu, R., P. Spiesz and H. J. H. Brouwers (2014). "Mix design and properties assessment of Ultra-High Performance Fibre Reinforced Concrete (UHPFRC)." Cement and concrete research **56**: 29-39.

Yu, R., P. Spiesz and H. J. H. Brouwers (2015). "Development of Ultra-High Performance Fibre Reinforced Concrete (UHPFRC): Towards an efficient utilization of binders and fibres." Construction and Building Materials **79**: 273-282.

Zanni, H., M. Cheyrezy, V. Maret, S. Philippot and P. Nieto (1996). "Investigation of hydration and pozzolanic reaction in reactive powder concrete (RPC) using 29Si NMR." Cement and concrete research **26**(1): 93-100.

Zeiml, M., R. Lackner, D. Leithner and J. Eberhardsteiner (2008). "Identification of residual gas-transport properties of concrete subjected to high temperatures." Cement and concrete research **38**(5): 699-716.

Zeiml, M., D. Leithner, R. Lackner and H. A. Mang (2006). "How do polypropylene fibers improve the spalling behavior of in-situ concrete?" Cement and concrete research **36**(5): 929-942.

Zhang, H. L. and C. T. Davie (2013). "A numerical investigation of the influence of pore pressures and thermally induced stresses for spalling of concrete exposed to elevated temperatures." Fire Safety Journal **59**: 102-110.

Zhang, Q., G. Ye and E. Koenders (2013). "Investigation of the structure of heated Portland cement paste by using various techniques." Construction and Building Materials **38**: 1040-1050.

Zhao, J. (2012). Fire-Induced Spalling Modeling of High-Performance Concrete, TU Delft, Delft University of Technology.

Zhao, J., J.-j. Zheng, G.-f. Peng and K. van Breugel (2014). "A meso-level investigation into the explosive spalling mechanism of high-performance concrete under fire exposure." Cement and concrete research **65**: 64-75.

Zhao, J., J.-J. Zheng, G.-F. Peng and K. van Breugel (2017). "Numerical analysis of heating rate effect on spalling of high-performance concrete under high temperature conditions." Construction and Building Materials **152**: 456-466.

Zhou, C., K. Li and X. Pang (2012). "Geometry of crack network and its impact on transport properties of concrete." Cement and concrete research **42**(9): 1261-1272.

References

Zhukov, V. (1976). "Reasons of explosive spalling of concrete by fire." Beton I zhelezobeton (Concrete and Reinforcement Concrete)(3).

Zunino, F., J. Castro and M. Lopez (2015). "Thermo-mechanical assessment of concrete microcracking damage due to early-age temperature rise." Construction and Building Materials **81**: 140-153.